

Control of Voltage-Source Converters and Variable-Speed Drives

Lennart Harnefors

Marko Hinkkanen

Oskar Wallmark

Alejandro Gómez Yepes

Preface

Contents

1	Introduction	9
1.1	Electric Energy	9
1.1.1	Sources	9
1.1.2	Generation	10
1.1.3	Transmission	10
1.1.4	Distribution	11
1.1.5	Consumption	11
1.2	Electrical Drives	12
1.2.1	Benefits of Electrical Drives	13
1.2.2	Motor Types	13
1.2.3	Variable-Speed Drives	15
1.3	Power Electronic Converters	15
1.3.1	DC–DC Converters	15
1.3.2	AC–DC Converters	16
1.3.3	DC–AC Converters	17
1.3.4	AC–AC Converters	18
1.4	Challenges in Control of Converters and Drives	20
2	Systems and Circuits in Power Electronics and Drives	23
2.1	Single-Phase AC Systems	23
2.1.1	Sinusoids and Phasors	23
2.1.2	Active and Reactive Powers	24
2.1.3	Complex Impedances	25
2.1.4	Harmonics	26
2.2	Linear Continuous-Time Systems	28
2.2.1	Definition of Linearity	28
2.2.2	Laplace Transform	28
2.2.3	Transfer Functions	30
2.2.4	Relation Between Poles and System Dynamics	31
2.2.5	Determination of Stability	32
2.2.6	Frequency Response	33
2.2.7	Rise Time and Bandwidth	34
2.2.8	Damping	35
2.2.9	Differential Operator	36
2.2.10	State-Space Models	37
2.3	Nonlinear Continuous-Time Systems	38
2.3.1	Global and Local Stability	40
2.3.2	Analysis of Local Stability by Linearization	40
2.4	Linear Discrete-Time Systems	43

2.4.1	Sampling Process	43
2.4.2	Sampling Theorem and Prefiltering	43
2.4.3	Z Transform	44
2.4.4	Difference Equations and Transfer Functions	45
2.4.5	Relation Between Poles and System Dynamics	46
2.4.6	Shift Operator	47
2.4.7	Euler Discretization	47
2.5	Three-Phase Systems	50
2.5.1	Sequences	50
2.5.2	Instantaneous Power	53
2.5.3	Wye (Y) and Delta (Δ) Connections	53
2.5.4	Multifrequency Waveforms With Balanced Harmonic Content	55
2.6	Space Vectors	56
2.6.1	Two-Phase Representation With Complex Space Vectors	56
2.6.2	Vector Representation of Positive- and Negative-Sequence Components	57
2.6.3	Relations Between Complex Space Vectors and Rotating Phasors	58
2.6.4	Real Space Vectors	60
2.6.5	Complex Gains	61
2.6.6	Coordinate Transformations	62
2.6.7	dq Transformation of Multifrequency Waveforms	63
2.6.8	Coordinate Transformations of Real Space Vectors	64
2.6.9	Instantaneous Power	65
2.6.10	Power of Multifrequency Waveforms	66
2.6.11	Selection of the Space-Vector Scaling Constant	67
2.7	Symmetrical Linear Systems	68
2.7.1	Complex System Models	68
2.7.2	Complex Transfer Functions	69
2.7.3	Coordinate Transformations of Symmetrical Systems	73
2.7.4	Discrete-Time Symmetrical Systems	75
2.8	Normalized (Per-Unit) Values	77
2.8.1	Single-Phase and DC Systems	78
2.8.2	Three-Phase Systems	80
3	Voltage-Source Converters	81
3.1	Buck Converters	81
3.1.1	Switch-Mode Operation	81
3.1.2	Load-Current Ripple	82
3.1.3	Hysteresis Current Control	83
3.2	Single-Phase Voltage-Source Converters	85
3.2.1	Pulsewidth Modulation: Bipolar Switching	85
3.2.2	Suboscillation Method: Bipolar Switching	87
3.2.3	Pulsewidth Modulation: Unipolar Switching	89
3.2.4	Frequency Spectra	89
3.2.5	Digital Implementation Using Synchronous Sampling	90
3.3	Three-Phase Voltage-Source Converters	93
3.3.1	Suboscillation Method	96
3.3.2	Symmetrical Suboscillation Method	97

3.3.3	Prevention of Overmodulation	98
3.3.4	Digital Implementation Using Synchronous Sampling	100
3.3.5	Switching Harmonics	102
4	DC Motor Drives	105
4.1	Mechanics for Rotational Motion	105
4.2	DC Machine Fundamentals	108
4.2.1	Principle	108
4.2.2	Electrical Model	109
4.2.3	Dynamic Model	111
4.2.4	Magnetization by Field Winding	112
4.2.5	Rating and Base Values	113
4.2.6	Normalization of the DC Machine Model	114
4.3	Open-Loop Dynamics	116
4.4	Current Control	120
4.4.1	One-Degree-of-Freedom Controller Design	120
4.4.2	Load-Disturbance Rejection	122
4.4.3	Feedforward of the Back EMF	123
4.4.4	Two-Degrees-of-Freedom Controller Design	123
4.4.5	Voltage Saturation and Antiwindup	125
4.4.6	Digital Implementation	127
4.4.7	Bandwidth Selection	128
4.5	Field Weakening	130
4.6	Speed Control	131
4.6.1	Speed Estimation for Sensorless Control	133
5	AC Motor Drives	135
5.1	AC Machine Fundamentals	135
5.1.1	Synchronous Machines	135
5.1.2	Induction Machines	141
5.2	Dynamic Model for the Induction Motor	142
5.2.1	Inverse- Γ Model	145
5.2.2	Transformation to Synchronous Coordinates	148
5.2.3	Perfect Field Orientation	149
5.2.4	Torque Production	150
5.2.5	Steady-State Relations	151
5.2.6	Field Weakening	151
5.2.7	Motor Parameters	152
5.2.8	Nominal Flux and Torque	152
5.2.9	Steady-State Relations for Line-Connected IMs	153
5.2.10	Transient Impedance	156
5.2.11	Starting Dynamics of Line-Connected IMs	158
5.2.12	Volts-per-Hertz Control	160
5.3	Dynamic Model for the Permanent-Magnet Synchronous Motor	162
5.3.1	Transformation to Synchronous Coordinates	163
5.3.2	Motor Parameters	164
5.3.3	Torque Production and Control Principle	164

5.3.4	Rotor Flux and Base Frequency	165
5.3.5	Field Weakening	165
5.3.6	Transient Impedance	166
5.3.7	Power Factor	166
5.3.8	Salient PMSMs and Reluctance SMs	167
5.4	Unified IM/PMSM Model	170
5.5	Mechanical Dynamics and Speed Control	171
5.5.1	Normalization	172
5.6	Determination of Motor Parameters	173
5.6.1	Induction Motors	173
5.6.2	Permanent-Magnet Synchronous Motors	176
5.6.3	Parameter Variations	177
6	Vector Control Fundamentals	179
6.1	Principle of Vector Control	179
6.1.1	Transformation to Synchronous Coordinates	180
6.2	Introduction to Vector Current Control	181
6.3	Review of Methods for Three-Phase Current Control	182
6.3.1	Hysteresis Control	182
6.3.2	Stationary-Frame PI Control	183
6.3.3	Synchronous-Frame PI Control	184
6.4	Design of Synchronous-Frame Current Controllers	185
6.4.1	Bandwidth Selection	187
6.4.2	PWM, Time-Delay Compensation, and Antiwindup	187
6.5	Synchronization Control Using a Phase-Locked Loop	189
6.5.1	Analysis	192
7	Vector Control of Grid-Connected VSCs	195
8	Vector Control of PMSM Drives	197
8.1	Position-Sensored Control Using Resolvers	197
8.1.1	Excitation	197
8.1.2	Tracking	199
8.2	Position-Sensorless Control Using Back-EMF Information	200
8.2.1	PLL for Sensorless PMSM Drives	201
8.2.2	Analysis and Parameter Selection	202
8.3	Position-Sensorless Control Using Saliency and Signal Injection	206
8.3.1	Signal Injection and Position Extraction	207
8.4	Vector Current Control of Salient PMSMs	209
8.5	Field-Weakening Control	211
8.5.1	Gain Selection	212
9	Vector Control of IM Drives	215
9.1	Speed-Sensored Control	216
9.1.1	Direct Field Orientation Using the Current Model	216
9.1.2	Properties of the Current Model	216
9.1.3	Indirect Field Orientation Using the Current Model	216
9.1.4	Analysis of the Current Model	218

9.1.5	Improved Flux Estimation	220
9.1.6	Modified Current Model	222
9.1.7	Analysis and Parameter Selection of the Modified Current Model	223
9.1.8	Parameter Sensitivity of the Modified Current Model	225
9.2	Speed-Sensorless Control	226
9.2.1	Direct Field Orientation Using the Voltage Model With Modifications . . .	227
9.2.2	Indirect Field Orientation Using the Statically Compensated Voltage Model	229
9.2.3	Properties of the Statically Compensated Voltage Model	231
9.2.4	Instability Phenomena for Regeneration-Mode Operation	233
9.2.5	Complete Stabilization of the Statically Compensated Voltage Model . .	234
9.3	Field-Weakening Control	236
9.3.1	Gain Selection	237
9.3.2	Maximum Torque	238
9.4	Direct Torque Control	242
9.4.1	Control Principle	243
9.4.2	Control System	246
9.4.3	Discussion	249
9.4.4	Stator-Flux Orientation	249
A	Lyapunov Stability Theory	253
B	CORDIC Algorithm	257

CHAPTER 1

Introduction

The purpose of this chapter is to give a brief overview of the field of electric power engineering, with particular focus on power electronic converters and drives. A general introduction to electric energy is first made. We then proceed with an introductory presentation of drives and the types of machines that are commonly used, followed by an overview of converters. The chapter is finished by summing up some of the various challenges that might face an engineer who is about to enter the field of control of converters and drives, and where in the book to find the information needed to solve various problems.

1.1 Electric Energy

The usage of energy in the world has been continuously increasing for the last century. In the Western world the energy usage has levelled off due to improved efficiency, whereas it still increases in countries which are under rapid development, notably China and India. Electric energy is not a primary energy source, but rather a means for transporting energy. Yet, it is the energy form that best fulfills requirements on flexibility and efficiency. Its main drawback is that storage of large amounts of electric energy is difficult. Pumped hydro storage, i.e., water that is pumped to reservoirs at higher elevation during periods of low load and released through turbines during periods of high load, is today the most effective method. Batteries may become more relied upon in the future, but they are still bulky and costly. Therefore, since electrical energy storage is difficult, costly, and also gives losses, it is desired that generation should match demand to the greatest possible extent.

1.1.1 Sources

A great percentage of all electric energy is generated from the **combustion of fossil fuels**—oil, coal, and natural gas—in thermal generating stations. Steam is raised in boilers and passed to steam turbines. Thermal generating stations typically have a rated capacity from 100 MW up to a few gigawatts, where the larger stations are equipped with ten or more turbine-generator sets. Due to the threat of global warming and, on the longer horizon, the (abundant but yet) limited supply of fuel, many countries have presently agreed to reduce the utilization of fossil fuel over the decades to follow.

In many countries, a significant contribution is obtained from **nuclear reactors**, where steam is produced from the heat generated by fission of uranium-235 atoms. Nuclear generating stations typically have a rated capacity of 1 GW and up. Nuclear fusion may eventually replace fission—thereby solving the problems of limited fuel supply and safe storage of used fuel—but due to the difficulties of handling the extremely high temperatures and pressures required for a controlled and encapsulated fusion reaction, it is difficult to predict exactly when this will occur.

It is generally agreed that a reduction in the usage of fossil fuel must be met by further improved energy efficiency and *renewable energy sources*. These include the following.

Hydroelectric (water) energy, possibly the oldest form of energy conversion, was utilized long before the term “renewable energy source” was even coined. Larger hydroelectric generating stations have a rated capacity which matches that of a thermal generating station. The Itaipu dam in South America was long the world’s largest hydroelectric installation, with a capacity of 14 GW shared by 20 generating units. Currently, the largest installation is the Three Gorges dam in China, with a capacity of 22.5 GW.

Biofuels. Humans have since long generated heat by burning wood, dung, and other fuels obtained from decaying biomass. In modern generating stations, such fuel, particularly wood chip, peat, vegetable oil, ethanol, and methane, can be burned to produce steam to drive turbines.

Geothermal energy. In some regions, for example in Iceland, Italy, and New Zealand, hot springs or lava streams come close enough to the earth’s surface to be tapped. Such energy sources have been used since the early 1900s.

Wind energy obtained from generators mounted horizontally on towers has become economically viable over the last couple of decades. This is because of the increasing capacity of wind-turbine generators, where the largest today are rated 10 MW. In Denmark, Germany, and Spain, wind energy already accounts for a significant share of the total generation. Wind energy is obviously intermittent to its nature and must be balanced by other sources.

Solar energy can either be converted to heat for steam production, by concentrating incident rays to a receiver using tracking heliostats, or be tapped by photovoltaics, i.e., directly converted to electricity. The latter generation method is currently growing quickly, particularly in central and southern Europe. The obvious drawback is that extraction is possible during at most 12 hours each day, on average. It is also intermittent because of clouds and fog. Solar energy therefore too must be balanced by other sources and by energy storage.

Tidal energy generation is feasible along coastlines with large tidal differences. It is cyclic to its nature, but a lot more predictable than wind. Tidal generating stations have been operational since the 1960s, but they are so far few.

1.1.2 Generation

The majority of all electric energy is created via rotating mechanical motion, where the prime mover is a hydro, steam, or wind turbine. Electrical machines are converters between mechanic and electric energy; in that direction in generator mode and in the opposite direction in motor mode.

The great majority of all electric energy is generated using synchronous machines (synchronous generators). The main exception so far is conversion of wind energy, where induction machines are often used. Both machine types are quite efficient: most synchronous generators have an efficiency of above 90%. Photovoltaic technology is one of the few exceptions where electric energy is generated without intermediate mechanical motion.

1.1.3 Transmission

Generators and consumers of electric energy often have significant geographic separation. For example, hydroelectric generating stations are often located in rivers flowing through sparsely populated regions. Transmission of electric energy over long distances requires high voltage, several hundred kilovolts, in order to give reasonably low currents and low resistive losses as a result. AC, unlike dc, transmission allows the usage of transformers for changing voltage levels. Three-phase ac

transmission, i.e., with three parallel lines, has several benefits over single-phase ac transmission. Therefore, already in the early 1900s it was decided to use three-phase ac for bulk transmission of electric energy.

Long-distance three-phase transmission is mostly made by overhead power lines, with rms line-to-line¹ voltages ranging from 100 kV up to (and in a few cases exceeding) 1000 kV. At these voltage levels close to 100% efficiency is obtained, even over very long distances. Since most generators are designed for a line-to-line voltage between 11 kV and 25 kV, step-up transformers are employed to connect generators to power lines.

For bulk transmission over long distances, high-voltage direct-current (HVDC) transmissions are attractive. The additional expense of power electronic converters for ac–dc conversion is offset by lower cost of the overhead transmission lines (or underground cables), as only two wires are required for a bipolar system as opposite to three wires in an ac line.

1.1.4 Distribution

Distribution networks supply electricity to the consumers, typically at line-to-line voltages between 2 kV and 35 kV. An ac transmission grid serves as bulk supply. It is tapped using step-down transformers located in one or several substation(s).

Larger consumers such as industries tap the distribution network directly. Most consumers, however, private homes included, draw electricity via step-down transformers providing a line-to-line voltage of a few hundred volts, for example 400 V in Europe and 190 V in North America. Larger loads—such as stoves, water heaters, and some washing machines—are connected to three-phase outlets, whereas the majority—lamps, computers, stereos, TV sets, etc.—draw power from single-phase outlets, which are connected between one of the three phases and neutral, i.e., a phase voltage. Hence, the nominal single-phase rms voltage is 230 V and 115 V, respectively, in Europe and North America. Single-phase loads are as evenly distributed between the three phases as possible in order to reduce the imbalance in the total current drawn by a distribution grid.

1.1.5 Consumption

The main end users of electric energy are industrial, residential (homes), and commercial (offices, shops, schools, hospitals, etc.). Industrial consumptions accounts for approximately 40%. The worldwide annual growth rate of electric-energy consumption has since the early 1900s remained constant at roughly 7%.

Even as the total energy consumption may level off or decrease in the future due to increase efficiency, it is likely that usage of electric energy will continue to grow at a fairly high rate. Where today the end user employs fossil fuel directly, in the future electric energy may in some cases be used instead. For example, transportation today depends to more than 90% on fossil fuel (refined oil and, to a lesser extent, natural gas); the main exception is electrified railways (including subways and light-rail lines). Transportation should gradually shift to reliance upon electric energy. It is likely that traffic-intensive railways which today use diesel haulage (notably in North America and Australia) eventually will be electrified. With improved battery technology and possibly electrified highways, we are also going to see abundant usage of electric and hybrid road vehicles. Knowledge of electric energy technology and electrical drives therefore should become all the more important to engineers in various disciplines.

¹The line-to-line voltage is $\sqrt{3}$ times larger than the line-to-neutral voltage (which is also called the phase voltage).

1.2 Electrical Drives

Since electric energy is mostly obtained using mechanical motion, it is not surprising that the opposite also is true, to a significant extent. Electrical motors are electrical machines which always or mostly operate in motor mode. An electrical drive consists of a motor, its mechanical load, and—if such is used—the motor control system, which may include a power electronic converter.

Between 50% and 60% of all *electric* energy produced, or about 20% of the *total* energy produced, is consumed in electrical drives. The majority of these are in the low-power (fractional kW) and medium-power (1–100 kW) ranges. Examples of application are electric drills, washing machines, fans and air conditioners, clocks and watches, CD and DVD players, and cameras and projectors. A modern automobile is equipped with up to 50 low-power electrical motors. In the higher power ranges we find industrial drives rated up to 100 MW. Typical industrial applications are pumps, fans, saws, winches, grinders, presses, hoists, and rollers.

Applications in electric traction include electric and diesel-electric locomotives, light-rail vehicles, and subway trains. As mentioned above, a growth area in the future will be electric and hybrid road vehicles.

The motor may be the most important component of a drive, but it is not the only one. As Figure 1.1 shows, the motor is often fed from a power electronic converter, which in turn is connected to a control unit (today often a digital signal processor, DSP). Therefore, to design and construct an electrical drive, knowledge in the following areas of engineering is needed:

- **Mechanics.** To model and understand the characteristics and dynamics of the mechanical load.
- **Electrical machines.** To understand the characteristics and dynamics of the motor, and to select the proper motor “off the shelf” for the application in case. Also, to obtain motor parameters needed for various control algorithms.
- **Power electronics.** To understand the operating principles and limitations of power electronic converters, and to select (or design) the converter best suited for the application in case.
- **Sensors and measurement (or estimation).** To find a cost-effective solution to the problem of measuring voltages, currents, fluxes, and rotor speed and/or position. Also, when a sensor cannot be used or is deemed too expensive, replace it by an estimation algorithm while understanding how this affects the performance of the drive.
- **Signal processing and control.** To apply filters when needed, and to design control algorithms for the power electronic converter that fulfill given demands on dynamic response and accuracy, etc., given limited knowledge of machine parameters and unavailability of certain measurements (i.e., to take into account that estimates are used instead).
- **Computer engineering.** To select and/or develop suitable hardware and software on which the signal processing, control, and measurement/estimation algorithms can be implemented.

As can be seen, electrical drives are a highly multi-disciplinary topic. As the title of this book suggests, the focus is signal processing and control, although all the above areas are covered at least briefly.

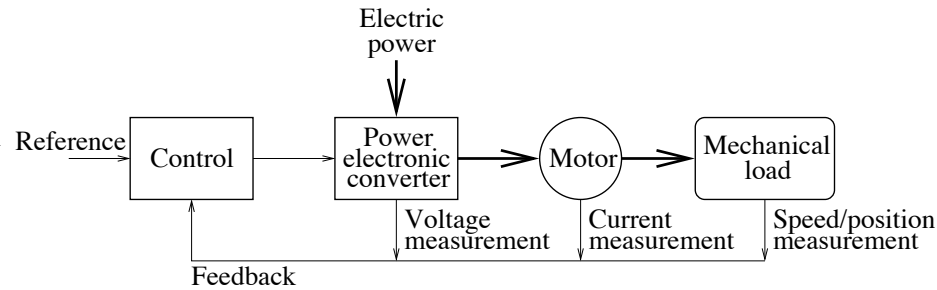


Figure 1.1. Block diagram of an electrical drive. Thick lines indicate flow of power; thin lines signals.

1.2.1 Benefits of Electrical Drives

Compared to other drive types, such as combustion engines and hydraulic or pneumatic drives, electrical drives have some very attractive properties:

- They are available in the entire power range, from less than 1 W to 100 MW.
- There is a wide range of speed and torque available. In rolling mills, torques in excess of 10^6 Nm are required, whereas in watches and medical applications, for example, the torque is sometimes less than 10^{-6} Nm.
- Electrical drives can be adapted to almost any operating condition. Whereas some drives require forced cooling, others can be completely encapsulated. Electrical drives can operate in liquids or be exposed to radioactive or potentially explosive environments without harm or risk.
- Refueling is not needed and service requirements are modest. There is no exhaust and the acoustic noise level is low.
- The efficiency is high (typically 75% to 95% for operation at rated load) and the low-load losses are minimal. The short-term overload capability is high.
- Finally, electrical drives can be designed to operate in both directions of rotation and in both directions of power flow. For example, an electric vehicle can run forward and backward at full speed, and can in both directions regenerate energy when braking. The latter is particularly attractive as compared to a combustion engine.

1.2.2 Motor Types

Electrical motors can be classified in two main categories.

- **DC motors** (DCMs) were the motors first invented for practical use. As is further discussed in Chapter 4, dc motors use a directly magnetized stator, whereas a mechanical commutator distributes current in the rotor, so that the desired torque is produced. The commutator utilizes sliding carbon brushes, which wear down and have to be replaced. A dc motor therefore requires significantly more maintenance than an ac motor (see below).

On the other hand, the commutator makes the dc motor controllable without power electronic converters. The dc motor was therefore up until the 1980s the only motor type available for variable-speed drives. Classic applications are electric traction, rolling mills, and servos.

- **AC motors** (ACMs) can be regarded as dc motors turned inside out: the rotor is magnetized directly or indirectly, and the desired torque is produced by applying a rotating (ac) stator current of proper magnitude, frequency, and phase. Except in constant-speed drives, this requires power electronic converters which are more advanced than for dc drives. So, whereas ac drives are advantageous due to less maintenance and higher efficiency, it was not until the late 1980s that the development of power semiconductors (and microprocessors for their control) finally reached levels that allowed performance comparable to dc drives. From the 1990s and on, ac drives have increasingly been replacing dc drives, particularly in industrial and traction applications.

There are mainly three sub-categories of ac motors.

1. **Induction motors** (IMs) use a so-called cage rotor, in which current is induced. Torque is produced due to the interaction of the stator current and the flux produced by the rotor current. As is further described in Section 5.2, this allows the IM to start by direct line connection. Called **direct line start**, this is very convenient, but the drive can be used only in constant-speed or near-constant-speed operation. In such applications the IM has been used since the late 1800s, but is today commonplace also in variable-speed drives.

Due to the induction of rotor current the IM rotates with a slip, i.e., slightly slower than the applied stator current when operating in motor mode.

2. **Synchronous motors** (SMs) use a directly magnetized rotor, either by permanent magnets (a so-called permanent-magnet SMs—PMSMs), or by a field winding in the rotor (so-called electrically excited SMs). “Synchronous” refers to the rotation, which is of the same frequency as the flux resulting from application of stator current. For this reason, an SM must be supplied from a power electronic converter to allow variable speed, but many constant-speed SMs allow direct line start. SMs have traditionally been used in high-power, constant-speed applications, but are today increasingly used also in variable-speed drives. Electrically excited SMs are typically utilized for high-power applications, whereas PMSMs mainly are used in high-performance variable-speed drives (such as servos) of low and medium power ratings. The dynamics and control of an electrically excited SM are in many respects similar to those of IMs and PMSMs, but there are nevertheless several special issues. Therefore, we have in this book elected to focus on IMs and PMSMs, which also are much more commonly used as motors.
3. **Reluctance motors** (RMs) in many ways resemble synchronous motors, but rely on reluctance rather than rotor magnetization for production of torque. As their construction is very simple and rugged—no magnets or rotor winding is used—reluctance motors are very attractive in low-power, variable-speed applications. Supply from a power electronic converter is required. The synchronous reluctance motor—or reluctance synchronous motor—is treated as a special case of the PMSM in Section 5.3. The more popular switched reluctance motor differs so much from other ac motor types, however, that it is not considered further in this book. For more information, see e.g., [60].

Figure 1.2 summarizes how the different motor types are characteristically used in the power range from fractional kW up to 100 MW.

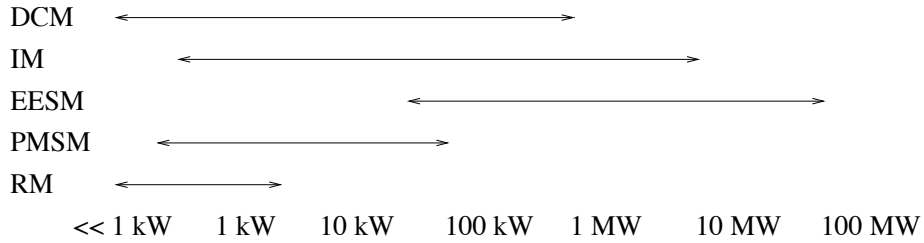


Figure 1.2. Power ranges for different motor types.

1.2.3 Variable-Speed Drives

As its title suggests, this book focuses to a great extent on variable-speed drives. The number of applications where variable speed is required—or at least preferred—is increasing, due to higher demands on precision and efficiency. As an example, whereas in bygone days it was considered perfectly fine that a washing machine always rotated with the same speed, it is nowadays taken for granted that different speeds should be used depending on the fabric being washed and the stage in the washing program.

Many applications, such as robotics, rolling mills, and paper machines, require accurate torque, speed, and position control, often with high dynamic requirements (short response times). In other applications, accuracy and dynamic performance matter less, but speed control is still highly important, as this implies significant energy savings. This is particularly true for pumps and fans. Controlling the flow of liquid or gas by adjusting the pump or fan speed, rather than having the motor operate at constant speed and using a throttle, means that the energy efficiency can improve tremendously.

The usual approach when teaching electrical drives is to start with constant-speed drives. Due to their increasing importance, we here consider variable-speed drives already from the beginning. Constant-speed drives then follow as special cases.

1.3 Power Electronic Converters

Variable-speed ac drives cannot be (fully) controlled without power electronic converters. Whereas variable-speed drives are one important application of power electronics converters, it is by no means the only one. Power electronic converters come in four fundamental variants, see Figure 1.3. The flow of power in this figure is generally—but not always—from left to right, i.e., the input port is on the left-hand side and the output port is on the right-hand side. Converters which do not allow and do allow power flow in both directions are, respectively, called unidirectional and bidirectional. The same terms apply with regards also to current flow.

1.3.1 DC–DC Converters

Converters of this category are mostly unidirectional, and act as transformers for direct voltage and current. Unlike a transformer, though, an output voltage which is variable within a wide range can be obtained. To lower the voltage, step-down or buck converters are used, whereas step-up or boost converters increase the voltage. The hybrid buck–boost converter allows output voltage variable between zero and (theoretically) infinity.

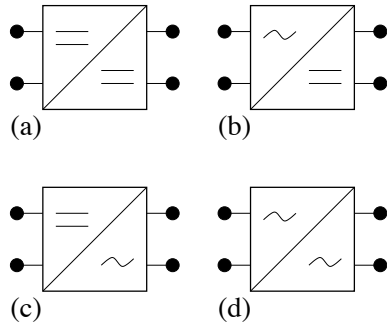


Figure 1.3. Power electronic converters. (a) dc–dc. (b) ac–dc. (c) dc–ac. (d) ac–ac.

DC–dc converters operate in switched mode: the output voltage is a train of pulses. Such converters are said to be self-commutated. This enables fast control, with response times in the millisecond range. The switching device is in most cases a transistor. Inductances and/or capacitances are needed to smoothen the output voltage and give a (virtually) ripple-free output current.

DC–dc converters are used in various applications, many of them low-power, including voltage supplies for dc circuits which require precise voltage control. Low-power dc–dc converters can be fully integrated, for example to permit variable voltage levels in different blocks of a CMOS circuit. In higher power ranges dc–dc converters are used for example to power variable-speed dc motor drives.

1.3.2 AC–DC Converters

Conversion from ac to dc is called rectification. There are two fundamental, but related, converter types in this category.

Diode Rectifiers

The diode rectifier is the most common converter, being used in most voltage supplies for low-power dc circuits. The “diamond-shaped” single-phase rectifier depicted in Figure 1.4(a) may be familiar to those readers who have studied the circuit diagram of, e.g., an audio amplifier. As shown in this figure, at the output of the rectifier, a capacitor is utilized in order to give a smooth direct voltage. The load is modeled as a direct-voltage source, but is in many cases partly or purely resistive.

Thyristor Converters

Diode rectifiers do not allow the direct voltage to be varied. This is remedied by replacing the diodes in Figure 1.4(a) by thyristors. Whereas a diode has a simple P–N junction, a thyristor has four layers, where the middle P layer is connected to a gate. This prevents the device from conducting when the anode–cathode voltage turns positive, until triggered by a short pulse at the gate. It is said that the thyristor’s turn-on instant is delayable. As shown in Figure 1.4(b), both an inductor and a capacitor may be used to smoothen the output direct voltage, but in many applications only one of the two components is installed. Thyristor converters allow negative output voltage; the

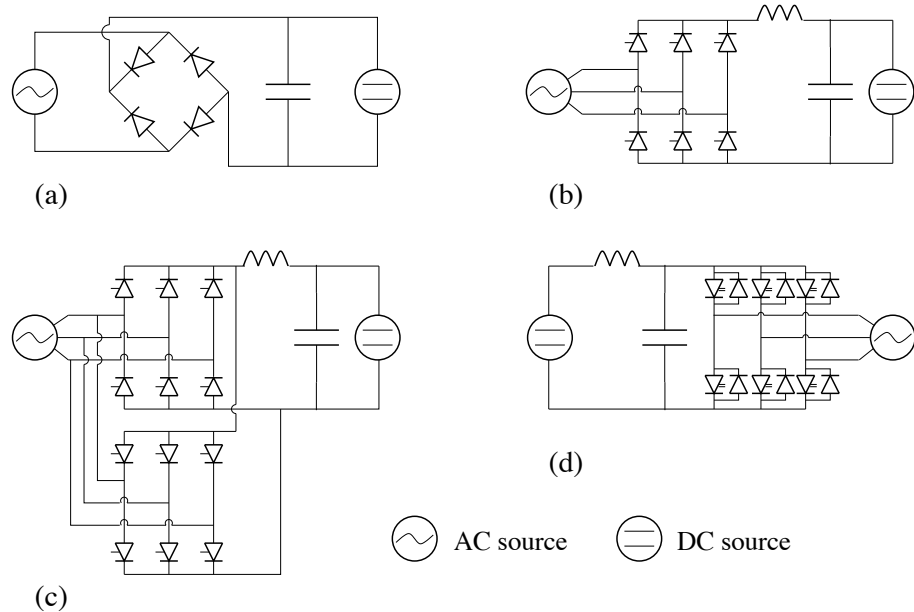


Figure 1.4. (a) Single-phase diode rectifier with a capacitor smoothing the direct voltage. (b) Three-phase thyristor converter with an inductor and/or a capacitor for smoothing the direct voltage. (c) Antiparallel-connected thyristor bridges, allowing bidirectional current flow. (d) Three-phase voltage-source converter.

direction of power flow is then reversed. Hence, thyristor converters are bidirectional with regards to power flow, and are said to operate in rectifier mode when the output voltage is positive and inverter mode otherwise (“invert” refers to inverted operation as compared to a rectifier).

One important application for thyristor converters is to feed variable-speed dc drives. Neglecting resistive losses, a dc motor—as will be seen in Chapter 4—can be modeled as a series connection of an inductance and a voltage source (the back emf). Figure 1.4(b) with the capacitor removed illustrates the circuit diagram. Other important applications are HVDC transmissions and static var compensators (SVCs). The latter allows control of the reactive power at a certain node in a power system, thereby stabilizing the voltage at that node. There is no transfer of active power between the ac and dc sides.

The direction of current in a thyristor converter cannot be reversed, since thyristors—like diodes—conduct only in one direction. To allow negative direct voltage *and* current, two antiparallel-connected thyristor bridges, as illustrated in Figure 1.4(c), must be used.

We finally note that, since thyristor converters do not employ switch-mode operation, their control is relatively slow, and they generate sizeable low-order current harmonics on the ac side. Thyristor converters as well as diode rectifiers are said to be line commutated.

1.3.3 DC–AC Converters

Converters of this category are referred to as inverters. Of course, a bidirectional ac–dc converter is also a bidirectional dc–ac converter, so a thyristor converter which operates in inverter mode may be referred to as an inverter. The term inverter is, however, often reserved for inherent dc–ac converters, which are able to actually *create* an alternating voltage of variable frequency. Similarly

to dc–dc converters, this requires switch-mode operation, which enables fast control with response times in the millisecond range.

A voltage-source inverter (VSI) uses a stiff direct voltage—kept up by one or several capacitor(s)—as source, which is “inverted” into ac. As switching devices, gate-turn-off (GTO) thyristors were initially used, but today transistors dominate. The circuit symbol for a general on/off-switching device is that of a diode with two gate symbols. Figure 1.4(d) shows the circuit diagram of a three-phase VSI. The antiparallel-connected diodes enable bidirectional current (and power) flow. To highlight that a VSI may operate in rectifier mode just as well as in inverter mode, the term voltage-source converter (VSC) will be used henceforth.

1.3.4 AC–AC Converters

First, we note that direct ac–ac conversion is rarely used. It is often beneficial to convert from ac to ac via an intermediate dc bus, which is often referred to as a dc link if it interconnects only two converters. Conversion from ac to ac has three important applications.

- **Variable-speed ac drives:** In many ac drive applications, a multi-terminal dc bus is not available. Power is drawn directly from a three-phase line using an ac–ac converter. The line side of the converter has constant frequency and the drive side variable frequency.
- **HVDC transmissions:** Two asynchronous ac grids—alternatively two distant nodes within one grid—may be joined together by an HVDC transmission, allowing controlled transfer of power. HVDC transmissions are also used to connect a distant source or load to an ac grid; examples include offshore wind farms and oil or gas platforms.
- **Frequency conversion:** Two ac systems with different fundamental frequencies can be coupled together by an ac–ac converter. A typical application of this is supply to electrified railways. For example, in many European countries, the three-phase grid has fundamental frequency 50 Hz, whereas the railways are electrified with 16 2/3-Hz single-phase system.

Indirect AC–AC Conversion

In ac drives, the converters on each terminal of the dc link are often placed adjacent to each other. This is known as a back-to-back converter system. The converters in most HVDC transmissions are located in different stations, which are separated by a dc cable or an overhead line. However, the cable or line can be accurately modeled as an inductive or capacitive dc link (see below) as seen from the converters, so the converters are electrically back-to-back also in this case.

There are three dc-link variants, see Figure 1.5. Selection is made depending on the converter types used.

- (a) **Voltage-stiff (capacitive) dc link:** This type of dc link is used with VSCs, which allows full bidirectional power and current flow. If unidirectional power flow is sufficient, a diode rectifier may be used as grid-side converter. Back-to-back VSCs with a voltage-stiff dc link are also increasingly used in HVDC transmissions.
- (b) **Current-stiff (inductive) dc link:** When thyristor converters are employed at both terminals, a current-stiff dc link is used. Line-commutated, i.e., thyristor-based, HVDC transmissions have this configuration.

- (c) **Resonant (inductive–capacitive) dc link:** Although this configuration is sometimes used when the left-port converter is a diode rectifier or a thyristor converter, cf. Figure 1.4(b), we here specifically mean the situation where the dc-link components are selected to give a very high LC resonant frequency (often above 100 kHz). Forcing the dc-link voltage to oscillate with the resonant frequency, together with a VSC this allows switchings to be made when the dc-link voltage is zero (and possibly also the current), which reduces losses and electromagnetic interference (EMI). Since extra components and relatively complicated control are required, resonant-link converters have so far been applied fairly sparsely. The interested reader is referred to the literature devoted to the topic [47].

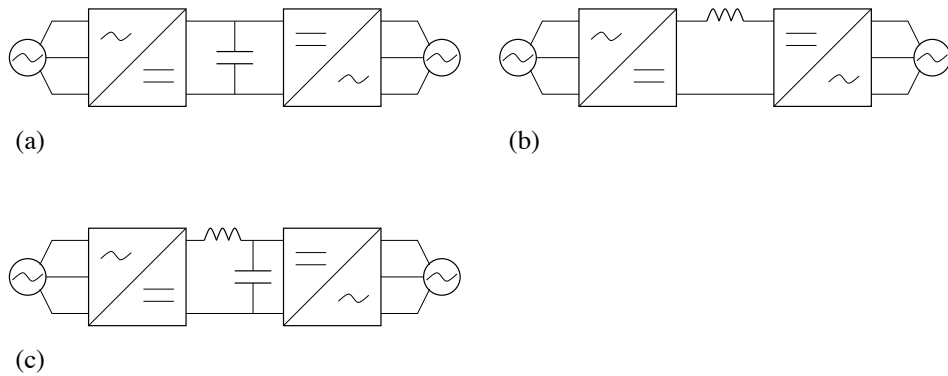


Figure 1.5. Indirect ac–ac conversion with three dc-link variants. (a) Voltage-stiff. (b) Current-stiff. (c) Resonant.

Direct AC–AC Conversion

There are two converter types which are able to convert directly from ac to ac without an intermediate dc link. Both are used in ac drive applications, but sparsely. The interested reader is again referred to the literature specializing in the topic, e.g., [75].

- **Matrix converters** interconnect two three-phase systems as illustrated in Figure 1.6. Each interconnection—marked by a dot in Figure 1.6—requires two switching devices to allow bidirectional current flow. That is, 18 switching devices are required for a three-phase matrix converter. This, along with other issues such as complicated control, has so far prevented widespread usage of matrix converters.
- **Cycloconverters** for three-phase ac–ac conversion consist of six thyristor bridges: two antiparallel-connected bridges—cf. Figure 1.4(c)—per phase, which enables bidirectional current flow. Cycloconverters inherit the drawbacks of thyristor rectifiers: slow control and large low-order current harmonics. They are predominantly used in high-power, variable-speed ac drives, particularly SM drives, where these drawbacks are acceptable.

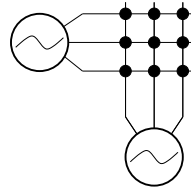


Figure 1.6. Three-phase matrix converter.

1.4 Challenges in Control of Converters and Drives

Converter and drives control is the focus of the book; what problems are there? In one sense, VSC control is straightforward, because similar solutions can be applied to solving various control problems, due to similarity between the various loads and systems connected to the VSC. In fact, many control problems boil down to controlling the current i through a load consisting of a resistance R , an inductance L , and a voltage source E (the motor's back emf) connected in series, by manipulating the converter output voltage v . This is illustrated in Figure 1.7.

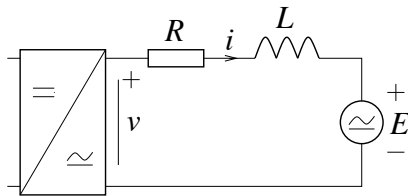


Figure 1.7. Model of a VSC with voltage v connected to an alternating or direct voltage source. The task is to properly control the current i .

Whereas VSC control is quite simple if the load is a dc motor, things immediately get more complicated for ac.

- It is easily verified that standard proportional-plus-integral (PI) controllers are not particularly useful for control of ac quantities. How can better controllers be designed? (This is answered in Chapter 6.)
- The VSC operates in switched mode. How can the output signal of a linear controller (for example, an improved PI controller) be converted to suitable switching signals? [Answer: pulsedwidth modulation (PWM), which is covered in Chapter 3.]
- In addition to correct voltage and frequency, the phase angle of the VSC's output voltage must also be correct, in order to obtain proper active and reactive powers. Thus, the switchings must be synchronized in some way with the back emf. How is that accomplished? [By a phase-locked loop (PLL), as shown in Chapter 6.]
- What if the back emf cannot be measured? How do we synchronize the converter in that case? (By developing further the PLL. This is often very challenging, however, and application-specific adaptations must be made. See Chapters 6, 8, and 9.)

We have so far discussed just control of a VSC. There are in many cases several cascaded or interconnected control loops, particularly in a back-to-back configuration where the load is a variable-speed ac drive fed via a dc link from an ac grid, as shown in Figure 1.8.

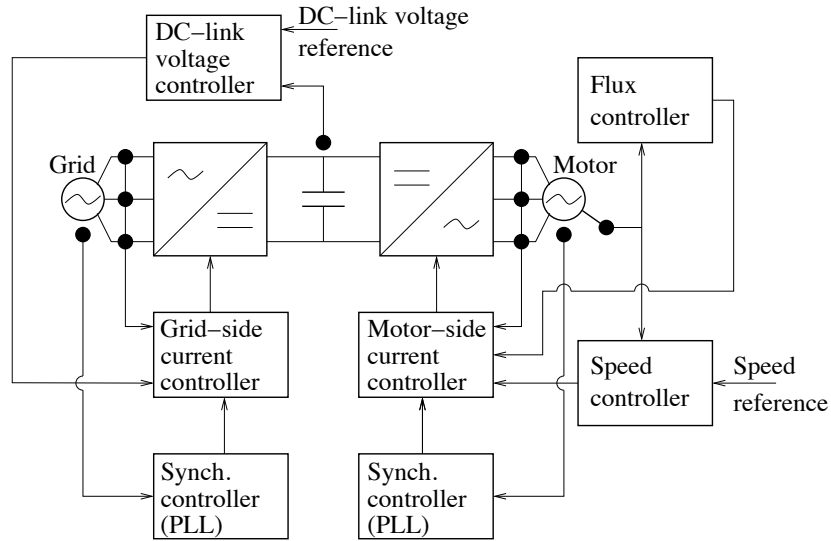


Figure 1.8. Loops in a back-to-back VSC control system.

There is a

1. **speed control loop**, by which the desired motor speed is obtained. The output of the speed controller is the reference torque (or power) of the motor, which is regulated by the
2. **motor-side current control loop**. If increased current to the motor is demanded, more power is drawn from the dc link, so a
3. **dc-link voltage control loop** is required to keep the dc-link voltage at the desired level. The output of the dc-link voltage controller is the power that should be drawn from the source, which is the reference for the
4. **grid-side current control loop**, which is the mirror image of the motor-side current control loop. In addition, there may be a
5. **flux control loop** for the ac motor, since the flux must be decreased to allow high speeds (so-called field weakening). Finally, it should not be forgotten that the
6. **synchronization** mentioned above is also a control loop. Two synchronization loops are required, one for each current control loop.

Thus, there are up to seven control loops, where loops 1 and 2 as well as loops 3 and 4, respectively, operate in cascade: the two current control loops are “slaves” to the speed and dc-link voltage control loops, respectively. What are the challenges facing the engineer whose task is to design the entire control system?

1. **Speed control loop.** To achieve performance that is robust to changes in the load torque and in the system's mechanical parameters (Section 4.6).
2. **Motor-side current control loop.** To permit control of amplitude and phase angle independently of each other, and to achieve robustness to changes in the back emf (Section 4.4 and Chapter 6).
3. **DC-link voltage control loop.** To achieve robustness to changes in the power drawn from the load-side converter.
4. **Grid-side current control loop.** To permit control of amplitude and phase angle independently of each other, and to achieve robustness to variations in the grid voltage, particularly voltage sags (Chapter 6).
5. **Flux control loop.** To achieve stability and insensitivity to various motor parameters (Sections 8.5 and 9.3).
6. **Synchronization loops.** To achieve stability and insensitivity to various parameters. This is particularly critical for variable-speed drives at low speeds (Chapters 6–9).

From this summary it is apparent that many of the challenges involve controller design that makes the control loop less sensitive to disturbances and changes in the system parameters. This is normally solved loop for loop. However, since there are as many as seven control loop, it is apparent that they may interact with each other in ways that are not desirable.

So, we see that control of VSCs and variable-speed drives can indeed be quite challenging. Although many problems have been solved—as will be seen by studying further this book—technology advances and new applications will certainly pose new challenges for researchers and development engineers for the foreseeable future.

CHAPTER 2

Systems and Circuits in Power Electronics and Drives

This chapter introduces general theory that will be relied upon in subsequent chapters. Many of the topics—especially those in the beginning of the chapter—should be well known already, so the presentation is often kept brief. Starting with single-phase ac systems, we move on to linear dynamic systems, covering the Laplace transform, transfer functions, and state-space models. Nonlinear systems are also covered briefly; this is perhaps a new topic to many readers. Sampling and discrete-time systems are covered next. We then discuss three-phase ac systems and the convenient analysis tool of space vectors, along with so-called symmetrical dynamic systems, which can be modeled with complex transfer functions. The chapter is finished by the principle of normalization using per-unit quantities.

2.1 Single-Phase AC Systems

2.1.1 Sinusoids and Phasors

From Fourier analysis it is known that all signals—periodic as well as transient—can be decomposed in a (usually infinite) number of sinusoids. The sinusoid is chosen as base waveform because it is the only signal that can pass a linear system without waveform distortion: its amplitude and phase are generally altered, but the output signal remains a sinusoid of the same frequency as the input signal. A sinusoidal signal, e.g., a voltage, is determined by its peak value (or amplitude) \hat{V} , angular frequency ω_1 , and phase angle φ_v

$$v(t) = \hat{V} \cos(\omega_1 t + \varphi_v). \quad (2.1)$$

The subscript 1 of ω_1 denotes the fundamental frequency, of which harmonics—see Paragraph 2.1.4—are multiples. The rotating phasor associated with (2.1) is, following the so-called “ $j\omega$ method,” given by

$$\bar{v}(t) = V e^{j(\omega_1 t + \varphi_v)} \quad (2.2)$$

where $V = \hat{V}/\sqrt{2}$ is the rms value, so $v(t) = \sqrt{2} \operatorname{Re}\{\bar{v}(t)\}$. Similarly, a sinusoidal current can be expressed as

$$i(t) = \hat{I} \cos(\omega_1 t + \varphi_i) = \sqrt{2} \operatorname{Re}\{\bar{i}(t)\}, \quad \bar{i}(t) = I e^{j(\omega_1 t + \varphi_i)} \quad (2.3)$$

where $I = \hat{I}/\sqrt{2}$. A certain voltage or current is often taken as the phase reference: its phase angle is by definition set to zero, e.g.,

$$v(t) = \hat{V} \cos \omega_1 t. \quad (2.4)$$

We further note that the sine function of course can be picked as base function instead of the cosine function, e.g., $v(t) = \hat{V} \sin \omega_1 t$. When calculating the actual voltage or current, the imaginary part of the phasor should then be taken instead of the real part, e.g., $v(t) = \sqrt{2} \operatorname{Im}\{\bar{v}(t)\}$, as illustrated in Figure 2.1.

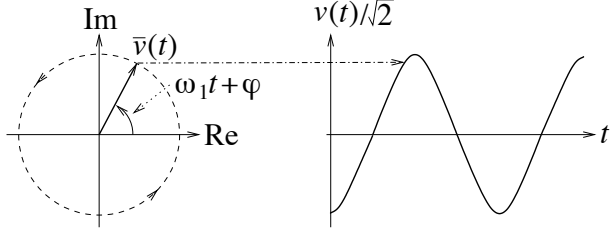


Figure 2.1. Rotating phasor $\bar{v}(t)$ projected on the imaginary axis yields $v(t)/\sqrt{2}$ when sine is used as base function.

Remark 2.1 Often, fixed phasors are used instead of rotating phasors. A fixed phasor can be considered as a snapshot of a rotating phasor at $t = 0$, e.g.,

$$\bar{v}(t) = V e^{j(\omega_1 t + \varphi_v)} \Rightarrow \bar{V} = \bar{v}(0) = V e^{j\varphi_v}. \quad (2.5)$$

2.1.2 Active and Reactive Powers

The instantaneous power developed in a circuit with input voltage $v(t)$ and input current $i(t)$ is given by $P(t) = v(t)i(t)$. For (2.1) and (2.3) we obtain

$$\begin{aligned} P(t) &= v(t)i(t) = \hat{V}\hat{I} \cos(\omega_1 t + \varphi_v) \cos(\omega_1 t + \varphi_i) \\ &= VI[\cos \varphi + \cos(2\omega_1 t + \varphi_v + \varphi_i)] \end{aligned} \quad (2.6)$$

where $\varphi = \varphi_v - \varphi_i$. The power oscillates with twice the fundamental frequency. Lamps in Europe thus blink with 100 Hz and the torque (which is proportional to the power according to the relation torque=power/angular speed) of a line-connected single-phase ac motor or a series dc motor pulsates with 100 Hz. The mean value of the instantaneous power is called the (mean) active power, and is given by

$$P = \langle P(t) \rangle = VI \cos \varphi \quad (2.7)$$

where $\cos \varphi$ is called the power factor. Maximum power, $P = VI$, is developed when $\varphi = 0$, i.e., $\cos \varphi = 1$ (unity power factor), zero power is developed when $\varphi = \pm 90^\circ$, and negative power (i.e., power is drawn from the circuit) is developed when $90^\circ < |\varphi| \leq 180^\circ$.

Phasors allow power calculations where the oscillating terms vanish averaging. The complex power (the modulus of which is called the apparent power) is introduced as

$$\bar{S} = \bar{v}(t)\bar{i}^*(t) \quad (2.8)$$

where the superscript * stands for complex conjugate. From this quantity, the active power can be obtained by taking the real part

$$P = \operatorname{Re}\{\bar{S}\} = VI \cos \varphi. \quad (2.9)$$

Taking instead the imaginary part, we obtain the reactive power

$$Q = \text{Im}\{\bar{S}\} = VI \sin \varphi. \quad (2.10)$$

When maximum active power is developed, i.e., for $\varphi = 0$, the reactive power is zero. It is desirable that loads should draw zero reactive power, i.e., have unity power factor, $\cos \varphi = 1$, since then the drawn current is fully utilized for active power. To distinguish apparent and reactive power from active power, the former are given the units volt–amps [VA] and volt–amps (reactive) [VAr], respectively, whereas active power is measured in watts [W].

2.1.3 Complex Impedances

Phasors allow straightforward calculations of voltage, current, and power using complex impedances. Since the derivative of a phasor corresponds to multiplication by $j\omega_1$, for example

$$\bar{v}(t) = V e^{j(\omega_1 t + \varphi_v)} \Rightarrow \frac{d\bar{v}(t)}{dt} = j\omega_1 V e^{j(\omega_1 t + \varphi_v)} = j\omega_1 \bar{v}(t) \quad (2.11)$$

the voltage–current relations for an inductor and a capacitor

$$v(t) = L \frac{di(t)}{dt} \quad i(t) = C \frac{dv(t)}{dt} \quad (2.12)$$

for phasors become

$$\bar{v}(t) = L \frac{d\bar{i}(t)}{dt} = j\omega_1 L \bar{i}(t) \quad \bar{i}(t) = C \frac{d\bar{v}(t)}{dt} = j\omega_1 C \bar{v}(t) \quad (2.13)$$

respectively. The complex impedances for an inductor and a capacitor are, thus,

$$Z_L(j\omega_1) = j\omega_1 L = jX_L \quad Z_C(j\omega_1) = \frac{1}{j\omega_1 C} = -jX_C \quad (2.14)$$

respectively, where $X_L = \omega_1 L$ and $X_C = 1/(\omega_1 C)$ are the reactances.

Example 2.1 Let us calculate the current through and the mean active and reactive powers developed in an RL and an RC series circuit, respectively, given that the voltage across the circuit is $v(t) = \sqrt{2}V \cos \omega_1 t$. The RL circuit has the complex impedance $Z_{RL}(j\omega_1) = R + j\omega_1 L$; thus we get

$$\bar{i}(t) = \frac{\bar{v}(t)}{Z_{RL}(j\omega_1)} = \frac{V e^{j\omega_1 t}}{R + j\omega_1 L} = \frac{V}{\sqrt{R^2 + (\omega_1 L)^2}} e^{j[\omega_1 t - \arctan(\omega_1 L/R)]}$$

and

$$i(t) = \frac{\sqrt{2}V}{\sqrt{R^2 + (\omega_1 L)^2}} \cos[\omega_1 t - \arctan(\omega_1 L/R)].$$

It can be observed that when $R = 0$, the current is displaced $-\arctan \infty = -90^\circ$ from the voltage. Furthermore,

$$\bar{S} = \bar{v}(t)\bar{i}^*(t) = \frac{V^2}{R - j\omega_1 L} = \frac{(R + j\omega_1 L)V^2}{R^2 + (\omega_1 L)^2}$$

giving

$$P = \text{Re}\{\bar{S}\} = \frac{RV^2}{R^2 + (\omega_1 L)^2} \quad Q = \text{Im}\{\bar{S}\} = \frac{\omega_1 LV^2}{R^2 + (\omega_1 L)^2}.$$

It can be noted that $P = 0$ when $R = 0$, which agrees with the finding that no active power is developed when the phase angle between the voltage and the current is $\pm 90^\circ$. It should also be noted that $Q \geq 0$. An inductive circuit is said to consume reactive power.

For the RC circuit, we just need to replace $\omega_1 L$ by $-1/(\omega_1 C)$, getting

$$\bar{i}(t) = \frac{\bar{v}(t)}{Z_{RC}(j\omega_1)} = \frac{Ve^{j\omega_1 t}}{R - j/\omega_1 C} = \frac{\sqrt{2}\omega_1 CV}{\sqrt{1 + (\omega_1 RC)^2}} e^{j[\omega_1 t + \arctan(1/\omega_1 RC)]}$$

and

$$i(t) = \frac{\sqrt{2}\omega_1 CV}{\sqrt{1 + (\omega_1 RC)^2}} \cos[\omega_1 t + \arctan(1/\omega_1 RC)].$$

In this case, when $R = 0$, the current is displaced $\arctan \infty = +90^\circ$ from the voltage. We now calculate the complex power:

$$\bar{S} = \bar{v}(t)\bar{i}^*(t) = \frac{V^2}{R + j/\omega_1 C} = \frac{(R - j/\omega_1 C)V^2}{R^2 + 1/(\omega_1 C)^2} = \frac{\omega_1 C(\omega_1 RC - j)V^2}{1 + (\omega_1 RC)^2}$$

giving

$$P = \text{Re}\{\bar{S}\} = \frac{(\omega_1 C)^2 RV^2}{1 + (\omega_1 RC)^2} \quad Q = \text{Im}\{\bar{S}\} = -\frac{\omega_1 CV^2}{1 + (\omega_1 RC)^2}.$$

Also in this case, $P = 0$ when $R = 0$, whereas $Q \leq 0$ for $\omega_1 > 0$. A capacitive circuit is said to produce reactive power



PROBLEM 2.1

How should R be chosen in the RL and RC circuits, respectively, in order to maximize the active power?

2.1.4 Harmonics

Suppose that $v(t)$ is a periodic waveform of zero mean with period $T_1 = 2\pi/\omega_1$. This waveform can be expanded into the Fourier series

$$v(t) = \sum_{h=1}^{\infty} a_h \cos h\omega_1 t + b_h \sin h\omega_1 t = \sum_{h=1}^{\infty} \hat{V}_h \cos(h\omega_1 t + \varphi_h) \quad (2.15)$$

where

$$\begin{aligned} a_h &= \frac{\omega_1}{\pi} \int_{-T_1/2}^{T_1/2} v(t) \cos h\omega_1 t dt & b_h &= \frac{\omega_1}{\pi} \int_{-T_1/2}^{T_1/2} v(t) \sin h\omega_1 t dt \\ \hat{V}_h^2 &= a_h^2 + b_h^2 & \tan \varphi_h &= -\frac{b_h}{a_h}. \end{aligned} \quad (2.16)$$

In (2.15), $h = 1$ gives the fundamental component, $\hat{V}_1 \cos(\omega_1 t + \varphi_1)$, whereas the components that are frequency multiples of the fundamental, $h = 2, 3, \dots$, are called harmonics. For the harmonics, direct calculations using (2.16) reveal the following results:

- 1) When $v(t)$ is half-wave symmetric, i.e., the negative half period is the mirror image of the positive half period, all even-order harmonics vanish. This is the case for most waveforms in electrical engineering. The Fourier series then reduces to

$$v(t) = \hat{V}_1 \cos(\omega_1 t + \varphi_1) + \hat{V}_3 \cos(3\omega_1 t + \varphi_3) + \hat{V}_5 \cos(5\omega_1 t + \varphi_5) + \dots$$

- 2) For many—although not all—waveforms, the amplitude \hat{V}_h decreases monotonically with h , and at least as fast as $1/h$. That is, the amplitude of the 5th harmonic is $3/5$ or less of that of the 3rd harmonic, etc. For example, an odd squarewave of zero mean and amplitude 1 has $a_h = 0$ for all h and

$$b_h = \begin{cases} \frac{4}{\pi h}, & h = 1, 3, 5, \dots \\ 0, & h = 2, 4, 6, \dots \end{cases}$$

PROBLEM 2.2

Show that!

Harmonics in electric circuits and systems appear partly due to nonlinear components, primarily semiconductors and—as we shall see in Chapter 5—nonlinear phenomena in electrical motors. Whereas, as mentioned, a linear circuit excited by a sinusoidal voltage draws a sinusoidal current of the same frequency as the voltage, a nonlinear circuit distorts the waveform. The nonlinear circuit is said to add harmonics. Furthermore, as will be seen in Chapter 3, power electronic converters create switched waveforms that are far from sinusoidal.

It is often realistic to assume that, at a certain node in a circuit, either the voltage or the current can be approximated as purely sinusoidal, whereas the other quantity contains harmonics. Suppose that the voltage is sinusoidal and is taken as phase reference

$$v(t) = \sqrt{2}V \cos \omega_1 t \tag{2.17}$$

whereas the current contains harmonics as

$$i(t) = \sum_{h=1,3,5,\dots}^{\infty} \sqrt{2}I_h \cos(h\omega_1 t + \varphi_h). \tag{2.18}$$

Since $2 \cos \omega_1 t \cos(h\omega_1 t + \varphi) = \cos[(h-1)\omega_1 t + \varphi] + \cos[(h+1)\omega_1 t + \varphi]$, we find that the instantaneous power is given by

$$\begin{aligned} P(t) = v(t)i(t) &= VI_1[\cos \varphi_1 + \cos(2\omega_1 t + \varphi_1)] \\ &\quad + VI_3[\cos(2\omega_1 t + \varphi_3) + \cos(4\omega_1 t + \varphi_3)] + \dots \end{aligned} \tag{2.19}$$

Only the fundamental frequency component produces power of nonzero mean; the harmonics merely produce power pulsations of 2, 4, 6, etc. times the fundamental frequency. This is one reason why the sinusoid is the desired waveform in electric power engineering: harmonics just add distortion that does not contribute to the efficiency of the system. For example, when a power electronic converter is connected to the grid, passive filters—at the very least a series inductance—must be used to suppress harmonics from the current drawn from or injected into the grid.

2.2 Linear Continuous-Time Systems

In the previous section, we considered steady-state ac excitation of *RLC* circuits. Such circuits are dynamic systems. When subjected to a change in some variable, e.g., the input voltage, a transient results before a steady state is again attained. In this section, general linear dynamic systems (but *RLC* circuits in particular) will be studied, using the Laplace transform as mathematical tool.

A dynamic system is often described in terms of its input and output signals. For a general dynamic system they are often denoted as $u(t)$ and $y(t)$, respectively; see Figure 2.2. The input signal is available for manipulation and the output signal describes the system's response to that manipulation. In the context of electric circuits, the input and output signals are voltages and/or currents (possibly magnetic flux linkages).

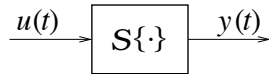


Figure 2.2. System $y(t) = \mathcal{S}\{u(t)\}$.

2.2.1 Definition of Linearity

A linear system \mathcal{S} is such that the principle of superposition holds. That is, if the input signal is the sum of two or more terms, for example

$$u(t) = a_1 u_1(t) + a_2 u_2(t) \quad (2.20)$$

then the output signal $y(t) = \mathcal{S}\{u(t)\}$ can be expressed as

$$y(t) = a_1 \mathcal{S}\{u_1(t)\} + a_2 \mathcal{S}\{u_2(t)\}. \quad (2.21)$$

If ideal components are assumed (i.e., parasitic phenomena such as magnetic saturation are neglected), all *RLC* circuits are linear systems.

PROBLEM 2.3

Dynamic systems are modeled using differential equations. Which ones of the following are models for linear systems?

- | | |
|--|---|
| a) $\frac{dy(t)}{dt} + ay(t) = b \sin u(t)$ | b) $\frac{dy(t)}{dt} + ay(t) = bu(t)$ |
| c) $\frac{dy(t)}{dt} + ay(t) = btu(t)$ | d) $\frac{dy(t)}{dt} + ay^3(t) = bu(t)$ |
| e) $\left[\frac{dy(t)}{dt} \right]^2 + ay(t) = bu(t)$ | f) $\frac{dy(t)}{dt} + ay(t) = bu(t)y(t)$ |

2.2.2 Laplace Transform

Phasors and complex impedances allow only calculation of the response to steady-state ac excitation. To calculate also the transient response, e.g., resulting from a switch being closed at a

Table 2.1. Laplace transform pairs.

Signal (for $t \geq 0$)		Laplace transform
e^{-at}	(Exponential)	$\frac{1}{s+a}$
$\delta(t)$	(Impulse)	1
1	(Step)	$\frac{1}{s}$
t	(Ramp)	$\frac{1}{s^2}$
$\cos \omega t$	(Cosinusoid)	$\frac{s}{s^2 + \omega^2}$
$\sin \omega t$	(Sinusoid)	$\frac{\omega}{s^2 + \omega^2}$
$\int_0^t u(\tau) d\tau$	(Integration)	$\frac{U(s)}{s}$
$u(t - T_d)$	(Time delay)	$e^{-sT_d} U(s)$
$y(t) = \int_0^\infty h(\tau)u(t - \tau) d\tau$	(Convolution)	$Y(s) = H(s)U(s).$

certain time (which is often taken as $t = 0$), the Laplace transform can instead be used. Having the definition

$$Y(s) = \mathcal{L}\{y(t)\} = \int_0^\infty y(t)e^{-st} dt \quad (2.22)$$

the Laplace transform has the important property that a time derivative is transformed to multiplication by s

$$\mathcal{L}\left\{\frac{dy(t)}{dt}\right\} = sY(s) - y(0-) \quad (2.23)$$

where often $y(0-) = 0$ can be assumed (the circuit or system is assumed not to be excited for $t < 0$). We have the correspondence

$$s \leftrightarrow \frac{d}{dt}. \quad (2.24)$$

So, when calculating the transient response of an electric circuit, the following Laplace impedances should be used instead of the corresponding complex impedances:

$$Z_L(s) = sL \quad Z_C(s) = \frac{1}{sC}. \quad (2.25)$$

Some important Laplace transform pairs are shown in Table 2.1.

Example 2.2 We wish to calculate the response of the current $i(t)$ through an LR series circuit to a direct voltage $v(t) = V$ (i.e., the step response) and an alternating voltage $v(t) = \sqrt{2}V \cos \omega_1 t$, respectively. Both voltages are applied at $t = 0$, and $i(t) = 0$ can be assumed for $t < 0$.

The Laplace transform of a constant signal $v(t) = V$ applied at $t = 0$ (i.e., a step of amplitude V) is $V(s) = V/s$. The transform of the current is obtained by dividing this by the Laplace impedance of the RL circuit

$$I(s) = \frac{V(s)}{sL + R} = \frac{V}{s(sL + R)} = \frac{V}{sL(s + R/L)} = \frac{V}{R} \left(\frac{1}{s} - \frac{1}{s + R/L} \right).$$

Rewriting the expression in partial fractions, as above, makes identification of the terms in Table 2.1 easy. We obtain

$$i(t) = \mathcal{L}^{-1}\{I(s)\} = \frac{V}{R}(1 - e^{-Rt/L}), \quad t \geq 0$$

where " \mathcal{L}^{-1} " denotes the inverse Laplace transform.

When calculating the response to the ac excitation, a lot of work would result were we to take the Laplace transform of $v(t)$ directly. Instead, we introduce the rotating phasor $\bar{v}(t) = V e^{j\omega_1 t}$, $t \geq 0$, whose Laplace transform is $\bar{V}(s) = V/(s - j\omega_1)$, giving

$$\begin{aligned} \bar{I}(s) &= \frac{V}{(s - j\omega_1)(sL + R)} = \frac{V}{L(s - j\omega_1)(s + R/L)} \\ &= \frac{V}{R + j\omega_1 L} \left(\frac{1}{s - j\omega_1} - \frac{1}{s + R/L} \right) \end{aligned}$$

and

$$\bar{i}(t) = \mathcal{L}^{-1}\{\bar{I}(s)\} = \frac{V}{R + j\omega_1 L} (e^{j\omega_1 t} - e^{-Rt/L}), \quad t \geq 0.$$

Taking the real part and multiplying by $\sqrt{2}$ then yields

$$i(t) = \frac{\sqrt{2}V}{\sqrt{R^2 + (\omega_1 L)^2}} \cos[\omega_1 t - \arctan(\omega_1 L/R)] - \frac{\sqrt{2}VR}{R^2 + (\omega_1 L)^2} e^{-Rt/L}, \quad t \geq 0.$$

The second term is the transient part of the response, which decays to zero with the time constant L/R , leaving the steady-state part (first term), which verifies Example 2.1.



PROBLEM 2.4

Find expressions for the current through an RC series circuit when the voltage across the circuit is given by **a**) $v(t) = V$, $t \geq 0$ and **b**) $v(t) = \sqrt{2}V \sin \omega_1 t$, $t \geq 0$, respectively.

2.2.3 Transfer Functions

The transfer function $H(s)$ is the quotient between the Laplace transforms of the output and input signals:

$$H(s) = \frac{\mathcal{L}\{\text{output signal}\}}{\mathcal{L}\{\text{input signal}\}} = \frac{Y(s)}{U(s)}. \quad (2.26)$$

Example 2.3 The transfer function of an RL series circuit with the voltage $v(t)$ across the circuit taken as input signal and the current $i(t)$ through the circuit as output signal is simply the admittance of the circuit:

$$H(s) = \frac{I(s)}{V(s)} = \frac{1}{sL + R}.$$

**PROBLEM 2.5**

Find the transfer function of an *RLC* series circuit with voltage input and current output.

PROBLEM 2.6

Consider an *RC* series circuit where the input signal is the voltage across both components and the output signal is the voltage across the capacitor.

- a) Find the transfer function for the circuit.
- b) Find the step response for a step of amplitude V : $u(t) = V$, $t \geq 0$.
- c) Find the response to a short-duration pulse $u(t)$ of amplitude V and duration T . **Hint:** $u(t) \approx AT\delta(t)$.

2.2.4 Relation Between Poles and System Dynamics

It is generally desired that a dynamic system should be stable. The stability property of a system can be linked to the system's impulse response $h(t)$, i.e., the response $y(t)$ to a short-duration pulse with pulse area 1: $u(t) = \delta(t)$. Because $\mathcal{L}\{\delta(t)\} = 1$, we have

$$y(t) = \mathcal{L}^{-1}\{H(s)\} = h(t). \quad (2.27)$$

The system is

- **asymptotically stable** if $h(t) \rightarrow 0$ as $t \rightarrow \infty$;
- **marginally stable** (or conditionally stable) if $h(t)$ is limited as $t \rightarrow \infty$;
- **unstable** if $|h(t)| \rightarrow \infty$ as $t \rightarrow \infty$.

The system's stability is associated with the locations of the poles of the transfer function. Expressing the transfer function as the quotient

$$H(s) = \frac{B(s)}{A(s)} = \frac{b_N s^N + b_{N-1} s^{N-1} + \cdots + b_0}{s^N + a_{N-1} s^{N-1} + \cdots + a_0} \quad (2.28)$$

where N is called the order of the system, the poles p_i , $i = 1, 2, \dots, N$ are the roots to the denominator polynomial $A(s)$, whereas the zeros z_i , $i = 1, 2, \dots, N$ are the roots to the numerator polynomial $B(s)$. This allows the factorization

$$H(s) = b_N \frac{(s - z_1)(s - z_2) \cdots (s - z_N)}{(s - p_1)(s - p_2) \cdots (s - p_N)}. \quad (2.29)$$

If all poles are of multiplicity 1 [an example where this is not true is $A(s) = (s + 1)^2$], then $H(s)$ can be expressed in partial fractions as

$$H(s) = k_0 + \frac{k_1}{s - p_1} + \frac{k_2}{s - p_2} + \cdots + \frac{k_N}{s - p_N} \quad (2.30)$$

giving the impulse response

$$h(t) = k_0\delta(t) + k_1 e^{p_1 t} + k_2 e^{p_2 t} + \cdots + k_N e^{p_N t}, \quad t \geq 0. \quad (2.31)$$

The poles may be complex, i.e., $p_i = \sigma_i + j\omega_i$, $i = 1, 2, \dots$. The term of the impulse response associated with the i th pole can thus be expressed as

$$k_i e^{p_i t} = k_i e^{(\sigma_i + j\omega_i)t} = k_i e^{\sigma_i t} (\cos \omega_i t + j \sin \omega_i t), \quad t \geq 0. \quad (2.32)$$

From (2.32) the following conclusions can be drawn regarding stability. The system is

- **asymptotically stable** if (and only if) $\operatorname{Re}\{p_i\} = \sigma_i < 0$, $i = 1, 2, \dots, N$, i.e., all poles are located in the left half of the s plane (LHP);
- **marginally stable** if there is at least one pole located on the imaginary axis: $\operatorname{Re}\{p_i\} = \sigma_i = 0$, but none in the right half of the s plane (RHP), and
- **unstable** if there is at least one pole located in the RHP: $\operatorname{Re}\{p_i\} = \sigma_i > 0$.

The result also holds for systems with poles of higher multiplicity than 1 with one exception: for the system to be marginally stable, any poles on the imaginary axis must be of multiplicity 1. Thus, the system $H(s) = 1/s$ is marginally stable, whereas $H(s) = 1/s^2$ is unstable. In addition to stability, (2.32) reveals the following properties of the system dynamics.

- The distance from the pole to the imaginary axis, i.e., the absolute value of the **real part**, $|\sigma_i|$, determines the **exponential divergence rate** for RHP poles ($\sigma_i > 0$) or the **exponential convergence rate** for LHP poles ($\sigma_i < 0$) associated with the i th pole. A pole further into the LHP gives faster exponential convergence than a pole close to the imaginary axis.
- The distance from the pole to the imaginary axis, i.e., the absolute value of the **imaginary part**, $|\omega_i|$, determines the **angular frequency of oscillation** associated with the i th pole. A pole further away from the real axis gives a higher oscillation frequency than a pole closer to the real axis. A pole on the negative real axis is associated with an exponential convergence which does not oscillate.

These properties are summarized in Figure 2.3.

Remark 2.2 If all coefficients of a transfer function are real, then the poles and zeros must appear in conjugated pair. For example, if there is a pole at $s = \sigma_1 + j\omega_1$ there must also be a pole at $s = \sigma_1 - j\omega_1$. All imaginary parts in (2.32) then add up to zero, making $h(t)$ real.

2.2.5 Determination of Stability

Solving the poles of a transfer function is often impractical, because the transfer function often does not have numerical coefficients, but analytic coefficients that are functions of the system parameters, such as RLC circuit parameters. The following rules are helpful for determination of the stability of a system:

- First- and second-order systems are asymptotically stable if (and only if) all denominator coefficients are positive ($a_1 > 0$ and $a_0 > 0$). $H(s) = 1/(s^2 + s + 1)$ is thus asymptotically stable, but not $H(s) = 1/(s^2 - s + 1)$.
- For higher-order systems it is necessary *but not sufficient* for asymptotic stability that all denominator coefficients are positive: $a_i > 0$, $i = 0, 1, \dots, N - 1$. $H(s) = 1/(s^3 - s^2 + s + 1)$ is thus not asymptotically stable, whereas nothing conclusive can be said about $H(s) = 1/(s^3 + s^2 + s + 1)$ without further checking, e.g., using the Routh–Hurwitz test.

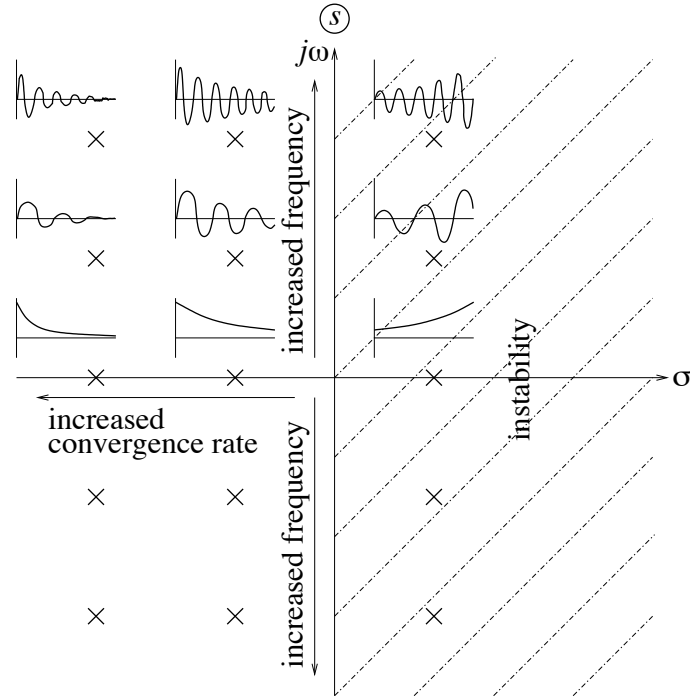


Figure 2.3. Pole locations in the s plane and the associated exponential responses.

- Passive RLC circuits are asymptotically stable for any system order. (In the unrealistic case when there is no resistance at all, the circuit is marginally stable.)

2.2.6 Frequency Response

The transform rule for the convolution shown in Table 2.1 reveals the connection between the Laplace transform and the $j\omega$ method. If the input signal to a system with transfer function $H(s)$ is taken as a complex phasor $u(t) = \hat{U}e^{j\omega t}$ (whose angular frequency ω is arbitrary), then the output signal is given by

$$y(t) = \int_0^\infty h(\tau) \hat{U} e^{j\omega(t-\tau)} d\tau = \underbrace{\left[\int_0^\infty h(\tau) \hat{U} e^{-j\omega\tau} d\tau \right]}_{H(j\omega)} \underbrace{\hat{U} e^{j\omega t}}_{u(t)} = H(j\omega)u(t). \quad (2.33)$$

We find that the frequency response for a certain system is evaluated simply by setting $s = j\omega$ in the transfer function. The special case $s = \omega = 0$ yields the static gain $H(0)$, i.e., the gain for a constant input signal. This follows also from the final value theorem, which says that, provided that $y(t)$ converges as $t \rightarrow \infty$, then

$$y(\infty) = \lim_{s \rightarrow 0} sY(s). \quad (2.34)$$

If $Y(s) = H(s)U(s)$ and the input signal is a unit step, i.e., $u(t) = 1, t \geq 0 \Rightarrow U(s) = 1/s$, then $y(t)$ converges provided that $H(s)$ is asymptotically stable. In that case, (2.34) can be applied to

calculate the final value

$$y(\infty) = \lim_{s \rightarrow 0} sY(s) = \lim_{s \rightarrow 0} s \frac{H(s)}{s} = H(0). \quad (2.35)$$

2.2.7 Rise Time and Bandwidth

The rise time of a system is defined as the time t_r required for the output signal to go from 10% to 90% of the final value, given that the input signal is a step, see Figure 2.4(a). For the first-order system

$$H(s) = \frac{b}{s+a} = \frac{k}{sT+1}, \quad T = \frac{1}{a}, \quad k = \frac{b}{a} \quad (2.36)$$

where T is the known as the time constant. We find that the time constant is the inverse distance from the pole to the imaginary axis. The rise time can be expressed as

$$t_r = T \ln 9 = \frac{\ln 9}{a} \quad (2.37)$$

where $\ln 9 \approx 2.2$.

PROBLEM 2.7

Show that!

PROBLEM 2.8

Show that if a step is applied to (2.36) at $t = 0$, then the step response has reached 63% of the final value at $t = T$.

The bandwidth of a system of low-pass characteristic [i.e., $|H(j0)| = H(0) > 0$ and $|H(j\infty)| = 0$] is defined as the angular frequency ω_B for which

$$\frac{|H(j\omega_B)|}{H(0)} = \frac{1}{\sqrt{2}} \quad (2.38)$$

as shown in Figure 2.4(b). The bandwidth of (2.36) is a .

PROBLEM 2.9

Show that!

Thus, (2.37) can also be expressed as

$$\text{rise time} = \frac{\ln 9}{\text{bandwidth}}$$

which holds exactly for (2.37) but approximately also for higher-order systems.

PROBLEM 2.10

Determine approximately the rise time of the system $H(s) = 1/(s^2 + 2s + 2)$.

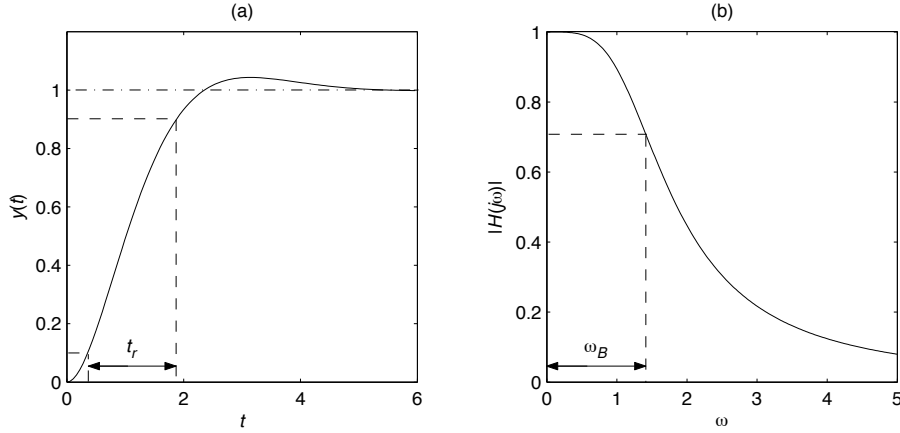


Figure 2.4. (a) Step response $y(t)$ with rise time t_r . (b) Magnitude function $|H(j\omega)|$ with bandwidth ω_B .

2.2.8 Damping

Second-order systems are often parametrized in the following way:

$$H(s) = \frac{k\omega_0^2}{s^2 + 2\zeta\omega_0 s + \omega_0^2} \quad (2.39)$$

where ω_0 (which is positive) is called the angular eigenfrequency of the undamped system and ζ the relative damping. If $0 \leq \zeta < 1$, the poles of the system are given by

$$s = \left(-\zeta \pm j\sqrt{1 - \zeta^2} \right) \omega_0. \quad (2.40)$$

When ζ is varied between 0 and 1, the poles move on a half circle with radius ω_0 in the left half plane. For $\zeta > 1$, the pole move along the negative real axis, one toward the origin and one toward $-\infty$. Step responses for a few different values of ζ are depicted in Figure 2.5(a) and their corresponding poles are depicted in Figure 2.5(b).

The following observations can be made.

- For $\zeta = 0$, the step response oscillates with constant amplitude. The angular frequency of the oscillation is ω_0 (which explains the name of this parameter). The poles are then located on the imaginary axis, at $s = \pm j\omega_0$.
- The overshoot, which is the maximal value of $y(t)$ with the final value (here, 1) subtracted, increases as ζ decreases, peaking at 100% for $\zeta = 0$. Large overshoot corresponds to poles closer to the imaginary axis.
- For $\zeta = 0.7$, there is only a small overshoot (about 5%). For this value of the relative damping, or more precisely, $\zeta = 1/\sqrt{2}$, the poles are located at $(-1 \pm j)\omega_0/\sqrt{2}$, i.e., with an angle of 45° relative both the real and imaginary axes.

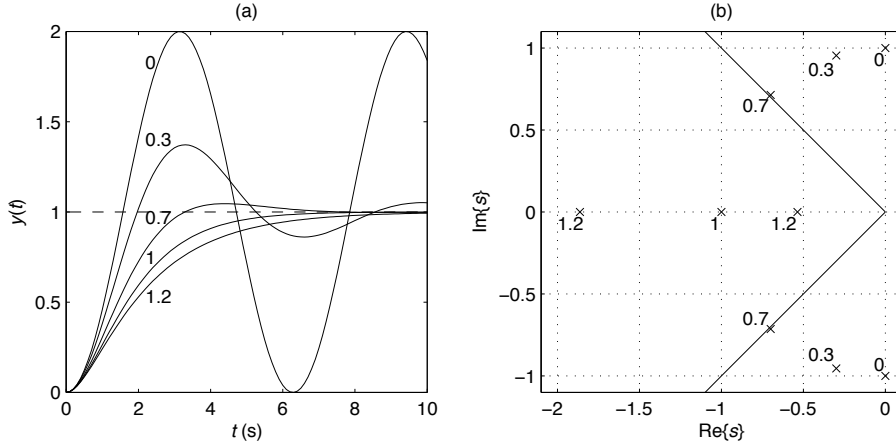


Figure 2.5. (a) Step responses and (b) poles of (2.39) for $k = \omega_0 = 1$ and five different values $\zeta = \{0, 0.3, 0.7, 1, 1.2\}$ as indicated.

- For $\zeta = 1$ there is no overshoot. The system is said to be critically damped for $\zeta = 1$. Both poles are located at $s = -\omega_0$.
- For $\zeta = 1.2$, a slower response is obtained than for $\zeta = 1$. This is because the poles then are located on the real axis, but one has moved closer to the origin as compared to $\zeta = 1$. This pole dominates and slows down the response. If $\zeta > 1$ the system is called overdamped.

If small overshoots are desired, ζ should not be made smaller than $1/\sqrt{2}$. This means that the poles should not be located closer to the imaginary axis than with an angle of 45° , i.e., to the left of the solid lines in Figure 2.5(b). This yields the recommendation

$$\frac{1}{\sqrt{2}} \leq \zeta \leq 1. \quad (2.41)$$

PROBLEM 2.11

How would letting $\omega_0 = 2$ alter the step responses in Figure 2.5?

2.2.9 Differential Operator

Sometimes it is convenient to use the differential operator $p = d/dt$. In many cases it can be used interchangeably with the Laplace variable s . A transfer function $H(s)$ is replaced by the corresponding transfer operator $H(p)$, giving the correspondence

$$Y(s) = H(s)U(s) \leftrightarrow y(t) = H(p)u(t). \quad (2.42)$$

Whereas $H(s)$ multiplies with the Laplace transformed input signal, $H(p)$ operates on the actual input signal, i.e., the function of time $u(t)$. For this reason we can never divide by $u(t)$ in the second equality in (2.42), as we can in the first equality: $Y(s)/U(s) = H(s)$.

Remark 2.3 The Laplace variable and the differential operator shall never be confused with the Laplace operator, which is the partial-derivative operator

$$\Delta = \nabla \cdot \nabla = \frac{\partial^2}{\partial x^2} + \frac{\partial^2}{\partial y^2} + \frac{\partial^2}{\partial z^2}$$

used in vector analysis.

2.2.10 State-Space Models

The state-space model for a linear system is given by

$$\dot{\mathbf{x}}(t) = \mathbf{A}\mathbf{x}(t) + \mathbf{B}u(t) \quad (2.43)$$

$$y(t) = \mathbf{C}\mathbf{x}(t) + Du(t) \quad (2.44)$$

where $\mathbf{x}(t)$ is the state vector, whose components $x_1(t), x_2(t), \dots, x_N(t)$ are called the state variables. Whereas the transfer function only gives an input–output description of a system, a state-space model also gives an internal description, because the state variables can be chosen as physical variables. \mathbf{A} , \mathbf{B} , and \mathbf{C} are matrices, whereas D is a scalar (as long as the input and output signals are scalars). For electric circuits, the state variables are normally chosen as

- inductor currents, and
- capacitor voltages.

By taking the Laplace transform and eliminating the state vector

$$\begin{aligned} s\mathbf{X}(s) &= \mathbf{AX}(s) + \mathbf{BU}(s) \Rightarrow (s\mathbf{I} - \mathbf{A})\mathbf{X}(s) = \mathbf{BU}(s) \Rightarrow \\ \mathbf{X}(s) &= (s\mathbf{I} - \mathbf{A})^{-1}\mathbf{BU}(s) \Rightarrow Y(s) = [\mathbf{C}(s\mathbf{I} - \mathbf{A})^{-1}\mathbf{B} + D]U(s) \end{aligned}$$

the transfer function corresponding to (2.43)–(2.44) is found to be

$$H(s) = \frac{Y(s)}{U(s)} = \mathbf{C}(s\mathbf{I} - \mathbf{A})^{-1}\mathbf{B} + D = \frac{\mathbf{C} \operatorname{adj}(s\mathbf{I} - \mathbf{A})\mathbf{B}}{\det(s\mathbf{I} - \mathbf{A})} + D \quad (2.45)$$

where $\operatorname{adj}(\cdot)$ is the adjoint matrix. The poles of the transfer function are given by the roots to the characteristic polynomial $\det(s\mathbf{I} - \mathbf{A})$. The roots of the characteristic polynomial are the eigenvalues of \mathbf{A} . Thus, since $\det(s\mathbf{I} - \mathbf{A})$ is the denominator polynomial of (2.45), the poles of the system are the same as the eigenvalues of \mathbf{A} . For 2×2 matrices, the determinant and the adjoint matrix are calculated as follows:

$$\det \begin{bmatrix} a & b \\ c & d \end{bmatrix} = ad - bc, \quad \operatorname{adj} \begin{bmatrix} a & b \\ c & d \end{bmatrix} = \begin{bmatrix} d & -b \\ -c & a \end{bmatrix}. \quad (2.46)$$

Example 2.4 The state-space model for an *RLC* series circuit, where the total voltage is the input signal $u(t)$ and the current is the output signal $y(t)$, can be found as follows. Let $x_1(t)$ be the current through the inductor (which equals the output signal) and let $x_2(t)$ be the voltage across the capacitor. Kirchhoff's second law then says that

$$Rx_1(t) + L \frac{dx_1(t)}{dt} + x_2(t) = u(t)$$

whereas the derivative of the capacitor voltage times C equals the current

$$C \frac{dx_2(t)}{dt} = x_1(t).$$

Rewriting these in state-space component form yields

$$\begin{aligned}\dot{x}_1(t) &= -\frac{R}{L}x_1(t) - \frac{1}{L}x_1(t) + \frac{1}{L}u(t) \\ \dot{x}_2(t) &= \frac{1}{C}x_1(t) \\ y(t) &= x_1(t)\end{aligned}$$

from which the state matrices are easily identified

$$\mathbf{A} = \begin{bmatrix} -\frac{R}{L} & -\frac{1}{L} \\ \frac{1}{C} & 0 \end{bmatrix} \quad \mathbf{B} = \begin{bmatrix} \frac{1}{L} \\ 0 \end{bmatrix} \quad \mathbf{C} = [1 \ 0]$$

whereas $D = 0$.



PROBLEM 2.12

A state-space model is not unique; there exist an infinite number of different, but from the “outside” equivalent, state-space models for a certain system.

- Find the state matrices for the system in Example 2.4 if instead $x_1(t)$ is taken as the capacitor voltage and $x_2(t)$ as the inductor current.
- Show that the same transfer function $H(s)$ is obtained for both choices of the state variables.
- Suppose that a new state vector $\mathbf{w}(t) = \mathbf{P}\mathbf{x}(t)$ (where \mathbf{P} is an invertible transformation matrix) is introduced in a general state-space system (2.43)–(2.44). Show that the transfer function (2.45) is invariant of \mathbf{P} .

PROBLEM 2.13

Figure 2.6 shows the circuit diagram of a so-called *LCL* filter.

- Find a state-space model for the system.
- Find the transfer function $H(s)$.
- For $L_1 = L_2 = L$, select C such that maximum input-to-output transfer of power is achieved for $u(t) = \sqrt{2}U \cos \omega_1 t$. Also find an expression for the maximum mean power developed in the resistor R . It can be assumed that $\omega_1 L \gg R$. **Hint:** $|H(j\omega_1)|^2$.
- Find an expression for the input impedance and characterize its properties when C is selected according to c). It can again be assumed that $\omega_1 L \gg R$.

2.3 Nonlinear Continuous-Time Systems

Although many dynamic systems can be modeled using linear models (transfer functions and state-space models), most are in reality nonlinear, more or less heavily so. The linear model is valid

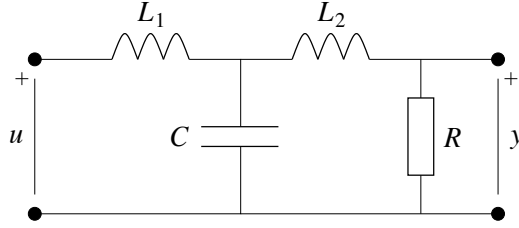


Figure 2.6. LCL filter.

only about a certain operating point; often, the linear condition (2.21) holds only when $u(t)$ is sufficiently small.

When power electronic converters and variable-speed drives are studied, nonlinear system models will inevitably be encountered. State-space models can be generalized to cover also nonlinear systems:

$$\dot{\mathbf{x}}(t) = \mathbf{f}(\mathbf{x}(t), u(t)) \quad (2.47)$$

$$y(t) = \mathbf{g}(\mathbf{x}(t)). \quad (2.48)$$

Equations (2.43)–(2.44) for $D = 0$ represent a special case of (2.47)–(2.48) with $\mathbf{f}(\mathbf{x}(t), u(t)) = \mathbf{A}\mathbf{x}(t) + \mathbf{B}u(t)$ and $\mathbf{g}(\mathbf{x}(t)) = \mathbf{C}\mathbf{x}(t)$. Naturally, it is much more difficult to analyze the stability of (2.47)–(2.48) than of the linear system (2.43)–(2.44). Although it represents only a special case, it is often necessary to restrict analysis to a constant input signal, as otherwise the analysis tends to become extremely complicated. A constant input signal allows $u(t)$ to be dropped from the state-space equations, obtaining what is known as an autonomous system:

$$\dot{\mathbf{x}}(t) = \mathbf{f}(\mathbf{x}(t)). \quad (2.49)$$

Quite often, the system is of order two, i.e., with $\mathbf{x}(t) = [x_1(t), x_2(t)]^T$, or can be approximated as such. We may then express the system in component form as

$$\dot{x}_1(t) = f_1(x_1(t), x_2(t)) \quad (2.50)$$

$$\dot{x}_2(t) = f_2(x_1(t), x_2(t)). \quad (2.51)$$

The questions of importance are: is (2.49) stable, and if so, to which value does $x(t)$ converge when initialized at a certain point $x(0)$ in the state space? Naturally, if $x(t)$ converges, then $\dot{x}(t) = 0$, so the points to which $x(t)$ may possibly converge—which are known as equilibrium points—are obtained by setting $\dot{x}(t) = 0$ in (2.49) and solving for $x(t)$. An equilibrium point \mathbf{x}^* thus satisfies the relation

$$\mathbf{f}(\mathbf{x}^*) = 0. \quad (2.52)$$

A linear autonomous system $\dot{\mathbf{x}}(t) = \mathbf{A}\mathbf{x}(t)$ has only one equilibrium point, the origin $\mathbf{x}^* = 0$, but a nonlinear system may have several. Consider for example the following system:

$$\dot{x}_1(t) = -x_1(t) + x_1^2(t) \quad (2.53)$$

$$\dot{x}_2(t) = x_1^2(t) - x_2(t). \quad (2.54)$$

There are two equilibrium points: $\mathbf{x}^{*(1)} = [0, 0]^T$ and $\mathbf{x}^{*(2)} = [1, 1]^T$.

2.3.1 Global and Local Stability

Some nonlinear systems have the excellent property that they are globally stable. This means that, regardless of the starting point $\mathbf{x}(0)$ in the state space, $\mathbf{x}(t)$ converges to the same equilibrium point \mathbf{x}^* . Global stability may be difficult to prove, though. So-called Lyapunov functions (or Lyapunov's second—or direct—method) are very powerful for this purpose, but are often hard to find; see Appendix A.

Local stability is easier to prove, as will be shown momentarily. Local stability implies that, if the starting point $\mathbf{x}(0)$ is close enough to the equilibrium point \mathbf{x}^* , then $\mathbf{x}(t)$ will converge to \mathbf{x}^* . As will be seen in the subsequent chapters, in control of converters and drives, the starting point is—with only a few exceptions—close to the equilibrium. Therefore, local stability is often good enough a property.

2.3.2 Analysis of Local Stability by Linearization

If $\mathbf{x}(t) \approx \mathbf{x}^*$ we have $\mathbf{f}(\mathbf{x}(t)) \approx 0$. Hence, $\mathbf{f}(\mathbf{x}(t))$ can be approximated as a first-order Taylor series expansion

$$\mathbf{f}(\mathbf{x}(t)) \approx \underbrace{\mathbf{f}(\mathbf{x}^*)}_{0} + \mathbf{f}'(\mathbf{x}^*)[\mathbf{x}(t) - \mathbf{x}^*]. \quad (2.55)$$

It therefore appears logical that close to an equilibrium point, (2.49) can be approximated as a linear system

$$\dot{\tilde{\mathbf{x}}}(t) = \mathbf{A}\tilde{\mathbf{x}}(t) \quad \mathbf{A} = \mathbf{f}'(\mathbf{x}^*) \quad (2.56)$$

where $\tilde{\mathbf{x}}(t) = \mathbf{x}(t) - \mathbf{x}^*$. Linearization is the most commonly used method for stability analysis of nonlinear systems and is also called Lyapunov's first (or indirect) method. Stability of the linearized system (2.56) can be analyzed simply by calculating the eigenvalues of \mathbf{A} . If we restrict the analysis to second-order systems—which is the case in the applications encountered in this book—this matrix is given by

$$\mathbf{A} = \mathbf{f}'(\mathbf{x}^*) = \begin{bmatrix} \frac{\partial f_1(x_1, x_2)}{\partial x_1} & \frac{\partial f_1(x_1, x_2)}{\partial x_2} \\ \frac{\partial f_2(x_1, x_2)}{\partial x_1} & \frac{\partial f_2(x_1, x_2)}{\partial x_2} \end{bmatrix}_{\mathbf{x}=\mathbf{x}^*}. \quad (2.57)$$

There are two eigenvalues, which we denote as λ_1 and λ_2 , i.e., the characteristic polynomial is given by

$$(s - \lambda_1)(s - \lambda_2) = s^2 - \underbrace{(\lambda_1 + \lambda_2)}_{a_1}s + \underbrace{\lambda_1\lambda_2}_{a_0}. \quad (2.58)$$

The type of equilibrium point is determined by the signs of the real parts of the eigenvalues.

1. **Stable equilibrium point—sink:** $\text{Re}\{\lambda_1\} < 0, \text{Re}\{\lambda_2\} < 0$ ($a_1 > 0, a_0 > 0$). Any trajectory starting in the vicinity of \mathbf{x}^* will converge to \mathbf{x}^* . The system behaves as an asymptotically stable linear system about \mathbf{x}^* .
2. **Unstable equilibrium point—source:** $\text{Re}\{\lambda_1\} > 0, \text{Re}\{\lambda_2\} > 0$ ($a_1 < 0, a_0 > 0$). Any trajectory starting in the vicinity of \mathbf{x}^* will diverge from \mathbf{x}^* . The system behaves as an unstable linear system about \mathbf{x}^* .

3. **Unstable equilibrium point—saddle point:** $\lambda_1 > 0, \lambda_2 < 0$ ($a_0 < 0$). (The eigenvalues are in this case always real.) Trajectories close to a saddle point tend first to approach the saddle point and then move away from it. Hence, most trajectories starting in the vicinity of \mathbf{x}^* will diverge from \mathbf{x}^* . Theoretically, there are also initial values $\mathbf{x}(0)$ for which $\mathbf{x}(t)$ will converge to \mathbf{x}^* . These are called the stable separatrices or stable manifolds, and are important, as they determine the stable regions about each sink [48].
4. **Center:** $\text{Re}\{\lambda_1\} = \text{Re}\{\lambda_2\} = 0$ ($a_1 = 0$). Nothing conclusive about stability can be said. Centers are not considered here; for more information, see [48].

Example 2.5 Suppose that an *RLC* circuit is connected to the input of a dc–dc converter as shown in Figure 2.7. The input voltage E is constant. If the converter can be assumed static and lossless, the following input–output power balance must hold:

$$v_1(t)i_1(t) = v_2(t)i_2(t).$$

If $v_2(t)$ and $i_2(t)$ are controlled such that the output power is constant: $v_2(t)i_2(t) = P$, the input current will be given by

$$i_1(t) = \frac{P}{v_1(t)}.$$

Unlike *RLC* circuits, the dc–dc converter has a nonlinear input voltage–current relation.

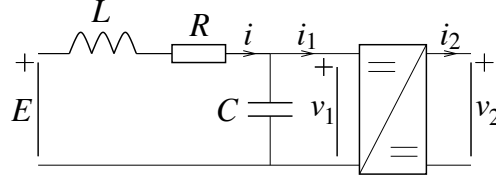


Figure 2.7. *RLC* circuit connected to a dc–dc converter.

Taking $i(t)$ and $v_1(t)$ as state variables, the following nonlinear state-space model is obtained:

$$\frac{di(t)}{dt} = -\frac{R}{L}i(t) - \frac{1}{L}v_1(t) + \frac{E}{L} \quad (2.59)$$

$$\frac{dv_1(t)}{dt} = \frac{1}{C}i(t) - \frac{1}{C} \underbrace{\frac{P}{v_1(t)}}_{i_1(t)}. \quad (2.60)$$

The equilibrium points (EPs) are found by solving for $i(t)$ on the right-hand side of (2.59) and substituting in (2.60), giving the following equation:

$$\begin{aligned} v_1^2 - Ev_1 + RP = 0 \Rightarrow v_1^{*(1,2)} &= \frac{E}{2} \pm \sqrt{\frac{E^2}{4} - PR} = \frac{E}{2} \left(1 \pm \sqrt{1 - \frac{4PR}{E^2}} \right) \\ &\approx \frac{E}{2} \left[1 \pm \left(1 - \frac{2PR}{E^2} \right) \right] = \begin{cases} E - \frac{PR}{E} \approx E & (\text{EP1}) \\ \frac{PR}{E} & (\text{EP2}) \end{cases} \end{aligned}$$

the approximations if R can be assumed small. Linearization of (2.59)–(2.60) involves only one term: $i_1(t)$, since all other terms are linear. Equation (2.57) can either be applied directly, or we can proceed as follows. Introduce $\tilde{v}_1(t) = v_1(t) - v_1^*$. Then

$$\begin{aligned} i_1(t) &= \frac{P}{v_1(t)} = \frac{P}{v_1^* + \tilde{v}_1(t)} = \frac{P}{v_1^*} \frac{1}{1 + \tilde{v}_1(t)/v_1^*} \approx \frac{P}{v_1^*} \left[1 - \frac{\tilde{v}_1(t)}{v_1^*} \right] \\ &= \frac{P}{v_1^*} - \frac{P}{(v_1^*)^2} \tilde{v}_1(t) \end{aligned}$$

where the approximation results from the MacLaurin series expansion $1/(1-x) = 1+x+x^2+\dots$, which is truncated after two terms. For $P > 0$ the dc–dc converter thus acts as a negative conductance $-P/(v_1^*)^2$. The linearized system is obtained as

$$\begin{aligned} \frac{d\tilde{i}(t)}{dt} &= -\frac{R}{L}\tilde{i}(t) - \frac{1}{L}\tilde{v}_1(t) \\ \frac{d\tilde{v}_1(t)}{dt} &= \frac{1}{C}\tilde{i}(t) + \frac{P}{C(v_1^*)^2}\tilde{v}_1(t) \end{aligned}$$

giving

$$\mathbf{A} = \begin{bmatrix} -\frac{R}{L} & -\frac{1}{L} \\ \frac{1}{C} & \frac{P}{C(v_1^*)^2} \end{bmatrix}$$

and the characteristic polynomial

$$\det(s\mathbf{I} - \mathbf{A}) = s^2 + \left[\frac{R}{L} - \frac{P}{C(v_1^*)^2} \right] s + \frac{1}{LC} \left[1 - \frac{PR}{(v_1^*)^2} \right].$$

For the two equilibrium points we obtain, respectively

$$\begin{aligned} \text{EP1: } & s^2 + \left(\frac{R}{L} - \frac{P}{CE^2} \right) s + \frac{1}{LC} \left(1 - \frac{PR}{E^2} \right) \\ & \approx s^2 + \left(\frac{R}{L} - \frac{P}{CE^2} \right) s + \frac{1}{LC} \\ \text{EP2: } & s^2 + \left[\frac{R}{L} - \frac{P}{C(PR/E)^2} \right] s + \frac{1}{LC} \left[1 - \frac{PR}{(PR/E)^2} \right] \\ & \approx s^2 - \frac{E^2}{PCR^2} s - \frac{E^2}{PLRC}. \end{aligned}$$

Thus, EP2 is a saddle point (unstable), whereas EP1 is a sink (asymptotically stable) if

$$\frac{R}{L} - \frac{P}{CE^2} > 0 \Rightarrow R > \frac{PL}{CE^2}$$

and otherwise a source (unstable). A sufficiently large resistance R is required to compensate for the negative conductance of the converter for $P > 0$. In Figure 2.8, a simulation for $E = 100$ V, $P = 500$ W, $L = 10$ mH, and $C = 1000 \mu\text{F}$ is shown, where $R = 1 \Omega$ for $0 \leq t < 0.5$ s. The initial values are $v_1(0) = 100$ V and $i(0) = 0$ A. It is seen that $v_1(t)$ converges to a steady-state value after an initial damped oscillation. The criterion for stability is $R > PL/CE^2 = 0.5 \Omega$. At $t = 0.5$ s, R is decreased to 0.45Ω . As can be seen, the equilibrium point turns unstable; an oscillation with increasing amplitude commences.

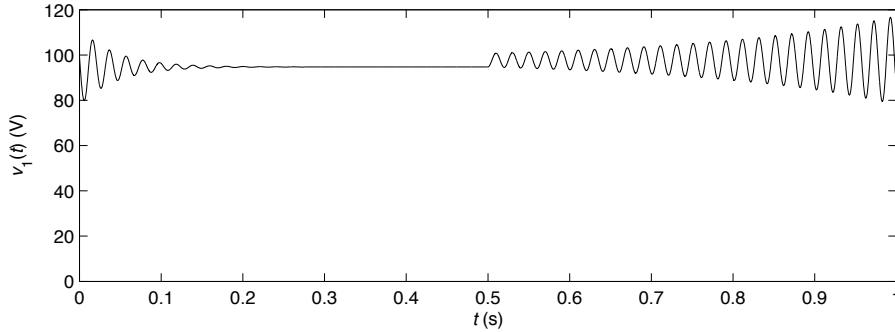


Figure 2.8. Simulation of an RLC circuit connected to the input of a dc–dc converter that draws constant power. At $t = 0.5$ s, resistance R is decreased.



PROBLEM 2.14

Characterize the equilibrium points of the nonlinear system (2.53)–(2.54).

PROBLEM 2.15

Suppose that in the T filter in Figure 2.6, $L_1 = L$ whereas $L_2 = 0$, and R is replaced by a nonlinear resistor with the following voltage–current characteristic:

$$v_R(t) = k i_R^3(t).$$

- a) Find a nonlinear state-space model for the system.
- b) Find and characterize the equilibrium points when the input signal is constant: $u(t) = U$. What can be said about the system’s stability properties?

2.4 Linear Discrete-Time Systems

2.4.1 Sampling Process

Virtually all converter control systems are today implemented digitally, i.e., they process discrete-time samples of continuous-time signals. The sampling process can be illustrated as a switch which closes periodically with the sampling interval T_s . Each time $t = kT_s$, where k (an integer) is called the sampling instant, that the switch closes a snapshot of the continuous-time signal $y(t)$ is taken. This is illustrated in Figure 2.9(a). A discrete-time signal

$$y_k = y(kT_s) \quad (2.61)$$

results, whose values are called samples. See Figure 2.9(b).

2.4.2 Sampling Theorem and Prefiltering

It is well known that a signal to be sampled should not contain components at frequencies above half the sampling frequency, $f_s/2$, where $f_s = 1/T_s$, which is also called the Nyquist frequency. In the

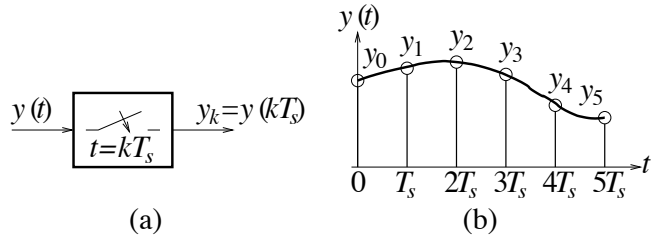


Figure 2.9. Sampling process illustrated (a) as a block and (b) in the time domain.

sampling process, such components will be aliased down into the frequency range $[0, f_s/2]$, possibly causing significant distortion. In situations where there are known to be significant components above the Nyquist frequency, prefiltering of the measured signal $y(t)$ should be applied before the signal is sampled. This can be made using a continuous-time low-pass filter (LPF), as shown in Figure 2.10(a). An alternative is oversampling, i.e., the measured signal is sampled L times as often as the desired sampling rate, such that all frequency components that are within the bandwidth of the measurement sensor are captured without aliasing. A discrete-time low-pass filter is then applied. The output signal of the low-pass filter is then decimated, meaning that every L th sample is picked out, giving the desired sampling rate. Often, oversampling, discrete-time prefiltering, and decimation are made using an FPGA. If needed, a combination of the two methods can be used, where both continuous- and discrete-time prefilters are applied. In this case, the continuous-time prefilter can have low order.

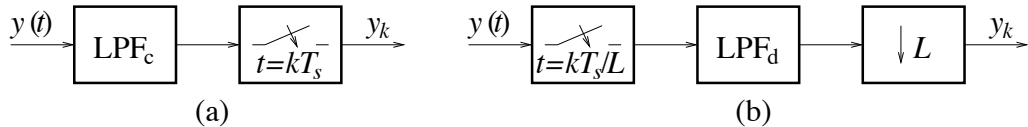


Figure 2.10. (a) Continuous-time prefiltering. (b) Oversampling, discrete-time prefiltering, and decimation.

2.4.3 Z Transform

The discrete-time correspondence to the Laplace transform is the Z transform, which is defined as

$$Y(z) = \mathcal{Z}\{y_k\} = \sum_{k=0}^{\infty} y_k z^{-k}. \quad (2.62)$$

One important property is the transform of a one-sample delay

$$\mathcal{Z}\{y_{k-1}\} = \sum_{k=0}^{\infty} y_{k-1} z^{-k} = \{k = n+1\} = \sum_{n=-1}^{\infty} y_n z^{-(n+1)} = y_{-1} + z^{-1} \underbrace{\sum_{n=0}^{\infty} y_n z^{-n}}_{Y(z)}. \quad (2.63)$$

Table 2.2. Z transform pairs.

Signal (for $k \geq 0$)		Z transform
a^k	(Exponential)	$\frac{z}{z-a}$
δ_k	(Unit pulse)	1
1	(Step)	$\frac{z}{z-1}$
k	(Ramp)	$\frac{z}{(z-1)^2}$
y_{k+1}	(Forward shift)	$z[Y(z) + y_0]$
$y_k = \sum_{n=0}^k h_n u_{k-n}$	(Convolution)	$Y(z) = H(z)U(z)$.

Assuming that $y_{-1} = 0$, we thus obtain

$$\mathcal{Z}\{y_{k-1}\} = z^{-1}Y(z). \quad (2.64)$$

In words, a one-sample delay is transformed to a multiplication by z^{-1} . Suppose that y_k is obtained by sampling of $y(t)$, as illustrated in Figure 2.9. A one-sample delay obviously corresponds to the time delay $y(t - T_s)$, whose Laplace transform is given by

$$\mathcal{L}\{y(t - T_s)\} = e^{-sT_s}Y(s). \quad (2.65)$$

This shows intuitively that the correspondence between the two transform variables is $z^{-1} = e^{-sT_s}$, i.e,

$$z = e^{sT_s}. \quad (2.66)$$

In complex analysis this is known as a conformal mapping. Some important Z transform pairs are given in Table 2.2.

2.4.4 Difference Equations and Transfer Functions

The discrete-time correspondence to differential equations are difference equations, which have the form

$$y_k + a_{N-1}y_{k-1} + a_{N-2}y_{k-2} + \cdots + a_0y_{k-N} = b_Nu_k + b_{N-1}u_{k-1} + b_{N-2}u_{k-2} + \cdots + b_0y_{k-N} \quad (2.67)$$

where N is the system order. Unlike a differential equation, a difference equation is its own numerical solution. The output at a certain sampling instant k is computed recursively as the sum of weighted input and output samples, back to the sampling instant $k - N$, as

$$y_k = b_Nu_k + b_{N-1}u_{k-1} + b_{N-2}u_{k-2} + \cdots + b_0y_{k-N} - a_{N-1}y_{k-1} - a_{N-2}y_{k-2} - \cdots - a_0y_{k-N} \quad (2.68)$$

By finding a discrete-time approximation—also called discretization—of a continuous-time system, this system can be simulated using the difference equation of the discretization. In a similar

fashion, filters and controllers can be designed as continuous-time systems and then be discretized for discrete-time implementation. To determine whether a certain discretization will be successful or not, some analysis is required, particularly stability theory for discrete-time systems. To this end, let us apply the Z transform to (2.67). The following transfer function is obtained:

$$\begin{aligned} H(z) = \frac{Y(z)}{U(z)} &= \frac{b_N + b_{N-1}z^{-1} + b_{N-2}z^{-2} + \cdots + b_0z^{-N}}{1 + a_{N-1}z^{-1} + a_{N-2}z^{-2} + \cdots + a_0z^{-N}} \\ &= \frac{b_N z^N + b_{N-1}z^{N-1} + b_{N-2}z^{N-2} + \cdots + b_0}{z^N + a_{N-1}z^{N-1} + a_{N-2}z^{N-2} + \cdots + a_0}. \end{aligned} \quad (2.69)$$

2.4.5 Relation Between Poles and System Dynamics

The Z transform allows the dynamics of a discrete-time system to be assessed using the poles of the transfer function in a similar fashion as continuous-time systems. The denominator and numerator of a general transfer function (2.69) can be factorized respectively in poles and zeros as

$$H(z) = b_0 \frac{(z - z_1)(z - z_2) \cdots (z - z_N)}{(z - p_1)(z - p_2) \cdots (z - p_N)}. \quad (2.70)$$

If all poles are of multiplicity 1, then $H(z)$ can be expressed in partial fractions as

$$H(s) = k_0 + \frac{k_1 z}{z - p_1} + \frac{k_2 z}{z - p_2} + \cdots + \frac{k_N z}{z - p_N} \quad (2.71)$$

giving the unit-pulse response

$$h_k = k_0 \delta_k + k_1 p_1^k + k_2 p_2^k + \cdots + k_N p_N^k, \quad k \geq 0. \quad (2.72)$$

The poles may be complex; for discrete-time systems it is convenient to use polar form as $p_i = r_i e^{j\Omega_i}$, $i = 1, 2, \dots$. The term of the unit-pulse response associated with the i th pole can thus be expressed as

$$(r_i e^{j\Omega_i})^k = r_i^k (\cos \Omega_i k + j \sin \Omega_i k), \quad k \geq 0. \quad (2.73)$$

From (2.73) the following conclusions can be drawn regarding system stability. The system is

- **asymptotically stable** if (and only if) $|p_i| = r_i < 1$, $i = 1, 2, \dots, N$, i.e., all poles are located within the unit circle in the z plane;
- **marginally stable** if there is at least one pole located on the unit circle: $|p_i| = r_i = 1$, but none outside, and
- **unstable** if there is at least one pole located outside the unit circle: $|p_i| = r_i > 1$.

The result also holds for systems with poles of higher multiplicity than 1 with one exception: for the system to be marginally stable, any poles on the unit circle must be of multiplicity 1. In addition to stability, (2.32) reveals the following properties of the system dynamics.

- The modulus of the pole, i.e., distance from the pole to the origin, $|p_i| = r_i$, determines the **exponential divergence rate** if $|p_i| > 1$ and the **exponential convergence rate** $|p_i| < 1$ associated with the i th pole. A pole closer to the origin gives faster exponential convergence than a pole close to the imaginary axis.

- The angle of the pole relative the positive real axis, Ω_i , determines the **normalized frequency of oscillation** associated with the i th pole. A pole with a larger angle gives a higher oscillation frequency than a pole with a smaller angle. A pole on the positive real axis within the unit circle, i.e., $0 \leq p_i < 1$ is associated with an exponential response that does not oscillate.

These properties can be derived from the corresponding properties of continuous-time systems by applying the mapping (2.66) between the s and z planes. They can also be deduced by sampling the exponential response $e^{(\sigma+j\omega)t}$, which gives

$$e^{(\sigma+j\omega)kT_s} = (e^{\sigma T_s})^k e^{j\omega kT_s} \quad (2.74)$$

showing that

$$r = e^{\sigma T_s} \quad \Omega = \omega T_s. \quad (2.75)$$

Now, it is obvious that asymptotic stability in the s plane, i.e., $\sigma < 0$, corresponds directly to asymptotic stability in the s plane, i.e., $r < 1$.

Discrete-time systems have two unique properties as compared to continuous-time systems.

- The fastest convergence rate of a discrete-time system is one sample. This corresponds to a unique point in the z plane: the origin. This fact can be deduced by letting $s \rightarrow -\infty$, which via (2.66) gives $z \rightarrow 0$. A continuous-time system cannot have an infinitely fast convergence rate, though, and therefore no corresponding point exists in the s plane.
- The highest oscillation frequency results from a pole on the negative real axis, i.e., $\Omega = \pi$. Equation (2.75) shows that this corresponds to the angular Nyquist frequency $\omega = \pi/T_s$. This property is a direct consequence of the sampling theorem.

The found properties are summarized in Figure 2.11.

2.4.6 Shift Operator

Sometimes it is convenient to apply the shift operator q , which corresponds to z in the same fashion as the differential operator p corresponds to s

$$qy_k = q_{k+1} \quad q^{-1}y_k = y_{k-1}. \quad (2.76)$$

2.4.7 Euler Discretization

It is often convenient to design filters, controllers, etc. in the s domain as if they were continuous-time systems. To allow discrete-time implementation, discretization of the continuous-time model is needed. Unfortunately, (2.66) cannot be applied directly for this purpose, because it would imply the substitution $s \rightarrow (\ln z)/T_s$, resulting in a transfer function which is irrational in z . Any discretization will therefore be an approximation and will consequently give altered properties as compared to the underlying continuous-time system.

We shall here consider the Euler discretization method, where a first-order MacLaurin expansion is made of the right-hand side of (2.66)

$$z = e^{sT_s} \approx 1 + sT_s. \quad (2.77)$$

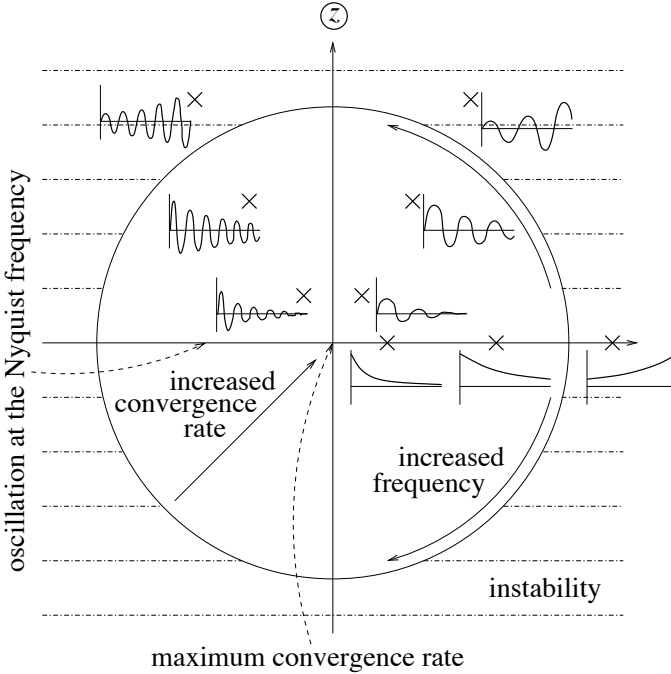


Figure 2.11. Pole locations in the z plane and the associated exponential responses.

Solving for s yields the substitution rule

$$s \rightarrow \frac{z - 1}{T_s} \quad (2.78)$$

which in the time domain corresponds to

$$\frac{dy(t)}{dt} = u(t) \rightarrow \frac{y_{k+1} - y_k}{T_s} = u_k. \quad (2.79)$$

This is a trapezoidal—or forward difference—derivative approximation. An Euler discretized integrator is thus obtained as

$$y_{k+1} = y_k + T_s u_k \quad (2.80)$$

which, by substituting $k \rightarrow k - 1$, also can be expressed as

$$y_k = y_{k-1} + T_s u_{k-1} \quad (2.81)$$

and whose block diagram is shown in Figure 2.12(a).

It may be noted in Figure 2.12(a) that a delayed integrator is obtained, because of the one-sample delay z^{-1} in the signal path from the input signal to the output signal. This delay makes the Euler method easy to apply, but caution must be exercised. We know that the unit circle is the boundary of the stability region in the z plane. Letting $z = e^{j\omega T_s}$ in (2.78) thus gives the

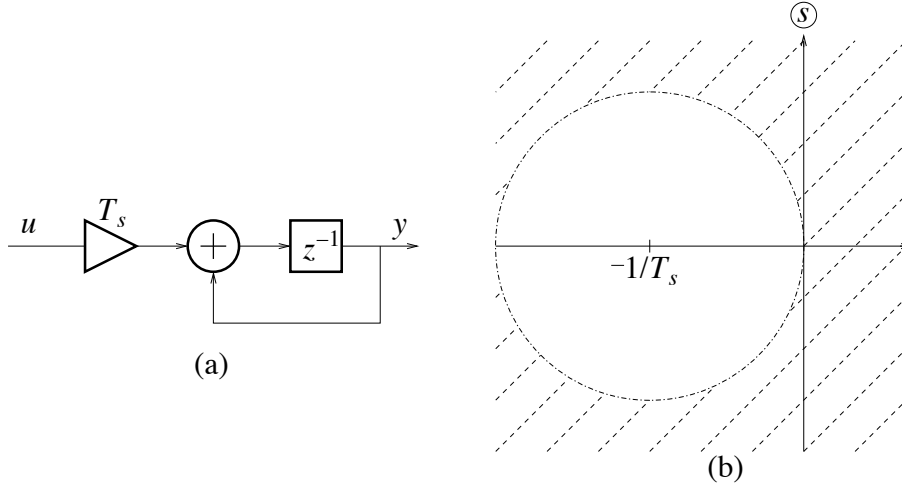


Figure 2.12. (a) Block diagram of an Euler discretized integrator. (b) Stability region in the s plane for Euler discretization.

mapping of the z -plane unit circle onto the s plane for Euler discretization. A circle which is centered at $s = -1/T_s$ and with radius $s = -1/T_s$ is obtained, as shown by the circle in Figure 2.12(b). This means that s -plane poles outside of this circle will be mapped to the outside of the z -plane unit circle. That is, even when the continuous-time system is stable, i.e., all poles are in the LHP, the Euler method may render an unstable discretization. In addition, the frequency response of an Euler discretized system will deviate from that of the underlying continuous-time system, particularly for higher frequencies. It is said that the frequency response becomes warped. The warping can be quantified by setting $s = j\omega$ in (2.66), giving $z = e^{j\omega T_s}$. Applying this to (2.78) yields

$$j\omega \rightarrow \frac{e^{j\omega T_s} - 1}{T_s}. \quad (2.82)$$

A MacLaurin expansion of the right-hand side of (2.82) yields

$$\frac{e^{j\omega T_s} - 1}{T_s} = \frac{1 + j\omega T_s + (j\omega T_s)^2/2! + \dots - 1}{T_s} \approx j\omega \quad (2.83)$$

where the approximation holds for small ω , but not for larger. Particularly, at the Nyquist frequency we have

$$\frac{e^{j(\omega_s/2)T_s} - 1}{T_s} = \frac{e^{j(\pi/T_s)T_s} - 1}{T_s} = -\frac{2}{T_s} \quad (2.84)$$

which is completely different from the right-hand side of (2.82), i.e., $j\omega_s/2 = j\pi/T_s$.

The Euler method is well suited for discretization of well-damped continuous-time systems, as long as T_s is sufficiently small. Poorly damped systems on the other hand, i.e., with poles very close to, or on, the imaginary axis in the s plane, will be rendered unstable by the Euler method. In the latter case there are two options.

- 1) Apply another discretization method, e.g., the prewarped Tustin method [81]

$$s \rightarrow K_T \frac{z - 1}{z + 1}, \quad K_T = \frac{\omega_h}{\tan(\frac{\omega_h T_s}{2})}. \quad (2.85)$$

This method maps the LHP to the inside of the z -plane unit circle, thus preserving the stability properties. It also gives an accurate mapping of the angular frequency ω_h , which can be verified by setting $z = e^{sT_s}$ and, in turn, $s = j\omega_h$ in (2.85). Unfortunately, Tustin discretization easily results in quite complicated equations.

- 2) Apply the Euler method to a well-damped s -domain system and then make a transformation in the z domain. This is often a more straightforward option, which will be exemplified in Paragraph 2.7.4.

2.5 Three-Phase Systems

A three-phase system is formed by three quantities, oscillating with the angular frequency ω_1 and separated in phase angle by (ideally) 120° ($2\pi/3$ radians). Three-phase systems are preferable to single-phase systems mainly for two reasons (which hold under idealized conditions).

- 1) The sum of the instantaneous values is zero.
- 2) The instantaneous three-phase power is constant.

As a consequence thereof, three-phase grids today handle the majority of all transmission and distribution of electric power, while three-phase machines and three-phase power electronic converters are used for power conversion.

The three phases are usually denoted as a , b , and c (sometimes as r , s , and t). The peak values of the three components are, if not exactly equal, then at least approximately equal. Phases b and c (ideally) lag 120° and 240° , respectively, behind phase a . A three-phase voltage system can be written as

$$\begin{aligned} v_a(t) &= \hat{V}_a \cos(\omega_1 t + \varphi_a) \\ v_b(t) &= \hat{V}_b \cos(\omega_1 t - 2\pi/3 + \varphi_b) \\ v_c(t) &= \hat{V}_c \cos(\omega_1 t - 4\pi/3 + \varphi_c) \end{aligned} \quad (2.86)$$

where $v_a(t)$, $v_b(t)$, and $v_c(t)$ are called the phase voltages. Hence, during normal operation (i.e., except when a larger disturbance occurs), $\hat{V}_a \approx \hat{V}_b \approx \hat{V}_c$ and $\varphi_a \approx \varphi_b \approx \varphi_c$. This is illustrated by the phasor diagram in Figure 2.13. The phasors rotate counterclockwise with angular frequency ω_1 (in Figure 2.13 they are frozen at $\omega_1 t + \varphi_a = 0$).

2.5.1 Sequences

As mentioned, the ideal situation is a three-phase system with equal peak values in all three phases, and exactly 120° phase distribution. This is called a balanced system. Taking v_a as phase reference, we have

$$\begin{aligned} v_a(t) &= \hat{V} \cos(\omega_1 t) \\ v_b(t) &= \hat{V} \cos(\omega_1 t - 2\pi/3) \\ v_c(t) &= \hat{V} \cos(\omega_1 t - 4\pi/3). \end{aligned} \quad (2.87)$$

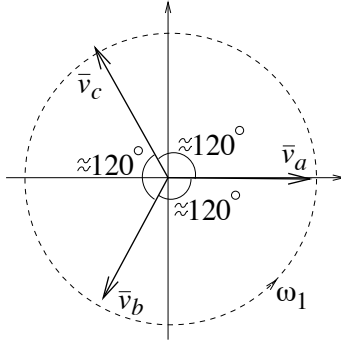


Figure 2.13. Phasor diagram of a three-phase system.

When phase b lags 120° behind phase a , as here, we have a *positive-sequence component*. If the ordering of phases is modified, e.g., phase b is taken as the phase lagging 240° behind phase a

$$\begin{aligned}v_a(t) &= \hat{V} \cos(\omega_1 t) \\v_b(t) &= \hat{V} \cos(\omega_1 t - 4\pi/3) \\v_c(t) &= \hat{V} \cos(\omega_1 t - 2\pi/3)\end{aligned}\tag{2.88}$$

then a *negative-sequence component* is obtained. Positive and negative sequences can be visualized as rotating counterclockwise and clockwise, respectively. This is very relevant for ac motors: if two of the phases feeding an ac motor are interchanged, the rotation of the motor is reversed.¹ Oscillograms of positive- and negative-sequence components are depicted in Figure 2.14. Ideally, a three-phase system should be pure positive sequence. Small negative-sequence voltage and current components appear during normal operation due to unbalanced impedances (this will be exemplified later), whereas large transient negative-sequence components appear during unbalanced faults, such as line-to-ground or line-to-line flashovers, for example caused by lightning strikes on overhead power lines. Since faults normally are cleared within a few periods of the fundamental, unbalances caused by large negative-sequence components typically have duration only of a few hundred milliseconds.

One interesting property of any three-phase system which is a positive sequence, a negative sequence, or a sum thereof is that the instantaneous sum of the components is zero:

$$v_a(t) + v_b(t) + v_c(t) = 0 \forall t.\tag{2.89}$$

In situations when (2.89) does not hold, the nonzero mean value

$$v_0(t) = \frac{v_a(t) + v_b(t) + v_c(t)}{3}\tag{2.90}$$

is called the *zero-sequence component*. This represents a common-mode unbalance among the three phases. If a neutral Y-point (star-point) connection is not used, i.e., the dashed line in Figure 2.15(a) is not present, then it is guaranteed that $i_a(t) + i_b(t) + i_c(t) = 0$, even if there should be a zero-sequence voltage component. That is, $\{v'_a(t), v'_b(t), v'_c(t)\}$ where

$$v'_a(t) = v_a(t) - v_0(t) \quad v'_b(t) = v_b(t) - v_0(t) \quad v'_c(t) = v_c(t) - v_0(t)\tag{2.91}$$

¹In German, three-phase current is very appropriately called *Drehstrom*—turning current.

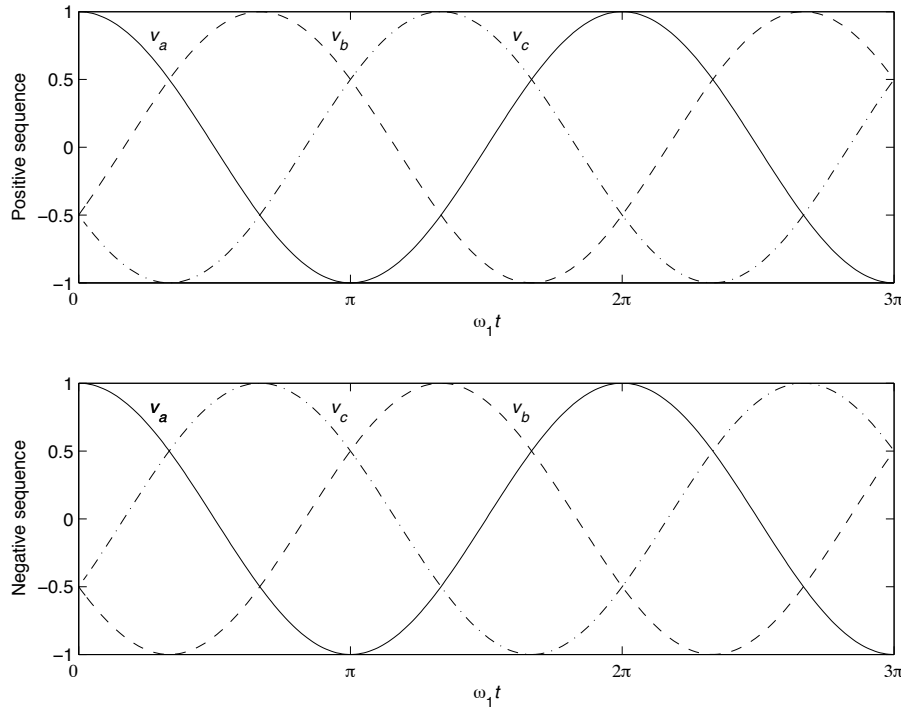


Figure 2.14. Positive-sequence and negative-sequence components.

or, in matrix/vector form,

$$\begin{bmatrix} v'_a(t) \\ v'_b(t) \\ v'_c(t) \end{bmatrix} = \frac{1}{3} \begin{bmatrix} 2 & -1 & -1 \\ -1 & 2 & -1 \\ -1 & -1 & 2 \end{bmatrix} \begin{bmatrix} v_a(t) \\ v_b(t) \\ v_c(t) \end{bmatrix} \quad (2.92)$$

for which $v'_a(t) + v'_b(t) + v'_c(t) = 0$, give the same phase currents as $\{v_a(t), v_b(t), v_c(t)\}$. A zero-sequence component may be freely added to or subtracted from the phase voltages without affecting the currents, as long as the Y point is left ungrounded. (A neutral wire is normally not needed in a three-phase system.)

The results are summarized below.

Result 2.1 The unbalanced three-phase system

$$\begin{bmatrix} v_a(t) \\ v_b(t) \\ v_c(t) \end{bmatrix} = \begin{bmatrix} \hat{V}_a \cos(\omega_1 t + \varphi_a) \\ \hat{V}_b \cos(\omega_1 t - 2\pi/3 + \varphi_b) \\ \hat{V}_c \cos(\omega_1 t - 4\pi/3 + \varphi_c) \end{bmatrix} \quad (2.93)$$

can be uniquely decomposed in a positive-sequence component, a negative-sequence component,

and a zero-sequence component as

$$\begin{bmatrix} v_a(t) \\ v_b(t) \\ v_c(t) \end{bmatrix} = \begin{bmatrix} \hat{V}_{+1} \cos(\omega_1 t + \varphi_{+1}) \\ \hat{V}_{+1} \cos(\omega_1 t - 2\pi/3 + \varphi_{+1}) \\ \hat{V}_{+1} \cos(\omega_1 t - 4\pi/3 + \varphi_{+1}) \end{bmatrix} + \begin{bmatrix} \hat{V}_{-1} \cos(\omega_1 t + \varphi_{-1}) \\ \hat{V}_{-1} \cos(\omega_1 t - 4\pi/3 + \varphi_{-1}) \\ \hat{V}_{-1} \cos(\omega_1 t - 2\pi/3 + \varphi_{-1}) \end{bmatrix} + \begin{bmatrix} v_0(t) \\ v_0(t) \\ v_0(t) \end{bmatrix} \quad (2.94)$$

where

$$v_0(t) = \hat{V}_0 \cos(\omega_1 t + \varphi_0) = \frac{v_a(t) + v_b(t) + v_c(t)}{3}. \quad (2.95)$$

2.5.2 Instantaneous Power

As stated initially, one of the benefits of three-phase electric power conversion is that the instantaneous power is ideally constant. To show this, let us consider a balanced impedance, i.e., three identical impedances Z connected to a positive-sequence voltage as given by (2.87); see Figure 2.15(a). This gives a positive-sequence current

$$\begin{aligned} i_a(t) &= \hat{I} \cos(\omega_1 t - \varphi) \\ i_b(t) &= \hat{I} \cos(\omega_1 t - 2\pi/3 - \varphi) \\ i_c(t) &= \hat{I} \cos(\omega_1 t - 4\pi/3 - \varphi) \end{aligned} \quad (2.96)$$

where $\hat{I} = \hat{V}/|Z(j\omega_1)|$ and $\varphi = \arg Z(j\omega_1)$. Through straightforward but tedious trigonometrical manipulations it is found that the total instantaneous active power $P(t)$ developed in the three impedances is given by

$$\begin{aligned} P(t) &= v_a(t)i_a(t) + v_b(t)i_b(t) + v_c(t)i_c(t) = \frac{3\hat{V}\hat{I}}{2} \cos \varphi \\ &= 3VI \cos \varphi \end{aligned} \quad (2.97)$$

where, as in the single-phase case, rms values are introduced as $V = \hat{V}/\sqrt{2}$ and $I = \hat{I}/\sqrt{2}$. In contrast, in a single-phase only the instantaneous power pulsates with the angular frequency $2\omega_1$ about the mean value $VI \cos \varphi$.

PROBLEM 2.16

A relevant question at this point is whether two-phase systems, such as

$$v_\alpha(t) = \hat{V} \cos \omega_1 t, \quad v_\beta(t) = \hat{V} \sin \omega_1 t$$

would be a feasible alternative to three-phase systems. Simple trigonometry shows that also in this case, the instantaneous active power is constant. Why are three-phase systems yet preferable to two-phase systems? Give one reason!

2.5.3 Wye (Y) and Delta (Δ) Connections

A balanced three-phase load with per-phase impedance Z can be connected either in a Y (or star) or in a Δ , as illustrated in Figures 2.15(a) and (b), respectively. Whereas in the Y connection

there is a phase voltage across each impedance, the Δ connection has a line-to-line voltage. From the geometry in Figure 2.15(c) it is found that the line-to-line voltages are given by

$$\begin{aligned} v_{ab}(t) &= v_a(t) - v_b(t) = \sqrt{3}\hat{V} \cos(\omega_1 t + \pi/6) \\ v_{bc}(t) &= v_b(t) - v_c(t) = \sqrt{3}\hat{V} \cos(\omega_1 t - \pi/2) \\ v_{ca}(t) &= v_c(t) - v_a(t) = \sqrt{3}\hat{V} \cos(\omega_1 t - 7\pi/6) \end{aligned} \quad (2.98)$$

still with $v_a(t)$ as phase reference. The peak value of each line-to-line voltage is $\sqrt{3}$ times larger than the peak value of each phase voltage. Thus, the total power developed in a three-phase load is increased three times when the connection is changed from a Y to a Δ : $P_\Delta = 3P_Y$.

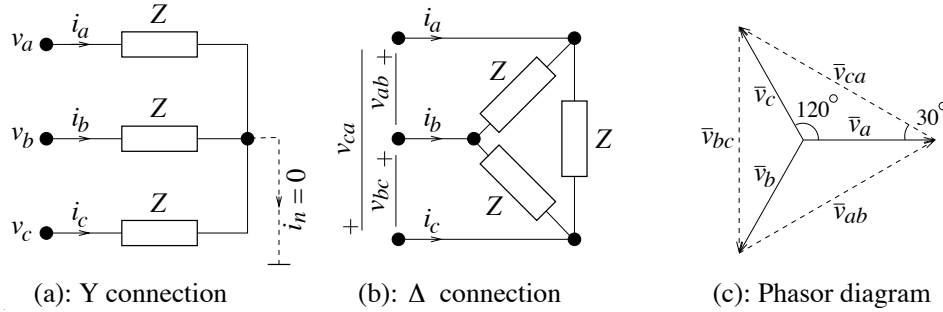


Figure 2.15. Balanced three-phase loads.

It is unimportant from the standpoint of dynamics and control whether a load is connected in a Y or in a Δ . A balanced Δ -connected load can be treated as if it were connected in a Y, but with all impedances reduced to $1/3$ of the actual values. This is called an equivalent Y.

PROBLEM 2.17

In a Y-connected three-phase load with a 230-V, 50-Hz phase voltage, the total active power is measured as 4.5 kW whereas the phase current is 9.2 A.

- What is the inductance per phase if the load is resistive-inductive?
- What is the capacitance per phase if the load is resistive-capacitive?

PROBLEM 2.18

A load whose resistance per phase is 8Ω is Δ -connected to a 230-V (rms phase voltage), 50-Hz grid. The load phase voltage is phase shifted 30° relative the load phase current.

- Determine the active and reactive powers as well as the phase current.
- Is the load inductive or capacitive? Determine the inductance or capacitance.
- What are the total active power and the line current if the load is instead Y-connected?

PROBLEM 2.19

In a three-phase load with 3Ω /phase connected to a 400-V (line-to-line voltage), 50-Hz grid, the total active power is measured as 145 kW and the line current as 440 A.

- Is the load connected in a Y or in a Δ ?

b) What is the power factor and the inductance per phase of the load?

PROBLEM 2.20

A balanced Δ -connected three-phase impedance is connected as load to a balanced three-phase grid, whose phase- a voltage is selected as phase reference:

$$v_a(t) = 230\sqrt{2} \cos \omega_1 t \text{ V}$$

where $\omega_1 = 100\pi$ rad/s. In phase b , the following current is measured:

$$i_b(t) = 11\sqrt{2} \cos(\omega_1 t - 55^\circ) \text{ A.}$$

Suggest a circuit diagram (with component values) of the impedance per phase of the Δ -connected load.

2.5.4 Multifrequency Waveforms With Balanced Harmonic Content

Major sources of harmonic pollution in three-phase grids are diode rectifiers and thyristor converters. They act as balanced but nonlinear loads, which draw balanced but nonsinusoidal currents. That is, the waveforms in the three phases are identical, only time shifted corresponding to 120° of the fundamental. Electrical machines tend to act in a similar way, though they usually draw less distorted currents. The dominant harmonics thus form a balanced, multifrequency three-phase system, which can be expressed as the Fourier series expansion (cf. Paragraph 2.1.4)

$$\begin{bmatrix} v_a(t) \\ v_b(t) \\ v_c(t) \end{bmatrix} = \sum_{h=1,3,5,\dots} \begin{bmatrix} \hat{V}_h \cos[h\omega_1 t + \varphi_h] \\ \hat{V}_h \cos[h(\omega_1 t - 2\pi/3) + \varphi_h] \\ \hat{V}_h \cos[h(\omega_1 t - 4\pi/3) + \varphi_h] \end{bmatrix}. \quad (2.99)$$

The 3rd, 5th, and 7th harmonics (with normalized amplitudes $\hat{V}_h = 1$ and zero phase angles $\varphi_h = 0$) are shown in Figure 2.16.

As can be seen, the 3rd harmonic has the same phase angle in all three phases, and is thus zero sequence. It is also seen that the 5th harmonic is negative sequence (cf. Figure 2.14) and the 7th harmonic is positive sequence. The obvious extension of this is

$$\begin{array}{ccccccccccccc} h = & 1 & 3 & 5 & 7 & 9 & 11 & 13 & 15 & \dots \\ \text{seq.} & + & 0 & - & + & 0 & - & + & 0 & \dots \end{array}$$

All harmonics that are multiples of 3—so-called triplen harmonics—are zero-sequence components. Therefore, even if there are triplen voltage harmonics there will be no triplen current harmonics as long as the Y point ungrounded, cf. Fig. 2.15. In a three-phase multifrequency system with balanced harmonics but where there may be a fundamental negative-sequence component, the signed frequency-component orders are as follows:

$$\dots -17 -11 -5 -1 +1 +7 +13 +19 \dots \quad (2.100)$$

or, more compactly written, ± 1 and $\pm 6n + 1$, $n = 1, 2, \dots$

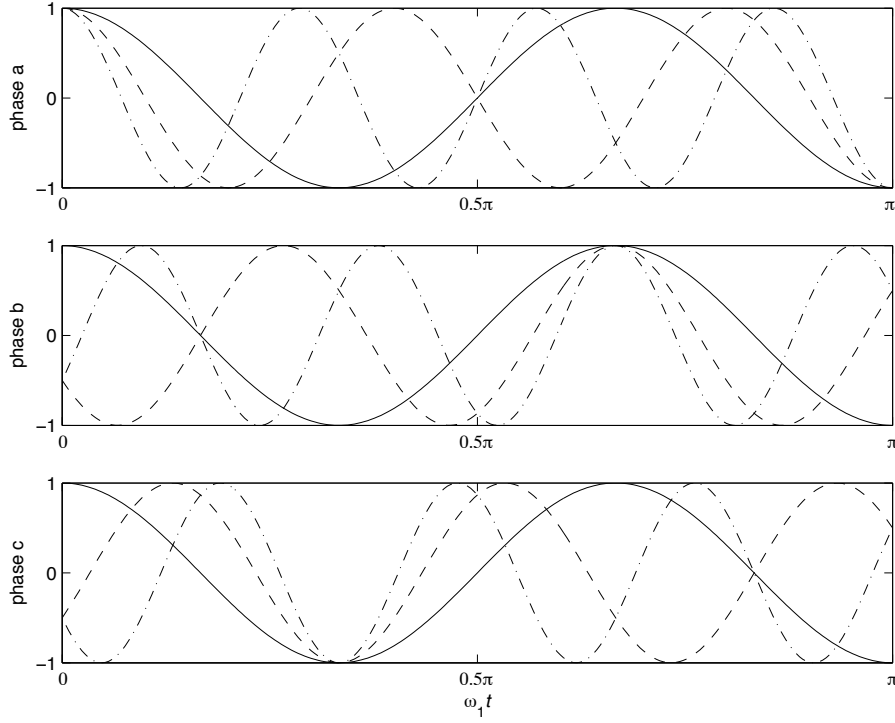


Figure 2.16. Three-phase harmonics: 3rd (solid), 5th (dashed), and 7th (dash-dotted).

2.6 Space Vectors

2.6.1 Two-Phase Representation With Complex Space Vectors

Previously it was concluded that zero-sequence components often can be disregarded, because if the Y point is ungrounded a zero-sequence current component is not drawn. The system of three-phase voltages $\{v_a(t), v_b(t), v_c(t)\}$ is, for practical purposes, equal to a system $\{v'_a(t), v'_b(t), v'_c(t)\}$, see (2.92), for which

$$v'_a(t) + v'_b(t) + v'_c(t) = 0 \forall t.$$

This removes one degree of freedom since one of the components— $v'_c(t)$, for example—always can be expressed in the other two, as $v'_c(t) = -[v'_a(t) + v'_b(t)]$. As a result, it is possible to describe a three-phase system as an equivalent two-phase system that has two perpendicular axes, denoted with the subscripts α and β . These axes can be considered as the real and imaginary axes in a complex plane, allowing a complex representation. The three-phase-to-two-phase transformation—which is also known as the Clarke transformation [20]—results in the complex space vector

$$\mathbf{v}^s(t) = v_\alpha(t) + jv_\beta(t) = \frac{2}{3}K[v_a(t) + e^{j2\pi/3}v_b(t) + e^{j4\pi/3}v_c(t)] \quad (2.101)$$

where K is known as the space-vector scaling constant. (We shall discuss the selection of K in Paragraph 2.6.11.) Figure 2.17 illustrates the construction of a space vector. The contributions of the phase voltages are equipped with their respective directions (i.e., the directions defined by

the unit vectors 1 , $e^{j2\pi/3}$, and $e^{j4\pi/3}$), then added together, and, finally, scaled with the constant $2K/3$.

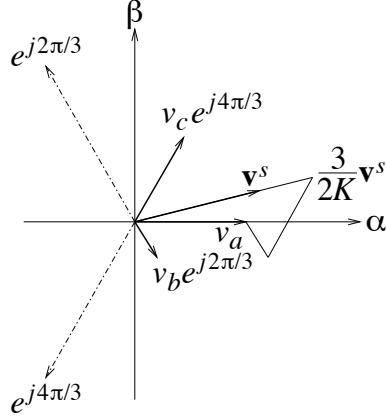


Figure 2.17. Construction of a voltage space vector.

“Space” in space vector originates from their first usage: to describe two-dimensional spatial flux distributions in ac machines. “Vector” is used rather than phasor, partly to make a distinction to phasors and partly because the complex notation of (2.101) sometimes needs to be replaced by the corresponding real notation in standard two-dimensional vector form (see further Paragraph 2.6.4)

$$\mathbf{v}^s(t) = \begin{bmatrix} v_\alpha(t) \\ v_\beta(t) \end{bmatrix} = \begin{bmatrix} \operatorname{Re}\{\mathbf{v}^s(t)\} \\ \operatorname{Im}\{\mathbf{v}^s(t)\} \end{bmatrix}. \quad (2.102)$$

The superscript s denotes that the space vector is expressed in *stationary coordinates*. It is also said that the space vector is referred to the stationary ($\alpha\beta$) frame. When referred to the $\alpha\beta$ frame, the space vector rotates with the same angular frequency as the three-phase quantities which it represents, i.e., normally the fundamental angular frequency ω_1 .

2.6.2 Vector Representation of Positive- and Negative-Sequence Components

Let study the three-phase-to-two-phase transformations of fundamental-frequency positive- and negative-sequence components. For the positive-sequence component

$$\begin{bmatrix} v_a(t) \\ v_b(t) \\ v_c(t) \end{bmatrix} = \begin{bmatrix} \hat{V}_{+1} \cos(\omega_1 t + \varphi_{+1}) \\ \hat{V}_{+1} \cos(\omega_1 t - 2\pi/3 + \varphi_{+1}) \\ \hat{V}_{+1} \cos(\omega_1 t - 4\pi/3 + \varphi_{+1}) \end{bmatrix} \quad (2.103)$$

by direct substitution in (2.101) it is found that the corresponding space vector is given by

$$\mathbf{v}^s(t) = K \hat{V}_{+1} e^{j(\omega_1 t + \varphi_{+1})}. \quad (2.104)$$

It can be observed that the space vector rotates counterclockwise in the $\alpha\beta$ plane and that it is aligned with the phase- a quantity $v_a(t)$. Transforming the negative-sequence component

$$\begin{bmatrix} v_a(t) \\ v_b(t) \\ v_c(t) \end{bmatrix} = \begin{bmatrix} \hat{V}_{-1} \cos(\omega_1 t + \varphi_{-1}) \\ \hat{V}_{-1} \cos(\omega_1 t - 4\pi/3 + \varphi_{-1}) \\ \hat{V}_{-1} \cos(\omega_1 t - 2\pi/3 + \varphi_{-1}) \end{bmatrix} \quad (2.105)$$

we obtain

$$\mathbf{v}^s(t) = K \hat{V}_{-1} e^{j(-\omega_1 t + \varphi_{-1})}. \quad (2.106)$$

Also this space vector is aligned with the phase- a quantity, but it rotates clockwise in the $\alpha\beta$ plane. Extension of this principle to harmonics is straightforward. As the 5th harmonic is negative sequence, the 7th is positive sequence and so on, the space vector of a multifrequency waveform with balanced harmonics, but possibly including a fundamental negative-sequence component, can be expressed as

$$\mathbf{v}^s(t) = K \left[\hat{V}_{+1} e^{j(\omega_1 t + \varphi_{+1})} + \hat{V}_{-1} e^{j(-\omega_1 t + \varphi_{-1})} + \hat{V}_{-5} e^{j(-5\omega_1 t + \varphi_{-5})} + \hat{V}_{+7} e^{j(7\omega_1 t + \varphi_{+7})} + \dots \right]. \quad (2.107)$$

2.6.3 Relations Between Complex Space Vectors and Rotating Phasors

Complex space vectors and rotating phasors are obviously related, but they are not the same. Their main similarities and differences are as follows.

- **Similarity.** Space vector can be regarded as rotating phasors generalized to three-phase systems. The space vector

$$\mathbf{v}^s(t) = K \hat{V} e^{j(\omega_1 t + \varphi)}$$

corresponds to the three-phase voltage

$$\begin{bmatrix} v_a(t) \\ v_b(t) \\ v_c(t) \end{bmatrix} = \begin{bmatrix} \hat{V} \cos(\omega_1 t + \varphi) \\ \hat{V} \cos(\omega_1 t - 2\pi/3 + \varphi) \\ \hat{V} \cos(\omega_1 t - 4\pi/3 + \varphi) \end{bmatrix}$$

just as the rotating phasor

$$\bar{v}(t) = \frac{\hat{V}}{\sqrt{2}} e^{j(\omega_1 t + \varphi)}$$

corresponds to the single-phase voltage (with cosine as base function)

$$v(t) = \hat{V} \cos(\omega_1 t + \varphi).$$

- **Differences.**

- 1) Each phasor normally represents just one frequency component, whereas a complex space vector can represent several, as shown in (2.107).
- 2) Whereas the phasor is only a mathematical tool for steady-state analysis of ac circuits, a complex space vector can be regarded as a complex-valued signal. Although voltages and

currents etc. are three-phase quantities, after measurement using suitable sensors followed by sampling, the signals can easily be transformed to two-phase quantities by code in a microprocessor.

3) For phasors and single-phase ac systems, the concept of negative frequency is not physically relevant. For example, replacing ω_1 in $v(t) = \sin \omega_1 t$ by $-\omega_1$ yields $v(t) = -\sin \omega_1 t = \sin(\omega_1 t + \pi)$, i.e., just a phase shift. For space vectors negative frequency is very relevant: positive and negative frequencies correspond to positive and negative sequences, respectively, cf. (2.107).

Example 2.6 In the three-phase system (2.86) the peak values are

$$\hat{V}_a = 591 \text{ V} \quad \hat{V}_b = 673 \text{ V} \quad \hat{V}_c = 465 \text{ V}$$

and the phase angles are

$$\varphi_a = 11.7^\circ \quad \varphi_b = -5.7^\circ \quad \varphi_c = -6.5^\circ.$$

We wish to calculate the corresponding space vector. The system is unbalanced, i.e., it contains both positive- and negative-sequence components. Let us first check that there is no zero-sequence component. We have

$$\begin{aligned} & 591 \cos(\omega_1 t + 0.204) + 673 \cos(\omega_1 t - 2\pi/3 - 0.0995) \\ & + 465 \cos(\omega_1 t - 4\pi/3 - 0.113) = 0.58 \cos(\omega_1 t) + 0.25 \sin(\omega_1 t) \end{aligned}$$

so the zero-sequence component is negligible. Using Euler's relations, we obtain the following space vector:

$$\begin{aligned} \mathbf{v}^s(t) &= \frac{2}{3} K \left[591 \frac{e^{j(\omega_1 t + 0.204)} + e^{-j(\omega_1 t + 0.204)}}{2} + e^{j2\pi/3} 673 \frac{e^{j(\omega_1 t - 2\pi/3 - 0.0995)} + e^{-j(\omega_1 t - 2\pi/3 - 0.0995)}}{2} \right. \\ &\quad \left. + e^{j4\pi/3} 465 \frac{e^{j(\omega_1 t - 4\pi/3 - 0.113)} + e^{-j(\omega_1 t - 4\pi/3 - 0.113)}}{2} \right] \text{ V} \end{aligned} \quad (2.108)$$

which through some effort can be simplified to

$$\mathbf{v}^s(t) = K[570e^{j\omega_1 t} + 120e^{-j(\omega_1 t + 1.5)}] \text{ V}.$$

♣

PROBLEM 2.21

At a certain time instant, an rms-value-scaled space vector is given as

$$\mathbf{v}^s = 130 + j75 \text{ V.}$$

A zero-sequence component exists, whose instantaneous value is 9 V. Determine the instantaneous values of the phase voltages.

2.6.4 Real Space Vectors

A complex space vector, e.g., $\mathbf{v}^s(t) = v_\alpha(t) + jv_\beta(t)$, is a complex variable. As such, it has a scalar notation, though with real and imaginary parts. This allows straightforward addition, multiplication, conjugation etc. using well-known complex arithmetics. Calculation involving complex space vectors is just somewhat more difficult to perform than calculation involving real scalar variables. For this reason, complex space vectors are very convenient and should be used whenever possible, which turns out to be in the majority of situations.

Sometimes, though, the real equivalent to a complex space vector has to be used. This is usually the case for digital implementation of control algorithms, because programming languages suitable for fast real-time applications, such as converter and drives control, do not always support complex variables. Another situation is when there are unbalanced three-phase impedances.

A real space vector is a standard vector with two elements, which is related to its corresponding complex space vector as shown in (2.102). By evaluating the real and imaginary parts of the three-phase-to-two-phase transformation (2.101), it is found that the real space vector is obtained by applying a transformation matrix \mathbf{T}_{32} as

$$\mathbf{v}^s(t) = \begin{bmatrix} v_\alpha(t) \\ v_\beta(t) \end{bmatrix} = K \underbrace{\begin{bmatrix} \frac{2}{3} & -\frac{1}{3} & -\frac{1}{3} \\ 0 & \frac{1}{\sqrt{3}} & -\frac{1}{\sqrt{3}} \end{bmatrix}}_{\mathbf{T}_{32}} \begin{bmatrix} v_a(t) \\ v_b(t) \\ v_c(t) \end{bmatrix}. \quad (2.109)$$

For the inverse transformation, i.e., when going from a two-phase representation to a three-phase representation, the natural choice of transformation matrix \mathbf{T}_{23} is

$$\underbrace{\begin{bmatrix} v'_a(t) \\ v'_b(t) \\ v'_c(t) \end{bmatrix}}_{\mathbf{T}_{23}} = \frac{1}{K} \begin{bmatrix} 1 & 0 \\ -\frac{1}{2} & \frac{\sqrt{3}}{2} \\ -\frac{1}{2} & -\frac{\sqrt{3}}{2} \end{bmatrix} \begin{bmatrix} v'_\alpha(t) \\ v'_\beta(t) \end{bmatrix} \quad (2.110)$$

since then $\mathbf{T}_{32}\mathbf{T}_{23} = \mathbf{I}$ (where \mathbf{I} here is the 2×2 identity matrix), and $[v_\alpha(t), v_\beta(t)]^T = [v'_\alpha(t), v'_\beta(t)]^T$ if (2.110) is substituted in (2.109). If, on the other hand, (2.109) is substituted in (2.110), we get

$$\underbrace{\begin{bmatrix} v'_a(t) \\ v'_b(t) \\ v'_c(t) \end{bmatrix}}_{\mathbf{T}_{23}\mathbf{T}_{32}} = \frac{1}{3} \begin{bmatrix} 2 & -1 & -1 \\ -1 & 2 & -1 \\ -1 & -1 & 2 \end{bmatrix} \begin{bmatrix} v_a(t) \\ v_b(t) \\ v_c(t) \end{bmatrix}. \quad (2.111)$$

This relation is identical to (2.92), i.e., the result obtained if the zero-sequence component $v_0 = [v_a(t) + v_b(t) + v_c(t)]/3$ is subtracted from all phase quantities. This shows that, when transforming from a three-phase representation to a two-phase representation and back to a three-phase representation, all that is lost is the zero-sequence component, should there be any.

2.6.5 Complex Gains

As will be evident in the chapters to follow, when modeling three-phase circuits or machines as well as when designing controllers for three-phase VSCs, space vectors are frequently multiplied by complex gains. Consider the multiplication of the input space vector $\mathbf{u}^s = u_\alpha + j u_\beta$ ² by the complex gain $\mathbf{c} = a + jb$, forming the output space vector $\mathbf{y}^s = y_\alpha + j y_\beta$, as shown in Figure 2.18(a). The multiplication can be resolved in its components, i.e., the real and imaginary parts, as

$$\mathbf{y}^s = \mathbf{c}\mathbf{u}^s = (a + jb)(u_\alpha + j u_\beta) = \underbrace{au_\alpha - bu_\beta}_{{y}_\alpha} + j \underbrace{(au_\beta + bu_\alpha)}_{{y}_\beta}. \quad (2.112)$$

A component-wise block diagram illustrating this multiplication is shown in Figure 2.18(b).

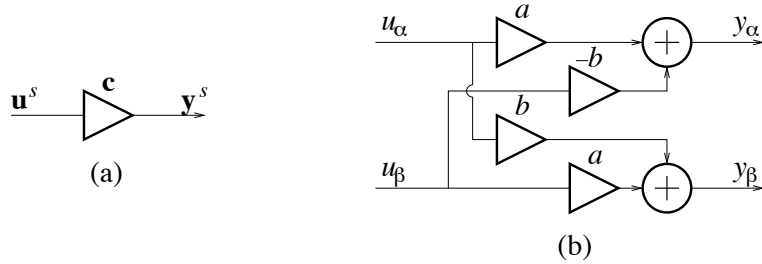


Figure 2.18. Block diagrams showing multiplication by the complex gain $\mathbf{c} = a + jb$. (a) Complex space-vector schematic. (b) Component-wise schematic.

It can be observed that component-wise realization of a complex gain involves four multiplications and two additions. It can also be noted that the real part of the complex gain gives a *direct mapping*: the d component of the input vector maps to the d component of the output vector with gain a , and similarly for the q component. On the other hand, the imaginary part of the complex gain gives a *cross coupling*: the d component of the input vector maps to the q component of the output vector with gain b , whereas the q component of the input vector maps to the d component of the output vector with gain $-b$. We thus find that the real correspondence to (2.112) can be expressed using a matrix gain \mathbf{C} as

$$\underbrace{\begin{bmatrix} y_\alpha \\ y_\beta \end{bmatrix}}_{\mathbf{y}^s} = \underbrace{\begin{bmatrix} a & -b \\ b & a \end{bmatrix}}_{\mathbf{C}} \underbrace{\begin{bmatrix} u_\alpha \\ u_\beta \end{bmatrix}}_{\mathbf{u}^s}. \quad (2.113)$$

A 2×2 matrix gain which can be expressed in this fashion, i.e., the diagonal elements are equal, whereas the antidiagonal elements are equal but with opposite signs, always has a corresponding complex gain. We shall call this property that the gain is *symmetrical*, see further Section 2.7.

The special cases of a real gain ($b = 0$) and an imaginary gain ($a = 0$) are illustrated in Figure 2.19. The number of multiplications here reduce to two and the additions vanish.

²For the sake of simplicity, from here on—with a few exceptions—we drop the time argument “(t).”

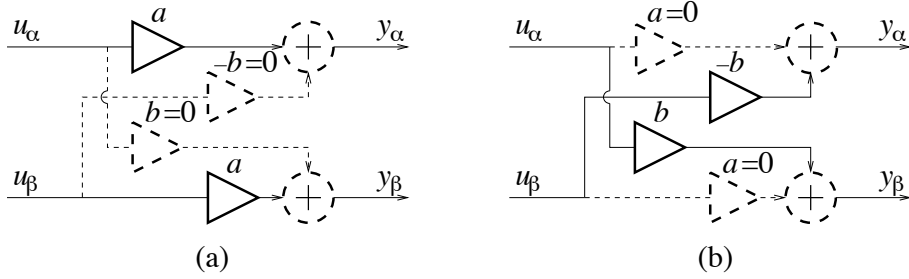


Figure 2.19. Block diagrams showing component-wise schematics of the special cases (a) real gain and (b) imaginary gain.

Remark 2.4 The correspondence between the complex gain \mathbf{c} and the matrix gain \mathbf{C} becomes yet more clear by the introduction of the matrix equivalent to j

$$\mathbf{J} = \begin{bmatrix} 0 & -1 \\ 1 & 0 \end{bmatrix}. \quad (2.114)$$

\mathbf{J} used as a matrix gain yields the mapping

$$\underbrace{\begin{bmatrix} 0 & -1 \\ 1 & 0 \end{bmatrix}}_{\mathbf{J}} \underbrace{\begin{bmatrix} u_\alpha \\ u_\beta \end{bmatrix}}_{\mathbf{u}^s} = \begin{bmatrix} -u_\beta \\ u_\alpha \end{bmatrix} \quad (2.115)$$

which is a direct correspondence to the mapping obtained by the corresponding complex gain j

$$j\mathbf{u}^s = j(u_\alpha + ju_\beta) = -u_\beta + ju_\alpha. \quad (2.116)$$

Using (2.114) allows us to express \mathbf{C} in (2.113) as

$$\mathbf{C} = a\mathbf{I} + b\mathbf{J} = a \begin{bmatrix} 1 & 0 \\ 0 & 1 \end{bmatrix} + b \begin{bmatrix} 0 & -1 \\ 1 & 0 \end{bmatrix} = \begin{bmatrix} a & -b \\ b & a \end{bmatrix} \quad (2.117)$$

showing clearly the correspondence to $\mathbf{c} = a + jb$.

2.6.6 Coordinate Transformations

Consider a fundamental positive-sequence space vector:

$$\mathbf{v}^s = K\hat{V}e^{j(\omega_1 t + \varphi)}. \quad (2.118)$$

The transformation

$$\mathbf{v} = e^{-j\omega_1 t}\mathbf{v}^s = K\hat{V}e^{j\varphi} \quad (2.119)$$

removes the rotation of the vector, making it similar to a fixed phasor, cf. (2.5). This is called the *dq transformation* (which is also known as the Park transformation) and can be regarded as observing the space vector from a coordinate system rotating with the angular fundamental frequency ω_1 . This coordinate system is called *synchronous coordinates*, and it is said that space

vector \mathbf{v} is referred to the synchronous (dq) frame. See Figure 2.20. We shall denote a space vector in synchronous coordinates without a superscript, and its components with the subscripts d and q :

$$\mathbf{v} = v_d + jv_q. \quad (2.120)$$

Since the rotation of the space vector is removed—provided that \mathbf{v}^s contains no other frequency components than the fundamental positive-sequence component—its components v_d and v_q will be constant in the steady state. This fact makes the dq transformation not useful just for analysis, e.g., of electrical machines, but also for implementation of controllers for three-phase VSCs. This is because it is easier to design controllers for quantities that are constant—rather than constantly oscillating—in the steady state. PI controllers, with some additions, can generally be relied upon.

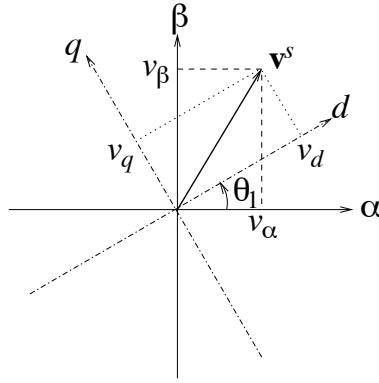


Figure 2.20. Projections of the vector \mathbf{v}^s on the $\alpha\beta$ and dq frames.

Equation (2.118) implies that ω_1 is constant, but this is rarely the case, particularly not for a variable-speed drive. To allow a varying fundamental frequency, the general definitions of the dq transformation and its inverse, the $\alpha\beta$ transformation, are given by

$$\mathbf{v} = e^{-j\theta_1} \mathbf{v}^s \quad (\text{dq transformation}) \quad (2.121)$$

$$\mathbf{v}^s = e^{j\theta_1} \mathbf{v} \quad (\alpha\beta \text{ transformation}) \quad (2.122)$$

where

$$\theta_1 = \int \omega_1 dt. \quad (2.123)$$

2.6.7 dq Transformation of Multifrequency Waveforms

Applying the dq transformation to the multifrequency space vector (2.107) gives

$$\mathbf{v} = K \left[\widehat{V}_{+1} e^{j\varphi_{+1}} + \widehat{V}_{-1} e^{j(-2\omega_1 t + \varphi_{-1})} + \widehat{V}_{-5} e^{j(-6\omega_1 t + \varphi_{-5})} + \widehat{V}_{+7} e^{j(6\omega_1 t + \varphi_{+7})} + \dots \right]. \quad (2.124)$$

The 5th and 7th harmonics are both transformed to 6th harmonics in synchronous coordinates (which are negative and positive sequence, respectively). Similarly, the 11th and 13th harmonics

are both transformed to 12th harmonics. In the dq frame, balanced harmonics thus have the angular frequencies $6n\omega_1$, $n = 1, 2, \dots$. The fundamental-frequency negative-sequence component is transformed to -2 . Thus, the orders as given with sign are transformed as

$$\begin{array}{ccccccccc} \alpha\beta & \dots & -11 & -5 & -1 & +1 & +7 & +13 & \dots \\ \downarrow & & \downarrow & \downarrow & \downarrow & \downarrow & \downarrow & \downarrow \\ dq & \dots & -12 & -6 & -2 & 0 & +6 & +12 & \dots \end{array} \quad (2.125)$$

2.6.8 Coordinate Transformations of Real Space Vectors

The dq transformation (2.121) can be resolved in the components of the $\alpha\beta$ - and dq -frame space vectors, as well as in the real and imaginary parts of the transformation factor $e^{-j\theta_1}$, as

$$\begin{aligned} \mathbf{v} = e^{-j\theta_1} \mathbf{v}^s &= (\cos \theta_1 - j \sin \theta_1)(v_\alpha + j v_\beta) \\ &= \underbrace{v_\alpha \cos \theta_1 + v_\beta \sin \theta_1}_{v_d} + j \underbrace{(-v_\alpha \sin \theta_1 + v_\beta \cos \theta_1)}_{v_q}. \end{aligned} \quad (2.126)$$

The underbraced component identities can be expressed with the help of a dq transformation matrix \mathbf{T}_{dq} , giving the following equivalence to (2.126) for the corresponding real space vectors:

$$\underbrace{\begin{bmatrix} v_d \\ v_q \end{bmatrix}}_{\mathbf{v}} = \underbrace{\begin{bmatrix} \cos \theta_1 & \sin \theta_1 \\ -\sin \theta_1 & \cos \theta_1 \end{bmatrix}}_{\mathbf{T}_{dq}} \underbrace{\begin{bmatrix} v_\alpha \\ v_\beta \end{bmatrix}}_{\mathbf{v}^s}. \quad (2.127)$$

Since $\alpha\beta$ transformation involves multiplication by the factor $e^{j\theta_1}$, the $\alpha\beta$ transformation matrix $\mathbf{T}_{\alpha\beta}$ is obtained by substituting $\theta_1 \rightarrow -\theta_1$ in \mathbf{T}_{dq} , giving

$$\underbrace{\begin{bmatrix} v_\alpha \\ v_\beta \end{bmatrix}}_{\mathbf{v}^s} = \underbrace{\begin{bmatrix} \cos \theta_1 & -\sin \theta_1 \\ \sin \theta_1 & \cos \theta_1 \end{bmatrix}}_{\mathbf{T}_{\alpha\beta}} \underbrace{\begin{bmatrix} v_d \\ v_q \end{bmatrix}}_{\mathbf{v}}. \quad (2.128)$$

Note that $\mathbf{T}_{\alpha\beta} = \mathbf{T}_{dq}^{-1} = \mathbf{T}_{dq}^T$; \mathbf{T}_{dq} and $\mathbf{T}_{\alpha\beta}$ are orthogonal matrices. A block diagram for the $\alpha\beta$ transformation is shown in Figure 2.21. Since the $\alpha\beta$ transformation $e^{j\theta_1}$ factor is a complex gain, Figure 2.21 obviously is a special case of Figure 2.18(b) with $a = \cos \theta_1$ and $b = \sin \theta_1$.

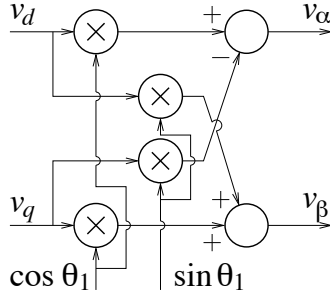


Figure 2.21. Block diagram for the $\alpha\beta$ transformation.

PROBLEM 2.22 _____

How should Figure 2.21 be modified in order to obtain the dq transformation?

PROBLEM 2.23 _____

Using the matrix correspondence \mathbf{J} to the imaginary unit j , as given by (2.114), should logically allow the correspondence

$$\mathbf{v}^s = e^{j\theta_1} \mathbf{v} \Leftrightarrow \mathbf{v}^s = e^{\mathbf{J}\theta_1} \mathbf{v}.$$

That is, $e^{\mathbf{J}\theta_1} = \mathbf{T}_{\alpha\beta}$. Show that! **Hint:** $\mathcal{L}\{e^{\mathbf{A}t}\} = (s\mathbf{I} - \mathbf{A})^{-1}$.

2.6.9 Instantaneous Power

Equation (2.8) states the well-known relation between the phasors for voltage and current and the complex power in a single-phase system. Based upon this, it may be conjectured that the complex power in a three-phase system is proportional to $\mathbf{v}^s(\mathbf{i}^s)^*$. Taking respectively the real and imaginary parts should then give the active and reactive powers. Proving this conjecture only requires some algebraic exercise. From the definition (2.101) of a complex space vector, we have

$$\mathbf{v}^s(\mathbf{i}^s)^* = \left(\frac{2K}{3}\right)^2 \left(v_a + e^{j2\pi/3} v_b + e^{j4\pi/3} v_c \right) \left(i_a + e^{j2\pi/3} i_b + e^{j4\pi/3} i_c \right)^*. \quad (2.129)$$

Observing that $e^{j4\pi/3} = e^{-j2\pi/3}$ and assuming that there is no zero-sequence current component, i.e., $i_a + i_b + i_c = 0$, we obtain

$$\begin{aligned} \mathbf{v}^s(\mathbf{i}^s)^* &= \left(\frac{2K}{3}\right)^2 \left[v_a i_a + v_b i_b + v_c i_c + \underbrace{\left(-\frac{1}{2} + j \frac{\sqrt{3}}{2} \right)}_{e^{j2\pi/3}} (v_a i_c + v_b i_a + v_c i_b) \right. \\ &\quad \left. + \underbrace{\left(-\frac{1}{2} - j \frac{\sqrt{3}}{2} \right)}_{e^{-j2\pi/3}} (v_a i_b + v_b i_c + v_c i_a) \right] \\ &= \left(\frac{2K}{3}\right)^2 \left[v_a i_a + v_b i_b + v_c i_c - \frac{1}{2} \left(v_a \underbrace{(i_b + i_c)}_{-i_a} + v_b \underbrace{(i_a + i_c)}_{-i_b} + v_c \underbrace{(i_a + i_b)}_{-i_c} \right) \right. \\ &\quad \left. + j \frac{\sqrt{3}}{2} (v_a(i_c - i_b) + v_b(i_a - i_c) + v_c(i_b - i_a)) \right] \\ &= \frac{2K^2}{3} \left[v_a i_a + v_b i_b + v_c i_c + j \frac{1}{\sqrt{3}} (v_a(i_c - i_b) + v_b(i_a - i_c) + v_c(i_b - i_a)) \right]. \end{aligned} \quad (2.130)$$

The instantaneous active power developed in a three-phase circuit is the sum of the instantaneous active powers per phase, i.e., $v_a i_a + v_b i_b + v_c i_c$. This shows that (2.130) should be scaled by $3/(2K^2)$

to obtain the complex power for all three phases, i.e.,

$$\mathbf{S} = \frac{3}{2K^2} \mathbf{v}^s (\mathbf{i}^s)^* = \frac{3}{2K^2} \mathbf{v} \mathbf{i}. \quad (2.131)$$

[Due to the complex conjugation of the current space vector, the expression is reference-frame invariant. Thus, as shown in (2.131), the relation for the corresponding *dq*-frame space vectors is formally identical to that for the $\alpha\beta$ -frame space vectors.] So, the instantaneous active power is given by

$$P = \text{Re}\{\mathbf{S}\} = \frac{3}{2K^2} \text{Re}\{\mathbf{v}^s (\mathbf{i}^s)^*\} = \frac{3}{2K^2} \text{Re}\{\mathbf{v} \mathbf{i}^*\} = v_a i_a + v_b i_b + v_c i_c \quad (2.132)$$

whereas the instantaneous reactive power is given by

$$\begin{aligned} Q &= \text{Im}\{\mathbf{S}\} = \frac{3}{2K^2} \text{Im}\{\mathbf{v}^s (\mathbf{i}^s)^*\} = \frac{3}{2K^2} \text{Im}\{\mathbf{v} \mathbf{i}^*\} \\ &= \frac{1}{\sqrt{3}} [v_a(i_c - i_b) + v_b(i_a - i_c) + v_c(i_b - i_a)]. \end{aligned} \quad (2.133)$$

It should be stressed that (2.131)–(2.133) give the instantaneous powers, unlike the corresponding relations for phasors representing single-phase systems, from which just the mean powers are obtained. In the ideal situation where both voltage and current consist of fundamental positive-sequence components

$$\mathbf{v}^s = K\sqrt{2}V e^{j\omega_1 t} \quad \mathbf{i}^s = K\sqrt{2}I e^{j(\omega_1 t + \varphi)} \quad (2.134)$$

(with the voltage taken as phase reference, for convenience), the instantaneous complex power is given by

$$\mathbf{S} = \frac{3}{2K^2} \mathbf{v}^s (\mathbf{i}^s)^* = \frac{3}{2} \sqrt{2}V \sqrt{2}I e^{j\varphi} = \underbrace{3VI \cos \varphi}_P + j \underbrace{3VI \sin \varphi}_Q \quad (2.135)$$

which is constant. Space vectors allows this fact to be concluded with considerably less work involved than the phase-quantity calculations needed to obtain the identical expression (2.97) for *P*.

2.6.10 Power of Multifrequency Waveforms

Suppose that the balanced voltage $\mathbf{v}^s = K\hat{V} e^{j\omega_1 t}$ is applied to an unbalanced and nonlinear load (this could be a diode rectifier or an ac machine connected to the grid via an unbalanced impedance), which draws a current containing a fundamental negative-sequence component plus balanced harmonics, cf. (2.107)

$$\mathbf{i}^s = K \left[\hat{I}_{+1} e^{j(\omega_1 t + \varphi_{+1})} + \hat{I}_{-1} e^{j(-\omega_1 t + \varphi_{-1})} + \hat{I}_{-5} e^{j(-5\omega_1 t + \varphi_{-5})} + \hat{I}_{+7} e^{j(7\omega_1 t + \varphi_{+7})} + \dots \right]. \quad (2.136)$$

The resulting active power is given by

$$\begin{aligned} P &= \frac{3}{2K^2} \text{Re}\{\mathbf{v}^s (\mathbf{i}^s)^*\} = \frac{3}{2K^2} \text{Re}\{(\mathbf{v}^s)^* \mathbf{i}^s\} = \frac{3}{2K} \hat{V} \text{Re}\{e^{-j\omega_1 t} \mathbf{i}^s\} \\ &= 3V \text{Re} \left\{ I_{+1} e^{j\varphi_{+1}} + I_{-1} e^{j(-2\omega_1 t + \varphi_{-1})} + I_{-5} e^{j(-6\omega_1 t + \varphi_{-5})} + I_{+7} e^{j(6\omega_1 t + \varphi_{+7})} + \dots \right\} \end{aligned} \quad (2.137)$$

where $V = \hat{V}/\sqrt{2}$, etc. It may be noted that the factor $(\mathbf{v}^s)^*$ in effect gives a dq transformation of \mathbf{i}^s , which results in multifrequency components similar to (2.124). The following observations can be made.

- 1) Only the fundamental positive-sequence current component (with rms value I_{+1}) contributes to the constant term; the fundamental negative-sequence component and the harmonics just cause pulsations.
- 2) The pulsations are of the angular frequencies $2\omega_1$ and $6n\omega_1$, $n = 1, 2, \dots$

Pulsations at $2\omega_1$ are generally more disturbing than those at higher frequencies. In a machine, power pulsations translate to torque pulsations, and low-frequency torque pulsations propagate easier and are more prone to excite mechanical resonances than high-frequency torque pulsations. Assuring a balanced impedance in the grid connection gives $I_{-1} = 0$. The lowest angular frequency of pulsation then becomes $6\omega_1$ rather than $2\omega_1$. If a 3rd harmonic had existed—which might have been the case for a system with, say, two or five phases—the lowest angular frequency of pulsation could yet have been $2\omega_1$. Hence, using either less or more phases than three would aggravate the problem of power pulsations due to harmonics, which provides yet more evidence that the choice to use three phases for electric power is wise.

Remark 2.5 There is a similarity between the pulsating versus ideally constant powers of single-versus three-phase systems and the smoother torque of a three-cylinder combustion engine as compared to a single-cylinder engine. Unlike the number of phases, however, adding yet more cylinders gives even smoother torque.

2.6.11 Selection of the Space-Vector Scaling Constant

The scaling constant K can be chosen arbitrarily. Depending on the situation, one choice may be more convenient than another. There are three standard selections. Selecting $K = 1$ we obtain for a fundamental positive-sequence component

$$\mathbf{v}^s = \hat{V} e^{j(\omega_1 t + \varphi)} \quad \mathbf{v} = \hat{V} e^{j\varphi} \quad (2.138)$$

so $K = 1$ gives peak-value scaling. $K = 1/\sqrt{2}$ yields

$$\mathbf{v}^s = \frac{\hat{V}}{\sqrt{2}} e^{j(\omega_1 t + \varphi)} \quad \mathbf{v} = \frac{\hat{V}}{\sqrt{2}} e^{j\varphi}. \quad (2.139)$$

That is, rms-value scaling. The expression (2.132) for the instantaneous complex power then reads $\mathbf{S} = 3\mathbf{v}\mathbf{i}^*$. To remove the factor 3, $K = \sqrt{3}/2$ should instead be chosen, giving

$$\mathbf{S} = \mathbf{v}\mathbf{i}^*. \quad (2.140)$$

$K = \sqrt{3}/2$ is therefore called the choice for power invariance.

To reiterate.

Peak-value scaling:	$K = 1$
RMS-value scaling:	$K = 1/\sqrt{2}$
Power-invariant scaling:	$K = \sqrt{3}/2$.

Although all formulas derived henceforth are invariant of the choice of K , rms-value scaling is used in most examples.

Remark 2.6 Because $\sqrt{3}/2$ is $\sqrt{3}$ times larger than $1/\sqrt{2}$, power-invariant scaling of voltages can be regarded also as scaling with respect to the line-to-line voltage.

2.7 Symmetrical Linear Systems

In Paragraph 2.6.5, the symmetry property of a complex gain was mentioned. In this section the symmetry property is extended to linear dynamic systems with space vectors as input and output signals.

2.7.1 Complex System Models

In Paragraph 2.6.3, one of the noted differences between complex space vectors and phasors was that a complex space vector can indeed be considered as a complex signal, not just as a tool for calculation. As such, it will pass through dynamic systems which can be described with complex models. These are, on the one hand, models of three-phase circuits, machines, etc. On the other hand, they may also be controllers, filters, and other algorithms for processing of space-vectors signals in a converter control system. Let us consider the perhaps most important example, a balanced impedance [see Figure 2.15(a)] with inductance L per phase. The phase quantities obviously obey the law of induction

$$v_a = L \frac{di_a}{dt} \quad v_b = L \frac{di_b}{dt} \quad v_c = L \frac{di_c}{dt}. \quad (2.141)$$

This would seem to form a third-order dynamic system. However, as the phase currents normally add up to zero, they are not linearly independent. As a result, the effective system order is reduced to two, which makes the following equivalent two-phase representation an appropriate model:

$$v_\alpha = L \frac{di_\alpha}{dt} \quad v_\beta = L \frac{di_\beta}{dt}. \quad (2.142)$$

In complex space-vector form, the model reduces further to

$$\mathbf{v}^s = L \frac{d\mathbf{i}^s}{dt} \quad (2.143)$$

which also can be represented by the complex Laplace impedance

$$\mathbf{Z}^s(s) = sL. \quad (2.144)$$

Because this impedance determines the relationship between the complex space vectors for voltage and current, we denote it as and call it a complex impedance, even though it is real valued for a real s . Furthermore, although (2.144) appears to be a system of order one, it is really a second-order system, being but a compact form of (2.142). This applies to all complex system models.

The true system order is twice the order of the complex system model.

Figure 2.22 illustrates the steps in the modeling process.

Example 2.7 We wish to calculate the response in the current \mathbf{i}^s when the voltage

$$\mathbf{v}^s = V e^{j\omega_1 t}$$

is applied at $t = 0$ to a series connection of an inductor L and a resistor R per phase (connected in a Y). Assuming that $\mathbf{i}^s(0) = 0$ and taking the Laplace transform of \mathbf{v}^s yields

$$\mathbf{V}^s(s) = \frac{V}{s - j\omega_1}.$$

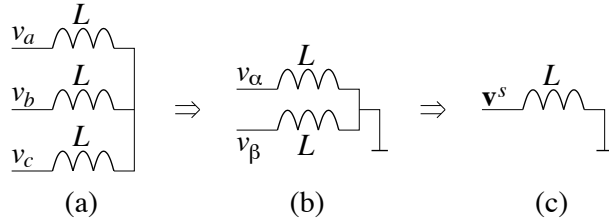


Figure 2.22. (a) Balanced inductors with ungrounded Y point. (b) Equivalent two-phase model. (c) Equivalent complex-space-vector model.

The Laplace transform of the current is found by division by the impedance $R + sL$

$$\mathbf{I}^s(s) = \frac{V}{(R + sL)(s - j\omega_1)} = \frac{V}{R + j\omega_1 L} \left(\frac{1}{s - j\omega_1} - \frac{1}{s + R/L} \right).$$

Inverse transformation results in

$$\mathbf{i}^s = \frac{V}{R + j\omega_1 L} \left(e^{j\omega_1 t} - e^{-Rt/L} \right), \quad t \geq 0.$$

The steady-state part is $\frac{V}{R + j\omega_1 L} e^{j\omega_1 t}$, which can be obtained also from phasor calculation simply by dividing by the complex impedance $R + j\omega_1 L$.

♣

2.7.2 Complex Transfer Functions

The Laplace impedance (2.144) is a special case of a general complex transfer function. Such are used for modeling of linear and time-invariant dynamic systems which have space vectors as input and output signals. A general complex transfer function may be written (if referred to the $\alpha\beta$ frame) as

$$\mathbf{H}^s(s) = H_\alpha(s) + jH_\beta(s) \quad (2.145)$$

and it may operate on the input space phasor \mathbf{u}^s , giving the output space vector \mathbf{y}^s as

$$\mathbf{y}^s = \mathbf{H}^s(p)\mathbf{u}^s. \quad (2.146)$$

In component form, (2.146) can be expressed as

$$\begin{aligned} \mathbf{y}^s &= [H_\alpha(p) + jH_\beta(p)](u_\alpha + ju_\beta) \\ &= \underbrace{H_\alpha(p)u_\alpha - H_\beta(p)u_\beta}_{y_\alpha} + j\underbrace{[H_\alpha(p)u_\beta + H_\beta(p)u_\alpha]}_{y_\beta} \end{aligned} \quad (2.147)$$

which implies the following correspondence for real space vectors:

$$\underbrace{\begin{bmatrix} y_\alpha \\ y_\beta \end{bmatrix}}_{\mathbf{y}^s} = \underbrace{\begin{bmatrix} H_\alpha(p) & -H_\beta(p) \\ H_\beta(p) & H_\alpha(p) \end{bmatrix}}_{\mathbf{H}^s(p)} \underbrace{\begin{bmatrix} u_\alpha \\ u_\beta \end{bmatrix}}_{\mathbf{u}^s}. \quad (2.148)$$

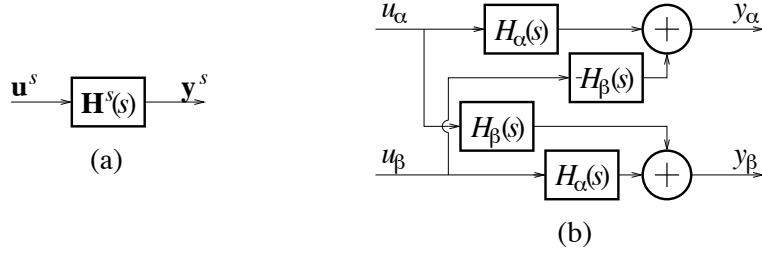


Figure 2.23. Block diagrams showing the complex transfer function $\mathbf{H}^s(s) = H_\alpha(s) + jH_\beta(s)$. (a) Complex space-vector schematic. (b) Component-wise schematic.

Figure 2.23 illustrates the principles. Notice the similarity to Figure 2.18.

From (2.148), two properties of complex transfer functions can be found.

- 1) Systems which are described by complex transfer functions are multivariable [77] with two inputs and two outputs, the respective α and β components.
- 2) $\mathbf{H}^s(s)$ is a special case of a general 2×2 transfer function matrix [77] with the restriction that the diagonal elements are equal, whereas the antidiagonal elements are equal but with a sign change (similarly to a complex gain).

A multivariable system that has these properties is referred to as *symmetrical* (also known as isotropic or rotational invariant). Examples of symmetrical systems are balanced impedances and round-rotor ac machines (see further Chapter 5). Even though they are multivariable, symmetrical systems can always be modeled using complex transfer functions. This significantly reduces the complexity of modeling, analysis, and design (e.g., of controllers) as compared to using transfer function matrices. Complex transfer functions can be handled with almost the same ease as real transfer functions, but they have some different properties.

- Unlike a real transfer function, the poles and zeros of a complex transfer function do not necessarily appear in conjugated pairs.
- Unlike a real transfer function $H(s)$, the frequency response of a complex transfer function is not necessarily symmetrical about $\omega = 0$ as $H(-j\omega) = H^*(j\omega)$. This property implies that positive- and negative-sequence components of the same frequency not necessarily have equal gains.

These properties are illustrated in the following example.

Example 2.8 Complex bandpass filter. Suppose that a three-phase current contains multi-frequency components as

$$\mathbf{i}^s = K \left[\hat{I}_{+1} e^{j(\omega_1 t + \varphi_{+1})} + \hat{I}_{-1} e^{j(-\omega_1 t + \varphi_{-1})} + \hat{I}_{-5} e^{j(-5\omega_1 t + \varphi_{-5})} + \hat{I}_{+7} e^{j(7\omega_1 t + \varphi_{+7})} + \dots \right].$$

We are interested in monitoring the fundamental positive-sequence component and therefore want to filter out all other components, giving the filtered space vector \mathbf{y}^s as shown in Figure 2.24.

The obvious solution would be to insert identical bandpass filters, with center frequency ω_1 , in the α and β channels. However, while this filtering would reject the harmonics, it would admit the

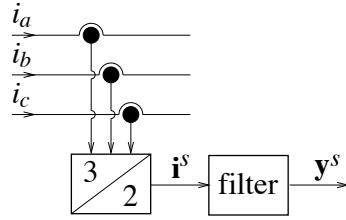


Figure 2.24. Filtering of measured current signal.

fundamental negative-sequence component. To reject also this component, a complex bandpass filter is needed. The simplest possible such filter is obtained by first considering a first-order low-pass filter

$$H_{LP}(s) = \frac{a}{s + a}.$$

This filter attenuates frequencies outside the passband $-a < \omega < a$ by 20 decibels per decade. The desired bandpass filter is obtained simply by translating the passband to be centered at $\omega = \omega_1$ instead of $\omega = 0$. This translation is obtained by substituting $s \rightarrow s - j\omega_1$, giving

$$H_{BP}(s) = H_{LP}(s - j\omega_1) = \frac{a}{s + a - j\omega_1}.$$

We now have $H_{BP}(j\omega_1) = 1$, whereas frequencies outside the passband $\omega_1 - a < \omega < \omega_1 + a$ are attenuated by 20 decibels per decade. Note also that there is one complex pole—not a pole pair—at $s = -a + j\omega_1$. It is instructive to find a realization of the filter in the form of a block diagram consisting of adders, multipliers, and integrators. (Such a realization is the basis for analog implementation using resistive-capacitive networks built around operational amplifiers. It can also be the basis for digital implementation, as will be shown in Paragraph 2.7.4.) For this sake, we rewrite the input-output-signal relation as

$$\mathbf{y}^s = \frac{a}{p + a - j\omega_1} \mathbf{i}^s \Rightarrow (p + a - j\omega_1) \mathbf{y}^s = a \mathbf{i}^s \Rightarrow p \mathbf{y}^s = a(\mathbf{i}^s - \mathbf{y}^s) + j\omega_1 \mathbf{y}^s.$$

Finally, we divide the relation by p , obtaining

$$\mathbf{y}^s = \frac{1}{p} [a(\mathbf{i}^s - \mathbf{y}^s) + j\omega_1 \mathbf{y}^s].$$

The block diagram which corresponds to this equation is shown in Figure 2.25(a). The filter consists of two adders, two multipliers (one real, by a , and one imaginary, by $j\omega_1$), and one integrator, all operating on complex space-vector signals. The corresponding component-wise block diagram is shown in Figure 2.25(b). The numbers of adders, multipliers, and integrators have now doubled. Because there are now two integrators, the true system order is revealed to be two, whereas that of the complex model is just one.



Example 2.9 Unbalanced inductances. Suppose that instead of the balanced inductances given by (2.141) we have unbalanced inductances as

$$v_a = L_a \frac{di_a}{dt} \quad v_b = L_b \frac{di_b}{dt} \quad v_c = L_c \frac{di_c}{dt}$$

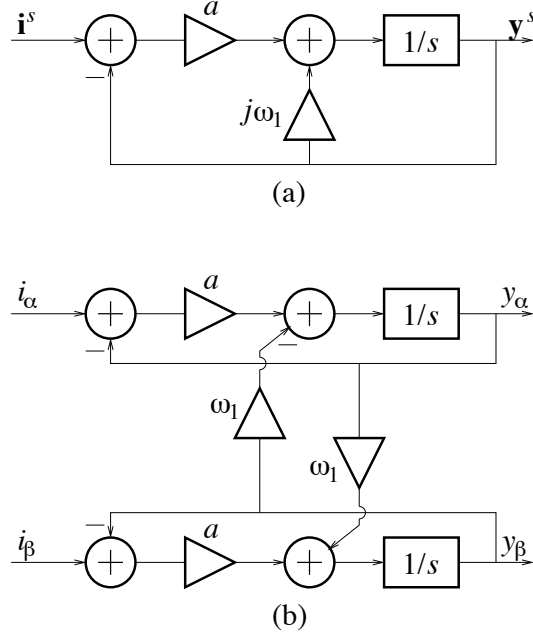


Figure 2.25. Block diagrams of complex bandpass filter with angular center frequency ω_1 . (a) Complex space-vector schematic. (b) Component-wise schematic.

or in vector form

$$\begin{bmatrix} v_a \\ v_b \\ v_c \end{bmatrix} = \begin{bmatrix} L_a & 0 & 0 \\ 0 & L_b & 0 \\ 0 & 0 & L_c \end{bmatrix} \frac{d}{dt} \begin{bmatrix} i_a \\ i_b \\ i_c \end{bmatrix}.$$

Transformation to a two-phase representation using (2.109) and (2.110) yields

$$\mathbf{v}^s = K \underbrace{\begin{bmatrix} \frac{2}{3} & -\frac{1}{3} & -\frac{1}{3} \\ 0 & \frac{1}{\sqrt{3}} & -\frac{1}{\sqrt{3}} \end{bmatrix}}_{T_{32}} \begin{bmatrix} L_a & 0 & 0 \\ 0 & L_b & 0 \\ 0 & 0 & L_c \end{bmatrix} \frac{1}{K} \underbrace{\begin{bmatrix} 1 & 0 \\ -\frac{1}{2} & \frac{\sqrt{3}}{2} \\ -\frac{1}{2} & -\frac{\sqrt{3}}{2} \end{bmatrix}}_{T_{23}} \frac{d\mathbf{i}^s}{dt}$$

which can be simplified to

$$\mathbf{v}^s = \begin{bmatrix} \frac{4L_a + L_b + L_c}{6} & \frac{L_c - L_b}{2\sqrt{3}} \\ \frac{L_c - L_b}{2\sqrt{3}} & \frac{L_b + L_c}{2} \end{bmatrix} \frac{d\mathbf{i}^s}{dt}.$$

This inductance matrix fulfills the requirements for a symmetrical system only when $L_a = L_c = L_b$, i.e., for balanced inductances, when it becomes diagonal.



2.7.3 Coordinate Transformations of Symmetrical Systems

Transformation of $\alpha\beta$ -frame quantities to the dq frame is convenient, as previously noted, since the quantities then become constant—rather than constantly oscillating—in the steady state. Consequently, it is useful to model and also to implement symmetrical systems that are dq -frame equivalents of $\alpha\beta$ -frame systems. Let us start by transforming the time derivative of a space vector from stationary coordinates to synchronous coordinates. Let \mathbf{y}^s be a general $\alpha\beta$ -transformed space vector

$$\mathbf{y}^s = e^{j\theta_1} \mathbf{y}. \quad (2.149)$$

Taking the time derivative yields, using the chain rule

$$\frac{d\mathbf{y}^s}{dt} = \frac{d(e^{j\theta_1} \mathbf{y})}{dt} = e^{j\theta_1} \left(j\omega_1 \mathbf{y} + \frac{d\mathbf{y}}{dt} \right). \quad (2.150)$$

That is, a term $j\omega_1 \mathbf{y}$ is added in the dq frame, which introduces a cross coupling between the d and q axes, cf. Figure 2.19(b) with $b = 1$. For a constant ω_1 the Laplace transform can be applied, showing that when transforming from stationary to synchronous coordinates the following substitution thus should be made:

$$s \rightarrow s + j\omega_1. \quad (2.151)$$

This is a logical result; the added term accounts for the synchronous rotation associated with the dq transformation. One implication thereof is that the Laplace impedance of an inductor—cf. (2.144)—when referred to the dq frame is

$$\mathbf{Z}(s) = (s + j\omega_1)L \quad (2.152)$$

which is illustrated in Figure 2.26.

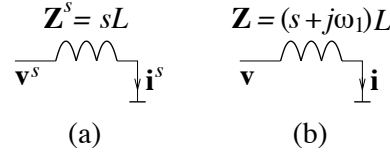


Figure 2.26. Complex inductor impedance in (a) stationary coordinates and (b) synchronous coordinates.

Example 2.10 Consider again the series-connected three-phase inductor and resistor in Example 2.7. We wish to verify the result by calculating in synchronous coordinates the current \mathbf{i}^s resulting from the application of the voltage $\mathbf{v}^s = V e^{j\omega_1 t}$ at $t = 0$. Transformation to synchronous coordinates yields $\mathbf{v} = V$, $t \geq 0$, whose Laplace transform is $\mathbf{V}(s) = V/s$. The impedance is in this case $R + (s + j\omega_1)L$, giving

$$\mathbf{I}(s) = \frac{V}{s[R + (s + j\omega_1)L]} = \frac{V}{R + j\omega_1 L} \left(\frac{1}{s} - \frac{1}{s + j\omega_1 + R/L} \right).$$

Inverse Laplace transformation yields

$$\mathbf{i} = \frac{V}{R + j\omega_1 L} \left[1 - e^{-(j\omega_1 + R/L)t} \right], \quad t \geq 0$$

and $\alpha\beta$ transformation finally gives the same result as in Example 2.7

$$\mathbf{i}^s = e^{j\omega_1 t} \mathbf{i} = \frac{V}{R + j\omega_1 L} \left(e^{j\omega_1 t} - e^{-Rt/L} \right), \quad t \geq 0.$$



The property given by (2.151) implies that a dq -frame correspondence to any symmetrical $\alpha\beta$ -frame dynamic system is straightforward to obtain. Consider a symmetrical system with complex transfer function $\mathbf{H}^s(s)$, whose input and output signals respectively are \mathbf{u}^s and \mathbf{y}^s . If another system is constructed as the dq transformation of $\mathbf{H}^s(s)$ according to (2.151)

$$\mathbf{H}(s) = \mathbf{H}^s(s + j\omega_1) \quad (2.153)$$

and whose input signal is the dq transformation of \mathbf{u}^s , then the system's $\alpha\beta$ -transformed output signal is identical to \mathbf{y}^s . This is illustrated in Figure 2.27; the configuration in Figure 2.27(b) is sometimes called the rotator-accompanied equivalent to the configuration in Figure 2.27(a), owing to the two coordinate transformations.

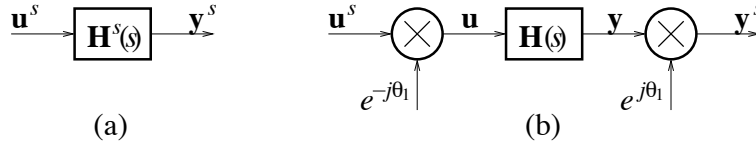


Figure 2.27. (a) Symmetrical system in the $\alpha\beta$ frame and (b) its dq -frame equivalent [provided that $\mathbf{H}(s) = \mathbf{H}^s(s + j\omega_1)$, $\dot{\theta}_1 = \omega_1$].

An $\alpha\beta$ -frame equivalent to a dq -frame symmetrical system can obviously be obtained as

$$\mathbf{H}^s(s) = \mathbf{H}(s - j\omega_1). \quad (2.154)$$

Example 2.11 Complex dq -frame-equivalent bandpass filter. In Example 2.25 we derived a complex $\alpha\beta$ -frame bandpass filter by first considering a low-pass filter, and then realizing that it can be modified into the desired bandpass filter by substituting $s \rightarrow s - j\omega_1$. That is, we effectively applied (2.154) without yet having derived the relation. Instead of making this substitution, the low-pass filter $\mathbf{H}_{LP}(s) = a/(s + a)$ can be realized in the dq frame and accompanied with rotators, as shown in Figure 2.28(b).

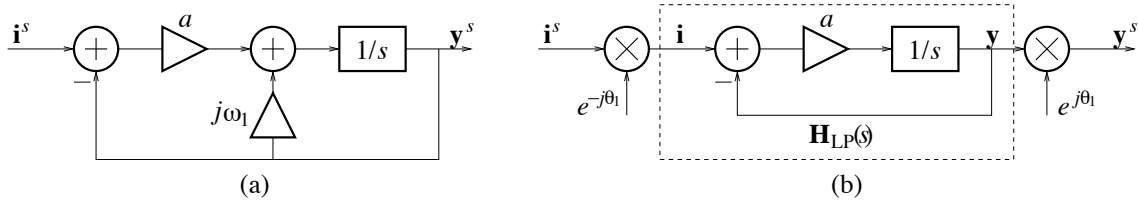


Figure 2.28. (a) $\alpha\beta$ -frame complex bandpass filter and (b) its rotator-accompanied dq -frame equivalent.

The original $\alpha\beta$ -frame filter, shown in Figure 2.28(a), is less costly to implement than its dq -frame equivalent, however. As found in Example 2.25, the former requires four adders and four multipliers. The latter, on the other hand, requires six adders and ten multipliers. This is because each complex multiplication, i.e., in this case the two coordinate transformations, require four multiplications and two additions, cf. Figure 2.18(b).



dq Transformation of a Time Delay

Another important implication of (2.151) is how an $\alpha\beta$ -frame time delay

$$\mathbf{y}^s(t) = \mathbf{u}^s(t - T_d) \Leftrightarrow \mathbf{y}^s(t) = e^{-pT_d} \mathbf{u}^s(t) \quad (2.155)$$

transforms to the dq frame. Applying (2.151) to (2.155) yields

$$\mathbf{y}(t) = e^{-(p+j\omega_1)T_d} \mathbf{u}(t) \Leftrightarrow \mathbf{y}(t) = e^{-j\omega_1 T_d} \mathbf{u}(t - T_d) \quad (2.156)$$

i.e., the time delay is transformed to a time delay and a complex gain $e^{-j\omega_1 T_d}$, which effectively causes a rotation of the dq frame by the angle $-\omega_1 T_d$. If the time delay is known, this rotation can be compensated by pre-multiplying \mathbf{u} or post-multiplying \mathbf{y} by the complex gain $e^{j\omega_1 T_d}$.

2.7.4 Discrete-Time Symmetrical Systems

So far, we have considered solely continuous-time symmetrical systems. Extension of the principles to discrete-time symmetrical systems is straightforward.

Discretization

As discussed in Paragraph 2.4.7, Euler discretization has to be applied with caution, since poorly damped continuous-time systems may result in unstable discretizations and an accurate mapping of the frequency response is obtained only for lower frequencies. We illustrate by an example.

Example 2.12 Euler discretized complex bandpass filters. Let us discretize the complex $\alpha\beta$ -frame in Example 2.25 together with its rotator-accompanied dq -frame equivalent in Example 2.11. Direct substitution $s \rightarrow (z - 1)/T_s$ in the block diagrams of Figure 2.28 yields the block diagrams shown in Figure 2.29.

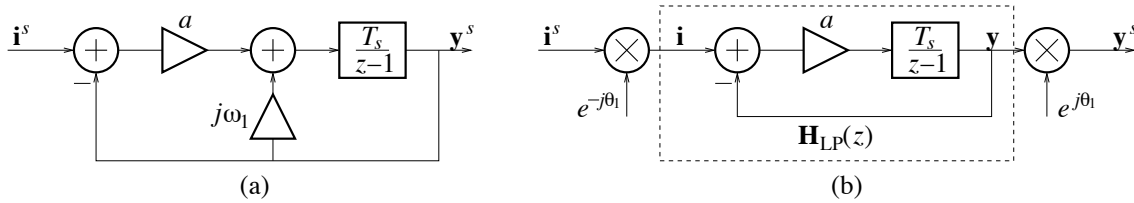


Figure 2.29. Euler discretizations of (a) $\alpha\beta$ -frame complex bandpass filter and (b) its rotator-accompanied dq -frame equivalent.

Let us analyze the obtained discrete-time systems. Transfer function $\mathbf{H}_{LP}(z)$ in Figure 2.29(b) is given by

$$\mathbf{H}_{LP}(z) = \frac{\frac{aT_s}{z-1}}{1 + \frac{aT_s}{z-1}} = \frac{aT_s}{z - 1 + aT_s}$$

whose pole is located at $z = 1 - aT_s$. Thus, $\mathbf{H}_{LP}(z)$ is asymptotically stable as long as $a < 2/T_s$, which agrees with the previously found stability criterion for the Euler method: the poles of the system to be discretized must be located within a circle with radius $1/T_s$ centered at $s = -1/T_s$.

The transfer function $\mathbf{H}_{BP}(z)$ from \mathbf{i}^s to \mathbf{y}^s in Figure 2.29(a) is given by

$$\mathbf{H}_{BP}(z) = \frac{\frac{aT_s}{z-1}}{1 + \frac{(a-j\omega_1)T_s}{z-1}} = \frac{aT_s}{z - 1 + (a - j\omega_1)T_s}.$$

The pole of $\mathbf{H}_{BP}(z)$ is located at $z = 1 - aT_s + j\omega_1 T_s$. That is, it is located within the unit circle if

$$\begin{aligned} |1 - aT_s + j\omega_1 T_s| &< 1 \Rightarrow (1 - aT_s)^2 + (\omega_1 T_s)^2 < 1 \Rightarrow \\ \omega_1 &< \frac{1}{T_s} \sqrt{1 - (1 - aT_s)^2} = \frac{1}{T_s} \sqrt{2aT_s - (aT_s)^2}. \end{aligned} \quad (2.157)$$

This criterion is often not difficult to fulfill. Suppose that a sampling frequency of 10 kHz is used, i.e., $T_s = 0.1$ ms, that $\omega_1 = 314$ rad/s, and $a = 0.1\omega_1 = 31.4$ rad/s. Then, the right-hand side of (2.157) equals 792 rad/s, so the filter is asymptotically stable. Remaining is to evaluate the frequency response. The fundamental frequency should ideally be admitted with unity gain and zero phase shift, but we get

$$\mathbf{H}_{BP}(e^{j\omega_1 T_s}) = \frac{aT_s}{e^{j\omega_1 T_s} - 1 + (a - j\omega_1)T_s}.$$

If the given numerical values are plugged into the expression, then $\mathbf{H}_{BP}(e^{j\omega_1 T_s}) = 1.19e^{j0.11^\circ}$, which shows that Euler discretization in this case is inappropriate, even though the discretized system is rendered stable.



Coordinate Transformations

We know from (2.151) that a dq transformation of an $\alpha\beta$ -frame symmetrical system is obtained by substituting $s \rightarrow s + j\omega_1$. This substitution can be directly applied to the relation (2.66) between the variables s and z , i.e., $z = e^{sT_s}$. Applying (2.151) to (2.66), we get

$$z \rightarrow e^{(s+j\omega_1)T_s} = e^{j\omega_1 T_s} \underbrace{e^{sT_s}}_z. \quad (2.158)$$

That is, dq transformation of an $\alpha\beta$ -frame discrete-time symmetrical system is obtained by the substitution

$$z \rightarrow e^{j\omega_1 T_s} z \quad (2.159)$$

whereas $\alpha\beta$ transformation of an dq -frame discrete-time symmetrical system is obtained by the substitution

$$z \rightarrow e^{-j\omega_1 T_s} z. \quad (2.160)$$

We illustrate the principle by an example.

Example 2.13 $\alpha\beta$ transformation of an Euler discretized lowpass filter. We now continue Example 2.12 with the objective of rectifying the partially failed Euler discretization of the $\alpha\beta$ -frame system, see Figure 2.29(a). Instead of direct Euler discretization in the $\alpha\beta$ frame, we make an $\alpha\beta$ transformation of the Euler discretized dq -frame low-pass filter shown in Figure 2.29(b). Applying (2.160) to $\mathbf{H}_{LP}(z)$ yields

$$\mathbf{H}_{BP}(z) = \mathbf{H}_{LP}(e^{-j\omega_1 T_s} z) = \frac{aT_s}{e^{-j\omega_1 T_s} z - 1 + aT_s} = \frac{aT_s e^{j\omega_1 T_s}}{z - (1 - aT_s) e^{j\omega_1 T_s}}.$$

The pole is now located at $z = (1 - aT_s) e^{j\omega_1 T_s}$, which is within the unit circle as long as $a < 2/T_s$. Moreover, $\mathbf{H}_{BP}(e^{j\omega_1 T_s}) = 1$, as desired. To find a realization of the filter, we write the input–output relation in the shift operator

$$\begin{aligned} \mathbf{y}^s &= \frac{aT_s e^{j\omega_1 T_s}}{q - (1 - aT_s) e^{j\omega_1 T_s}} \mathbf{i}^s \Rightarrow q\mathbf{y}^s = e^{j\omega_1 T_s} [aT_s \mathbf{i}^s + (1 - aT_s) \mathbf{y}^s] \Rightarrow \\ \mathbf{y}^s &= q^{-1} e^{j\omega_1 T_s} [aT_s (\mathbf{i}^s - \mathbf{y}^s) + \mathbf{y}^s] \end{aligned}$$

which corresponds to the block diagram shown in Figure 2.30. This is an equivalent to the $\alpha\beta$ -frame realization shown Figure 2.29(b), whereas that shown in Figure 2.29(a) is not. Magnitude and phase diagrams for $\omega_1 = 314$ rad/s, $a = 0.1\omega_1 = 31.4$ rad/s, and $T_s = 0.1$ ms are shown in Figure 2.31. It can be observed that the $\alpha\beta$ -transformed Euler discretized low-pass filter has frequency-domain properties which are near identical to those if the underlying continuous-time filter.

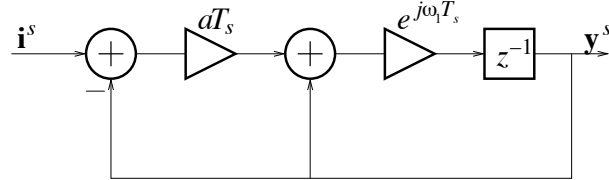


Figure 2.30. Complex bandpass filter obtained by $\alpha\beta$ transformation of an Euler discretized lowpass filter.



2.8 Normalized (Per-Unit) Values

It is common practice to use *normalized* or *per-unit* (pu) quantities in electric power engineering. Normalization is done with respect to a set of *base values*, which account for the nominal (rated) operation of a system.

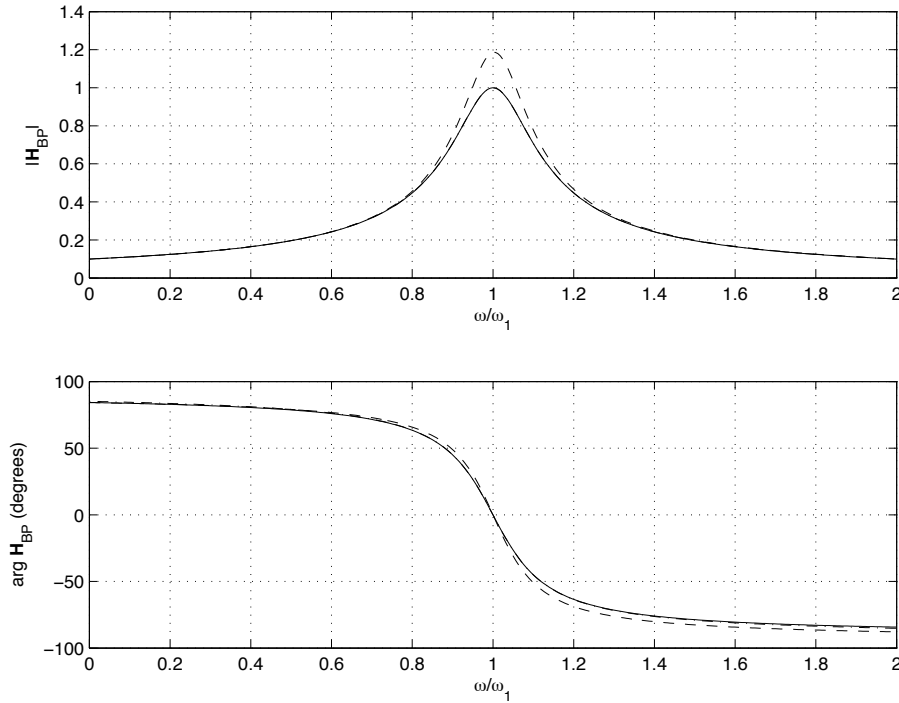


Figure 2.31. Magnitude and phase functions for (solid) continuous-time bandpass filter, (dashed) Euler discretized bandpass filter, and (dash-dotted) $\alpha\beta$ -transformed Euler discretized low-pass filter.

2.8.1 Single-Phase and DC Systems

The fundamental base values are selected equal to the nominal values (the latter denoted by the subscript N):

$$\begin{aligned} \text{Voltage: } & V_{\text{base}} = V_N \\ \text{Current: } & I_{\text{base}} = I_N \\ \text{Frequency: } & \omega_{\text{base}} = \omega_N. \end{aligned} \tag{2.161}$$

Using the fundamental base values, normalized quantities (denoted by the subscript n) are introduced as follows:

$$\begin{aligned} \text{Voltage: } & v_n = v/V_{\text{base}} \\ \text{Current: } & i_n = i/I_{\text{base}} \\ \text{Angular frequency: } & \omega_n = \omega/\omega_{\text{base}} \\ \text{Time: } & t_n = t/t_{\text{base}} = \omega_{\text{base}}t. \end{aligned} \tag{2.162}$$

Then, $i_n = 1$ pu, for example, tells that nominal current is flowing. From (2.161), the following additional base values (and others) can be derived:

$$\begin{aligned} \text{Power: } & P_{\text{base}} = V_{\text{base}}I_{\text{base}} \\ \text{Impedance: } & Z_{\text{base}} = V_{\text{base}}/I_{\text{base}} \\ \text{Inductance: } & L_{\text{base}} = Z_{\text{base}}/\omega_{\text{base}} \\ \text{Capacitance: } & C_{\text{base}} = 1/(\omega_{\text{base}}Z_{\text{base}}). \end{aligned} \tag{2.163}$$

For an ac system, $P_{\text{base}} = Q_{\text{base}} = S_{\text{base}}$, where the latter respectively are the base values for reactive and apparent powers.

Although normalization should not be overdone (for example, equations which are valid only in per-unit quantities are not recommended, or should at the very least be used sparingly), there are several benefits. Regardless of power rating, most circuit parameters tend to be constrained to a range about 1 pu: from 0.01 pu up to 5 pu, i.e., a spread of 500. For example, inductances are typically in the range from 0.05 pu to 4 pu, and resistances from 0.01 pu to 0.1 pu. Variables (voltages, currents, etc.) are often confined to the range between -1 pu and 1 pu , since an absolute value larger than 1 pu is larger than the nominal value.

To have variables that are confined to a range from 0 to 1 is also beneficial for the implementation of control algorithms on a DSP. This is particularly important for fixed-point arithmetics, where the available number range is limited.

Example 2.14 The differential equation describing an RL series circuit is given by

$$L \frac{di}{dt} + Ri = v$$

where i is the current through and v is the voltage across both the resistance and the inductance. Let us first normalize v , i , and t :

$$L \frac{d(i_n I_{\text{base}})}{d(t_n / \omega_{\text{base}})} + R(i_n I_{\text{base}}) = (v_n V_{\text{base}})$$

which can be rewritten as

$$\underbrace{L \frac{\omega_{\text{base}} I_{\text{base}}}{V_{\text{base}}} \frac{di_n}{dt_n}}_{1/L_{\text{base}}} + \underbrace{R \frac{I_{\text{base}}}{V_{\text{base}}}}_{1/Z_{\text{base}}} i_n = v_n$$

and

$$L_n \frac{di_n}{dt_n} + R_n i_n = v_n. \quad (2.164)$$

This differential equation is formally equal to the original one; the equation is formally unchanged regardless whether it is normalized or not. For this reason, the subscript n is normally omitted, as it should be evident anyhow whether a quantity is normalized or not.



Remark 2.7 Note that in per-unit value the reactance (at base frequency) of an inductor is the same as the inductance:

$$X_{Ln} = \frac{X_L}{Z_{\text{base}}} = \frac{\omega_{\text{base}} L}{Z_{\text{base}}} = L_n.$$

So, we could write (2.164) also as

$$X_{Ln} \frac{di_n}{dt_n} + R_n i_n = v_n.$$

Although this notation sometimes occurs in the literature, its usage is discouraged. It is good practice to stay with a notation which holds regardless if the quantities are normalized or not.

PROBLEM 2.24

A passive LC filter is tuned to remove the 3rd harmonic from the current in a 230-V, 50-Hz network.

- a) If $C_n = 20 \text{ pu}$, what is then most likely L_n ? **Hint:** Make reasonable assumptions, including that the resonant frequency of the LC circuit is equal to the frequency that is to be removed.
- b) If $C = 56 \mu\text{F}$, what are then L and I_{base} ?

2.8.2 Three-Phase Systems

For space vectors, the selection of base values should include the space-vector scaling constant K as follows:

$$\begin{aligned} \text{Voltage: } V_{\text{base}} &= \sqrt{2}KV_N \\ \text{Current: } I_{\text{base}} &= \sqrt{2}KI_N \\ \text{Frequency: } \omega_{\text{base}} &= \omega_N. \end{aligned} \quad (2.165)$$

where V_N and I_N are the nominal rms phase voltage and current, respectively. The quantities are then normalized as in the single-phase case:

$$\begin{aligned} \text{Voltage: } \mathbf{v}_n &= \mathbf{v}/V_{\text{base}} \\ \text{Current: } \mathbf{i}_n &= \mathbf{i}/I_{\text{base}} \\ \text{Angular frequency: } \omega_n &= \omega/\omega_{\text{base}} \\ \text{Time: } t_n &= \omega_{\text{base}}t. \end{aligned} \quad (2.166)$$

A space-vector modulus of 1 pu then corresponds nominal voltage or current, irrespective of how the scaling constant is selected. From (2.165), the following additional base values (and others) can be derived:

$$\begin{aligned} \text{Power: } S_{\text{base}} &= P_{\text{base}} = Q_{\text{base}} = 3V_NI_N = \frac{3}{2K^2}V_{\text{base}}I_{\text{base}} \\ \text{Impedance: } Z_{\text{base}} &= V_N/I_N = V_{\text{base}}/I_{\text{base}} \\ \text{Inductance: } L_{\text{base}} &= Z_{\text{base}}/\omega_{\text{base}} \\ \text{Capacitance: } C_{\text{base}} &= 1/(\omega_{\text{base}}Z_{\text{base}}). \end{aligned} \quad (2.167)$$

This has the effect that the relation (2.131) for the complex power simplifies to

$$\begin{aligned} \mathbf{S} &= \frac{3}{2K^2}\mathbf{v}\mathbf{i}^* = \frac{3}{2K^2}V_{\text{base}}\mathbf{v}_nI_{\text{base}}\mathbf{i}_n^* = S_{\text{base}}\mathbf{v}_n\mathbf{i}_n^* \\ \Rightarrow \mathbf{S}_n &= \mathbf{v}_n\mathbf{i}_n^* \end{aligned} \quad (2.168)$$

so $\mathbf{S}_n = 1 \text{ pu}$, quite logically, corresponds to nominal power. This is an exception to the rule that the normalized equation is formally identical to the original one. Caution should be exercised when using equations involving normalized power quantities!

CHAPTER 3

Voltage-Source Converters

This chapter focuses mainly on operating principles and pulsedwidth-modulation (PWM) techniques for single-phase and (primarily) three-phase VSCs. VSCs build on the same principle as dc–dc converters. Therefore, to enhance the understanding of the operating principle of a VSC, we begin by a brief introduction to the dc–dc buck converter and the principle of hysteresis current control.

3.1 Buck Converters

DC–dc converters can be considered as “dc transformers.” There are several dc–dc converter types, of which we shall make a brief introduction to the buck (or step-down) converter. Its circuit diagram is shown in Figure 3.1. The converter is fed from a dc link, whose voltage V_{dc} is assumed constant, as is the load voltage V .

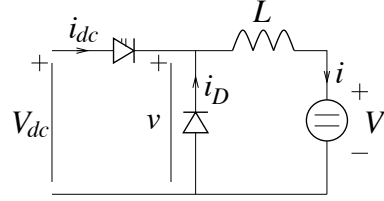


Figure 3.1. Circuit diagram for the buck converter.

3.1.1 Switch-Mode Operation

The device shown in Figure 3.1 as a diode symbol to which two gates symbols are added is a turn-on–turn-off switch, which generally is transistor. In the ON state the voltage drop across the switch is small, whereas in the OFF state no current is conducted by the switch. The duty cycle D , which is the ratio between the ON time t_+ and the switching period T_{sw} : $D = t_+/T_{sw}$, determines the mean value of voltage v . To keep the mean value of current i constant, the mean value of v must equal the load voltage V . Thus, the following relation must hold:

$$V = DV_{dc}, \quad 0 \leq D \leq 1. \quad (3.1)$$

The dc-link voltage is “stepped down” by the factor D ; hence, the name of the converter. Due to the switch-mode operation, the waveform of v becomes “chopped” or pulsedwidth modulated; a train of pulses. Typical switching frequencies $f_{sw} = 1/T_{sw}$ are from 1 kHz up to about 50 kHz.

The chopped waveform of v is acceptable in many applications (for example dc motors), as long as the output current i is fairly smooth. This is why a sufficiently large inductance L has to be

included in the circuit. Furthermore, an alternative path for the output current when the transistor is switched OFF must be provided, which is the reason for including the so-called freewheeling diode in Figure 3.1.

Referring to Figure 3.2, when the switch is turned ON, i increases, flowing through the switch; when turned OFF, i decreases, flowing through the diode. If the switching is made fast enough, then the resulting ripple Δi will be low (the ripple in Figure 3.2 is exaggerated).

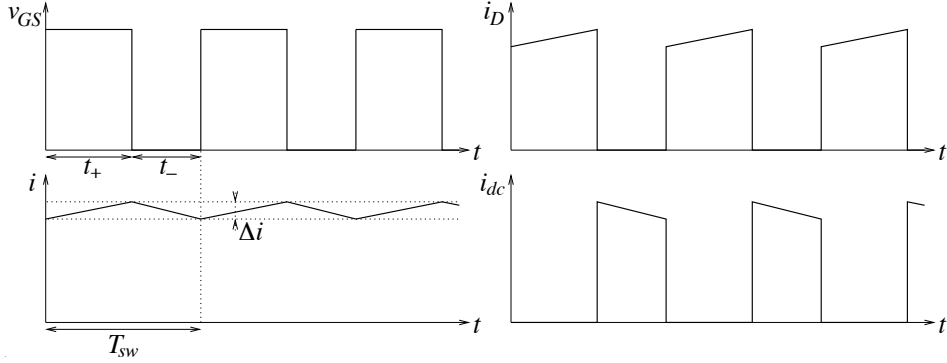


Figure 3.2. Output voltage and current waveforms in the step-down converter.

3.1.2 Load-Current Ripple

Let us calculate the ripple Δi by finding its relation to the switching frequency $f_{sw} = 1/T_{sw}$ and the duty cycle D . In order for i in Figure 3.1(b) to remain constant, $DV_{dc} = V$. When the switching valve is turned ON, for $0 \leq t < t_+$, we have

$$L \frac{di}{dt} = V_{dc} - V = (1 - D)V_{dc} \quad (3.2)$$

giving

$$\begin{aligned} \Delta i &= \frac{1}{L} \int_0^{t_+} (1 - D)V_{dc} dt = \frac{(1 - D)V_{dc}t_+}{L} = \{D = t_+/T_{sw} = t_+f_{sw}\} \\ &= \frac{D(1 - D)V_{dc}}{f_{sw}L}. \end{aligned} \quad (3.3)$$

This function has its maximum for $D = 1/2$, i.e., $V = V_{dc}/2$

$$\Delta i_{\max} = \frac{V_{dc}}{4f_{sw}L}. \quad (3.4)$$

As could be conjectured, increasing the inductance and/or the switching frequency reduces the ripple.

PROBLEM 3.1

A buck converter in an automobile using $V_{dc} = 12$ V feeds, via a series-connected inductance, a resistive load of 12Ω . There are three choices of the switching frequency and the inductance: 4 kHz, 8 kHz, and 16 kHz and 10 mH, 20 mH, and 30 mH, respectively. It is desired that

the switching frequency and the inductance both should be as low as possible. Are there any combinations that give a ripple less than 0.5% of the maximum current?

PROBLEM 3.2

A buck converter with $V_{dc} = 100$ V supplies variable voltage to a dc motor. The dc motor can be modeled as a 40-mH inductance in series with a back emf. The back emf is proportional to the motor speed, which is variable. The load torque is constant, however, so the motor current is also constant: 8 A.

- Select the switching frequency such that the ripple in the motor current never exceeds 0.2 A.
- What is the current ripple when the motor operates at 80% of its maximum attainable speed?

3.1.3 Hysteresis Current Control

In many applications it is desired to control the output current i in a closed loop. Methods for current control are discussed in Chapter 4 (when the output current is dc) and in Chapter 6 (when the output current is three-phase ac). However, it is instructive to study already at this stage a simple and popular method for current control of switched converters.

Temperatures in ovens and electric radiators are controlled by switching the electric power on and off. When the temperature exceeds a certain level, power is switched off, whereas power is switched on again when the temperature dips below a certain level. The span within which the temperature is allowed to vary is called the tolerance band.

PROBLEM 3.3

Suggest at least two more applications where this type of control is used.

This method is called hysteresis control, alternatively on/off control or tolerance-band control. Although the switching frequency is quite low (fraction of 1 Hz) in the mentioned applications, the same principle can be applied also to power electronic converters switching at 1 kHz and above, simply by choosing a sufficiently narrow tolerance band.

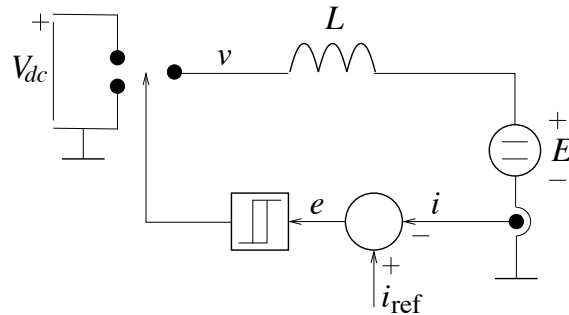


Figure 3.3. Hysteresis control of the buck converter.

Let us consider a buck converter feeding a load with a constant voltage E , as shown in Figure 3.3, where the semiconductor switch and the freewheeling diode are replaced by a so-called change-over switch model. The block which controls the switch is called a hysteresis comparator. Suppose

that the switch is initially turned off, i.e., $v = 0$. The current i then decreases, and once it dips below its reference i_{ref} , the control error $e = i_{\text{ref}} - i$ turns positive. When e exceeds the tolerance band, $e > \Delta i/2$, the output of comparator goes high, causing the switch to turn on. Now, $v = V_{dc}$, so the current increases until $e < -\Delta i/2$, when the switch turns off. Typical curves are illustrated in Figure 3.4.

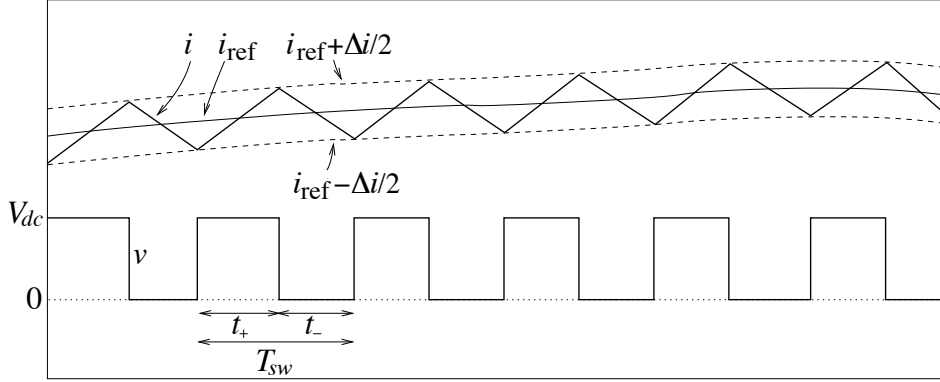


Figure 3.4. Voltage and current waveforms in hysteresis control.

Obviously, by decreasing the tolerance band Δi , the current ripple is decreased accordingly, while the mean switching frequency increases. For buck converters, the mean switching frequency is found from (3.3)

$$f_{sw} = \frac{D(1-D)V_{dc}}{L\Delta i} \quad (3.5)$$

where the maximum switching frequency is obtained for $D = 1/2$

$$f_{sw}^{\max} = \frac{V_{dc}}{4L\Delta i}. \quad (3.6)$$

Hysteresis current control has some benefits. The method is simple to implement, and the response to a reference step is very quick. The main drawback is the varying switching frequency. This is particularly troublesome for $D \approx 0$ and $D \approx 1$, when f_{sw} will be low. A low switching frequency gives a low-frequency current ripple. In a dc motor drive, this gives low-frequency torque ripple, which may excite mechanical resonances. Switching of power semiconductors also leads to the emission of electromagnetic interference (EMI), a problem which is more pronounced at higher switching frequencies than at lower. It is more difficult to satisfactorily protect sensitive equipment against EMI if the switching frequency varies than if it is held constant.

The varying switching frequency problem can be circumvented by tuning Δi on-line. If Δi is selected proportionally to $D(1-D)$, then it is seen in (3.5) that f_{sw} will stay constant. A variable Δi can be achieved by implementing the hysteresis control system digitally. This requires a very high sampling frequency to prevent timing errors. Another way is to use analog implementation but to adjust Δi digitally via a D/A converter.

3.2 Single-Phase Voltage-Source Converters

The buck converter in Figure 3.2 is capable only of supplying positive output voltage and current. It is straightforward to improve the configuration so that positive output voltage and/or current can be handled. In the circuit depicted in Figure 3.5(a), three more switches have been added, together with antiparallel-connected (freewheeling) diodes. The configuration has two legs, A and B, as indicated in Figure 3.5(a). The switching modes are illustrated by the change-over switch model in Figure 3.5(b). By switching the legs pairwise, such that the upper valve of leg A is turned on at the same time as the lower valve of leg B, we get $v = V_{dc}$. This is called the positive switching mode: SW+. Switching the legs vice versa (i.e., upper valve of leg B ON, lower valve of leg A OFF), we get $v = -V_{dc}$: SW-. If both legs are switched the same way (i.e., both upper valves ON or OFF), we get $v = 0$: SW0.

By suitable combination of these three switching modes, any switched waveform can be generated, dc or ac. The converter is therefore called a single-phase inverter, since it “inverts” the dc-link voltage into any waveform. Other names are, full-bridge converter, H-bridge converter and, as the title of Section 3.2 indicates, single-phase VSC. Owing to the antiparallel-connected diodes, the single-phase VSC is capable of handling also negative current. The four modes of operation excluding SW0 are illustrated in Figure 3.6(a)–(d). Being able to use positive and negative voltage and current (which for dc motor drives enables forward and reverse speed as well as electric braking) is called four-quadrant operation, cf. Figure 3.6(e).

In addition to four-quadrant dc motor drives, an important application for single-phase VSCs is as active front ends in ac rail traction. The converter then operates in rectifier mode, feeding power from the catenary (alternating voltage v) to the dc link. Three-phase VSCs are connected to the dc link, feeding traction ac motors. Usage of a single-phase VSC instead of a diode rectifier permits regeneration of power to the catenary when the rail vehicle is braked.

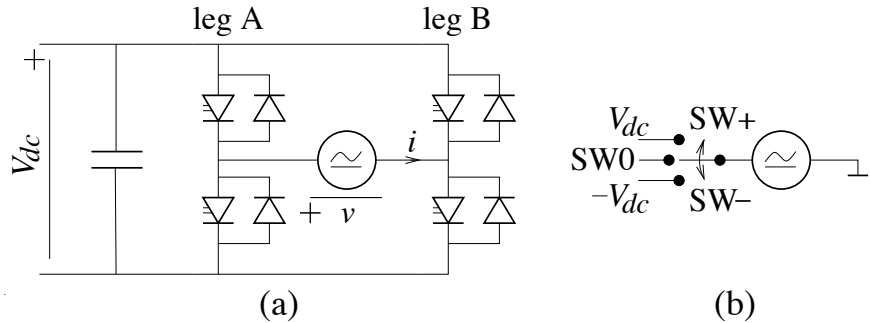


Figure 3.5. Single-phase VSC. (a) Circuit diagram. (b) Change-over switch model.

3.2.1 Pulsewidth Modulation: Bipolar Switching

Due to the switch-mode operation, the desired voltage is obtained only in mean. Let us begin by using only SW+ and SW-, not SW0, which is called bipolar switching. Referring to Figures 3.2 and 3.6, it is obvious that the mean value of v can be expressed as

$$V = \frac{1}{T} [t_+ V_{dc} + t_- (-V_{dc})] = (2D - 1)V_{dc}, \quad D = \frac{t_+}{T_{sw}} \quad (3.7)$$

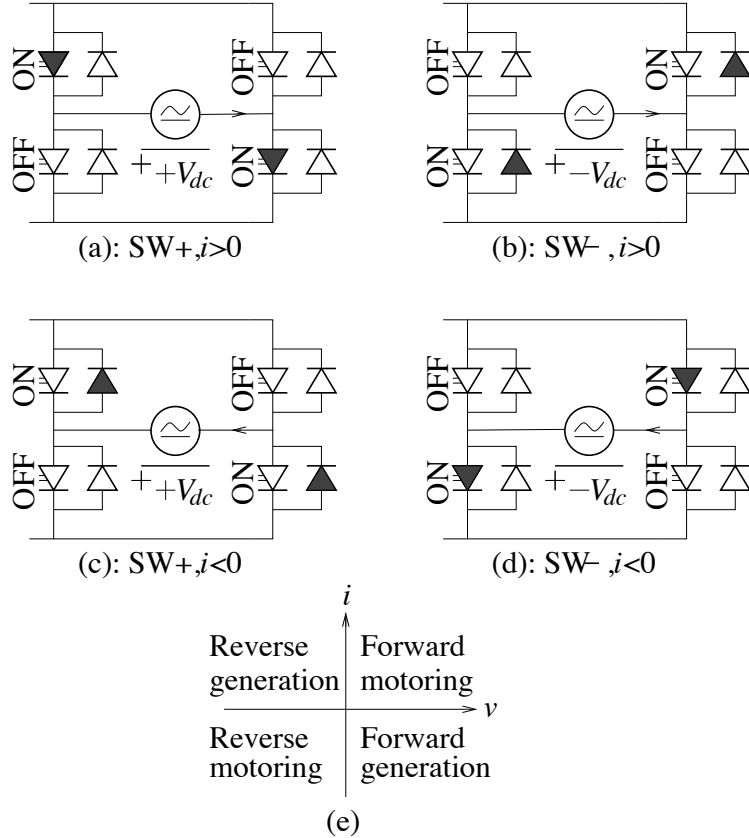


Figure 3.6. Single-phase VSC: four switching modes, (a)–(d), with v and i positive or negative. (Conducting devices are shaded.) (e): The four quadrants of operation for a dc motor drive.

where t_+ and t_- are the intervals in which $\text{SW}+$ and $\text{SW}-$, respectively, are used. Thus, if $D = 1 \Leftrightarrow t_+ = T_{sw}$ (only $\text{SW}+$ is used), we get $V = V_{dc}$; if $D = 1/2 \Leftrightarrow t_+ = t_- = T_{sw}/2$ ($\text{SW}+$ and $\text{SW}-$ are used equally long times), we get $V = 0$, and if $t_+ = 0$ (only $\text{SW}-$ is used), we get $V = -V_{dc}$. Quite similarly to the output voltage of a buck converter, the resulting voltage waveform becomes pulsewidth modulated; see Figure 3.7.

If the right-hand side of (3.7) is made equal to the reference (desired value) v_{ref} for the output voltage

$$D = \frac{v_{\text{ref}}/V_{dc} + 1}{2} \quad (3.8)$$

then the instantaneous output voltage can be expressed as

$$v = v_{\text{ref}} + \text{switching harmonics.} \quad (3.9)$$

The switching harmonics (see Paragraph 3.2.4) cause ripple in i . As for the buck converter, the load must be inductive for the output current to be smooth enough. The higher the switching frequency, the lower the current ripple. From a control standpoint the switching harmonics can

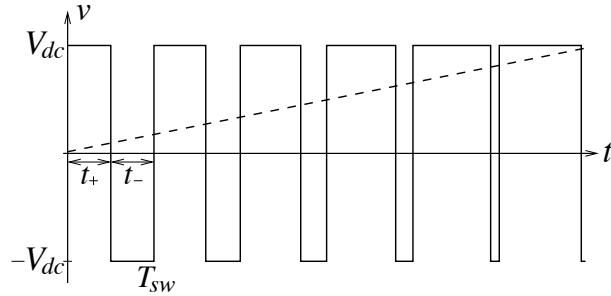


Figure 3.7. Pulsewidth-modulated voltage waveform (solid) and reference value (dashed).

usually be disregarded, and the converter treated as an actuator that, with a time delay which often can be neglected, see Paragraph 3.12, generates the desired voltage: $v = v_{\text{ref}}$.

PROBLEM 3.4

Derive a formula similar to (3.3) for the output current ripple of the single-phase VSC using bipolar switching.

PROBLEM 3.5

Hysteresis control is useful also for single-phase VSCs. Replacing the buck converter by a single-phase VSC simply implies changing the output voltage when the switch is aligned downward in Figure 3.3 from 0 to $-V_{dc}$. Express the switching frequency in a formula similar to (3.5), assuming $R \approx 0$.

3.2.2 Suboscillation Method: Bipolar Switching

We now wish to generate appropriate converter leg switching signals from the reference signal v_{ref} . The classical method for this is the suboscillation (or triangle comparison) method. The idea is to compare a reference signal $s = v_{\text{ref}}/V_{dc}$ to a triangular carrier signal of amplitude 1. When s is larger than the carrier, SW+ is used; otherwise SW-. This is illustrated in Figures 3.8. The only difference as compared to Figure 3.7 is that the switchings are made symmetrically within the period $0 < t < T_{sw}$, not at the beginning of the period. Simple geometry gives

$$t_+ = \frac{(1+s)T_{sw}}{2} \quad t_- = T_{sw} - t_+ = \frac{(1-s)T_{sw}}{2}. \quad (3.10)$$

Thus, the mean voltage over one switching period is found to be

$$\langle v \rangle = \frac{1}{T_{sw}} \int_0^{T_{sw}} v dt = \frac{1}{T_{sw}} [t_+ V_{dc} + t_- (-V_{dc})] = sV_{dc} = v_{\text{ref}} \quad (3.11)$$

just as desired.

The system in Figure 3.8 is straightforward to implement using analog circuitry. Custom-made triangle-wave generator chips are available, and an analog comparator is easily constructed using an operational amplifier. Analog PWM implementation was state of the art up until at least the early 1990s.

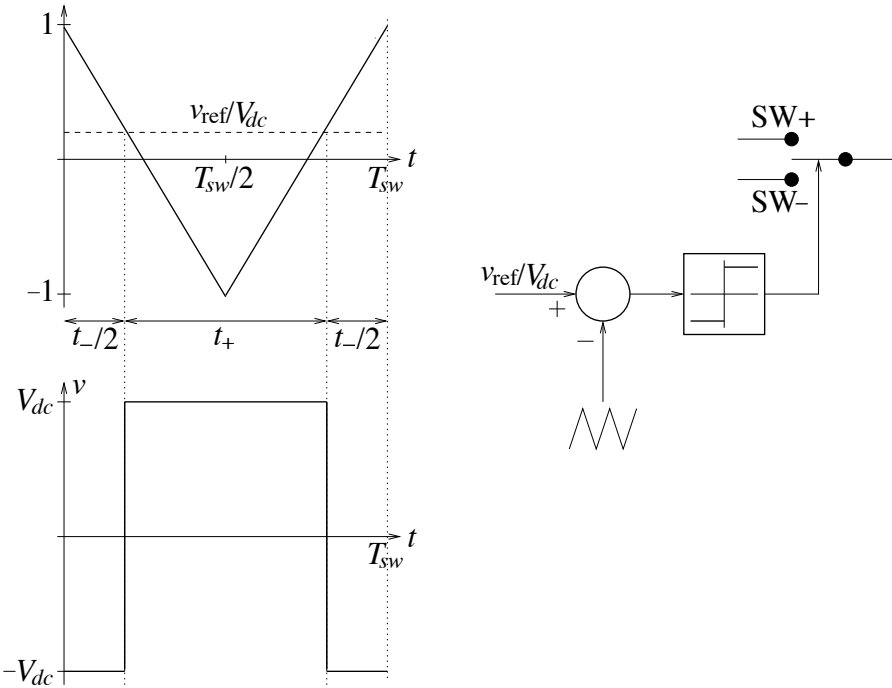


Figure 3.8. Suboscillation PWM method.

PROBLEM 3.6

A single-phase bipolar-switched VSC is used to power the dc motor driving a forklift truck. The battery gives $V_{dc} = 50$ V, the motor's back emf is proportional to the speed, its inductance is 50 mH, and its current may be at most 100 A.

- Select the switching frequency such that the current ripple never exceeds 1 A. **Hint:** Problem 3.4.
- At half the base speed, the motor is braked with the current -8 A. For this operating condition, sketch the switching waveforms as well as the currents through the upper switching valve and the antiparallel-connected diode in leg A during one switching period.

PROBLEM 3.7

Using a single-phase bipolar-switching VSC with $V_{dc} = 513$ V, a sinusoidal voltage $v = 110\sqrt{2}\sin(120\pi t)$ is to be generated in order to supply electrical equipment imported to Europe from the United States. The switching frequency is 5 kHz and the load can be assumed resistive-inductive with 2Ω och 100 mH.

- Sketch for one switching period the switching waveform as well as the currents through the upper switching valve and the antiparallel-connected diode in leg A at $t = 18$ ms.
- Determine the current ripple at $t = 18$ ms. (With current ripple it is here meant the deviation from the ideal sinusoidal waveform.) **Hint:** Problem 3.4.

- c) Suppose that the VSC's dc link is supplied from a 400-V (line-to-line voltage), 50-Hz grid via a three-phase diode rectifier. What is then the line inductance?

3.2.3 Pulsewidth Modulation: Unipolar Switching

The performance of a pulsewidth-modulated converter can be improved if SW0 is also used. If positive voltage is desired, SW+ and SW0 should be combined rather than SW+ and SW-. Likewise, for negative voltage, SW- and SW0 should be combined. The resulting PWM scheme is called unipolar switching, because SW+ and SW- are not combined.

Unipolar switching is accomplished by skewing the switching events, such that legs A and B are not switched simultaneously. The method is perhaps best understood by considering its implementation using the suboscillation method. Leg A is switched as in bipolar switching: the normalized reference signal v_{ref}/V_{dc} is compared to a triangular carrier signal with amplitude 1. Leg B, however, is switched by comparing $-v_{\text{ref}}/V_{dc}$ to the triangular carrier signal. With the vector (A, B) indicating the switching state— $(A, B) = (1, 0)$ indicates that leg A is switched on and leg B is switched off, etc.—the sequence in bipolar switching is simply

$$\cdots - (1, 0) - (0, 1) - (1, 0) - \cdots$$

whereas in unipolar switching, the sequence is

$$\cdots - (1, 1) - (1, 0) - (0, 0) - (1, 0) - (1, 1) - \cdots .$$

That is, $(0, 1)$ is not used at all, so the pulsewidth-modulated voltage is always positive. For negative voltage, the sequence is instead

$$\cdots - (1, 1) - (0, 1) - (0, 0) - (0, 1) - (1, 1) - \cdots$$

and now $(1, 0)$ is never used.

Unipolar switching is preferable to bipolar switching. One reason is that the voltage step at each switching event is smaller: V_{dc} instead of $2V_{dc}$, resulting in a smaller current ripple.

PROBLEM 3.8

This problem is identical to Problem 3.7, but unipolar switching is used.

3.2.4 Frequency Spectra

Switched voltage waveforms contain harmonics. If the reference voltage v_{ref} is a sinusoid, analytic expressions for the harmonic content of v unfortunately cannot be derived; numerical calculations must be relied upon. In Figures 3.9 and 3.10, voltage and current waveforms as well as voltage frequency spectra are depicted for a sinusoidal reference voltage of peak value 100 V and frequency 50 Hz. The load is an RL series circuit with $R = 1 \Omega$ and $L = 10 \text{ mH}$, and the switching frequency is 1 kHz. The following conclusions can be drawn.

- For bipolar switching there are clusters of harmonics around nf_{sw} , $n = 1, 2, 3, \dots$. The amplitude of the strongest harmonic of each cluster decreases as $1/n$.
- For unipolar switching there are clusters of harmonics around $2nf_{sw}$, $n = 1, 2, 3, \dots$. That is, the switching frequency is effectively doubled. Again, the amplitude of the strongest harmonic of each cluster decreases as $1/n$.

- Due to the lower harmonic content, the output current has much less ripple for unipolar switching than for bipolar switching.

Thus, we have verified that unipolar switching is preferable. This is particularly true for low switching frequencies: $f_{sw} < 1$ kHz, when the lowest-order harmonic is in the range of hundreds of hertz.

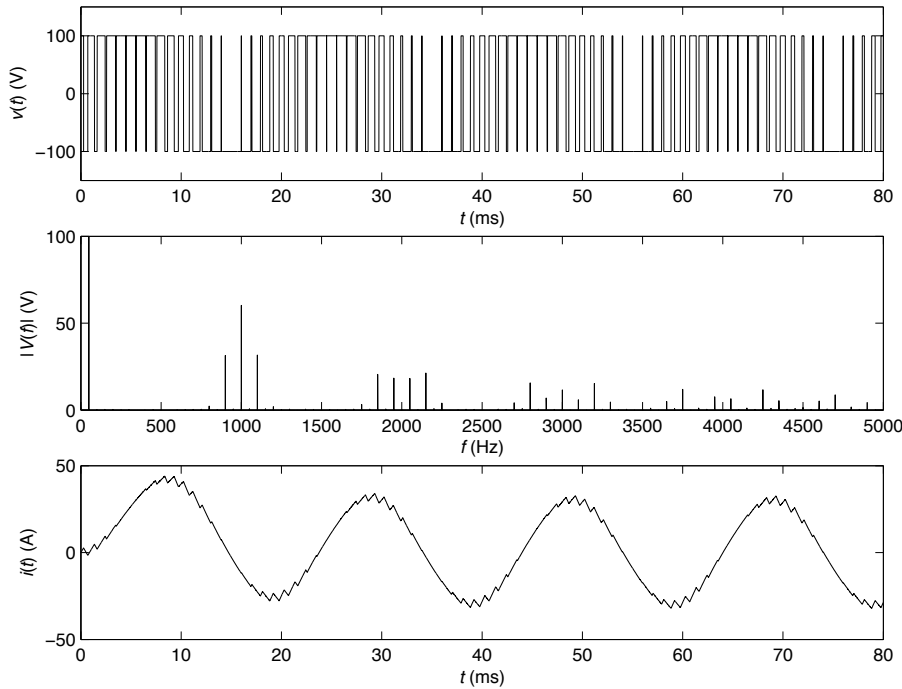


Figure 3.9. Bipolar switching with $V_{dc} = 100$ V and $f_{sw} = 1$ kHz: voltage waveform, voltage frequency spectrum, and current waveform.

3.2.5 Digital Implementation Using Synchronous Sampling

In a digital current control system, i is sampled with the sampling period T_s . To avoid EMI from spikes that occur due to switched-mode operation, it is preferable to synchronize sampling and switching, so that samples of i are taken in between switchings. This coincides with the positive and negative peak values of the suboscillation triangular carrier waveform, see Figure 3.11. The sampling frequency is thus selected as twice the switching frequency

$$f_s = 2f_{sw}. \quad (3.12)$$

Using synchronous sampling, approximately the mean value of the current is obtained at the sampling instants. Thus, not only is EMI avoided, but so is also the ripple in i . This warrants us neglecting the switching harmonics in (3.9). Quite often, synchronous sampling is effective enough so that prefiltering of i (see Paragraph 2.4.1) is unnecessary.

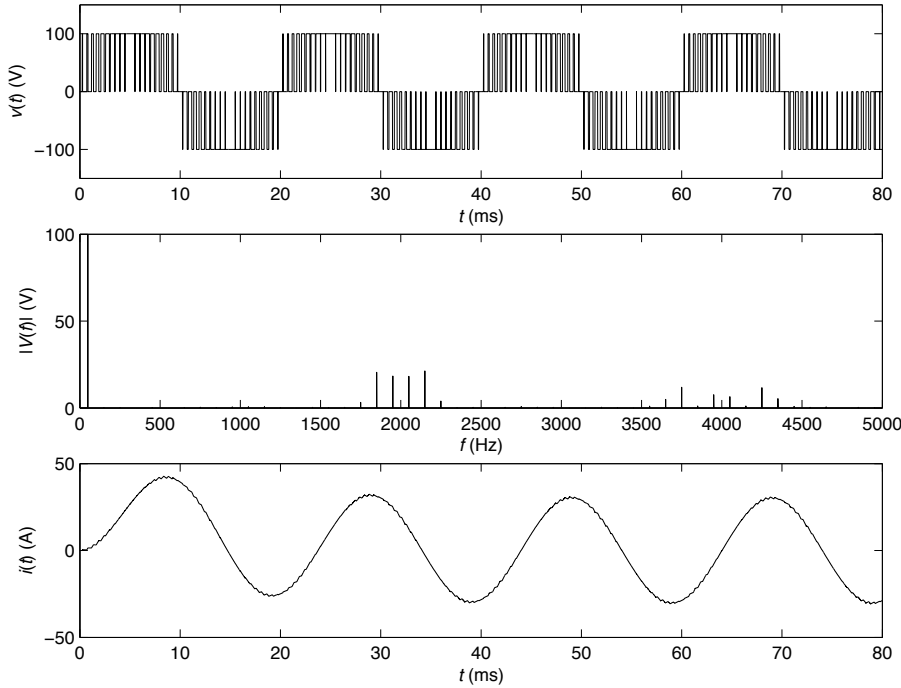


Figure 3.10. Unipolar switching with $V_{dc} = 100$ V and $f_{sw} = 1$ kHz: voltage waveform, voltage frequency spectrum, and current waveform.

Digital PWM can be implemented using only one timer. When the timer runs out, a processor interrupt is triggered and the proper switching is executed. (Alternatively, the switching logic can be implemented directly in hardware, e.g., using an FPGA.) As shown in Figure 3.12, the timer can be reloaded with the proper countdown time Δt_k at the sampling instants, i.e., at time $t = kT_s$. If the switching state is SW+ when the timer is reloaded, then $\Delta t_k = t_+/2$, otherwise $\Delta t_k = t_-/2$. From (3.10) with $T_{sw} = 2T_s$ and $s = s_k$, we obtain

$$\Delta t_k = \begin{cases} (1 + s_k)T_s/2 & \text{if switching state=SW+} \\ (1 - s_k)T_s/2 & \text{if switching state=SW-.} \end{cases} \quad (3.13)$$

PWM Time Delay

The countdown time is confined to the interval $[0, T_s]$. If $\Delta t_k = 0$, then the switching is executed immediately, and if $\Delta t_k = T_s$, then the timer is reloaded immediately after it has run out. These extremes correspond to short-duration pulses, such as that centered at $t = (k+3)T_s$ in Figure 3.12. Except for such sudden changes (as that exemplified in Figure 3.12), the switching and sampling frequencies are normally high enough in relation to the system dynamics, so that the change in the reference signal between two consecutive sampling instants is small, i.e., $s_{k+1} \approx s_k$. Consequently, since the switching state alternates between SW+ and SW- with every sampling instant, the mean countdown time for two consecutive switching events is given by

$$\frac{\Delta t_k + \Delta t_{k+1}}{2} = \frac{T_s}{2} \pm \frac{(s_k - s_{k+1})T_s}{4} \approx \frac{T_s}{2}. \quad (3.14)$$

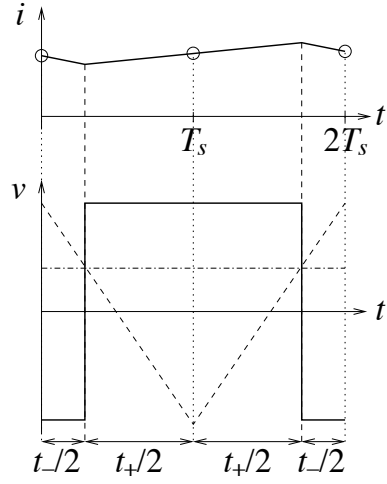


Figure 3.11. Synchronous sampling with the suboscillation method: current i is sampled in between switchings, at $t = \{0, T_s, 2T_s, \dots\}$. The switching frequency is $1/(2T_s)$.

Thus, seen over one switching period the mean time delay from timer reloading to switching execution—which we shall call the PWM time delay—is approximately $T_s/2$.

Controller Time Delay

Reference s_k is generally computed by a current controller, see further Section 4.4. The current controller must include a one-sample delay, i.e., the most recent current sample used in the computation of s_k by the current controller is i_{k-1} , as shown by the dotted lines in Figure 3.12. If this time delay were not included, then timing errors would result for short-duration pulses. This is exemplified in Figure 3.13, which shows a similar switching sequence as in Figure 3.12, but without the controller time delay. The reload time instants are now postponed by the computational time delay T_c , and consequently the countdown time is adjusted as

$$\Delta t'_k = \Delta t_k - T_c. \quad (3.15)$$

Since $T_c \ll T_s$, this scheme works flawlessly until the short-duration pulse centered at $t = (k+3)T_s$ is reached. Here, $\Delta t_{k+3} < T_c$, so the control system resorts to setting $\Delta t'_{k+3} = 0$, i.e., the switching is executed immediately. The delayed switching gives slightly higher mean voltage and current, as can be observed by comparing with the ideal dashed curves in Figure 3.13.

Total Time Delay

It is found that the mean total time delay for PWM using synchronous sampling is given by

$$T_d = 1.5T_s \quad (3.16)$$

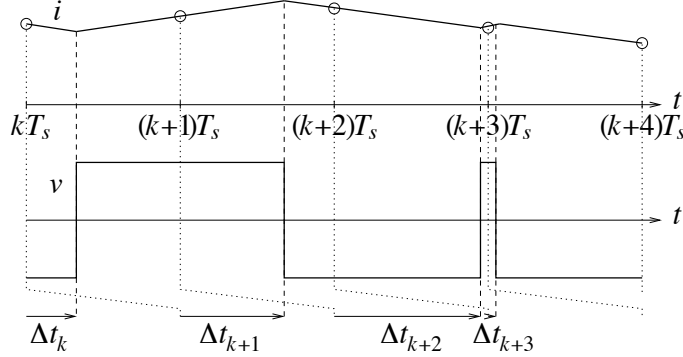


Figure 3.12. Digital PWM with a one-sample controller time delay.

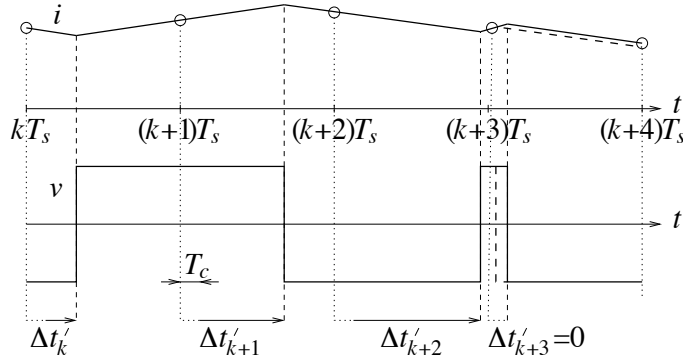


Figure 3.13. Digital PWM without a controller time delay: timing errors result for short pulses.

of which T_s results from the controller time delay and $0.5T_s$ results from the PWM time delay.

3.3 Three-Phase Voltage-Source Converters

Adding one more leg to the single-phase VSC in Figure 3.5, we obtain the three-phase VSC shown in Figure 3.14. The corresponding change-over switch model is shown in Figure 3.15(a).

The circuit shown in Figure 3.14 is ungrounded, but for convenience the middle of the dc link is selected as neutral point in the calculations to follow. As for the single-phase VSC, we introduce a switching vector (a, b, c) . For example, $(a, b, c) = (1, 0, 0)$ means that leg a is switched on, giving $v_a = V_{dc}/2$, and legs b and c are switched off, giving $v_b = v_c = -V_{dc}/2$, corresponding to Figure 3.15(a). Let us now introduce the space vector for the converter output voltage, as defined in (2.101)

$$\mathbf{v}^s = \frac{2K}{3}(v_a + e^{j2\pi/3}v_b + e^{j4\pi/3}v_c). \quad (3.17)$$

Because the phase voltages only can attain $\pm V_{dc}/2$, \mathbf{v}^s can attain only the following values:

$$v_\alpha = \left\{ 0, \pm \frac{KV_{dc}}{3}, \pm \frac{2KV_{dc}}{3} \right\}, \quad v_\beta = \left\{ 0, \pm \frac{KV_{dc}}{\sqrt{3}} \right\}. \quad (3.18)$$

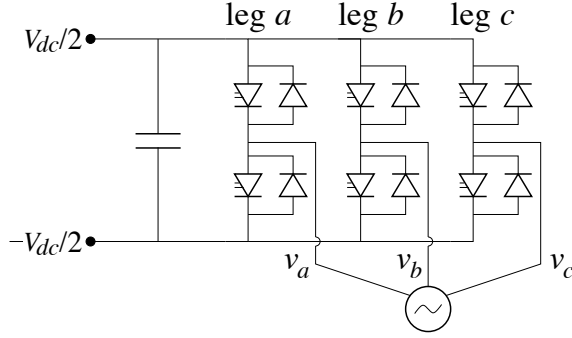


Figure 3.14. Three-phase VSC.

The resulting vector diagram is depicted in Figure 3.15(b). The maximum modulus of the voltage vector is

$$|\mathbf{v}^s|_{\max} = \frac{2KV_{dc}}{3} \quad (3.19)$$

which is attained for all switching states except (1, 1, 1) and (0, 0, 0), which both yield the zero vector. A rotating voltage vector of maximum modulus is obtained by repeating the switching sequence

$$(1, 0, 0) - (1, 1, 0) - (0, 1, 0) - (0, 1, 1) - (0, 0, 1) - (1, 0, 1)$$

i.e., the zero vector is not used at all. This switching mode is known as six-step.

PROBLEM 3.9

What is a binary sequence of this type called?

It is rather obvious that by combining all switching states appropriately using PWM—including the zero vector—any location within the hexagon in Figure 3.15(b) can be accessed, i.e., any voltage vector within the hexagon can be created *in mean*. For instance, $[v_\alpha, v_\beta] = [KV_{dc}/3, 0]$ can be obtained by switching (0, 0, 0) and (1, 0, 0) equally long times. However, the circle in Figure 3.15(b), which touches the sides of the hexagon, is the limit for linear modulation. Simple geometry shows that this circle has a radius of $\sqrt{3}/2$ times the maximum voltage vector

$$\text{circle radius} = \frac{\sqrt{3}}{2} |\mathbf{v}^s|_{\max} = \frac{KV_{dc}}{\sqrt{3}}. \quad (3.20)$$

Therefore, as shown in Figure 3.15(b), it is logical to select the voltage base value V_{base} (see Section 2.8) as

$$V_{\text{base}} = \frac{KV_{dc}}{\sqrt{3}}. \quad (3.21)$$

The relation to the nominal rms phase voltage V_N is obtained for $K = 1/\sqrt{2}$

$$V_N = \frac{V_{dc}}{\sqrt{6}}. \quad (3.22)$$

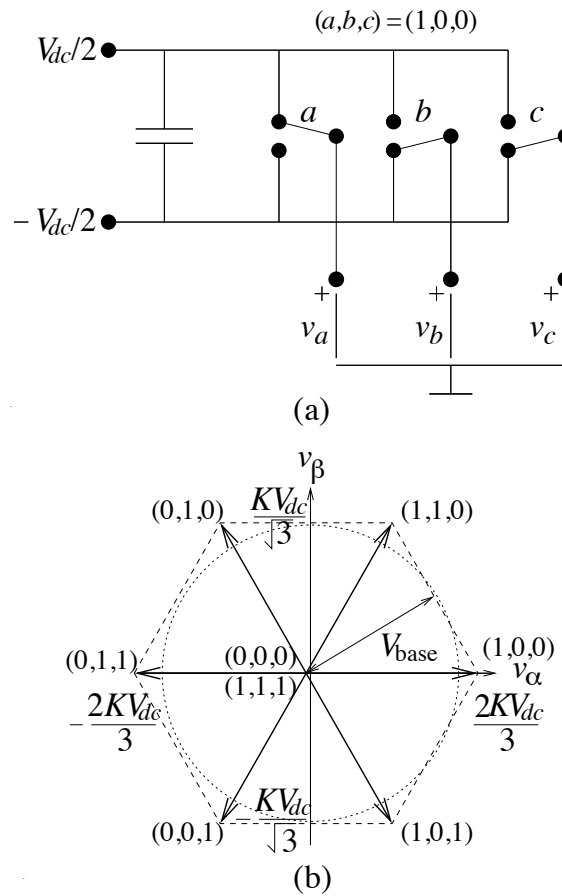


Figure 3.15. (a) Change-over switch model for a three-phase VSC. (b) Space-vector diagram.

PROBLEM 3.10

Suppose that a VSC is fed from a three-phase grid via a diode rectifier. What is the maximum relation between the converter output phase voltage and the grid phase voltage?

PROBLEM 3.11

The vector

$$\mathbf{v}^s = \frac{KV_{dc}}{2\sqrt{3}} e^{j30^\circ}$$

can be created in mean by the switching sequence

$$(0, 0, 0) - (1, 0, 0) - (1, 1, 0) - (1, 1, 1) - (1, 1, 0) - (1, 0, 0) - (0, 0, 0).$$

Determine the percentage of the switching period each switching state should be applied.

Hint: As we shall soon see, it is useful to create the zero vector by switching $(0, 0, 0)$ and $(1, 1, 1)$ equally long times.

PROBLEM 3.12

Suggest a switching sequence by which the vector

$$\mathbf{v}^s = \frac{3KV_{dc}}{4\sqrt{3}} e^{j210^\circ}$$

can be created in mean. Also determine the percentage of the switching period each switching state should be applied.

PROBLEM 3.13

Sketch within the space-vector hexagon the vector obtained in mean by the switching sequence (where the percentages are the applications of each vector relative the switching period)

$$(0,0,0) [10\%] - (0,0,1) [20\%] - (1,0,1) [10\%] - (1,1,1) [20\%] - \\ (1,0,1) [10\%] - (0,0,1) [20\%] - (0,0,0) [10\%].$$

3.3.1 Suboscillation Method

In Section 3.2 we used the suboscillation method for PWM of a single-phase VSC. Extension to a three-phase VSC, given the phase reference signals $s_{a,b,c}$, is straightforward. As for the single-phase VSC, these reference signals are confined to the interval $[-1, 1]$. Three comparators, one for each phase leg, are constructed. The mean phase voltages that result can be computed similarly to (3.11), but since the phase voltages are defined relative the neutral point, we need to substitute $V_{dc} \rightarrow V_{dc}/2$

$$v_{a,b,c} = \frac{1}{T} \left[t_+^{a,b,c} \frac{V_{dc}}{2} + t_-^{a,b,c} \left(-\frac{V_{dc}}{2} \right) \right] = \frac{s_{a,b,c} V_{dc}}{2}. \quad (3.23)$$

This results in the following voltage space vector:

$$\begin{bmatrix} v_\alpha \\ v_\beta \end{bmatrix} = K \begin{bmatrix} \frac{2}{3} & -\frac{1}{3} & -\frac{1}{3} \\ 0 & \frac{1}{\sqrt{3}} & -\frac{1}{\sqrt{3}} \end{bmatrix} \begin{bmatrix} v_a \\ v_b \\ v_c \end{bmatrix} = \frac{KV_{dc}}{2} \begin{bmatrix} \frac{2}{3} & -\frac{1}{3} & -\frac{1}{3} \\ 0 & \frac{1}{\sqrt{3}} & -\frac{1}{\sqrt{3}} \end{bmatrix} \begin{bmatrix} s_a \\ s_b \\ s_c \end{bmatrix}. \quad (3.24)$$

So, if the reference signals $s_{a,b,c}$ are calculated from the voltage reference vector $\mathbf{v}_{\text{ref}}^s = v_\alpha^{\text{ref}} + jv_\beta^{\text{ref}}$ as

$$\begin{bmatrix} s_a \\ s_b \\ s_c \end{bmatrix} = \frac{2}{KV_{dc}} \begin{bmatrix} 1 & 0 \\ -\frac{1}{2} & \frac{\sqrt{3}}{2} \\ -\frac{1}{2} & -\frac{\sqrt{3}}{2} \end{bmatrix} \begin{bmatrix} v_\alpha^{\text{ref}} \\ v_\beta^{\text{ref}} \end{bmatrix} = \frac{2}{\sqrt{3}V_{\text{base}}} \begin{bmatrix} 1 & 0 \\ -\frac{1}{2} & \frac{\sqrt{3}}{2} \\ -\frac{1}{2} & -\frac{\sqrt{3}}{2} \end{bmatrix} \begin{bmatrix} v_\alpha^{\text{ref}} \\ v_\beta^{\text{ref}} \end{bmatrix} \\ = \frac{1}{V_{\text{base}}} \begin{bmatrix} \frac{2}{\sqrt{3}} & 0 \\ -\frac{1}{\sqrt{3}} & 1 \\ -\frac{1}{\sqrt{3}} & -1 \end{bmatrix} \begin{bmatrix} v_\alpha^{\text{ref}} \\ v_\beta^{\text{ref}} \end{bmatrix} \quad (3.25)$$

we obtain $\mathbf{v}^s = \mathbf{v}_{\text{ref}}^s$ in mean.

3.3.2 Symmetrical Suboscillation Method

The three-phase suboscillation method is associated with a problem. Suppose that $\mathbf{v}_{\text{ref}}^s = V_{\text{base}}$. Equation (3.25) then yields $s_a = 2/\sqrt{3}$ and $s_b = s_c = -1/\sqrt{3}$. But $s_a > 1$, so the reference signal exceeds the triangular carrier signal, leading to so-called overmodulation, which gives highly distorted voltages. Apparently, the maximum permissible vector modulus is $\sqrt{3}V_{\text{base}}/2 = 0.87V_{\text{base}}$, since then $s_a = 1$. The area which can be accessed by the suboscillation method is depicted in Figure 3.16.

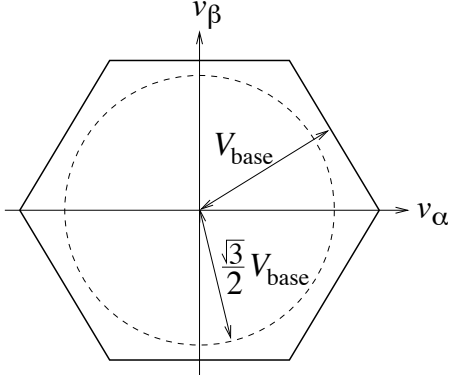


Figure 3.16. Voltage limitation for the suboscillation method: only vectors within the dashed circle can be generated (maximum modulus: $\sqrt{3}V_{\text{base}}/2$).

To circumvent the problem of reduced output voltage associated with the suboscillation method, zero-sequence components can be added to the reference signals. As discussed previously, this does not result in zero-sequence currents as long as the Y point is ungrounded. Several variants for zero-sequence addition have been proposed. One variant that is intuitive as well as simple to implement is known as the symmetrical suboscillation method, which will now be described.

First, we observe that if the same deviation Δ is subtracted from all reference signals, giving $s'_{a,b,c} = s_{a,b,c} - \Delta$, a zero-sequence component is added. The resulting voltage space vector is then not altered. The key to extending the modulation range to the entire hexagon is to select Δ so that

$$\max(s'_a, s'_b, s'_c) = -\min(s'_a, s'_b, s'_c). \quad (3.26)$$

This implies selecting

$$\Delta = \frac{\max(s_a, s_b, s_c) + \min(s_a, s_b, s_c)}{2} \quad s'_{a,b,c} = s_{a,b,c} - \Delta. \quad (3.27)$$

The method makes the reference signals symmetric with respect to the maximum and minimum values; hence, its name [79].

Example 3.1 Let us consider the case $\mathbf{v}_{\text{ref}}^s = \sqrt{3}V_{\text{base}}/2$, i.e., the maximum space vector which can be generated using the standard suboscillation method. This yields the reference signals $s_a = 1$, $s_b = s_c = -1/2$. From (3.27) we get $\Delta = (1 - 1/2)/2 = 1/4$ and $s'_a = 3/4$, $s'_b = s'_c = -3/4$. The reference signals are now symmetrized. Figure 3.17 illustrates the method in the time domain.

It is seen that (s_a, s_b, s_c) and (s'_a, s'_b, s'_c) both yield the same space vector (in mean). The difference between them is how the zero vector is generated. For (s_a, s_b, s_c) , the zero vector is applied by switching $(1, 1, 1)$ in the middle of the switching interval. For (s'_a, s'_b, s'_c) , three zero vectors are generated: at the beginning and the end of the switching interval by switching $(0, 0, 0)$, and in the middle by switching $(1, 1, 1)$. The total time the zero vector is applied is equal in the two cases. However, for the choice (s'_a, s'_b, s'_c) , we see that the reference signals can be further increased by $1/4$ before the edges of the triangular carrier signal are touched. Then $(s'_a, s'_b, s'_c) = (1, 0, 0)$, and the maximum voltage vector is obtained.

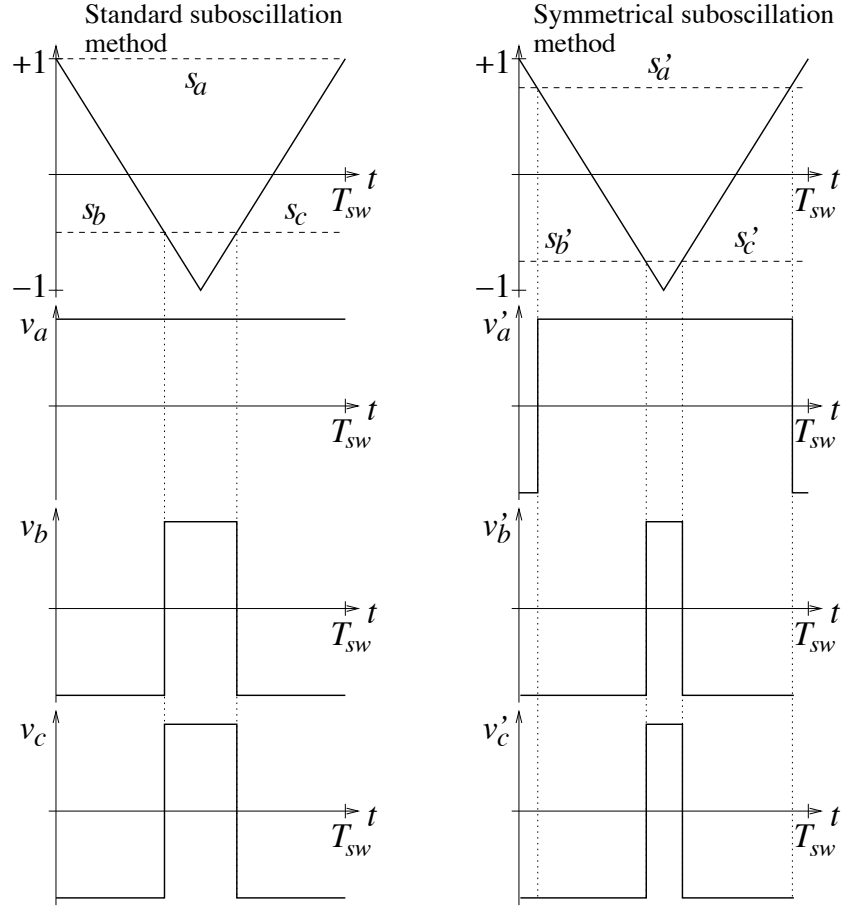


Figure 3.17. Two choices of the reference signals which yield the same space vector in mean.



3.3.3 Prevention of Overmodulation

The symmetrical suboscillation method allows the entire hexagon to be accessed. Yet, overmodulation will result should any of the reference signals (s'_a, s'_b, s'_c) exceed the interval $[-1, +1]$. In

that case, (s'_a, s'_b, s'_c) must be scaled such that the maximum value equals 1

$$m = \max(s'_a, s'_b, s'_c); \quad \text{if } m > 1 : \quad s'_{a,b,c} \rightarrow s'_{a,b,c}/m \quad (3.28)$$

or simpler

$$s'_{a,b,c} \rightarrow \frac{s'_{a,b,c}}{\max(1, s'_a, s'_b, s'_c)}. \quad (3.29)$$

This has the effect of reducing the modulus of the resulting voltage space vector without modifying its angle. This is called the minimum phase error method and is one of many ways of selecting the voltage vector in order to prevent overmodulation. One benefit of this method is that it obviously is very simple to implement. An alternative is the minimum magnitude error method. Both are illustrated in Figure 3.18; for more details, see [37]. The voltage reference vector that results from application of the described method is denoted as \bar{v}_{ref}^s and is called the realizable or saturated reference. Since the algorithm which performs the vector modulus reduction is an integral part of the PWM generation, the following notation is used:

$$\bar{v}_{\text{ref}}^s = \text{PWM}(\mathbf{v}_{\text{ref}}^s). \quad (3.30)$$

Reduced vector modulus, i.e., $|\bar{v}_{\text{ref}}^s| < |\mathbf{v}_{\text{ref}}^s|$, is known as operation in the saturated region.

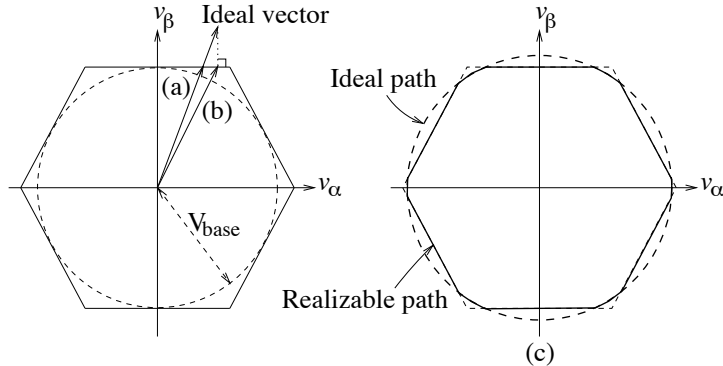


Figure 3.18. Prevention of overmodulation. Realizable vectors for (a) minimum phase error method, and (b) minimum magnitude error method. (c) Ideal (circular) and realizable (distorted) vector paths.

Algorithm 3.1 shows PWM using the symmetrical suboscillation and minimum phase error methods. In addition to the modified reference signals (s'_a, s'_b, s'_c) it also computes the components of the realizable space vector $\bar{v}_{\text{ref}}^s = \bar{v}_\alpha^{\text{ref}} + j\bar{v}_\beta^{\text{ref}}$.

Algorithm 3.1**Three-Phase PWM Using the Symmetrical Suboscillation and Minimum Phase Error Methods**

$$\begin{bmatrix} s_a \\ s_b \\ s_c \end{bmatrix} = \frac{1}{V_{\text{base}}} \begin{bmatrix} \frac{2}{\sqrt{3}} & 0 \\ -\frac{1}{\sqrt{3}} & 1 \\ -\frac{1}{\sqrt{3}} & -1 \end{bmatrix} \begin{bmatrix} v_{\alpha}^{\text{ref}} \\ v_{\beta}^{\text{ref}} \end{bmatrix}$$

$$s'_{a,b,c} = s_{a,b,c} - \frac{\max(s_a, s_b, s_c) + \min(s_a, s_b, s_c)}{2}$$

$$s'_{a,b,c} = \frac{s'_{a,b,c}}{\max(1, s'_a, s'_b, s'_c)}$$

$$\begin{bmatrix} \bar{v}_{\alpha}^{\text{ref}} \\ \bar{v}_{\beta}^{\text{ref}} \end{bmatrix} = V_{\text{base}} \begin{bmatrix} \frac{1}{\sqrt{3}} & -\frac{1}{2\sqrt{3}} & -\frac{1}{2\sqrt{3}} \\ 0 & \frac{1}{2} & -\frac{1}{2} \end{bmatrix} \begin{bmatrix} s'_a \\ s'_b \\ s'_c \end{bmatrix}$$

3.3.4 Digital Implementation Using Synchronous Sampling

PWM with synchronous sampling for a three-phase VSC can be implemented on a per-phase basis, following the principles outlined in Paragraph 3.3.4. That is, three timers, one for each phase modulator, are needed. Implementing the symmetrical suboscillation method digitally yields a PWM scheme which is equivalent or closely related to the space-vector-modulation method proposed by Holtz, see [10, Chapter 3]. However, by using both space vectors and three-phase quantities for computation of the countdown times, a much simpler algorithm is obtained compared to a direct implementation of space vector modulation.

PROBLEM 3.14

In Figure 3.19, switching waveforms of a three-phase PWM converter are shown.

- What is the switching frequency?
- The switching waveforms reveal that three different space vectors are generated, each one during a couple of switching periods. Then, the vector is changed. Determine at which time instants this happens, and plot the vectors in an $\alpha\beta$ plane (PWM hexagon).

PROBLEM 3.15

A three-phase VSC employs the symmetrical suboscillation method for PWM. The switching frequency is 1 kHz. In Figure 3.20, the instantaneous output voltage vector in the $\alpha\beta$ plane is shown (as dots, one dot per vector generated over one switching period). Peak-value scaling is used ($K = 1$).

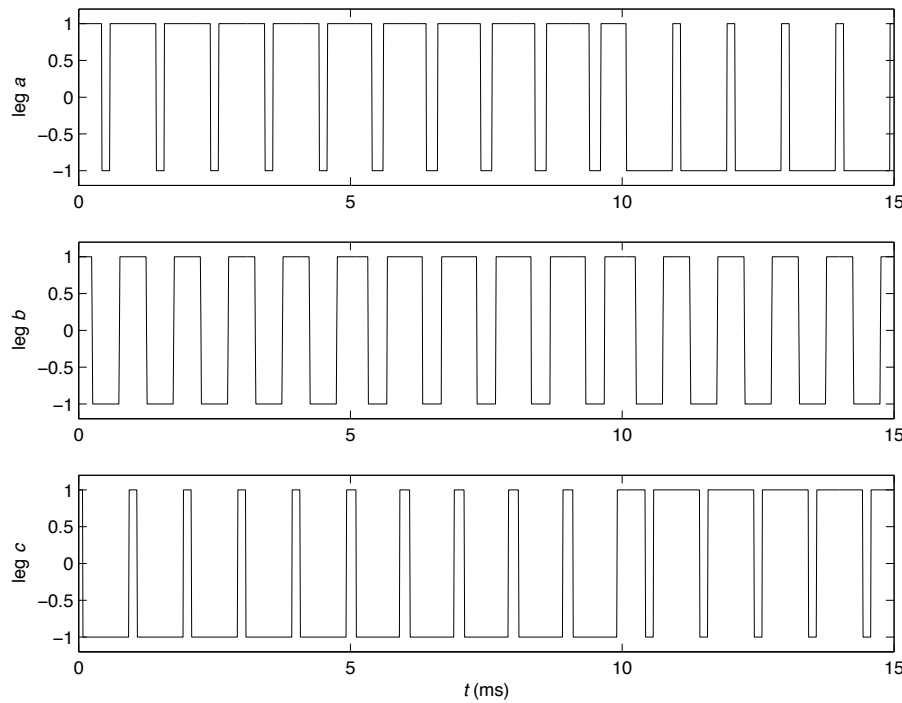


Figure 3.19. Switching waveforms.

- In Figure 3.20(a), the output voltage is a stationary sinusoid (considering the fundamental frequency component). What are its frequency and rms value?
- Figure 3.20(b) illustrates a vector diagram for an ac motor drive, where the motor is accelerating. Determine approximately the start and stop frequencies, and how long the acceleration takes.
- What is the converter's dc-link voltage?
- Sketch the switching waveforms during one switching period for the marked vector!

PROBLEM 3.16

For a three-phase VSC, Figure 3.21 shows the reference signals (to the triangular-carrier comparator) during one switching period at three different time instants.

- What is the switching frequency?
- For each of the three time instants, sketch the switching waveforms over one switching period, as well as the voltage vector which is generated in mean.
- What is the fundamental frequency of the voltage?

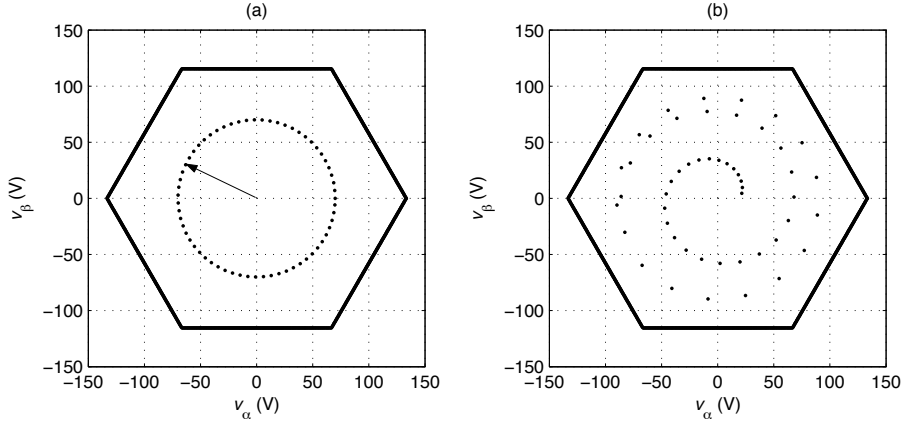


Figure 3.20. Vector diagrams.

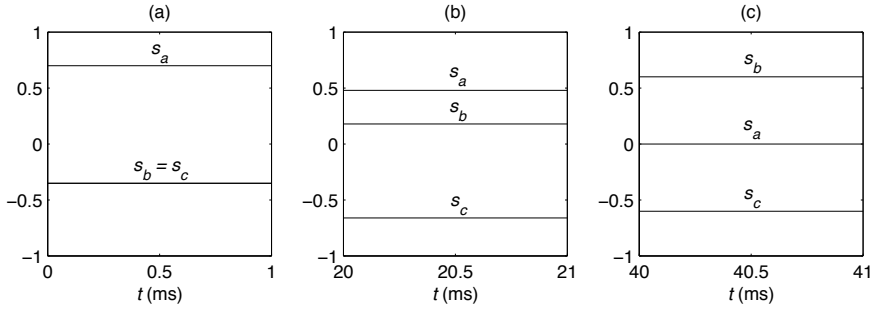


Figure 3.21. Reference signals.

3.3.5 Switching Harmonics

The amount of subharmonics that result from PWM is significantly reduced if the pulse number $m_f = f_{sw}/f_1$, i.e., the quotient between the switching and fundamental frequencies, is selected as an integer. This is called synchronized switching. For even-order harmonics to be avoided the pulse number should be odd. It is particularly important to use synchronous switching when the switching frequency is low; as a rule of thumb for $m_f < 21$.

Synchronous switching is relatively straightforward to implement for grid-connected VSCs, where the fundamental frequency is near constant. For variable-speed ac drives on the other hand, a varying switching frequency is required. The switching frequency should be confined between a lower limit and an upper limit. The solution is to vary the pulse number on line. Figure 3.22 shows a typical example thereof. For low f_1 , a constant switching frequency is used: $f_{sw} = 500$ Hz. This is followed by $m_f = 21$, $m_f = 15$, and $m_f = 9$ as the fundamental frequency increases. The change in modulation ratio occurs when f_{sw} reaches the maximum switching frequency, in this example 1000 Hz.

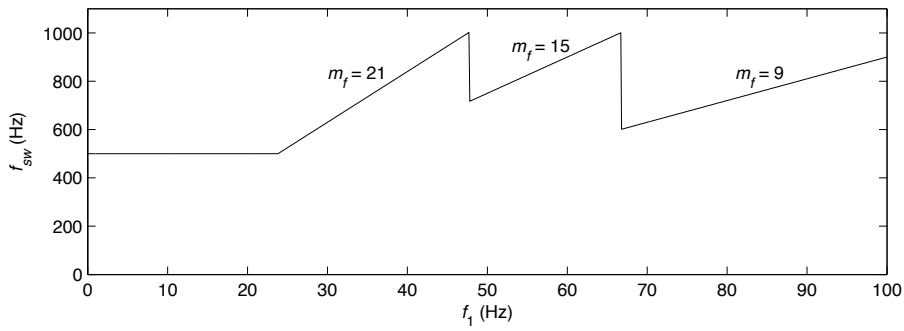


Figure 3.22. Synchronized switching: the switching frequency is selected as a multiple of the fundamental frequency (except for low fundamental frequencies).

CHAPTER 4

DC Motor Drives

DC motor drives may today be somewhat obsolete, but they are not unimportant to study. One—and perhaps the strongest—reason is that dc motor drives are conceptually much easier to grasp than ac motor drives. The models involve scalar quantities, whereas for ac drives vector models have to be used. For this reason it convenient to introduce topics that are important also for ac motor drives, such as dynamic models, current control, speed control, etc., in the context of dc motor drives. Many of the introduced models and control methods can be extended to ac motor drives by making generalizations from scalar to vector quantities, as will be shown in the subsequent chapters. Much can be gained from a pedagogical standpoint by starting at the dc motor drives end.

After a brief study of the mechanics for rotational motion, we in this chapter derive from electromagnetic theory a model for the dc motor. The open-loop dynamics are studied, and the benefit of using closed-loop current control in variable-speed drives is explained. We then proceed with current and speed controller designs.

4.1 Mechanics for Rotational Motion

From basic mechanics we know that to make a body with mass m move, a force F must be applied. An acceleration a , given by

$$a = \frac{F}{m} \quad (4.1)$$

then results. This sets the body in motion with a velocity (speed) v , given by

$$v = \int a dt = \frac{1}{m} \int F dt \Leftrightarrow m \frac{dv}{dt} = F \quad (4.2)$$

yielding in turn the position x

$$x = \int v dt \Leftrightarrow \frac{dx}{dt} = v. \quad (4.3)$$

The power P is the incremental work Fdx performed over the incremental time dt

$$P = F \frac{dx}{dt} = Fv. \quad (4.4)$$

The above equations are valid for a system in linear motion. For a system in rotational motion, the following closely related relations apply:

$$a_r = \frac{\tau}{J} \quad (4.5)$$

$$\omega = \int a_r dt = \frac{1}{J} \int \tau dt \Leftrightarrow J \frac{d\omega}{dt} = \tau \quad (4.6)$$

$$\theta = \int \omega dt \Leftrightarrow \frac{d\theta}{dt} = \omega \quad (4.7)$$

$$P = \tau \frac{d\theta}{dt} = \tau \omega \quad (4.8)$$

where τ is the torque, $a_r = \dot{\omega}$ is the angular acceleration, ω is the angular speed, θ is the angle, and J is the moment of inertia. The correspondences between quantities in linear and rotational motion are summarized in Table 4.1.

Table 4.1. Correspondences between quantities for linear and rotational motion.

Linear	SI unit	Rotational	SI unit
F	N=kNm/s ²	τ	Nm=kNm ² /s ²
a	m/s ²	a_r	rad/s ²
v	m/s	ω	rad/s
x	m	θ	rad
m	kg	J	kgm ²

The moment of inertia for a rotating body is given by the volume integral

$$J = \int r^2 dm. \quad (4.9)$$

That is, every mass element of the body is weighted by the square of the radius (relative the center of rotation) for that element, and integrated over the entire volume.

Example 4.1 In electrical drives, the most common rotational object is a solid cylinder with an approximately uniform mass density ρ . The rotor of the electrical motor itself, as well as many mechanical loads, are shaped like this. Let the cylinder have radius r and axial length l . To calculate J , we sectionalize the cylinder as shown in Figure 4.1. As $dm = \rho dV$ and $dV = 2\pi r' l dr'$, the following expression is obtained:

$$J = 2\pi\rho l \int_0^r r'^3 dr' = \frac{\pi}{2} \rho lr^4.$$

Alternatively, with the total mass of the cylinder given as $m = \rho V$, where $V = \pi r^2 l$ is the total volume, we obtain

$$J = \frac{mr^2}{2}. \quad (4.10)$$

To obtain a small J , it is seen that the radius should be as small as possible. Long and slender motors ($l > r$), such that J is kept small, are therefore preferable in applications which use high speeds and/or rapid accelerations. Motors that rotate slowly, on the other hand, are often designed so that $r > l$, since it is then not important to keep J small.

To appreciate how J varies with the size of the motor, consider first a small motor, whose rotor weighs 1 kg and has a radius of 3 cm: this yields $J = 4.5 \cdot 10^{-4} \text{ kgm}^2$. The rotor of a medium-sized motor may have $m = 100 \text{ kg}$ and $r = 1 \text{ dm}$, giving $J = 0.5 \text{ kgm}^2$. A large motor, finally, may weigh 1 ton and have $r = 0.5 \text{ m}$, yielding $J = 125 \text{ kgm}^2$.

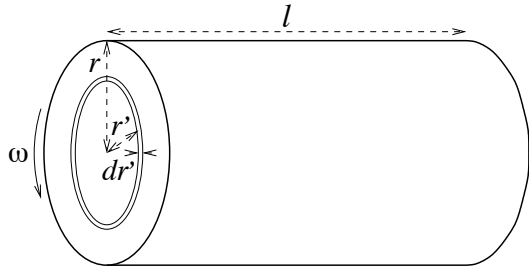


Figure 4.1. Rotating cylinder.



PROBLEM 4.1

In order for a dc motor to produce a nominal torque of 20 Nm, it has been determined that the rotor's radial surface area must be 0.3 m^2 to obtain sufficiently high flux. Select the radius and axial length of the rotor so that the nominal acceleration when the motor is not loaded mechanically is at least 50 rad/s^2 . The rotor can be assumed to have a mass density of 7500 kg/m^3 .

PROBLEM 4.2

Hollow cylinder. Find an expression similar to (4.10) for the inertia of a hollow cylinder with inner radius r_1 , outer radius r_2 , and mass m .

PROBLEM 4.3

Gearing. In many applications, a motor drives a load which consists of two or more rotating bodies interconnected by geared wheels, as in Figure 4.2(a). The gears engage at the point P. The wheels are axially coupled to rotating bodies with inertias J_1 and J_2 , respectively. Suppose that, as shown in the figure, an electrical motor applies a torque τ_e on the wheel with radius r_1 .

- Find the relation between the angular speeds ω_1 and ω_2 .
- Show that, as “seen” from the applied torque, the total inertia of the system is

$$J = J_1 + \left(\frac{r_1}{r_2} \right)^2 J_2.$$

Hint: At the point P, the peripheral speeds v_1 and v_2 are equal, as are the tangential forces F_1 and F_2 . Furthermore: $\tau = Fr$, $v = \omega r$.

PROBLEM 4.4

Hoist drive. In Figure 4.2(b), a motor with torque τ_e drives a hoist with mass m using a wheel of radius r and inertia J . The gravitational force is mg . The dynamics of the drive can be described as

$$J' \frac{d\omega}{dt} = \tau_e - \tau_l.$$

Find expressions for the equivalent inertia J' (which is larger than J due to the mass m) and the load torque τ_l . **Hint:** $\tau = Fr$, $F = m\dot{v}$, $v = \omega r$.

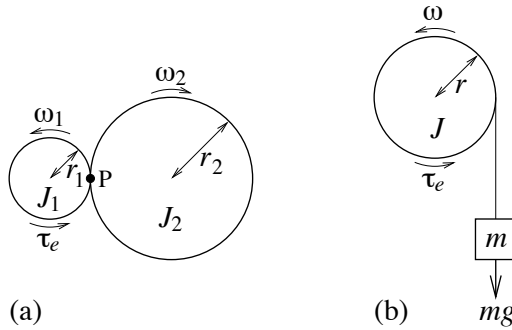


Figure 4.2. (a) Two rotating bodies interconnected by geared wheels. (b) Hoist drive.

PROBLEM 4.5

In an electrical motor drive, the mechanical load consists only of an inertia $J = 1.0 \text{ kgm}^2$. It is specified that the speed shall vary sinusoidally: $\omega = \hat{\omega} \cos \omega_0 t$, where $\hat{\omega} = 10 \text{ rad/s}$ and $\omega_0 = 200\pi \text{ rad/s}$.

- a) Determine in degrees the amplitude of the oscillation in the shaft angle θ .
- b) Determine the maximum torque that has to be supplied from the motor.
- c) Determine also the maximum and mean powers.

4.2 DC Machine Fundamentals

DC machines can be used as both motors and generators. Although the focus of the chapter is dc motor drives, we in this section nevertheless use the term “machine,” for generality.

4.2.1 Principle

The rotor, or armature, of a dc machine is cylindrical. Slots are machined in the surface, where the armature winding is placed. In Figure 4.3, two opposite conductors of the armature winding are shown. Around the rotor a magnetized stator is placed. Both the stator and the rotor can be constructed either as a solid steel forging or by using laminated steel sheets. Figure 4.3 shows a two-pole stator, magnetized by a permanent magnet. Alternatively, magnetization can be made by a separate field winding, as is further discussed in Paragraph 4.2.4.

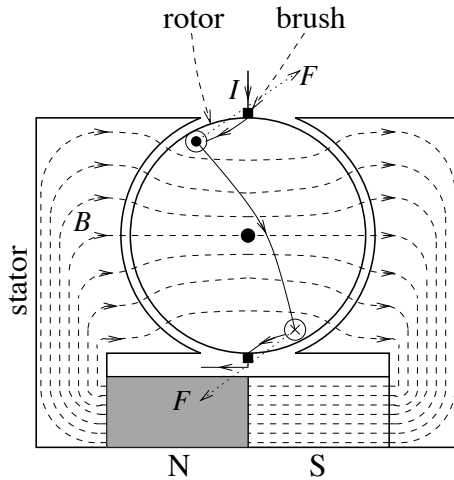


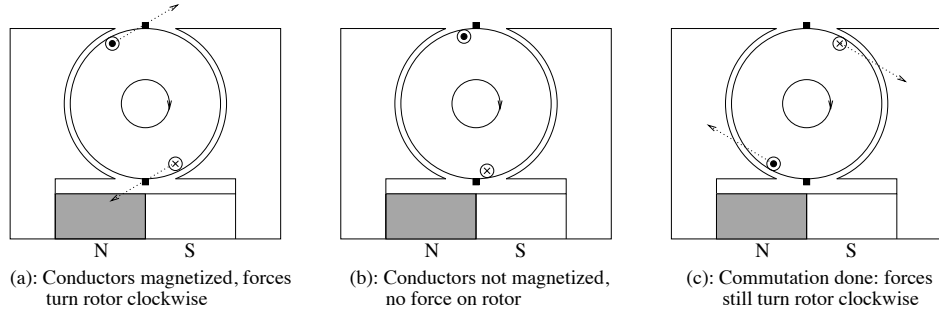
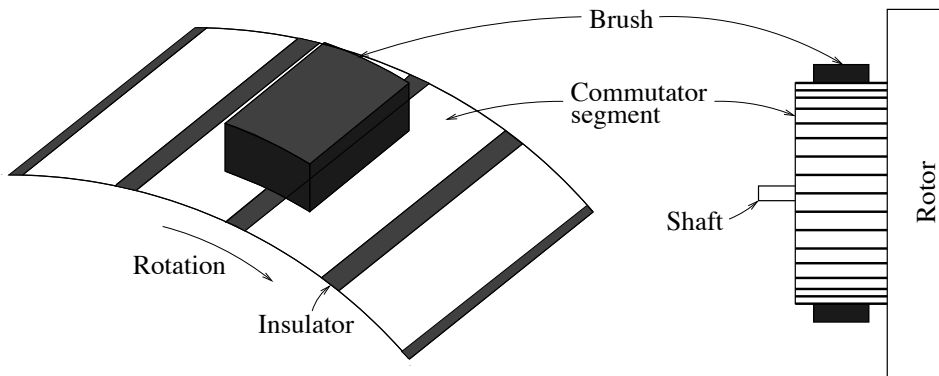
Figure 4.3. DC machine principle.

The density of the magnetic flux that crosses the airgap between the stator and the rotor is B . When a current I flows through one rotor conductor, as shown in Figure 4.3, a force $F = BIl$ starts to act on the conductor, where l is the axial length of the rotor. This force turns the rotor clockwise. Because the flux crosses the airgap perpendicularly to the rotor surface, the force on the conductor stays constant as long as the conductor is enclosed by either one of the stator poles, as shown in Figure 4.4(a). The rotor sectors which are not enclosed by the two stator poles (i.e., around each brush) are unmagnetized. When the conductor passes an unmagnetized sector, see Figure 4.4(b), then no force acts upon it. Once the conductor by the rotation of the rotor moves within the opposite stator pole, if the direction the current is kept, then a force that counteracts the rotation will result. Therefore, the direction of the current must be changed when the conductor passes the brush. This is called commutation and is illustrated in Figure 4.4(c).

In a dc motor, commutation is made by the commutator, which typically is constructed as illustrated in Figure 4.5. The armature winding consists of several coils that are placed in the rotor slots. Each coil is connected between two opposite segments of the commutator. The brushes, through which the armature current is carried, slide on the commutator, commuting as many times per revolution as there are coils. The brushes are usually made of carbon; thus they wear down, but can be replaced inexpensively. This allows the commutator—which is made of copper and therefore is costly to replace—to be kept free of wear. The need for replacing brushes regularly makes dc machines less attractive than ac machines (which do not use brushes). Also, there is a voltage drop of about 1 V across each brush, giving extra losses. (This effect is neglected in the following, however.)

4.2.2 Electrical Model

Let the stator and rotor dimensions be given by Figure 4.6. Furthermore, let us assume that the rotor has a total of N turns in its series-connected coils. There are two parallel paths in the winding, so each of the $2N$ conductors (exemplified by $2N = 32$ in Figure 4.6) carries the

**Figure 4.4.** Principle of commutation.**Figure 4.5.** Commutator.

current $i/2$.¹ A force $Bil/2$ thus acts on each magnetized conductor. Assuming that the number of conductors is fairly large, we can calculate the number of magnetized conductors as the quotient between total pole span $2w$ and the rotor circumference $2\pi r$. Hence, the total force F that acts on the rotor is given by

$$F = \frac{2w}{2\pi r} 2NB \frac{i}{2} l = \frac{NBwl}{\pi r} i. \quad (4.11)$$

But wl is the cross-sectional area of each pole, and, since magnetic flux Φ is flux density times cross-sectional area, we have $\Phi = Bwl$. This yields the simplified expression

$$F = \frac{N\Phi}{\pi r} i. \quad (4.12)$$

The electrical torque τ_e produced by the machine is related to the total force as $\tau_e = Fr$, so

$$\tau_e = \psi i, \quad \psi = \frac{N\Phi}{\pi}. \quad (4.13)$$

Here, we have introduced a new quantity: the flux linkage ψ , which is the actual flux scaled by the number of turns (and $1/\pi$; a difference compared to the standard definition of flux linkage). By

¹We from now on assume that the armature current is time varying (but constant in the steady state), so i is used rather than I .

using flux linkage rather than actual flux, we avoid dragging the factor N/π along in the equations. Flux linkage (in various forms) will be used frequently in the following, also for ac machines. Quite often, we for simplicity drop “linkage” and refer to ψ only as “flux.”

It is also well known that, if a conductor of length l is moved with velocity v in a magnetic field with flux density B , then a voltage Blv is induced across the conductor. Therefore, once the machine starts rotating, an induced voltage will appear across the armature winding. Let the angular rotor speed be ω_r . Then, $v = \omega_r r$, so across each magnetized conductor, an induced voltage $Bl\omega_r r$ appears. No voltage is induced in the conductors that are not magnetized, so the total induced voltage—which is also known as the back emf—is given by

$$E = \frac{2w}{2\pi r} N Bl\omega_r r = \psi\omega_r. \quad (4.14)$$

Note the similarity to the torque equation (4.13): the only difference is that i is replaced by ω_r .

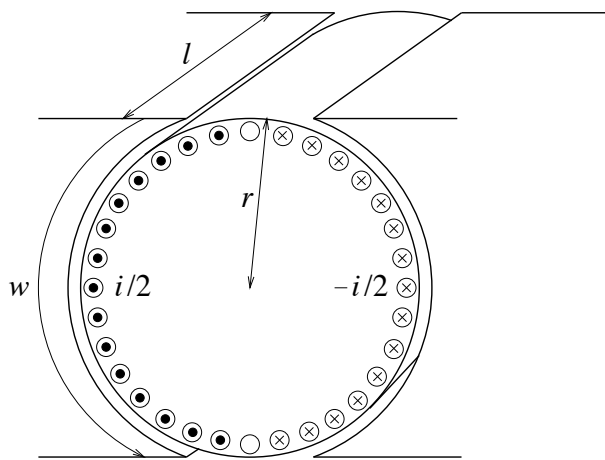


Figure 4.6. DC machine with 32 rotor slots and stator/rotor dimensions.

PROBLEM 4.6

For the machine in Problem 4.1, $w/\pi r = 80\%$. How many turns N are required for the machine to produce the desired torque 20 Nm if the nominal armature current is 20 A and $B = 1.5$ T?

PROBLEM 4.7

$E = \psi\omega_r$ can also be derived from the relation $\tau_e = \psi i$ and “power = angular speed \times torque.” Do that!

4.2.3 Dynamic Model

We are now ready for the final model of the dc machine, which is simply the back emf in series with an inductance and a resistance. This is simply because coils—which have resistive losses—wound around an iron core also become inductive. So, the complete dc machine model is that given by the equivalent circuit of Figure 4.7.

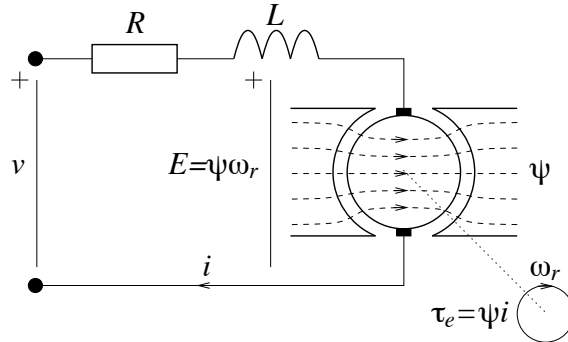


Figure 4.7. Equivalent circuit for the dc machine.

From the equivalent circuit it is straightforward to write down the dynamic equations for the machine. Suppose that a voltage v is applied across the machine terminals. Then the electrical dynamics are given by

$$v - Ri - L \frac{di}{dt} = E = \psi\omega_r. \quad (4.15)$$

Furthermore, the mechanical dynamics are

$$J \frac{d\omega_r}{dt} = \tau_e - \tau_l = \psi i - \tau_l \quad (4.16)$$

where τ_l is the load torque and J is the total inertia of the rotor and the mechanical load. Normally, the load torque increases with the speed. As a simplification, let us temporarily assume that the load torque is proportional to the speed as $\tau_l = b\omega_r$, where b is called the viscous damping constant. The machine model then becomes linear

$$L \frac{di}{dt} = v - Ri - \psi\omega_r \quad (4.17)$$

$$J \frac{d\omega_r}{dt} = \psi i - b\omega_r. \quad (4.18)$$

We see that the electrical and mechanical dynamics are interlinked: the back emf $\psi\omega_r$ links (4.18) to (4.17) and the electrical torque ψi vice versa. How this affects the total dynamics will be investigated in Section 4.3.

4.2.4 Magnetization by Field Winding

Figure 4.3 shows the stator to be magnetized by a permanent magnet. Although this is common for machines of lower power ratings (1 kW and below), the flux is more commonly supplied by a separate field winding, carrying the field current (or magnetizing current) i_f , as illustrated in Figure 4.8(a). The relation between i_f and ψ can be expressed as

$$\psi = f(i_f), \quad \frac{f(i_f)}{i_f} = L_f \quad (4.19)$$

where L_f is called the field-winding inductance. For smaller values of i_f the relation to ψ is linear, i.e., L_f is constant. However, as i_f increases the iron enters saturation, leading to a decreasing

L_f . The field current is normally selected such that the iron gets only slightly saturated, as shown in Figure 4.8(b), giving the base flux ψ_{base} ; also called nominal or rated flux, see further below. (Driving the iron further into saturation would create excessive losses due to a large i_f and thus substantial heating in the field circuit.)

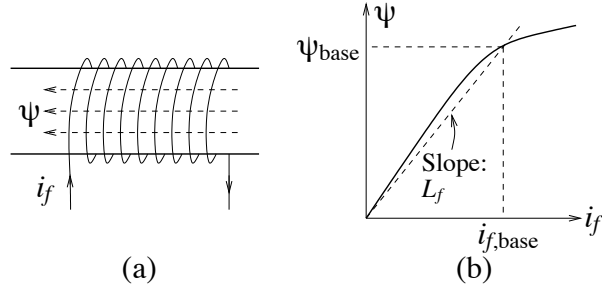


Figure 4.8. (a) Magnetization by field winding. (b) Relation field current–flux linkage.

The field winding usually has more turns than the armature winding, so in most cases, $L_f > L$ ($L_f \approx 10L$ is not unreasonable). Fast changes in the field current (and, in turn, in ψ) are therefore difficult to achieve. For quick torque changes, ψ should be kept constant and i be modified.

PROBLEM 4.8

A dc motor is driving a fan, whose load torque is 5 Nm at the nominal speed 1800 rpm. The motor is fed from a constant 200-V source. Speed control is accomplished by varying the magnetization. The inductance of the field winding is 2 H and the armature resistance is 2 Ω . Determine the field current needed to give nominal speed.

4.2.5 Rating and Base Values

Rather obviously, a dc machine of larger size will be able to produce more power than a smaller one. If one were to try squeezing significantly more power out of a machine than intended in the design, the heating due to losses in the armature winding would be excessive. Simply put, the machine would burn up. The nominal or rated (maximally allowed in the steady state) operating conditions are specified by the manufacturer on data sheets and/or the machine's so-called name plate (which is mounted on the machine housing). Let us go through the steps by which the rating in principle is set.

First, the base armature voltage V_{base} is determined. This is given by the voltage allowed between adjacent commutator segments (for machines without commutators, the winding insulation determines the limit). Clearly, bigger-sized machines can withstand higher voltage levels than smaller. If the machine is supplied from a power electronic converter, it is natural to set V_{base} to the maximum output voltage of the converter, unless this exceeds the maximum permissible armature voltage. For a single-phase VSC—see Section 3.2—this is given by the dc-link voltage, so it is logical to set $V_{\text{base}} = V_{dc}$.

Second, the base flux linkage ψ_{base} is determined, as described above.

Next, we can determine the base speed. Considering (4.17) in the steady state, we have

$$v = Ri + \psi\omega_r. \quad (4.20)$$

Normally, the resistive voltage drop Ri is much smaller than the back emf $\psi\omega_r$, especially so when the torque is low, yielding a small armature current i . Thus, we may approximate $v \approx \psi\omega_r$. From

Table 4.2. DC-machine base values.

Voltage	V_{base}	(Limited by commutator or converter)
Current	I_{base}	(Limited by power losses or converter)
Flux linkage	ψ_{base}	(Limited by magnetic saturation)
Speed	ω_{base}	$= V_{\text{base}}/\psi_{\text{base}}$
Time	t_{base}	$= 1/\omega_{\text{base}}$
Power	P_{base}	$= V_{\text{base}}I_{\text{base}}$
Torque	τ_{base}	$= P_{\text{base}}/\omega_{\text{base}}$
Impedance	Z_{base}	$= V_{\text{base}}/I_{\text{base}}$
Inductance	L_{base}	$= Z_{\text{base}}/\omega_{\text{base}}$
Inertia	J_{base}	$= \tau_{\text{base}}/\omega_{\text{base}}^2$
Viscous damping constant	b_{base}	$= \tau_{\text{base}}/\omega_{\text{base}}$

this relation the base speed is obtained as

$$\omega_{\text{base}} = \frac{V_{\text{base}}}{\psi_{\text{base}}} \quad (4.21)$$

Next to be determined is the base current. Multiplying (4.20) by i , we obtain the input–output power balance

$$\underbrace{vi}_{P_{\text{in}}} = \underbrace{Ri^2}_{P_{\text{loss}}} + \underbrace{\psi\omega_r i}_{P_{\text{out}}} \quad (4.22)$$

In general, the efficiency of a dc machine is fairly high (although not as high as for an ac machine), with $\eta = P_{\text{out}}/P_{\text{in}}$ up to 80%. Still, it is the power loss $P_{\text{loss}} = Ri^2$ that is the limiting factor, since this is converted to heat in the armature circuit. The base current I_{base} is given by

$$I_{\text{base}} = \sqrt{\frac{P_{\text{loss}}^{\max}}{R}} \quad (4.23)$$

where P_{loss}^{\max} is the maximum acceptable power loss. Furthermore, if supplied from a power electronic converter which is rated at a lower current than the machine, then this is of course what determines I_{base} . From the fundamental base values for voltage, current, and flux, an extended list of base values is shown in Table 4.2.

4.2.6 Normalization of the DC Machine Model

The dc machine model is normalized in the same fashion as described in Section 2.8. Normalization of the electrical dynamics is straightforward. Consider (4.17)

$$L \frac{di}{dt} = v - Ri - \psi\omega_r \quad (4.24)$$

Let us introduce normalized values as defined in Table 4.2

$$\left(L_n \cdot \frac{Z_{\text{base}}}{\omega_{\text{base}}} \right) \frac{d(i_n \cdot I_{\text{base}})}{d(t_n/\omega_{\text{base}})} = (v_n \cdot V_{\text{base}}) - (R_n \cdot Z_{\text{base}})(i_n \cdot I_{\text{base}}) - (\psi_n \cdot \psi_{\text{base}})(\omega_{rn} \cdot \omega_{\text{base}}). \quad (4.25)$$

But $Z_{\text{base}}I_{\text{base}} = V_{\text{base}}$ and $\psi_{\text{base}} = V_{\text{base}}/\omega_{\text{base}}$, so we obtain

$$L_n \frac{di_n}{dt_n} = v_n - R_n i_n - \psi_n \omega_{rn}. \quad (4.26)$$

As in Section 2.8, the differential equation is formally unchanged by the normalization. We now introduce normalized quantities in the mechanical dynamics (4.18)

$$J \frac{d(\omega_{rn} \cdot \omega_{\text{base}})}{dt_n/\omega_{\text{base}}} = (\psi_n \cdot V_{\text{base}}/\omega_{\text{base}})(i_n \cdot I_{\text{base}}) - b(\omega_{rn} \cdot \omega_{\text{base}}) \quad (4.27)$$

giving

$$\left(J \cdot \frac{\omega_{\text{base}}^3}{V_{\text{base}} I_{\text{base}}} \right) \frac{d\omega_{rn}}{dt_n} = \psi_n i_n - \left(b \cdot \frac{\omega_{\text{base}}^2}{V_{\text{base}} I_{\text{base}}} \right) \omega_{rn} \quad (4.28)$$

which verifies the base values for inertia and viscous damping constant in Table 4.2 and gives the following normalized equation:

$$J_n \frac{d\omega_{rn}}{dt_n} = \psi_n i_n - b_n \omega_{rn}. \quad (4.29)$$

Again, the normalized equation is formally equal to the original equation.

Example 4.2 Suppose that we have a dc machine with the following data.

Base voltage:	$V_{\text{base}} = 100 \text{ V}$
Base current:	$I_{\text{base}} = 10 \text{ A}$
Base flux:	$\psi_{\text{base}} = 2 \text{ Vs}$
Armature inductance:	$L = 60 \text{ mH}$
Armature resistance:	$R = 1 \Omega$
Inertia:	$J = 2.4 \text{ kgm}^2$
Viscous damping constant:	$b = 0.4 \text{ kgm}^2/\text{s}$

The base power is then 1 kW and the base speed is

$$\omega_{\text{base}} = \frac{V_{\text{base}}}{\psi_{\text{base}}} = 50 \text{ rad/s.}$$

We obtain the impedance base value as $Z_{\text{base}} = V_{\text{base}}/I_{\text{base}} = 10 \Omega$, giving

$$R_n = \frac{R}{Z_{\text{base}}} = 0.1 \text{ pu} \quad L_n = \frac{\omega_{\text{base}} L}{Z_{\text{base}}} = 0.3 \text{ pu.}$$

The mechanical base values are

$$J_{\text{base}} = \frac{V_{\text{base}} I_{\text{base}}}{\omega_{\text{base}}^3} = 8 \cdot 10^{-3} \text{ kgm}^2 \quad b_{\text{base}} = \frac{V_{\text{base}} I_{\text{base}}}{\omega_{\text{base}}^2} = 0.4 \text{ kgm}^2/\text{s}$$

giving

$$J_n = 300 \text{ pu} \quad b_n = 1 \text{ pu.}$$

Note the large value of the normalized inertia; one notable exception to the rule that the per-unit parameter values are in the range of 1 or below.



PROBLEM 4.9

A dc motor with base voltage, current, and flux 400 V, 50 A, and 5 Vs, respectively, has a nominal efficiency of 78%.

- a) Determine the armature resistance in pu and in ohms.
- b) Find the base speed and the speed at nominal load in rad/s.

4.3 Open-Loop Dynamics

It is now time to revisit the electrical and mechanical dynamics (4.17)–(4.18), rewritten here for clarity

$$L \frac{di}{dt} = v - Ri - \psi\omega_r \quad (4.30)$$

$$J \frac{d\omega_r}{dt} = \psi i - b\omega_r. \quad (4.31)$$

These equations correspond to the block diagram in Figure 4.9. (As we henceforth discuss only motors, we now return to the term “motor” rather than “machine.”)

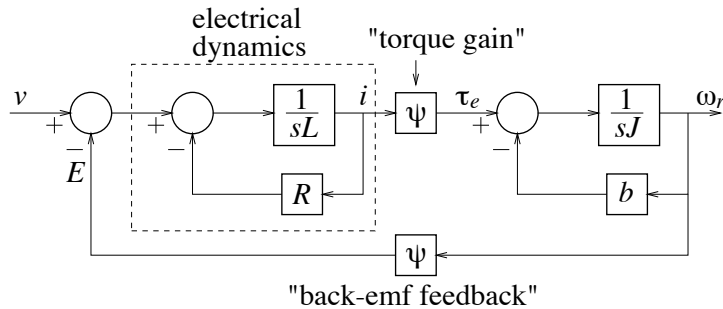


Figure 4.9. Block diagram of the dc-motor dynamics.

From this block diagram it is quite obvious that the flux ψ has the effect of interlinking the electrical and mechanical dynamics, as we already found by inspecting the equations. As feedforward there is the gain in the electrical torque, ψi , and as feedback we have the back emf $E = \psi\omega_r$. Suppose that the flux is reduced to zero, $\psi = 0$. The couplings between the electrical and the mechanical dynamics then disappear, breaking the system into two noninteracting first-order subsystems. Expressing both in the form $Tdy/dt = ku - y$, we have

$$\frac{L}{R} \frac{di}{dt} = \frac{1}{R} v - i \quad (4.32)$$

$$\frac{J}{b} \frac{d\omega_r}{dt} = -\omega_r. \quad (4.33)$$

Hence, the electrical and mechanical time constants are, respectively, given as

$$T_e = \frac{L}{R} \quad T_m = \frac{J}{b}. \quad (4.34)$$

The electrical time constant is much smaller than the mechanical: for the parameter values of Example 4.2 we have $T_e = 3$ pu and $T_m = 300$ pu, corresponding to 9.6 ms and 0.96 s, respectively, for $\omega_{\text{base}} = 50$ rad/s. Therefore, the electrical and the mechanical dynamics are on different time scales when the motor is unmagnetized. (Although we here used a particular example, this is almost always the case.)

What happens when the flux is restored to its nominal value? Based on Figure 4.9, we make the following conjectures:

- The mechanical dynamics will be speeded up as ψ increases, due to the feedback formed by the back emf.
- The electrical dynamics—forming via R an inner closed-loop system—will remain roughly the same regardless of ψ .

Let us verify this, and also find out really how fast the mechanical dynamics become. With $\mathbf{x} = [i, \omega_r]^T$, (4.30)–(4.31) can be described in state-space form as $\dot{\mathbf{x}} = \mathbf{Ax} + \mathbf{Bv}$, where

$$\mathbf{A} = \begin{bmatrix} -\frac{R}{L} & -\frac{\psi}{L} \\ \frac{\psi}{J} & -\frac{b}{J} \end{bmatrix} \quad \mathbf{B} = \begin{bmatrix} \frac{1}{L} \\ 0 \end{bmatrix}. \quad (4.35)$$

Matrix \mathbf{A} has the following characteristic polynomial:

$$\begin{aligned} \det(s\mathbf{I} - \mathbf{A}) &= \left(s + \frac{R}{L}\right) \left(s + \frac{b}{J}\right) + \frac{\psi^2}{LJ} \\ &= s^2 + \left(\frac{R}{L} + \frac{b}{J}\right)s + \frac{Rb + \psi^2}{LJ}. \end{aligned} \quad (4.36)$$

In Figure 4.10, loci for the poles are depicted, again for the parameter values of Example 4.2, as ψ varies from 0 to 1 pu. For $\psi = 0$, there is a separation of two decades between the electrical and the mechanical dynamics; the respective poles are located at $s = -1/T_e = -R/L = -0.33$ and $s = -1/T_m = -b/J = -0.0033$. As ψ increases, the slow (mechanical) pole moves away from the origin, becoming faster, whereas the fast (electrical) pole moves toward the origin, becoming slower. However, the relative movement of the fast pole is not significant; the pole stays in the vicinity of $s = -0.3$. On the other hand, the relative movement of the slow pole is as much as one decade, starting at $s = -0.0033$ and ending at $s = -0.04$. Thus, we have verified both above conjectures as true.

For most dc motors, the electrical dynamics are significantly faster than the mechanical dynamics (note in Figure 4.10 that even for $\psi = 1$ pu, the separation is one decade). Therefore, we may consider the electrical dynamics in the steady state as seen from the mechanical dynamics. The transfer function $G_e(s)$ of the electrical dynamics, from v to i in Figure 4.9, is

$$G_e(s) = \frac{1}{sL + R}. \quad (4.37)$$

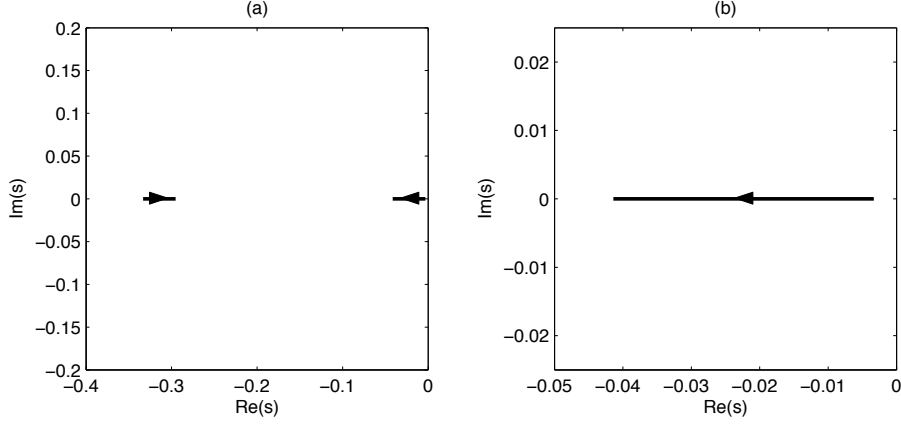


Figure 4.10. Loci for the poles of the dc motor model for $0 \leq \psi \leq 1$ pu. (a) Fast (electrical) and slow (mechanical) poles. (b) Enlarge of the slow pole.

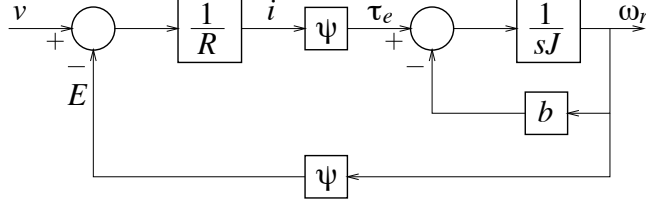


Figure 4.11. Block diagram with the electrical dynamics considered in the steady state as seen from the mechanical dynamics, obtaining a reduced-order model.

Steady state implies letting $s = 0$, so the electrical dynamics can be replaced by the steady-state gain $1/R$. See Figure 4.11.

We then arrive at the following reduced-order model for the dc motor:

$$J \frac{d\omega_r}{dt} = \frac{\psi v}{R} - \left(b + \frac{\psi^2}{R} \right) \omega_r \quad (4.38)$$

and, since $b \ll \psi^2/R$ normally,

$$RJ \frac{d\omega_r}{dt} = \psi v - \psi^2 \omega_r \quad (4.39)$$

giving the transfer function

$$G_v(s) = \frac{\psi}{sRJ + \psi^2} \quad (4.40)$$

(where the subscript v stands for “voltage input”) from v to ω_r . The pole is located at $s = -\psi^2/RJ$. At nominal flux and with $R = 0.1$ pu and $J = 300$ pu, this is equal to $s = -0.033$, which agrees with Figure 4.10(b).

Let us finally simulate a start of the dc motor in Example 4.2, with $\psi = 1$ pu. Figure 4.12 shows the result. We see that the speed rises with approximately the time constant 0.6 s, i.e., 30 pu. This is the inverse absolute value of the pole at $s = -0.033$, and thus agrees with the theoretical result. It can also be noted that the current rises fast: the time constant here is about 0.06 s (3 pu), corresponding to the electrical pole at $s = -R/L = -0.3$.

Notable is the large current peak. The reason for this is obvious: when the motor is standing still, there is no back emf. Only the armature resistance then limits the current. The peak is undesirable, however. Even though the motor itself can withstand a starting current much larger than base current—provided that the duration is short enough—it may cause the tripping of an overcurrent relay. To avoid this problem, closed-loop current control is preferably used for variable-speed dc drives. This is the topic of the next section.

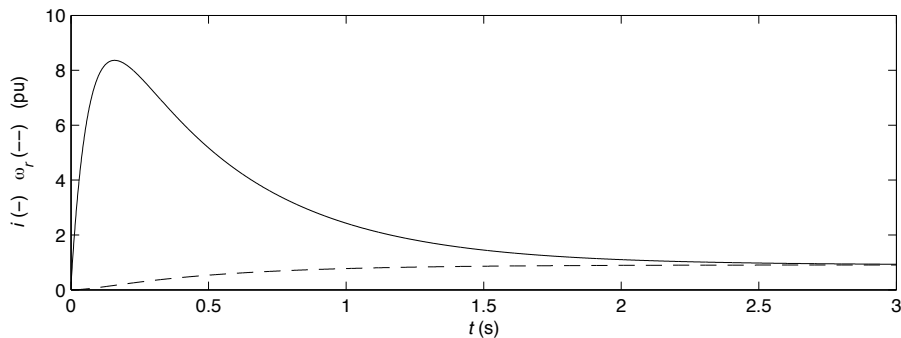


Figure 4.12. Open-loop start of a dc motor.

PROBLEM 4.10

A dc motor with armature resistance 0.3Ω is started by direct connection to a 100-V source. After 5.5 s the speed has reached 120 rad/s . The speed then settles to 150 rad/s in the steady state. Determine the total inertia and the motor's flux linkage.

PROBLEM 4.11

A dc motor with total inertia 1.8 kgm^2 and armature resistance 0.5Ω is fed from a 200-V source and is rotating with 1500 rpm . An external load torque $\tau_L = 30 \text{ Nm}$ is applied at $t = 0$. Calculate the speed at $t = 1.5 \text{ s}$. **Hint:** The dynamics (4.39) are modified to

$$RJ \frac{d\omega_r}{dt} = \psi v - R\tau_L - \psi^2 \omega_r.$$

PROBLEM 4.12

A dc motor with $R = 4 \Omega$ and $\psi = 2 \text{ Vs}$ is driving a load with a relatively high total inertia: $J = 8 \text{ kgm}^2$. The viscous damping is not negligible, but the constant b is unknown. To find b , an experiment is conducted. A 48-V source is connected to the motor's armature terminals, and the motor is allowed to accelerate, taking 15.3 s to attain 90% of the steady-state speed. Find b and the steady-state speed.

4.4 Current Control

We shall in this section study armature current control of dc motor drives. High-performance control is considered, which implies that the motor is fed from a PWM converter. Such dc motors drives are today largely obsolete, having been replaced by ac motor drives in most applications. The section thus primarily serves as an introduction to the concept of current control that will be built upon in Chapter 6, where vector current control for ac motor drives is considered.

The reasons for using closed-loop current control are to further improve the response time of the armature current i , to allow precise torque control, and (as mentioned above) to prevent i from exceeding a certain maximum allowed value (which in the steady state is I_{base} , whereas at transients a larger value I_{max} may be allowed). We have, from (4.17) (where $E = \psi\omega_r$)

$$L \frac{di}{dt} = v - Ri - E. \quad (4.41)$$

Using the transfer function (4.37), this can be expressed as the block diagram in Figure 4.13(a). Note that the back emf E enters $G_e(s)$ in the same way as the input signal v (but with opposite sign). Since the mechanical dynamics are slow, these can be disregarded as seen from the current control loop, and E treated as a disturbance. A disturbance entering the process in the same way as the control input is known as a load disturbance.

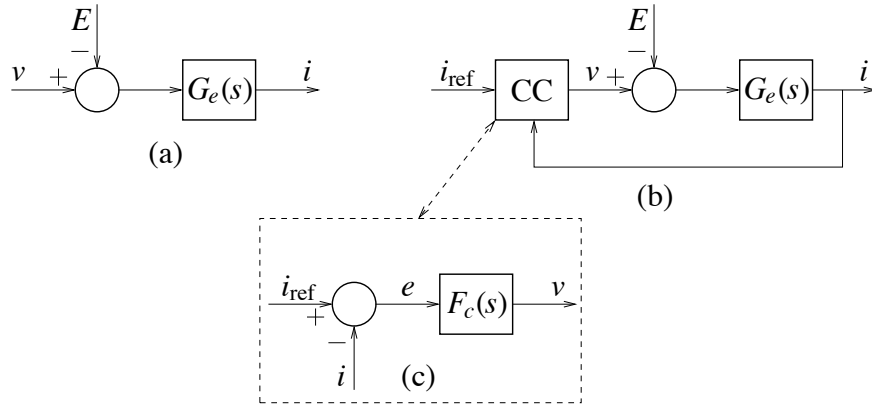


Figure 4.13. Block diagram of the electrical dynamics with $G_e(s) = 1/(sL + R)$ and the back emf E acting as load disturbance. (a) Open-loop. (b) Closed-loop (“CC” is the current controller). (c) One-degree-of-freedom PI controller.

We now close the loop around the electrical dynamics, as shown in Figure 4.13(b). The armature current i is measured and compared to the reference (setpoint) i_{ref} . The error signal $e = i_{\text{ref}} - i$ forms the input to the current controller—see Figure 4.13(c)—which manipulates the voltage v via a power electronic converter, such that i follows i_{ref} quickly and accurately.

4.4.1 One-Degree-of-Freedom Controller Design

Since the electrical dynamics are of order one, a simple PI controller is appropriate (the order of the controller need not be higher than that of the controlled process)

$$F_c(s) = k_p + \frac{k_i}{s}. \quad (4.42)$$

As the controller operates on the error e only, as shown in Figure 4.13(c) (not also on i individually), this is called a one-degree-of-freedom PI controller. (This is by far the most common type of controller used in practice. For example, it is used in more than 90% of all control loops in the process industry.)

Let us now select the controller parameters k_p and k_i . It is not uncommon that this is done by trial and error. This, however, is inconvenient. Since we know (or at least have good estimates of) the motor parameters, it is logical to use this knowledge for selecting suitable k_p and k_i . A convenient method is direct synthesis [73]. The idea is as follows. Let us start with a specification for the 10%–90% rise time t_{rc} of the closed-loop system. Typically, rise times in the millisecond range can be obtained using state-of-the-art dc–dc converters or single-phase VSCs. With $G_e(s)$ being of order one, it is apparent that a closed-loop transfer function of order one also can be obtained. Let $G_{cc}(s)$ be the closed-loop transfer function from i_{ref} to i . We now specify that $G_{cc}(s)$ (ideally) should be

$$G_{cc}(s) = \frac{\alpha_c}{s + \alpha_c} = \frac{\alpha_c/s}{1 + \alpha_c/s} \quad (4.43)$$

where α_c is the closed-loop system bandwidth. In the steady state, there should then be no control error, since $G_{cc}(0) = 1$. From (2.37) it is known that the relation between bandwidth and rise time is $\alpha_c t_{rc} = \ln 9$, so the specification for t_{rc} can be directly translated to a specification for α_c . But

$$G_{cc}(s) = \frac{F_c(s)G_e(s)}{1 + F_c(s)G_e(s)} \quad (4.44)$$

so if $F_c(s)G_e(s) = \alpha_c/s$, the desired closed-loop system (4.43) is obtained. This yields

$$F_c(s) = \frac{\alpha_c}{s} G_e^{-1}(s) = \frac{\alpha_c}{s} (sL + R) = \alpha_c L + \frac{\alpha_c R}{s}. \quad (4.45)$$

That is,

$$k_p = \alpha_c \hat{L} \quad k_i = \alpha_c \hat{R} \quad (4.46)$$

where “hats” are introduced to denote model motor parameters (which should be as close estimates of the true motor parameters as possible). The controller parameters are now expressed directly in the desired closed-loop bandwidth and the model motor parameters \hat{L} and \hat{R} , so trial-and-error steps are avoided.

Since the controller is designed using the inverse of $G_e(s)$ —(4.45)—the pole of $G_e(s)$ is canceled (ideally, if $\hat{L} = L$ and $\hat{R} = R$). The motor dynamics are “replaced by something better.” Direct synthesis is a special case of internal model control (IMC) [26, 62]. We may therefore refer to the selection (4.46) also as “IMC design.”

Example 4.3 Let us design and evaluate a current controller for the dc motor drive in Example 4.2. This time, however, the mechanical load is lighter, $J = 50$ pu. The mechanical time constant is then $J/b = 50$ pu, i.e., 1 s, giving a rise time in the rotor speed of 2.2 s. If we select the rise time in the current control loop as 22 ms (which is rather undemanding for modern power electronic converters), there is a two-decade separation between the electrical and the mechanical dynamics. Thus, in per-unit quantities, $t_{rc} = 1.1$, giving $\alpha_c = 2.2/1.1 = 2$. The controller parameters are obtained as

$$k_p = 0.6 \text{ pu} \quad k_i = 0.2 \text{ pu.}$$

We evaluate the controller by starting the motor at $t = 0$ by stepping i_{ref} from 0 to 1 pu, see Figure 4.14(a). Although the desired rise time is obtained, the result is far from satisfactory: i does not reach the reference (at least not over the time interval displayed). Below, it is explained why.

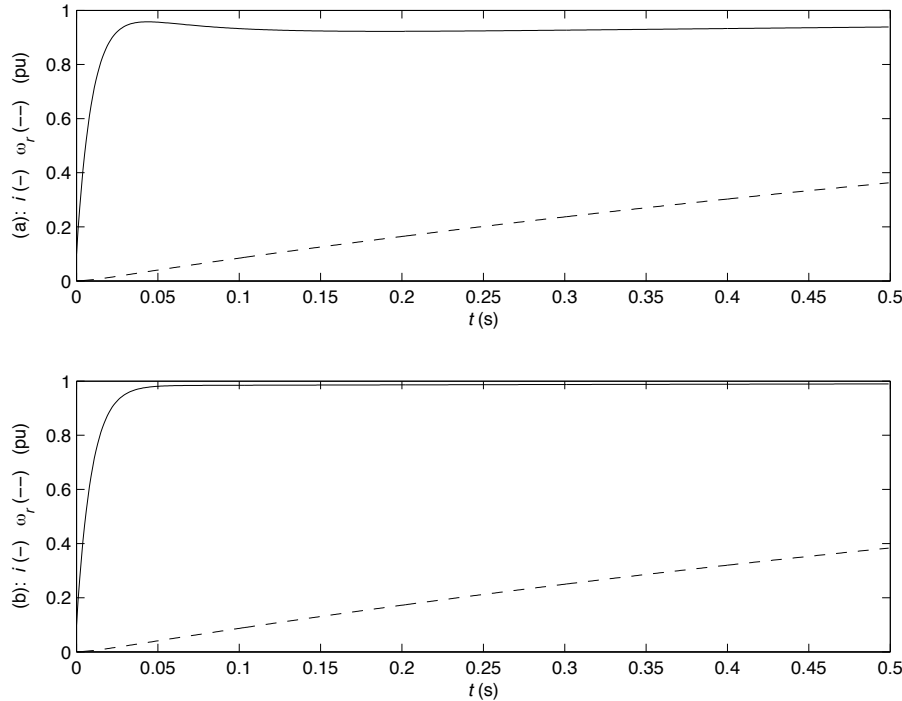


Figure 4.14. Start of a dc motor with (a) one-degree-of freedom PI current control and (b) two-degrees-of-freedom PI current control.

4.4.2 Load-Disturbance Rejection

The reason for the poor accuracy that can be observed in Figure 4.14(a) is the load disturbance caused by the back emf [cf. Figure 4.13(b)]. Let us analyze the ability of the control system to suppress a load disturbance. From Figure 4.13 the transfer function from the disturbance E to the control error e can be calculated as

$$G_{Ee}(s) = \frac{G_e(s)}{1 + F_c(s)G_e(s)} = \frac{s}{s + \alpha_c} G_e(s) = \frac{s}{s + \alpha_c} \frac{1}{sL + R}. \quad (4.47)$$

$G_{Ee}(s)$ has a zero at the origin, which implies differentiation. Therefore, a constant disturbance E will be fully rejected, but not one that is time varying. The steady-state gain from dE/dt to the control error is $[G_{Ee}(s)/s]_{s=0} = 1/\alpha_c R$. That is, if dE/dt is approximated as constant—implying that the speed varies as a ramp, which is a reasonable approximation seen over a limited time

interval—we obtain

$$e = \frac{1}{\alpha_c R} \frac{dE}{dt} = \frac{\psi}{\alpha_c R} \frac{d\omega_r}{dt}. \quad (4.48)$$

The mechanical dynamics (4.18) give

$$\frac{d\omega_r}{dt} = \frac{1}{J} (\psi i - b\omega_r) \quad (4.49)$$

and

$$e = \frac{\psi}{\alpha_c R J} (\psi i - b\omega_r). \quad (4.50)$$

Returning now to Example 4.3, approximating $i \approx 1$ pu and $\omega_r \approx 0.2$ pu (the mean value over the displayed interval), we get

$$e = \frac{1}{2 \cdot 0.1 \cdot 50} (1 - 0.2) = 0.08 \text{ pu}. \quad (4.51)$$

This agrees well with Figure 4.14(a).

Not until ω_r reaches a steady state does the current control error fully disappear. In some cases, a control error of this size (nearly 10% of the 1-pu reference step) is unimportant. Then again, in other cases—for example, when high-accuracy torque control is required—this is too large an error. Equation (4.50) allows straightforward checking.

4.4.3 Feedforward of the Back EMF

If the speed ω_r is measured, one remedy of poor load-disturbance rejection is to add a term

$$\hat{E} = \hat{\psi}\omega_r \quad (4.52)$$

to the current controller output, as shown in Figure 4.15(a). As the flux linkage is usually known with good accuracy, \hat{E} should be a good estimate of $E = \psi\omega_r$. The influence of E is thus cancelled.

Unfortunately, many dc motor drives do not use a speed sensor, because the speed easily can be estimated, as we shall see in Paragraph 4.6.1. Another method for improved disturbance rejection is then needed.

4.4.4 Two-Degrees-of-Freedom Controller Design

Poor rejection of load disturbances is characteristic for designs that involve pole cancellation, such as direct synthesis. The performance can be improved somewhat by modifying (4.46) so that the integral action increases. This, however, has the effect of giving overshoots when the reference is changed.

It is seen in (4.50) that if R could be increased, the control error would decrease. Rather than actually adding more resistance (which of course is highly undesirable, due to increased losses), we introduce an inner feedback loop as shown in Figure 4.15(a), using an “active resistance” R_a . This technique was proposed in [12].

The closed-loop system $G'_e(s)$ from v' to i is now

$$G'_e(s) = \frac{G_e(s)}{1 + R_a G_e(s)} = \frac{1}{sL + R + R_a}. \quad (4.53)$$

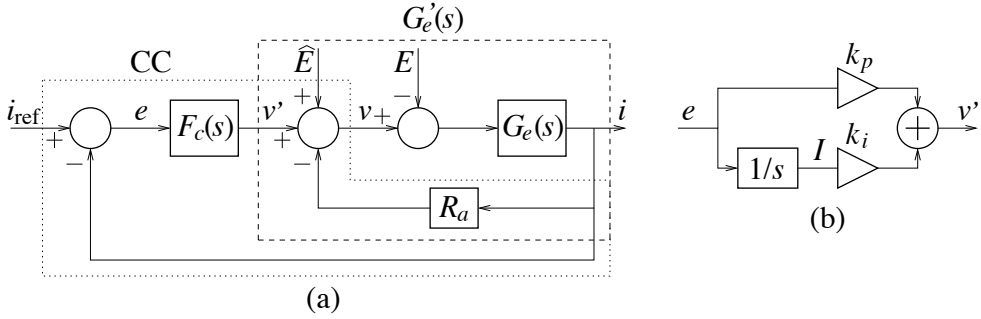


Figure 4.15. (a) Two-degrees-of-freedom current controller (CC) using an “active resistance” R_a and possibly including feedforward of the back-EMF estimate \hat{E} . $G_e(s) = 1/(sL + R)$. (b) Detail of PI controller $F_c(s)$, where I is the integrator state variable.

The resistance has in effect been increased from R to $R + R_a$, but since this is done just using signals—involving no energy transfer—there will be no additional power loss. The PI controller $F_c(s)$ —see Figure 4.15(b)—can now be designed using direct synthesis

$$F_c(s) = \frac{\alpha_c}{s} G'_e(s)^{-1} = \alpha_c \frac{sL + R + R_a}{s} = k_p + \frac{k_i}{s}. \quad (4.54)$$

That is,

$$k_p = \alpha_c \hat{L} \quad k_i = \alpha_c (\hat{R} + R_a). \quad (4.55)$$

Regarding the selection of R_a , it is useful to make the inner feedback loop $G'_e(s)$ as fast as the total closed-loop system, i.e., with bandwidth α_c . Then, R_a should be selected such that $(R + R_a)/L = \alpha_c$, giving

$$R_a = \alpha_c \hat{L} - \hat{R}. \quad (4.56)$$

This in turn yields the controller parameters

$$k_p = \alpha_c \hat{L} \quad k_i = \alpha_c^2 \hat{L}. \quad (4.57)$$

The described method yields a controller that has two inputs: the control error, but also i directly via the “active resistance.” Therefore, it is called a two-degrees-of-freedom PI controller. Note that the controller [i.e., the dotted box in Figure 4.15(a)] still fits within the structure of Figure 4.13(b).

It is straightforward to show that the control error formula (4.50) is unchanged, except that R is replaced by $R + R_a$

$$e = \frac{\psi}{\alpha_c(R + R_a)J} (\psi i - b\omega_r) \quad (4.58)$$

and, with R_a given by (4.56) (if $\hat{R} = R$ and $\hat{L} = L$),

$$e = \frac{\psi}{\alpha_c^2 LJ} (\psi i - b\omega_r). \quad (4.59)$$

Evaluating this for Example 4.3, we find that

$$e = \frac{1}{2^2 \cdot 0.3 \cdot 50} (1 - 0.2) = 0.013 \quad (4.60)$$

which is much more acceptable a value than (4.51). We also repeat the simulation of Example 4.3, obtaining the result shown in Figure 4.14(b). As can be seen, the performance is now much improved, and in agreement with the theory.

PROBLEM 4.13

Show (4.58)!

4.4.5 Voltage Saturation and Antiwindup

So far, we have treated the current control loop as an ideal, linear system. In practice, this is not correct. The armature voltage v cannot be made arbitrarily large; it is limited by an upper and a lower value. Both are determined by the rating of the power electronic converter that supplies the voltage. For a single-phase VSC the lower and upper limits are $-V_{\text{base}}$ and V_{base} , respectively. In Example 4.3—although not shown—the voltage never reached 1 pu, so no problems were encountered. However, for large steps in i_{ref} , the current controller's output signal often exceeds V_{base} , especially for higher rotor speeds when the back emf is large, requiring in turn a large armature voltage. The true voltage v is therefore becomes a saturation of the ideal voltage. We shall denote the saturation function as

$$\bar{x} = \text{sat}(x, a) = \begin{cases} -a, & x < -a \\ x, & -a \leq x \leq a \\ a, & x > a \end{cases} = \min(|x|, a) \text{sgn}(x). \quad (4.61)$$

The saturation function is illustrated in Figure 4.16(a). With v_{ref} as the ideal voltage reference (i.e., the output signal of the current controller) and \bar{v}_{ref} as the saturated voltage reference, we thus have

$$\bar{v}_{\text{ref}} = \text{sat}(v_{\text{ref}}, V_{\text{base}}). \quad (4.62)$$

Obviously, \bar{v}_{ref} rather than v_{ref} should be used as reference to the pulsewidth modulator (so $v = \bar{v}_{\text{ref}} + \text{switching harmonics}$), see Section 3.2. Because of the saturation the current control loop contains a nonlinearity, as shown in Figure 4.16(a).

Example 4.4 Let us again simulate the system of Example 4.3, this time with two-degrees-of-freedom controller design. As previously, the motor is started at $t = 0$, but now overcurrent is allowed: i_{ref} is stepped from 0 to 4 pu (it is assumed that the duration of the application of overcurrent is short enough, so that nothing goes wrong). Figure 4.17(a) shows the result. As we can see, i makes a fairly large overshoot. This occurs due to integrator windup: the integral term of the PI controller keeps accumulating the control error during the time of maximum voltage output. When i starts to get close to i_{ref} , the integrator has wound up, so v_{ref} remains large. Therefore, i shoots over i_{ref} until the windup has been worked off by accumulation of negative control error.



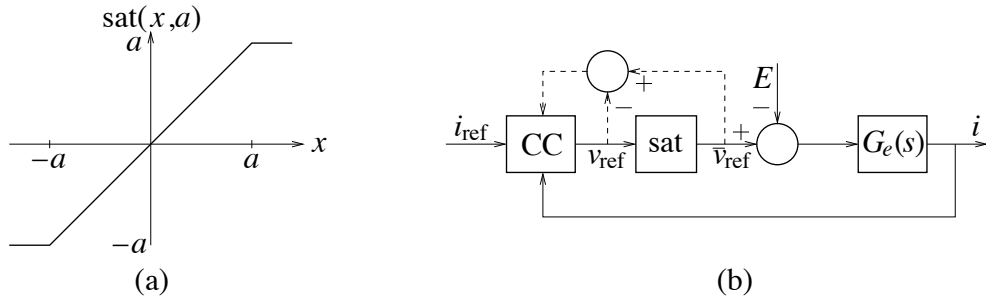


Figure 4.16. (a) Saturation function. (b) Current control loop with voltage saturation, where dashed lines indicate signal paths for “back calculation.”

“Back Calculation”

Example 4.4 illustrates well the performance degradation that typically results from integrator windup. Clearly it is important to prevent that windup occurs, and several methods have been proposed for this purpose. We shall here consider a method where the integrator input is altered from the actual control error e to a modified control error \bar{e} . Including this alteration the controller shown in Figure 4.15 can be described by the control law

$$\frac{dI}{dt} = \bar{e} \quad (4.63)$$

$$v_{\text{ref}} = k_p e + k_i I - R_a i + \hat{E} \quad (4.64)$$

$$\bar{v}_{\text{ref}} = \text{sat}(v_{\text{ref}}, V_{\text{base}}). \quad (4.65)$$

How should \bar{e} be chosen in order to prevent windup? Notice that e is still used in the proportional part, i.e., in (4.64). Yet, let us suppose for a moment that \bar{e} were used also in (4.64). Let us further assume that \bar{e} is chosen such that (4.64) with $e \rightarrow \bar{e}$ gives \bar{v}_{ref}

$$\bar{v}_{\text{ref}} = k_p \bar{e} + k_i I - R_a i + \hat{E}. \quad (4.66)$$

In other words, the modified control error \bar{e} is assumed to be such that saturated operation never is entered, instead the linear law (4.66) balances on the saturation boundary. Obviously, integrator windup then would not occur! Subtracting (4.64) from (4.66) allows us to find an expression for the modified control error as

$$\bar{e} = e + \frac{1}{k_p}(\bar{v}_{\text{ref}} - v_{\text{ref}}). \quad (4.67)$$

The method is called “back calculation,” because given the saturated reference \bar{v}_{ref} , (4.67) calculates “backwards” to obtain the modified control error \bar{e} that would be needed to balance on the saturation boundary. Notice that the modified control law (4.66) is never implemented, only the “back-calculation” algorithm (4.67), which is indicated by the dashed lines in Figure 4.16. Let us for clarity rewrite (4.63)–(4.65) with (4.67) incorporated. The control law including “back

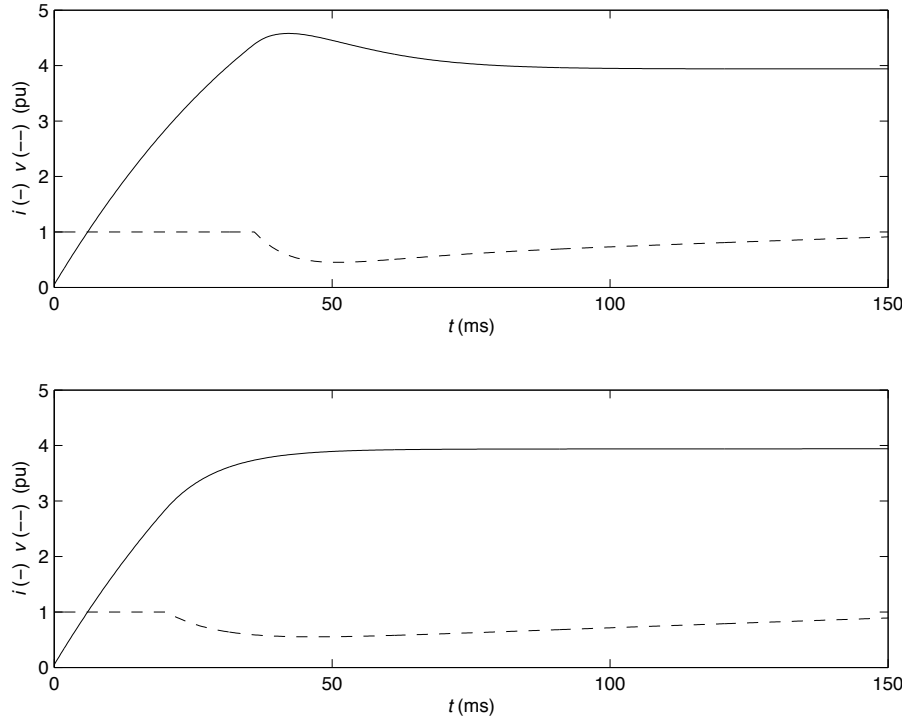


Figure 4.17. Start of dc motor with two-degrees-of freedom PI current control. (a) Without “back calculation.” (b) With “back calculation.”

calculation” is given by

$$\frac{dI}{dt} = e + \frac{1}{k_p}(\bar{v}_{\text{ref}} - v_{\text{ref}}) \quad (4.68)$$

$$v_{\text{ref}} = k_p e + k_i I - R_a i + \hat{E} \quad (4.69)$$

$$\bar{v}_{\text{ref}} = \text{sat}(v_{\text{ref}}, V_{\text{base}}). \quad (4.70)$$

Example 4.5 We repeat the simulation of Example 4.4 that gave Figure 4.17(a), this time with “back calculation” included. Performance is now acceptable, as can be observed in Figure 4.17(b).



4.4.6 Digital Implementation

Up until the early 1990s, analog implementation of control algorithms for electrical drives was state of the art. At that time, the development of microprocessors and DSPs started reaching levels that permitted digital implementation at reasonable costs. Naturally, digital implementation is preferable to analog, since the algorithms can be modified easily and nonlinear algorithms (which are frequently used in ac drives, as we shall see later) can be implemented without difficulties.

Digital implementation calls for discretization of the control algorithms derived in continuous time, see Paragraph 2.4.7. Applying the Euler method (2.79) for discretization of the integrator

(4.68), control law (4.68)–(4.70) results in Algorithm 4.1 and the block diagram shown in Figure 4.18.

Algorithm 4.1

Current Controller for DC Drives

$$\begin{aligned} e &= i_{\text{ref}} - i \\ v_{\text{ref}} &= k_p e + k_i I - R_a i + \hat{E} \\ \bar{v}_{\text{ref}} &= \text{sat}(v_{\text{ref}}, V_{\text{base}}) \\ I &= I + T_s \left[e + \frac{1}{k_p} (\bar{v}_{\text{ref}} - v_{\text{ref}}) \right] \end{aligned}$$

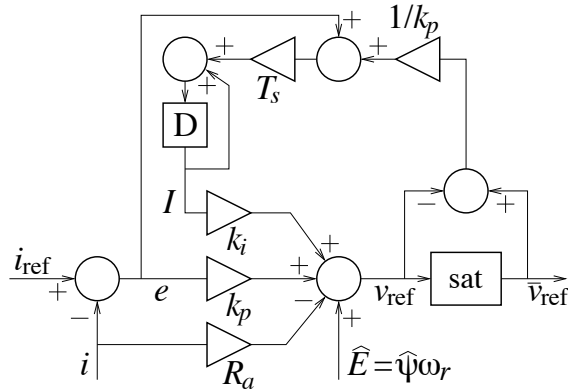


Figure 4.18. Digitally implemented two-degrees-of-freedom current controller.

4.4.7 Bandwidth Selection

The closed-loop bandwidth α_c must not be selected too high in relation to the sampling frequency, or system performance will degrade, possibly so far that instability results. In the current control loop the total time delay $T_d = 1.5T_s$, which is the sum of the controller and PWM time delays, see (3.16), must be taken into account. For a worst-case scenario, we assume a small armature resistance. The electrical dynamics, including the time delay, are then given by the transfer function

$$G_e(s)e^{-sT_d} = \frac{e^{-sT_d}}{sL}. \quad (4.71)$$

One-Degree-of-Freedom PI Control

Stability of the closed-loop system can be analyzed by applying the Nyquist criterion. The controller is given by (4.45) as $F_c(s) = (\alpha_c/s)G_e^{-1}(s)$. This yields the open-loop transfer function

$$G_k(s) = F_c(s)G_e(s)e^{-sT_d} = \frac{\alpha_c e^{-sT_d}}{s}. \quad (4.72)$$

$|G_k(j\alpha_c)| = 1$, i.e., α_c is the crossover frequency of the open-loop system. In order for the Nyquist curve not to encircle the critical point -1 , the phase angle at the crossover frequency must be larger than $-\pi$, i.e., $\arg G_k(j\alpha_c) = -\pi/2 - \alpha_c T_d > -\pi \Rightarrow \alpha_c T_d < \pi/2$. For $T_d = 1.5T_s = 3\pi/\omega_s$ we thus obtain the criterion $\alpha_c < \omega_s/6$ for asymptotic stability. The following recommendation for bandwidth selection is given:

$$\alpha_c < 0.1\omega_s \quad (4.73)$$

which gives the phase and gain margins 36° and 1.7, respectively, see Figure 4.19(a).

Two-Degrees-of-Freedom PI Control

In this case, the integral gain is set as $k_i = \alpha_c^2 L$, whereas the proportional gain is effectively doubled owing to the “active resistance” inner feedback loop. This yields the following open-loop transfer function:

$$G_k(s) = [F_c(s) + R_a]G_e(s)e^{-sT_d} = \left(2\alpha_c L + \frac{\alpha_c^2 L}{s}\right) \frac{e^{-sT_d}}{sL} = \frac{\alpha_c(2s + \alpha_c)e^{-sT_d}}{s^2}. \quad (4.74)$$

For $T_d = 1.5T_s = 3\pi/\omega_s$ it is found that the crossover frequency is now $\alpha_k = \sqrt{2 + \sqrt{5}}\alpha_c \approx 2.06\alpha_c$ and that $\alpha_c < 0.07\omega_s$ is required for asymptotic stability. The following recommendation for bandwidth selection is given:

$$\alpha_c < 0.04\omega_s \quad (4.75)$$

which gives the phase and gain margins 32° and 1.9, respectively, see Figure 4.19(b).

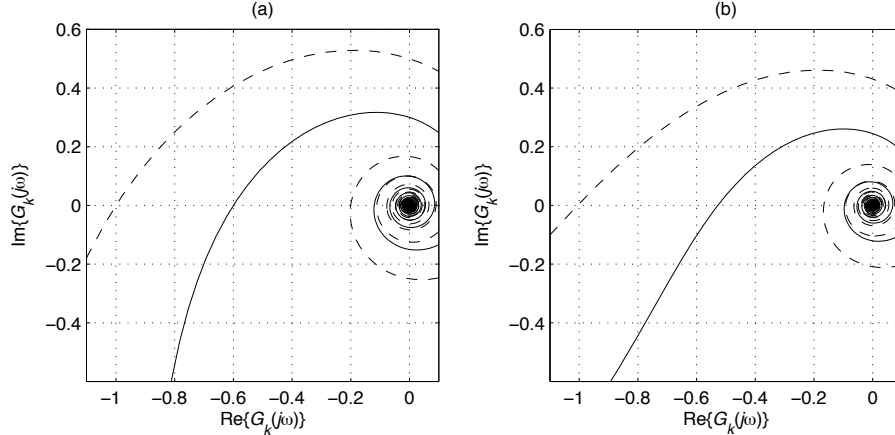


Figure 4.19. Nyquist curves for (a) one-degree-of-freedom PI control with (solid) $\alpha_c = 0.1\omega_s$ and (dashed) $\alpha_c = 0.17\omega_s$; and (b) two-degrees-of-freedom PI control with (solid) $\alpha_c = 0.04\omega_s$ and (dashed) $\alpha_c = 0.07\omega_s$.

PROBLEM 4.14

A dc motor has the following per-unit parameters: $L = 0.2$, $R = 0.1$, $\psi = 1$, $J = 200$, and $b = 0.1$. The base speed is 100 rad/s.

- Determine the efficiency $\eta = \text{output power}/\text{input power}$ at nominal speed and load.
- Determine the armature current and speed in per-unit values at nominal load if the flux is reduced such that $\psi = 0.2 \text{ pu}$.
- The drive control system for the dc motor, which uses a PWM converter with a 1-kHz switching frequency and a DSP sampling at 2 kHz, the current control law is pre-coded in the following way (excluding antiwindup and saturation):
$$v_{\text{ref}} = K_p(\beta i_{\text{ref}} - i) + K_i \int (i_{\text{ref}} - i) dt.$$

This is a two-degrees-of-freedom PI controller that uses the so-called “setpoint weighting” algorithm (factor β). The parameters are free to select by the operator. Determine the parameters such that performance identical to the two-degrees-of-freedom PI controller presented in this section is obtained.

4.5 Field Weakening

When neglecting the armature resistance, then $v = E = \omega_r \psi$ in the steady state. Since $|v|$ cannot exceed V_{base} , $|\omega_r|$ cannot exceed $V_{\text{base}}/\psi_{\text{base}} = \omega_{\text{base}}$. The dc motor is prevented by the back emf $E = \psi \omega_r$ from operating at speeds higher than base speed for a constant ψ . The operating range can be extended to speeds higher than $|\omega_{\text{base}}|$ by lowering ψ , which is called field weakening. (The method is of course not applicable to dc motors magnetized by permanent magnets.) By selecting

$$\psi = \begin{cases} \psi_{\text{base}}, & |\omega_r| \leq \omega_{\text{base}} \\ \frac{\omega_{\text{base}}}{|\omega_r|} \psi_{\text{base}}, & |\omega_r| > \omega_{\text{base}} \end{cases} \quad (4.76)$$

(see also Figure 4.20), $|\omega_r|$ can in theory increase arbitrarily much. Since the electrical torque is given by $\tau_e = \psi i$, the torque capability is gradually reduced as the motor goes further into the field-weakening region. Therefore, a point is eventually reached when the speed cannot increase further due to lack of torque. Also, sparking in the commutator is a problem which puts a limit on the speed in the field-weakening region. This in practice limits the maximum speed to about $3\omega_{\text{base}}$.

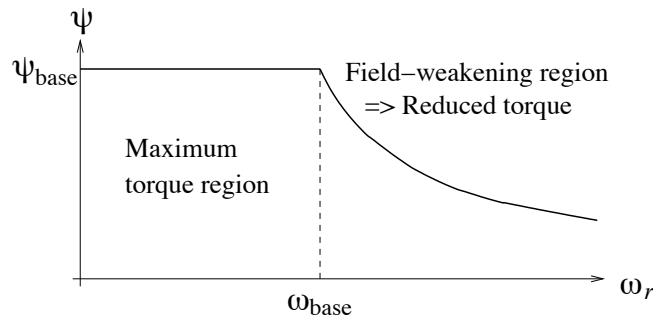


Figure 4.20. Principle of field weakening.

Remark 4.1 Analogy to field weakening: vehicle drive. An interesting analogy to the relation $\tau_e = \psi i$ and the concept of field weakening can be made for an vehicle (e.g., an automobile) drive, where a gear box is used. Higher gear allows higher speed, but reduces the torque capability. (When high torque is needed, e.g., for sufficient acceleration when overtaking another vehicle, the driver often drops a gear.)

Thus, the gear box corresponds to ψ : applying a higher gear is analogous to reducing the flux. But unlike a dc motor, the “field weakening” of the gear box is made in steps.² The power delivered from the combustion engine corresponds to i , and is controlled by the accelerator.

There is another interesting analogy. As concluded earlier, the armature current can be changed quickly, owing to a relatively small armature inductance. The flux linkage on the other hand takes longer to change, because the field-winding inductance is much larger than the armature inductance. Similarly, the power of the combustion engine is quickly changed, simply by depressing or relieving the accelerator, whereas switching gears takes longer time.

PROBLEM 4.15

In commercial propeller aircraft, the propeller blades can be pitched. Such a plane is normally operated in the following way. On the ground, the propellers are revved up to their nominal speed. Since the blades are not pitched, no torque is produced, and the plane does not move. A small pitch gives enough torque for the plane to taxi to the runway. There, maximum pitch is applied, the plane accelerates, and takes off. At cruising altitude, the propeller speed is reduced in order to save fuel.

- What are the correspondences to i and ψ in a propeller aircraft?
- When landing, the propeller speed is again increased to the nominal, even though only light torque is required. Why? Is this similar to how a dc motor is operated?

4.6 Speed Control

In addition to a current control loop, many drives also use an outer speed control loop. The speed is measured or estimated—the latter called speed-sensorless control, see Paragraph 4.6.1—and fed back to a speed controller, whose output is the armature current reference.

In a cascade control structure, the bandwidth of the outer loop should be 1/10 or less of the bandwidth of the inner loop. With α_s as bandwidth of the speed loop, we thus have the recommendation

$$\alpha_s \leq 0.1\alpha_c. \quad (4.77)$$

Consider again the mechanical dynamics (4.18). So far it has been assumed that the load torque is proportional to the speed: $\tau_l = b\omega_r$. As mentioned previously, this is a useful but not always correct simplifications. In many applications, such as pumps and fans, the load torque is proportional to the square of the speed. In other applications, such as rail vehicles, hoists (see Problem 4.4), and escalators, a large part of the load torque can be attributed to gravity and is speed independent. A more accurate model for the load torque is thus

$$\tau_l = b\omega_r + \tau_L. \quad (4.78)$$

²One notable exception was the belt drive developed by the Dutch automobile manufacturer DAF (acquired by Volvo in 1975).

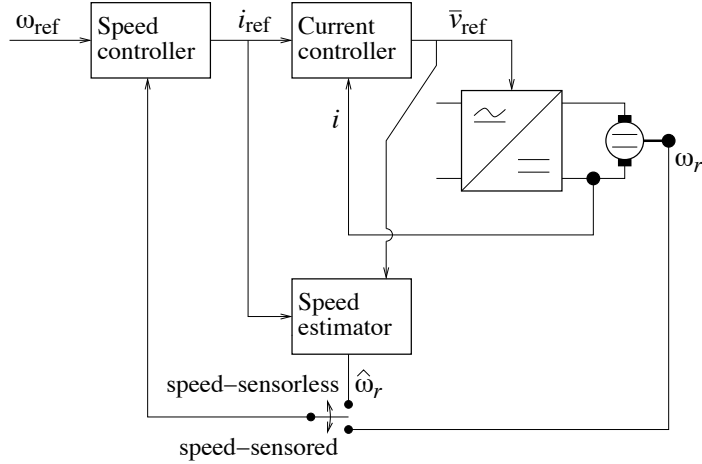


Figure 4.21. Cascaded current and speed control loops.

That is, a viscous part plus a part due to external conditions (the “external load torque”). This gives the following model for the mechanical dynamics:

$$J \frac{d\omega_r}{dt} = \psi i - b\omega_r - \tau_L. \quad (4.79)$$

Let us now design the speed controller, assuming that cascaded current control is used, with the speed controller’s output being the reference to the current controller. The external load torque τ_L enters the system as a load disturbance, much like the back emf in the current control loop. Load disturbances (in the form of load torque variations) tend to be more pronounced in the speed control loop than in the current control loop. It is therefore advisable to incorporate a correspondence to the “active resistance” used in the current controller also in the speed control loop. By introducing an inner feedback loop in the form of an “active viscous damping,” as

$$i = i' - b_a \omega_r \quad (4.80)$$

the pole of (4.79) can be moved from $-b/J$ to $-\alpha_s$, where α_s is the desired closed-loop bandwidth. The dynamics are then

$$\begin{aligned} \frac{d\omega_r}{dt} &= \frac{\psi}{J}(i' - b_a \omega_r) - \frac{b}{J}\omega_r - \frac{\tau_L}{J} \\ &= \frac{\psi}{J}i' - \underbrace{\frac{b_a \psi + b}{J}}_{\alpha_s} \omega_r - \frac{\tau_L}{J}. \end{aligned} \quad (4.81)$$

Hence, if

$$b_a = \frac{\alpha_s \hat{J} - \hat{b}}{\hat{\psi}} \quad (4.82)$$

(where “hat” as usual indicates model parameter), the dynamics of the inner loop created by the “active viscous damping” will have bandwidth α_s , assuming accurate model parameters, giving

the following transfer function from i' to ω_r :

$$G_s(s) = \frac{\psi/J}{s + \alpha_s}. \quad (4.83)$$

For fast speed control loops, $\alpha_s J \gg b$, so $b_a \approx \alpha_s \hat{J}/\hat{\psi}$; the viscous damping constant is then unimportant for the controller design. Having designed the inner loop, the outer control loop is then closed with a PI controller. With controller design using direct synthesis and model parameters replacing true ones, we obtain

$$F_s(s) = \frac{\alpha_s}{s} G_s^{-1}(s) = k_{ps} + \frac{k_{is}}{s} \quad (4.84)$$

where

$$k_{ps} = \frac{\alpha_s \hat{J}}{\hat{\psi}} \quad k_{is} = \frac{\alpha_s^2 \hat{J}}{\hat{\psi}}. \quad (4.85)$$

The output of the speed controller is the reference for the current controller. The final two steps in the controller design remain. First, limitation of i_{ref} is required, so that

$$|i_{\text{ref}}| \leq I_{\max}$$

where $I_{\max} = I_{\text{base}}$ in the steady state, whereas overcurrent, $I_{\max} > I_{\text{base}}$, may be allowed short term (seconds, in some cases up to one minute, depending on the thermal characteristics of the motor). Second, “back calculation” should be incorporated. We obtain the algorithm shown below, which corresponds to the block diagram shown in Figure 4.22.

Algorithm 4.2

Speed Controller for DC Drives

$$\begin{aligned} e_s &= \omega_{\text{ref}} - \omega_r \\ i_{\text{ref}}^{\text{nom}} &= k_{ps} e_s + k_{is} I_s - b_a \omega_r \\ i_{\text{ref}} &= \text{sat}(i_{\text{ref}}^{\text{nom}}, I_{\max}) \\ I_s &= I_s + T_s \left[e_s + \frac{1}{k_{ps}} (i_{\text{ref}} - i_{\text{ref}}^{\text{nom}}) \right] \end{aligned}$$

4.6.1 Speed Estimation for Sensorless Control

Unless very precise speed control is required, a speed sensor is not needed in a dc motor drive. Because the back emf is proportional to the speed and differs from the armature voltage only by the voltage drop across the armature resistance: $v = Ri + \psi\omega_r$ in the steady state, a speed estimate is readily computed as

$$\hat{\omega}_r = \frac{v - \hat{R}i}{\hat{\psi}} \quad (4.86)$$

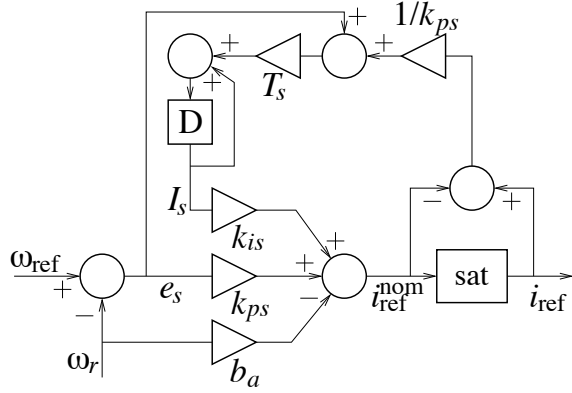


Figure 4.22. Digitally implemented two-degrees-of-freedom speed controller.

where \hat{R} is an estimate of the armature resistance. When $\hat{\omega}_r$ is fed back to the speed controller, an algebraic loop is created, however, because (the reference for) i is the speed controller's output. This can be resolved by embedding (4.86) in a low-pass filter

$$\dot{\hat{\omega}}_r = \alpha_l \left(\frac{\bar{v}_{ref} - \hat{R}i_{ref}}{\hat{\psi}} - \hat{\omega}_r \right) \quad (4.87)$$

where α_l is the filter bandwidth. Note that instead of the measured voltage and current, their reference values can preferably be used (the saturated reference \bar{v}_{ref} is the output of the current controller, cf. Algorithm 4.1). Using references rather than measured signals reduces the noise content of the speed estimate. The filter bandwidth shall be selected significantly larger than the speed-control-loop bandwidth, i.e.,

$$\alpha_l \gg \alpha_s. \quad (4.88)$$

No undesirable lagging effect due to the low-pass filter then occurs.

PROBLEM 4.16

Feedforward of the back emf in the current controller cannot be used when the speed is estimated. Explain why!

PROBLEM 4.17

Suppose that the term $\hat{R}i$ in (4.87) is neglected, being small. Would this resolve the algebraic loop? Explain carefully!

CHAPTER 5

AC Motor Drives

The objective of this chapter is to derive models for, and study operating principles of, ac motors. As much as possible we rely on the theory developed for the dc motor in Chapter 4. Traditional texts on ac motors tend to have their main focus on line-connected motors. In such, the stator (i.e., fundamental) frequency is constant (e.g., 50 Hz in Europe and 60 Hz in North America), and steady-state analysis is often sufficient. The classical tools in this are phasor diagrams and equivalent circuits.

As our focus is variable-speed drives with converter-fed motors, the picture is more complicated. Unlike when directly fed, the converter allows variable stator frequency, and also variable amplitude and phase of the stator voltage. When the amplitude, phase, or frequency of the stator voltage is changed, the motor enters a transient mode which cannot be described by a phasor diagram or a traditional equivalent circuit.

Space vectors are the main tool for dynamic analysis of ac motors. Dynamic space-vector models for the induction motor and the permanent-magnet synchronous motor are introduced, and the classical volts-per-hertz control method is discussed. For the sake of completeness, we also briefly study line-connected induction motors. The chapter is finished by discussions on speed control and determination of motor parameters.

5.1 AC Machine Fundamentals

In this section, fundamental properties for ac machines¹ are presented. Figure 5.1—which will be explained in more detail below—shows the basic physical principles of three-phase synchronous and induction machines. The stator is modeled as an equivalent two-phase winding with two perpendicular coils. The SM uses a directly magnetized rotor, oriented along the d axis of the synchronously rotating dq coordinate system. The IM instead has a rotor winding, here modeled as two short-circuited coils.

5.1.1 Synchronous Machines

An SM is, in principle, a dc machine turned inside out. The magnetization (rotor flux) is produced from inside the rotor, as shown in Figure 5.1(a), either by permanent magnets or by a field winding supplied from an external dc source. The former is called a permanent-magnet SM and the latter an electrically excited SM.

In the latter case, if the rotor is round—see further below—the field winding is placed in slots in the rotor surface, as shown in Figure 5.2. Unlike the armature current in a dc motor, the current of the field winding needs no commutation, so the commutator is replaced by two slip rings, on

¹As the properties are general for both motors and generators, we use the term “machine” in this section, even though “motor” is preferred elsewhere.

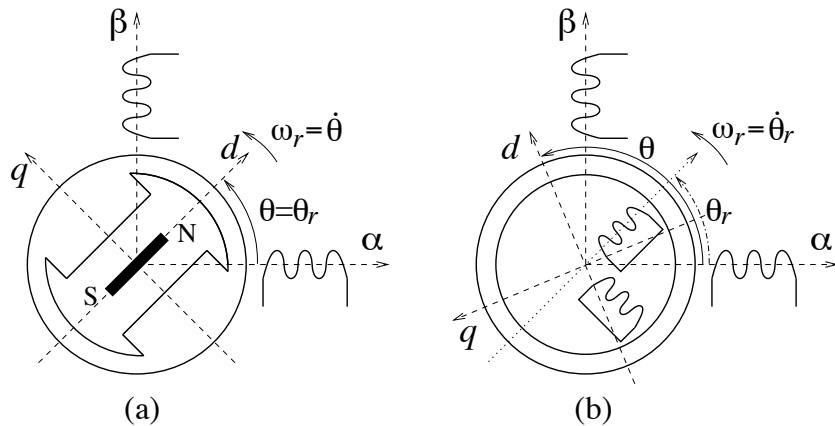


Figure 5.1. (a) Synchronous machine. (b) Induction machine. Symbols: θ —flux angle, θ_r —rotor position, ω_r —angular rotor speed.

which metal—not carbon, as in dc motors—brushes slide. The brushes therefore do not wear down as in a dc motor, so the SM requires significantly less maintenance. SMs of high power ratings often have a brushless exciter instead of slip rings. This is a smaller three-phase machine fitted on the same shaft as the SM, whose rotor phase voltages are rectified to supply the field winding. As the field current cannot be directly measured, brushless-exciter SMs are somewhat more difficult to control than SMs with slip rings.

Corresponding to the armature winding of the dc motor—which carries the torque-producing armature current—is the stator winding. This is placed in slots in the stator, as shown in Figure 5.2, and is wound with several turns of insulated copper wire. To prevent large core losses resulting from the ac excitation, the stator core is made of laminated steel.

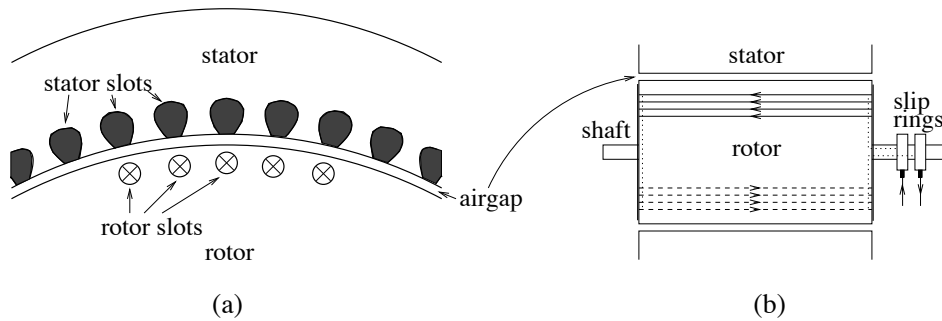


Figure 5.2. Constructional principle of a round-rotor SM. (a) Stator–rotor cross-sectional view. (b) View from the side.

Torque is produced by the interaction of the airgap flux, i.e., the part of the rotor flux that crosses the airgap, see Figure 5.3, and the stator current. The rotor leakage flux, i.e., the part of the rotor flux that closes back into the rotor without crossing the airgap (not shown in Figure 5.3), does not contribute to the torque and should be kept low. Therefore, the airgap should be narrow. The airgap width has to be a compromise, however, as manufacturing as well as cooling

(during operation) become easier for wider airgaps. Typical airgap widths of SMs are between 1 and 3 mm.

Electrically excited SMs are used as generators in large-scale generating stations. As motors they are used in for example pumps, compressors, and rolling mills, typically in applications which require very high power, up into the megawatt range. Having no commutator the SM has low losses, with efficiencies typically between 90% and 95%.

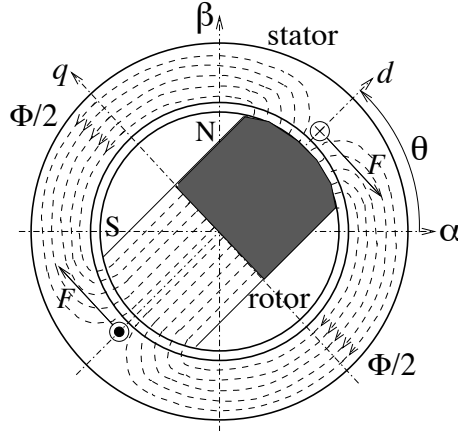


Figure 5.3. Two-pole SM with flux paths.

Number of Pole Pairs

The term synchronous refers to the rotation of the rotor, which is synchronous with the flux generated by the stator current. An SM rotates with a mechanical rotor speed ω_m , which is determined by the electrical rotor speed ω_r [which in the steady state equals the angular frequency ω_1 of the applied stator voltage, cf. Figure 5.1(a)] and the number of pole pairs n_p

$$\omega_r = n_p \omega_m. \quad (5.1)$$

A four-pole SM (two pole pairs) rotates with half the speed of a two-pole machine (one pole pair), assuming that both have the same stator frequency. A two-pole machine connected to a 50-Hz grid rotates with 3000 rpm, a four-pole machine rotates with 1500 rpm, and so on. Figure 5.4 illustrates the difference between two-pole and four-pole machines.

Operating Principle

Consider the two-pole SM in Figure 5.3. A synchronously rotating dq coordinate system, aligned with the rotor flux, is introduced. This coordinate system is displaced from the stationary $\alpha\beta$ coordinate system by the flux angle θ . The d axis is the magnetic axis. When current is applied in the stator (in Figure 5.3 only two conductors are shown, for clarity), forces F perpendicular to the d axis appear in the stator. But since the stator is fixed, counterforces appear which instead drive the rotor counterclockwise (opposite the direction of the stator forces).

Clearly, for the forces (i.e., the torque) to be constant, the stator current must be ac with the same angular frequency ω_1 as the rotation of the rotor: $\omega_1 = \dot{\theta}$. Furthermore, in order to

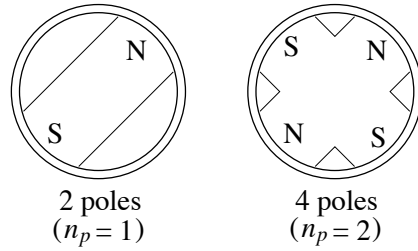


Figure 5.4. Different numbers of poles.

obtain maximum production of torque, the stator current has to be properly vectorially placed in relation to the rotor flux. The flux angle θ therefore has to be known with good accuracy by the control system. Since the flux angle coincides with the physical rotor position—cf. Figure 5.1(a)—measuring this (using a digital position encoder or a resolver, see Chapter 8) directly gives the flux position. This makes control of an SM fairly straightforward, as long as a position sensor is used. If not—a case which is called sensorless control—the flux angle has to be estimated.

Locations of the d and q Current Components

Suppose that it is desired to generate the flux shown in Figure 5.3 from the stator rather than from within the rotor. (This is done in an induction machine, see below.) Current then has to be applied as shown in Figure 5.5. Although the current is geometrically applied in the q direction, we *define* this as a current applied in the d direction, since then a d -direction flux is obtained.

The dq current coordinate system is determined by the corresponding flux coordinate system.

The current applied in Figure 5.3 is therefore a full q -direction current.

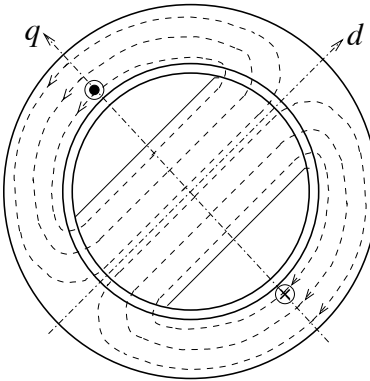


Figure 5.5. Flux-producing stator current component: by definition in the d direction.

Round and Salient Rotors

Rotors for SMs are either round (also called cylindrical or nonsalient) or salient (with salient poles), as shown in Figure 5.6. Round-rotor SMs are used in applications with higher speeds, for example generators driven by steam turbines in fossil-fuel or nuclear generating stations. Such machines have low pole number, typically between four and eight. Salient SMs are designed for slower rotation, and have higher pole number, up to 120. Typical applications of such are generators driven by hydro turbines in hydroelectric generating stations and motors for rolling mills. Note in Figure 5.6 that the field winding in a salient SM is placed around the poles, not in the rotor surface as in a round-rotor SM.

A round-rotor SM has a smooth airgap, i.e., the mutual inductance between the stator and the rotor is constant all along the rotor periphery. In a salient SM the airgap width is minimal at the poles (N and S in Figure 5.6) and maximal in between the poles. Hence, the mutual inductance—which decreases with the airgap width—is maximal at the poles and minimal in between. In salient machines, nonlinear effects tend to be more pronounced than in round-rotor machines, giving a higher amount of harmonics—so-called space harmonics—in the airgap flux, see Remark 5.2 below. Dynamic models which include these effects are quite complicated. Therefore, it is normally assumed that the mutual inductance L_m varies sinusoidally with the rotor position:

$$L_m(\theta) = \frac{1}{2}(L_0 + L_g \cos 2\theta) \text{ where } L_0 = L_{md} + L_{mq} \text{ and } L_g = L_{md} - L_{mq}. \quad (5.2)$$

On the d axis, $L_m(0) = L_m(180^\circ) = L_{md}$, whereas on the q axis, $L_m(\pm 90^\circ) = L_{mq}$, where $L_{md} > L_{mq}$. This approximation gives a model in which the space harmonics are disregarded, but also one that is only slightly more complicated than that of a round-rotor machine. See further Section 5.3.

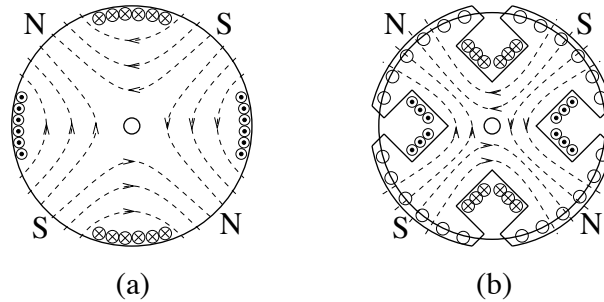


Figure 5.6. Four-pole SM rotors showing flux paths as well as field- and damper-winding placements. (a) Round rotor. (b) Salient rotor.

Damper Winding

The SM rotor in Figure 5.6(b) is outfitted with a damper winding. This is a so-called cage winding, consisting of bars placed in the surface of the poles, which are interconnected at each axial end of the rotor by a short-circuit ring, as shown in the figure. The bars are slots that are machined in the rotor and filled with aluminum, copper, or bronze. The rotor itself is made of laminated steel. Alternatively, the poles or the entire rotor core can be made as a solid steel forging. This

is feasible since the SM rotates synchronously in the steady state; the core losses will be low for normal operation. At transients, the core losses give an effect similar to that of a damper winding.

Most electrically excited SMs have a damper winding, for two reasons. In a synchronous motor, the damper winding allows starting by direct line connection (in a similar fashion as an induction motor, as will be seen). Called a line start, the field winding is short circuited until the speed reaches about 95% of synchronous speed, when it is excited. In a synchronous generator the damper winding reduces angular oscillations at transients, which is important from the standpoint of power system stability.

Permanent-Magnet Synchronous Machines

The alternative to supplying the fundamental magnetization from an external dc source is to use permanent magnets. These are made of high-remanent magnetic materials, such as SmCo or NdFeB, and can either be mounted on the rotor surface, set in openings in the rotor surface, or be buried (mounted inside the rotor), as shown in Figure 5.7. The permeability of magnet material is about the same as for air. Therefore, the rotor of a PMSM with inset or buried magnets is salient: the flux “sees a wider airgap” in the d direction than in the q direction. But, unlike the salient rotor in Figure 5.6(b), the mutual inductance between the stator and the rotor in Figure 5.7(b, c) is *minimal* in the d direction: $L_{md} < L_{mq}$. The rotor with surface-mounted magnets in Figure 5.7(a) is, on the other hand, magnetically round. Benefits of PMSMs are that a very high efficiency is obtained (90%–98%), and that no field current supply is needed. High cost of magnet materials and constructional difficulties are the main drawbacks. Traditionally, PMSMs have been used as motors in applications requiring lower power, such as industrial robots and in aerospace. There are today PMSMs rated several hundred kilowatts on the market, however.

PMSMs are normally converter fed, but in some applications—such as pumps—line-connected PMSMs are used. Such motors must be equipped with a damper winding to allow asynchronous line starting. To design a line-connected PMSM is a nontrivial task. On the one hand, the magnets will give a strong pulsating torque during the asynchronous start, which might cause lockup at a low speed when the startup load torque is high. On the other hand, for low load torques synchronization may not be accomplished; the rotor instead oscillates around a speed slightly lower than synchronous. (As its field winding is short circuited during the asynchronous start, these problems normally do not occur for an electrically excited SM.)

For more information about analysis and design of PMSMs, see [68].

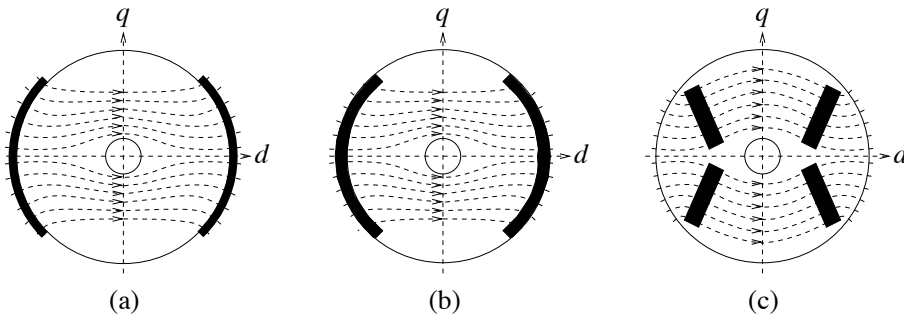


Figure 5.7. Two-pole PMSM rotors with (a) surface-mounted magnets, (b) inset magnets, and (c) buried magnets.

5.1.2 Induction Machines

An induction machine is similar to a round-rotor SM with a cage damper winding, but no field winding or permanent magnets, as shown in Figure 5.1(b). The IM is most common as motor in industrial applications and electric traction (mainly rail vehicles), but is also used in some appliances such as washing machines. The IM is robust, inexpensive, and durable, which accounts for its popularity and wide use. It is also cheaper and simpler to use in both line-connected and converter-fed drives than electrically excited SMs, as no field winding supply is needed.

On the other hand, the IM has a fairly low starting torque when used as a line-connected motor (which is a problem also for the SM). When fed from a converter, the control is much more complicated than for a dc motor. Performance limitations in the performance of power electronic converters and control equipment prevented the IM from becoming widely used in variable-speed drives up until the mid-1980s, but is today commonplace.

IMs are more efficient than dc machines, but less efficient than SMs. Typical efficiencies are from 85% to 90%.

Although most IMs have a cage rotor, some are instead equipped with a three-phase rotor winding, connected to three slip rings (which are similar to the slips rings that supply the field winding in an SM). One application for the slip-ringed IM is as wind-turbine generator, where the stator is connected directly to the mains, whereas the rotor is connected to the mains via a power electronic converter (normally a back-to-back VSC configuration). This is called a doubly-fed IM. The converter allows full control, whereas most of the power goes directly to the grid via the stator, giving a system with higher efficiency as compared to a standard converter-connected IM with a cage rotor. Slip-ringed IMs will not be treated further in this book, however.

For more information of the physics and design principles of IMs, [68] is recommended.

Operating Principle

Unlike the SM, the IM is magnetized from the stator. As long the IM rotates synchronously, no current is induced in the rotor. Once the IM is loaded mechanically, the rotor starts lagging behind the synchronous rotation of the flux. Current is then induced in the rotor winding—according to Lenz' law—giving forces that counteract the lagging effect. This gives the electrical torque. The *slip* s is defined as²

$$s = \frac{\omega_1 - \omega_r}{\omega_1} \quad (5.3)$$

and

$$\omega_2 = s\omega_1 = \omega_1 - \omega_r \quad (5.4)$$

is called the angular slip frequency. At normal operation the slip is fairly small, only up to about 5%.

As discussed above, measuring the physical position of the rotor of the SM immediately gives the flux angle, since $\theta = \theta_r$, cf. Figure 5.1(a). This is not the case for the IM due to the slip. Flux-angle measurement of the IM requires sensors such as search coils or Hall elements placed in the airgap. These are expensive and delicate, and should therefore be avoided. Hence, the rotor flux of the IM is not readily measurable; it has to be estimated. This is greatly complicates the control of the IM.

²We in this chapter use the derivative operator p also to denote the Laplace transform variable, to avoid risk for confusion with the slip.

Constructional Principle

Figure 5.8 shows the constructional principle of the IM. The rotor cage is similar to the damper winding of an SM, except that the rotor slots normally are skewed. The method reduces nonlinear effects, and in turn the harmonic content of the flux, with less torque pulsations and lower acoustic noise as result. Due to the asynchronous rotation, the rotor must be made of laminated steel in order to keep the core losses low.

Since the magnetization is done from the stator, it is more important than for SMs to make the airgap narrow. A wide airgap translates to a small mutual inductance, demanding a large stator magnetizing current in order to produce the desired rotor flux. This causes higher losses in the stator winding, giving lower efficiency. IMs rated 100 kW or below have airgaps less than 1 mm wide.

We finally note that also induction machines can be constructed with a number of pole pairs higher than 1. In this case, there is no difference of the rotor design principle as compared to $n_p = 1$, but rather in the way the stator is wound.

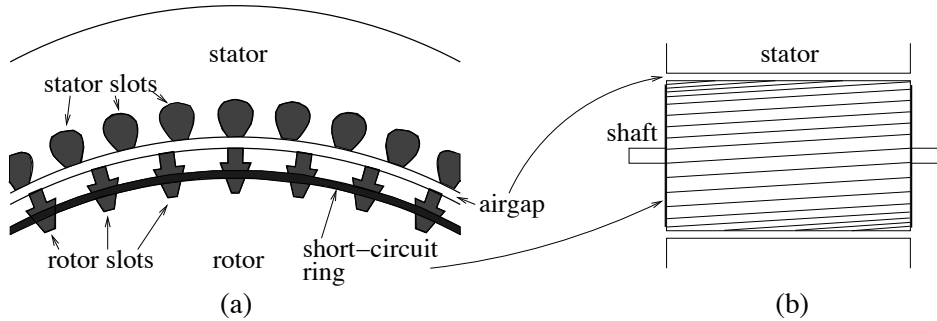


Figure 5.8. Constructional principle of an induction machine. (a) Stator–rotor cross-sectional view. (b) View from the side.

5.2 Dynamic Model for the Induction Motor

Let us first consider the stator circuit. The resistance R_s of the stator winding is (for all practical purposes) equal in all three phases. From the law of induction it follows that the part of the stator voltage which is not dissipated in the stator resistance will build up a flux in the stator winding. Hence, with \mathbf{v}_s^s as the stator-voltage space vector, the following relation must hold:

$$\mathbf{v}_s^s - R_s \mathbf{i}_s^s - \frac{d\psi_s^s}{dt} = 0 \quad (5.5)$$

where \mathbf{i}_s^s and ψ_s^s are the space vectors for the stator current and the stator flux linkage, respectively. The rotor circuit, with winding resistance R_r , can be considered in a similar way. Suppose that the rotor is observed from a coordinate system—rotor coordinates—which rotates with the same speed as the rotor: ω_r . Let us denote rotor coordinates with the superscript r . As the coordinate system is rotor fixed, there will be no induced voltage due to the rotation, so the rotor-flux dynamics as expressed in rotor coordinates are formally identical to the stator-flux dynamics (5.5)

$$\mathbf{v}_r^r - R_r \mathbf{i}_r^r - \frac{d\psi_r^r}{dt} = 0 \quad (5.6)$$

where \mathbf{v}_r^r , \mathbf{i}_r^r , and $\boldsymbol{\psi}_r^r$ are the rotor-voltage, rotor-current, and rotor-flux space vectors, respectively. But the rotor winding is short-circuited, so $\mathbf{v}_r^r = 0$. Now, let us transform \mathbf{i}_r^r and $\boldsymbol{\psi}_r^r$ to stationary coordinates. This is an $\alpha\beta$ transformation using the rotor position $\theta_r = \int \omega_r dt$

$$\mathbf{i}_r^s = e^{j\theta_r} \mathbf{i}_r^r \quad \boldsymbol{\psi}_r^s = e^{j\theta_r} \boldsymbol{\psi}_r^r. \quad (5.7)$$

Equation (5.6) is transformed as

$$\begin{aligned} 0 - R_r e^{-j\theta_r} \mathbf{i}_r^s - \frac{d(e^{-j\theta_r} \boldsymbol{\psi}_r^s)}{dt} &= 0 \\ \Rightarrow -R_r e^{-j\theta_r} \mathbf{i}_r^s - \left(-j\omega_r e^{-j\theta_r} \boldsymbol{\psi}_r^s + e^{-j\theta_r} \frac{d\boldsymbol{\psi}_r^s}{dt} \right) &= 0 \\ \Rightarrow j\omega_r \boldsymbol{\psi}_r^s - R_r \mathbf{i}_r^s - \frac{d\boldsymbol{\psi}_r^s}{dt} &= 0. \end{aligned} \quad (5.8)$$

The induction motor is thus described by the following equations:

$$\frac{d\boldsymbol{\psi}_s^s}{dt} = \mathbf{v}_s^s - R_s \mathbf{i}_s^s \quad (\text{stator}) \quad (5.9)$$

$$\frac{d\boldsymbol{\psi}_r^s}{dt} = j\omega_r \boldsymbol{\psi}_r^s - R_r \mathbf{i}_r^s \quad (\text{rotor}). \quad (5.10)$$

Let us now find a relation between the stator and rotor flux linkages. The rotor winding is referred to the stator, i.e., the rotor winding is represented by coils in the α and β directions, cf. Figure 5.1(b). Assuming linear magnetic conditions, the airgap flux $\boldsymbol{\psi}_a^s$ can then be expressed as

$$\boldsymbol{\psi}_a^s = L_m \mathbf{i}_m^s, \quad \mathbf{i}_m^s = \mathbf{i}_s^s + \mathbf{i}_r^s \quad (5.11)$$

where L_m is the mutual inductance between the stator and the rotor, which is also called the magnetizing inductance, and \mathbf{i}_m^s is the magnetizing current. The stator flux is the sum of the airgap flux and the stator leakage flux, the latter which under linear magnetic conditions is proportional to the stator current only. Similar reasoning for the rotor flux yields

$$\boldsymbol{\psi}_s^s = L_m \mathbf{i}_m^s + L_{sl} \mathbf{i}_s^s \quad (5.12)$$

$$\boldsymbol{\psi}_r^s = L_m \mathbf{i}_m^s + L_{rl} \mathbf{i}_r^s \quad (5.13)$$

where L_{sl} and L_{rl} are the stator and rotor leakage inductances, respectively. The leakage inductances are typically 10% of L_m or less. Alternatively, with $L_s = L_m + L_{sl}$ and $L_r = L_m + L_{rl}$ as the stator and rotor self inductances, respectively, the relations can be expressed as

$$\boldsymbol{\psi}_s^s = L_s \mathbf{i}_s^s + L_m \mathbf{i}_r^s \quad (5.14)$$

$$\boldsymbol{\psi}_r^s = L_m \mathbf{i}_m^s + L_r \mathbf{i}_r^s. \quad (5.15)$$

Combining (5.12)–(5.13) with (5.9)–(5.10), assuming constant inductances, yields

$$\mathbf{v}_s^s - R_s \mathbf{i}_s^s - L_{sl} \frac{d\mathbf{i}_s^s}{dt} - L_m \frac{d\mathbf{i}_m^s}{dt} = 0 \quad (5.16)$$

$$j\omega_r \boldsymbol{\psi}_r^s - R_r \mathbf{i}_r^s - L_{rl} \frac{d\mathbf{i}_r^s}{dt} - L_m \frac{d\mathbf{i}_m^s}{dt} = 0. \quad (5.17)$$

These equations describe the dynamic equivalent circuit depicted in Figure 5.9. As there are three inductances configurated in a “T,” this is known as the T-equivalent circuit.

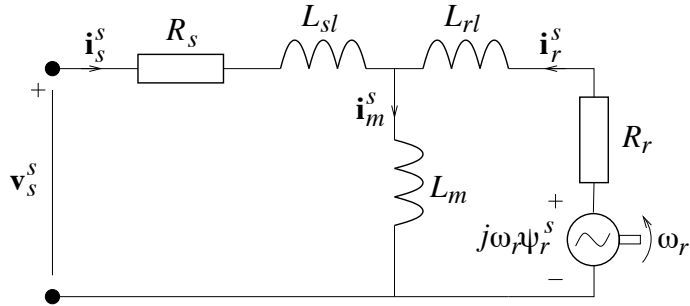


Figure 5.9. Dynamic T-equivalent circuit for the induction motor.

This is the traditional equivalent circuit for the IM commonly found in literature on electrical machines, with two exceptions. First, rather than a resistance R_r/s in the rotor circuit, we find the rotor resistance R_r in series with a voltage source. This voltage source—to be called the rotor emf—corresponds to the back emf of the dc motor, and is the device that converts between electrical and mechanical power. The power developed in the rotor emf goes to the shaft. Second, electric power engineers often tend to become so fascinated with the equivalent circuit that they seem to forget completely that an electrical motor is also mechanical. In an attempt to prevent this, we shall draw the equivalent circuit with a rotating shaft sticking out of the rotor-emf symbol.

As the name suggests, the dynamic equivalent circuit is valid also at transient conditions. If merely steady-state conditions are considered, the equivalent circuit can be simplified. In the steady state, i.e., with $p = j\omega_1$, the voltage across L_m and L_{rl} is given by

$$j\omega_1(L_m i_m^s + L_{rl} i_r^s) = j\omega_1 \psi_r^s. \quad (5.18)$$

But this is also the voltage across R_r and the rotor emf, so

$$\begin{aligned} j\omega_1 \psi_r^s &= j\omega_r \psi_r^s - R_r i_r^s \Rightarrow j\omega_2 \psi_r^s = -R_r i_r^s \\ \Rightarrow j\omega_1 \psi_r^s &= -\frac{\omega_1}{\omega_2} R_r i_r^s = -\frac{R_r}{s} i_r^s. \end{aligned} \quad (5.19)$$

This equation corresponds to the standard equivalent circuit with a total resistance R_r/s on the rotor side. Of this, R_r is the actual rotor resistance, whereas the remaining part, $(1 - s)R_r/s$, corresponds to the rotor emf. The rotor emf of the IM happens to be proportional to and in phase with the rotor current in the steady state. Hence, it can be modeled as a resistance. Note that the equivalent circuit in Figure 5.10 is valid only in the steady state, so it cannot be used to draw any conclusions regarding the behavior of the induction motor in a variable-speed drive.

Remark 5.1 Stator/rotor turns ratio. In the model derived, we have not taken into account that the stator and rotor windings have different numbers of turns per phase N_s and N_r , where $N_s > N_r$ normally (especially if the rotor winding is a short-circuited cage). The rotor current i_r^s is therefore not the actual measurable rotor current, which we may denote as $i_r^{s''}$, but the rotor current *referred to the stator*. From the relation between the primary and secondary currents in a transformer, we have

$$i_r^{s''} = \frac{N_s}{N_r} i_r^s.$$

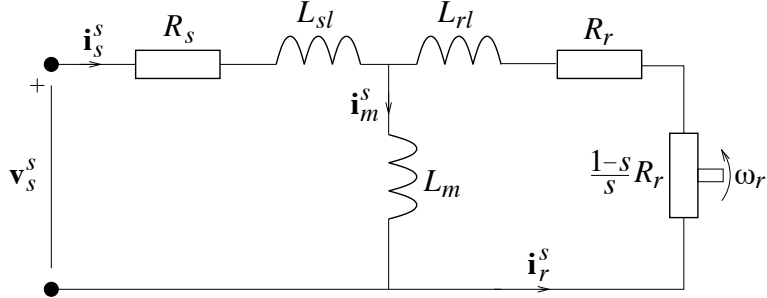


Figure 5.10. Steady-state T-equivalent circuit for the induction motor.

Similarly, R_r is the rotor resistance reflected to the stator. The physical rotor resistance R''_r is given by

$$R''_r = \left(\frac{N_r}{N_s} \right)^2 R_r$$

and is thus normally much smaller than R_r (and R_s).

Remark 5.2 Sinusoidally distributed winding. Throughout this chapter it is implicitly assumed that the airgap flux is sinusoidally distributed. In the theory for ac machines it is seen that this requires a so-called sinusoidally distributed winding in the stator. In practice, this is not the case. The airgap flux will deviate somewhat from the ideal sinusoid; it is said to contain space harmonics, which are neglected in our models. The number of turns per phase N_s in the stator is not the actual number of turns, but the equivalent number of turns which would produce the ideal airgap flux by a sinusoidally distributed winding [68].

5.2.1 Inverse- Γ Model

Although the T-equivalent dynamic model is physically relevant, it is less good for dynamic analysis and controller design due to the fact that it is over parametrized. The three inductor currents are not linearly independent, as $\mathbf{i}_m^s = \mathbf{i}_s^s + \mathbf{i}_r^s$. One leakage inductance—not two—is sufficient. This simplification is achieved by defining new rotor variables as

$$\Psi_R^s = b\Psi_r^s \quad \mathbf{i}_R^s = \frac{\mathbf{i}_r^s}{b} \quad (5.20)$$

where b is a transformation factor to be chosen. (All transformed quantities have upper-case subscripts.) Substitution of these definitions in the flux equations (5.14)–(5.15) yields

$$\Psi_s^s = L_s \mathbf{i}_s^s + bL_m \mathbf{i}_R^s \quad (5.21)$$

$$\Psi_R^s = bL_m \mathbf{i}_s^s + b^2 L_r \mathbf{i}_R^s \quad (5.22)$$

By choosing b such that the stator and rotor currents have equal coefficients in (5.22), i.e., $bL_m = b^2 L_r \Rightarrow b = L_m / L_r$, the leakage inductance on the rotor side is eliminated; the leakage is referred to the stator side, and the inverse- Γ model is obtained. When using this definition, the flux equations

(5.21)–(5.22) are transformed to

$$\psi_s^s = L_s \mathbf{i}_s^s + \frac{L_m^2}{L_r} \mathbf{i}_R^s \quad (5.23)$$

$$\psi_R^s = \frac{L_m^2}{L_r} (\mathbf{i}_s^s + \mathbf{i}_R^s) \quad (5.24)$$

which, with $\mathbf{i}_M^s = \mathbf{i}_s^s + \mathbf{i}_R^s$ as the magnetizing current of the inverse- Γ model, also can be expressed as

$$\psi_s^s = L_\sigma \mathbf{i}_s^s + L_M \mathbf{i}_M^s \quad (5.25)$$

$$\psi_R^s = L_M \mathbf{i}_M^s \quad (5.26)$$

where new parameters, L_M and L_σ , have been introduced. These are the transformed magnetizing inductance and total leakage inductance, respectively

$$L_M = \frac{L_m^2}{L_r} \quad (5.27)$$

$$L_\sigma = L_s - L_M = L_s - \frac{L_m^2}{L_r} = \frac{L_m(L_{sl} + L_{rl}) + L_{sl}L_{rl}}{L_m + L_{rl}} \approx L_{sl} + L_{rl}. \quad (5.28)$$

The stator equation (5.9) remains unchanged, and the transformed rotor equation is formally equal to (5.10)

$$\frac{d\psi_s^s}{dt} = \mathbf{v}_s^s - R_s \mathbf{i}_s^s \quad (\text{stator}) \quad (5.29)$$

$$\frac{d\psi_R^s}{dt} = j\omega_r \psi_R^s - R_R \mathbf{i}_R^s \quad (\text{rotor}) \quad (5.30)$$

where the transformed rotor resistance

$$R_R = \left(\frac{L_m}{L_r} \right)^2 R_r \quad (5.31)$$

has been introduced. Combining (5.29)–(5.30) with (5.25)–(5.26), assuming constant inductances, yields

$$\mathbf{v}_s^s - R_s \mathbf{i}_s^s - L_\sigma \frac{d\mathbf{i}_s^s}{dt} - L_M \frac{d\mathbf{i}_M^s}{dt} = 0 \quad (5.32)$$

$$j\omega_r \psi_R^s - R_R \mathbf{i}_R^s - L_M \frac{d\mathbf{i}_M^s}{dt} = 0. \quad (5.33)$$

These equations form the dynamic equivalent circuit depicted in Figure 5.11. They define the motor model in terms of stator and rotor currents. Many drives incorporate a control loop for the stator current, see further Chapter 6. Therefore, it is natural to take \mathbf{i}_s^s as a state variable. The rotor current, however, usually cannot be measured. It is therefore convenient to eliminate the rotor current from the equations and use the rotor flux linkage ψ_R^s as the second state variable. Substitution of (5.32)–(5.33) together with

$$\mathbf{i}_R^s = \mathbf{i}_M^s - \mathbf{i}_s^s = \frac{\psi_R^s}{L_M} - \mathbf{i}_s^s \quad (5.34)$$

in (5.29)–(5.30) yields

$$L_\sigma \frac{d\mathbf{i}_s^s}{dt} = \mathbf{v}_s^s - R_s \mathbf{i}_s^s - \underbrace{\frac{d\psi_R^s}{dt}}_{\mathbf{E}^s} \quad (5.35)$$

$$\frac{d\psi_R^s}{dt} = R_R \mathbf{i}_s^s - \left(\frac{R_R}{L_M} - j\omega_r \right) \psi_R^s \quad (5.36)$$

where we introduce the symbol \mathbf{E}^s for the time derivative of the rotor flux. \mathbf{E}^s —to be called the *flux emf*—can be eliminated from (5.35) by using (5.36), giving

$$L_\sigma \frac{d\mathbf{i}_s^s}{dt} = \mathbf{v}_s^s - (R_s + R_R) \mathbf{i}_s^s - \underbrace{\left(j\omega_r - \frac{R_R}{L_M} \right) \psi_R^s}_{\mathbf{E}_b^s} \quad (5.37)$$

where \mathbf{E}_b^s is the *back emf*. Except at low speeds, the back emf is predominantly determined by the term $j\omega_r \psi_R^s$. It is thus approximately equal to the rotor emf, and differs from the flux emf only by the term $R_R \mathbf{i}_s^s$, which is small at higher speeds

$$\mathbf{E}_b^s = \left(j\omega_r - \frac{R_R}{L_M} \right) \psi_R^s \approx j\omega_r \psi_R^s \approx R_R \mathbf{i}_s^s - \left(\frac{R_R}{L_M} - j\omega_r \right) \psi_R^s = \frac{d\psi_R^s}{dt} = \mathbf{E}^s \quad (5.38)$$

or in words

$$\text{back emf} \approx \text{rotor emf} \approx \text{flux emf}.$$

We finally note that just as for the T model, the rotor emf is proportional to and in phase with the rotor current in the steady state, giving the equivalent circuit depicted in Figure 5.12.

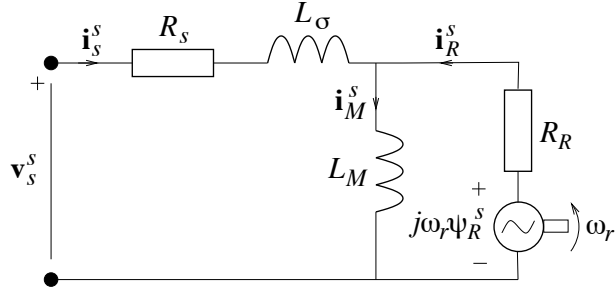


Figure 5.11. Dynamic inverse- Γ -equivalent circuit for the induction motor.

PROBLEM 5.1

It is also possible to eliminate the leakage inductance on the stator side, referring the leakage to the rotor side instead, giving the so-called Γ model. Find the correspondences of (5.35) and (5.36) for the Γ model! **Hint:** Now the stator and rotor current should have equal coefficients in (5.21).

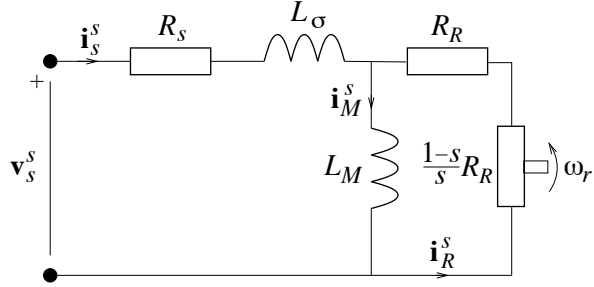


Figure 5.12. Steady-state inverse- Γ -equivalent circuit for the induction motor.

5.2.2 Transformation to Synchronous Coordinates

It is often convenient to express ac motor models in synchronous coordinates. We can use (2.151), i.e., $p \rightarrow p + j\omega_1$, to immediately obtain the differential equations in synchronous coordinates corresponding to (5.35)–(5.36)

$$L_\sigma \frac{di_s}{dt} = \mathbf{v}_s - (R_s + j\omega_1 L_\sigma) \mathbf{i}_s - j\omega_1 \boldsymbol{\psi}_R - \frac{d\boldsymbol{\psi}_R}{dt} \quad (5.39)$$

$$\frac{d\boldsymbol{\psi}_R}{dt} = R_R \mathbf{i}_s - \left(\frac{R_R}{L_M} + j\omega_2 \right) \boldsymbol{\psi}_R \quad (5.40)$$

or, with (5.40) substituted in (5.39)

$$L_\sigma \frac{di_s}{dt} = \mathbf{v}_s - (R_s + R_R + j\omega_1 L_\sigma) \mathbf{i}_s - \underbrace{\left(j\omega_r - \frac{R_R}{L_M} \right) \boldsymbol{\psi}_R}_{\text{back emf } \mathbf{E}_b} \quad (5.41)$$

$$\frac{d\boldsymbol{\psi}_R}{dt} = R_R \mathbf{i}_s - \left(\frac{R_R}{L_M} + j\omega_2 \right) \boldsymbol{\psi}_R. \quad (5.42)$$

Equations (5.41)–(5.42) can be illustrated by the block diagram in Figure 5.13. There are both similarities and differences to the block diagram of the dc motor, Figure 4.9. In both block diagrams there are three feedback loops, where the outer loop is that of the back emf. The flux dynamics act similarly to the mechanical dynamics of the dc motor. The mechanical dynamics of the IM (which for simplicity are represented only as a box with current and flux input; see the sequel for details) are connected in parallel to the flux dynamics, and interact nonlinearly with the electrical subsystem. A nonlinear fifth-order system with the state variables i_d , i_q , ψ_d , ψ_q , and ω_r is formed.

Even though the flux dynamics are slow (sometimes comparable to the mechanical dynamics), the electrical dynamics can often yet be considered linear, but with varying coefficients: $j\omega_r$ multiplied with $\boldsymbol{\psi}_R$. However, as we shall see in Chapter 9, many IM control methods indirectly involve a nonlinear feedback of the flux to the angular stator frequency ω_1 . The flux dynamics then become highly nonlinear, and the system may turn unstable under some circumstances. Careful analysis is needed in the design of the control system.

PROBLEM 5.2

In Figure 5.13 it is seen that the IM has three inputs in synchronous coordinates: v_d , v_q

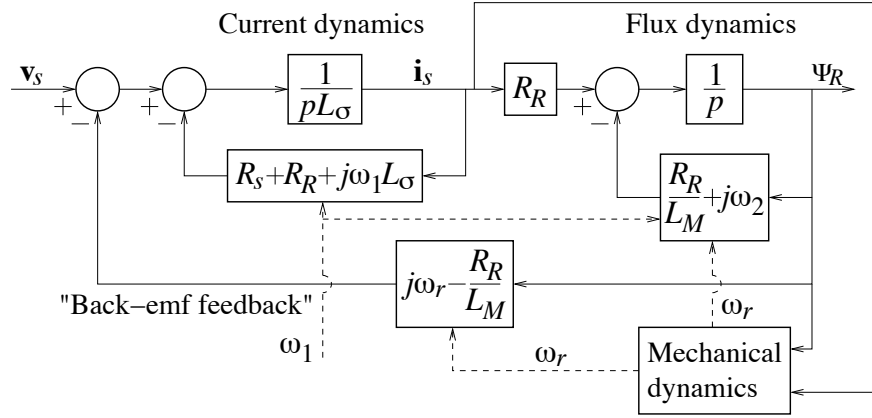


Figure 5.13. Block diagram of the induction motor dynamics. Solid and dashed lines indicate space-vector and scalar signal paths, respectively.

(components of \mathbf{v}_s), and ω_1 . In stator coordinates, only two inputs are available: v_α and v_β (components of \mathbf{v}_s^s). This appears to be a discrepancy, but is it? Please clarify!

5.2.3 Perfect Field Orientation

Quite similarly to the orientation of the dq coordinate system along the rotor flux of the SM—cf. Figures 5.1 and 5.3—it is particularly useful to select the dq transformation angle equal to the flux angle:

$$\theta_1 = \arg \psi_R^s. \quad (5.43)$$

The dq reference frame will then be aligned with the rotor flux also for the IM, so that ψ_R becomes real: $\psi_R = \psi_R$. We shall call this perfect field orientation. With $\mathbf{i}_s = i_d + j i_q$, (5.40) then reduces to

$$\frac{d\psi_R}{dt} = R_R(i_d + j i_q) - \left(\frac{R_R}{L_M} + j \omega_2 \right) \psi_R. \quad (5.44)$$

Identifying the real and imaginary parts and solving for ω_2 in the latter yields

$$\frac{d\psi_R}{dt} = R_R i_d - \frac{R_R}{L_M} \psi_R \quad (5.45)$$

$$\omega_2 = \omega_1 - \omega_r = \frac{R_R i_d}{\psi_R}. \quad (5.46)$$

Under perfect field orientation, the flux modulus has first-order dynamics, with input i_d and time constant $T_r = L_M/R_R$, called the rotor time constant. In the steady state,

$$\psi_R = L_M i_d. \quad (5.47)$$

Thus, i_d controls the flux level, and plays the part of the field current in a dc motor. Therefore, i_d is called the *flux-producing current component*, and should be controlled such that

$$i_d = \frac{\psi_{\text{ref}}}{\hat{L}_M} \quad (5.48)$$

where ψ_{ref} is the flux reference, i.e., the desired flux level, and \hat{L}_M is an estimate of the magnetizing inductance.

Furthermore, we have found a simple relation, (5.46), between the angular slip frequency, the flux modulus, and the current component i_q . This is known as the *slip relation*.

If perfect field orientation were possible to achieve, control of the IM would only be slightly more difficult than of the dc motor. The problem is that the rotor flux is not readily available for measurement, but has to be estimated. See Chapter 9.

5.2.4 Torque Production

Active power is developed at three³ locations in the equivalent circuit (Figure 5.11): in the stator and rotor resistances and in the rotor emf. The first two give losses—so-called copper losses—whereas the latter is converted to mechanical power. Following (2.132), we can calculate this as (where the subscript e stands for electric power to the shaft)

$$P_e = -\frac{3}{2K^2} \operatorname{Re} \{j\omega_r \Psi_R \mathbf{i}_R^*\} \quad (5.49)$$

the minus sign as \mathbf{i}_R is defined with a direction opposite to the rotor emf. But for a complex number $z = x + jy$ we have $\operatorname{Re}\{jz\} = \operatorname{Re}\{j(x + jy)\} = -y = -\operatorname{Im}\{z\}$, so

$$\begin{aligned} P_e &= \frac{3\omega_r}{2K^2} \operatorname{Im} \{\Psi_R \mathbf{i}_R^*\} = \frac{3\omega_r}{2K^2} \operatorname{Im} \left\{ \Psi_R \left(\frac{\Psi_R}{L_M} - \mathbf{i}_s \right)^* \right\} = -\frac{3\omega_r}{2K^2} \operatorname{Im} \{\Psi_R \mathbf{i}_s^*\} \\ &= \frac{3\omega_r}{2K^2} \operatorname{Im} \{\Psi_R^* \mathbf{i}_s\}. \end{aligned} \quad (5.50)$$

Because power = torque \times angular speed and $\omega_r = n_p \omega_m$, we obtain the following relation for the electrical torque:

$$\tau_e = \frac{P_e}{\omega_m} = \frac{n_p P_e}{\omega_r} = \frac{3n_p}{2K^2} \operatorname{Im} \{\Psi_R^* \mathbf{i}_s\}. \quad (5.51)$$

In component form with $\Psi_R = \psi_d + j\psi_q$, we have

$$\tau_e = \frac{3n_p}{2K^2} (\psi_d i_q - \psi_q i_d). \quad (5.52)$$

It is interesting to note that the relation holds also for the stator flux. We have

$$\tau_e = \frac{3n_p}{2K^2} \operatorname{Im} \{\Psi_R^* \mathbf{i}_s\} = \{\Psi_R = \Psi_s - L_\sigma \mathbf{i}_s\} = \frac{3n_p}{2K^2} \operatorname{Im} \{\Psi_s^* \mathbf{i}_s\}. \quad (5.53)$$

Because the power formula is invariant of the coordinate system used, the torque can also be expressed as

$$\tau_e = \frac{3n_p}{2K^2} \operatorname{Im} \{(\Psi_R^s)^* \mathbf{i}_s^s\} = \frac{3n_p}{2K^2} \operatorname{Im} \{(\Psi_s^s)^* \mathbf{i}_s^s\}. \quad (5.54)$$

³Neglected here are the core losses: magnetic hysteresis and eddy-current losses, which occur mainly in the rotor. These can be modeled as a resistance in parallel with the magnetizing inductance in the equivalent circuit.

Perfect Field Orientation

For the special—but important—case of perfect field orientation, $\psi_R = \psi_d = \psi_R$, the torque is given by

$$\tau_e = \frac{3n_p}{2K^2} \operatorname{Im}\{\psi_R(i_d + ji_q)\} = \frac{3n_p}{2K^2} \psi_R i_q. \quad (5.55)$$

The q -direction stator current component then controls the production of torque, just like the armature current of a dc motor. For this reason, i_q is called the *torque-producing current component*.

Note in the slip relation (5.46) that $\omega_2 = 0 \Leftrightarrow \omega_1 = \omega_r$ when $i_q = 0$; the IM then rotates synchronously. This is a natural consequence of field orientation: since there is no torque production when $i_q = 0$, there is no induced rotor current either. The IM must then rotate synchronously!

Impact of Harmonics

Let us briefly discuss to the case of multifrequency waveforms. In Paragraph 2.6.9 we considered the power produced by a perfectly sinusoidal voltage and a multifrequency current. In (5.54) it is the current \mathbf{i}_s^s that is (almost) perfectly sinusoidal. This is particularly true when closed-loop current control is used, see Chapter 6. The flux, on the other hand, will contain harmonics due to nonlinearities; the amount depending on motor design features. Hence, the conclusion of Paragraph 2.6.9, that the pulsations will contain the angular frequencies $6n\omega_1$, $n = 1, 2, \dots$, clearly holds for an IM.

5.2.5 Steady-State Relations

In the steady state, (5.39) can be expressed as

$$\mathbf{v}_s = (R_s + j\omega_1 L_\sigma) \mathbf{i}_s + j\omega_1 \boldsymbol{\psi}_R. \quad (5.56)$$

It is of particular interest to consider higher speeds—which allows the term $R_s \mathbf{i}_s$ to be neglected—and perfect orientation (which is a reasonable assumption at higher speeds, see Chapter 9). In component form we then have

$$v_d = -\omega_1 L_\sigma i_q \quad (5.57)$$

$$v_q = \omega_1 (L_\sigma i_d + \psi_R) = \{(5.47)\} = \omega_1 (L_\sigma + L_M) i_d. \quad (5.58)$$

Thus, at low loads when i_q is small, v_q dominates the stator voltage. For a constant i_d , it is seen the stator voltage must increase with the stator frequency (i.e., with the rotor speed).

5.2.6 Field Weakening

The modulus of the stator voltage vector is limited to V_{base} . When

$$|\mathbf{v}_s| = \sqrt{v_d^2 + v_q^2} = \{(5.57), (5.58)\} = |\omega_1| L_\sigma \sqrt{i_q^2 + \left(\frac{L_\sigma + L_M}{L_\sigma}\right)^2 i_d^2} = V_{\text{base}}$$

then $|\omega_1|$ can increase further only if i_d is decreased. As for the dc motor, this is called field weakening. This way, the IM can normally be operated at speeds up to four or five times base speed. Field-weakening operation of the IM is studied in Section 9.3.

5.2.7 Motor Parameters

Typical per-unit values for induction motors rated less than 100 kW are

$$\begin{aligned} \text{Magnetizing inductance } L_M &: 1.5 - 3 \\ \text{Leakage inductance } L_\sigma &: 0.15 - 0.3 \\ \text{Resistance } R_s, R_R &: 0.01 - 0.1. \end{aligned}$$

A motor of low power rating (say, 1 kW) tends to have a smaller per-unit magnetizing inductance and a larger per-unit stator resistance than a motor of higher rating. Yet, the ranges are quite narrow, so it is fairly obvious that similar or even identical control algorithms can be applied to any induction motor, regardless of rating. The theory and methods for PWM, vector control, and current control discussed in the preceding and following chapters are therefore generally applicable. It is not unusual that a control system designed for a 1-kW drive can be modified for a 100-kW drive simply by altering the controller parameters and using a more powerful converter, often with a lower switching frequency. This is a privilege of the ac drives control engineer which is seldom enjoyed by a control engineer in another field of application. Imagine trying to apply a control system designed for a single-engine propeller aircraft to a supersonic fighter!

5.2.8 Nominal Flux and Torque

Suppose that the IM is operated at nominal conditions, i.e., $|v_s| = V_{\text{base}}$, $|\mathbf{i}_s| = I_{\text{base}}$, and $\omega_1 = \omega_{\text{base}}$. The steady-state voltage-current relations (5.57)–(5.58) can then be expressed as

$$v_d = -\omega_{\text{base}} L_\sigma i_q \quad (5.59)$$

$$v_q = \omega_{\text{base}} (L_\sigma + L_M) i_d. \quad (5.60)$$

Because $v_d^2 + v_q^2 = V_{\text{base}}^2$, we obtain

$$\begin{aligned} \left(\frac{V_{\text{base}}}{\omega_{\text{base}}}\right)^2 &= \frac{v_d^2 + v_q^2}{\omega_{\text{base}}^2} = \{(5.59), (5.60)\} = (L_\sigma i_q)^2 + (L_\sigma + L_M)^2 i_d^2 \\ &= L_\sigma^2 \underbrace{(i_d^2 + i_q^2)}_{I_{\text{base}}^2} + L_M (L_M + 2L_\sigma) i_d^2. \end{aligned} \quad (5.61)$$

Solving for i_d gives the nominal flux-producing current component and, in turn, the flux level as follows:

$$i_d^N = \sqrt{\frac{\left(\frac{V_{\text{base}}}{\omega_{\text{base}}}\right)^2 - (L_\sigma I_{\text{base}})^2}{L_M (L_M + 2L_\sigma)}} \quad (5.62)$$

$$\psi_R^N = L_M i_d^N = \frac{V_{\text{base}}}{\omega_{\text{base}}} \sqrt{\frac{1 - \left(\frac{\omega_{\text{base}} L_\sigma I_{\text{base}}}{V_{\text{base}}}\right)^2}{1 + 2L_\sigma/L_M}} = \frac{V_{\text{base}}}{\omega_{\text{base}}} \sqrt{\frac{1 - \left(\frac{\omega_{\text{base}} L_\sigma}{Z_{\text{base}}}\right)^2}{1 + 2L_\sigma/L_M}}. \quad (5.63)$$

But $V_{\text{base}}/\omega_{\text{base}}$ and $Z_{\text{base}}/\omega_{\text{base}}$ are the base values for flux and inductance, respectively, so the nominal flux can also be expressed in normalized form as

$$\psi_{Rn}^N = \sqrt{\frac{1 - L_{\sigma n}^2}{1 + 2L_\sigma/L_M}}. \quad (5.64)$$

For the typical per-unit values $L_\sigma = 0.2$ and $L_M = 2$ we have $\psi_R = 0.89$ pu. Unlike a dc motor (and, as we shall see, an SM) nominal rotor flux of the IM is *not* 1 pu!

PROBLEM 5.3

What is the nominal stator flux?

Furthermore, the nominal torque is given by

$$\tau_e^N = \frac{3n_p}{2K^2} \psi_R^N i_q^N = \underbrace{\frac{3n_p}{2K^2} \frac{V_{\text{base}} I_{\text{base}}}{\omega_{\text{base}}} \kappa}_{\tau_{\text{base}}} \underbrace{\psi_{Rn}^N i_{qn}^N}_{\kappa} \quad (5.65)$$

where the factor $\kappa < 1$ and $\tau_{\text{base}} = n_p P_{\text{base}} / \omega_{\text{base}}$ (note that this is different from the base torque used for the dc motor in Table 4.2). For the same typical per-unit values $L_\sigma = 0.2$ and $L_M = 2$ as previously, we obtain $i_q^N = \sqrt{I_{\text{base}}^2 - (i_d^N)^2} = \sqrt{1 - (0.89/2)^2} = 0.90$ pu, giving $\kappa = 0.89 \cdot 0.90 = 0.80$. A closed-form expression for κ can be derived:

$$\begin{aligned} \kappa &= \frac{\omega_{\text{base}}}{V_{\text{base}} I_{\text{base}}} \psi_R^N i_q^N = \frac{\omega_{\text{base}}}{V_{\text{base}} I_{\text{base}}} \psi_R^N \sqrt{I_{\text{base}}^2 - (i_d^N)^2} \\ &= \frac{1}{I_{\text{base}}} \sqrt{\frac{1 - L_{\sigma n}^2}{1 + 2L_\sigma/L_M} \left[I_{\text{base}}^2 - \frac{\left(\frac{V_{\text{base}}}{\omega_{\text{base}}}\right)^2 - (L_\sigma I_{\text{base}})^2}{L_M(L_M + 2L_\sigma)} \right]} \\ &= \frac{1}{1 + 2L_\sigma/L_M} \sqrt{(1 - L_{\sigma n}^2) \left[\left(1 + \frac{L_\sigma}{L_M}\right)^2 - \frac{1}{L_{Mn}^2} \right]}. \end{aligned} \quad (5.66)$$

Note that when the base torque is selected as in (5.65), then $\tau_{en} = \kappa < 1$ pu for nominal operation of the IM.

5.2.9 Steady-State Relations for Line-Connected IMs

Although we here focus on variable-speed drives, most induction motors are in fact operated at constant or near-constant speeds in line-connected applications. Because the magnetization of the IM is made from the stator terminals, the IM can be started by direct line connection. Before going into details about dynamics and control of the IM, it is instructive first to have a brief look at some steady-state theory for line-connected IMs. We do so using synchronous coordinates.

Obviously, for a line-connected motor the stator frequency is constant, $\omega_1 = \omega_{\text{base}} = 1$ pu, so the voltage drop across the stator resistance can be neglected. So may also the magnetizing current, if $L_\sigma \ll L_M$, when we are concerned with the torque-producing rotor current only. Consider Figure 5.12; the impedance seen from the stator is then

$$\mathbf{Z}(j\omega_1) = j\omega_1 L_\sigma + \frac{R_R}{s} \quad (5.67)$$

so the rotor current is given by

$$\mathbf{i}_R = -\frac{\mathbf{v}_s}{\mathbf{Z}(j\omega_1)} = -\frac{\mathbf{v}_s}{j\omega_1 L_\sigma + R_R/s}. \quad (5.68)$$

The power to the shaft is the power developed in the “resistance” corresponding to the rotor emf

$$\frac{1-s}{s} R_R = \frac{1 - \frac{\omega_1 - \omega_r}{\omega_1}}{\frac{\omega_1 - \omega_r}{\omega_1}} R_R = \frac{\omega_r}{\omega_2} R_R$$

giving $P_e = \frac{3}{2K^2} \frac{\omega_r}{\omega_2} R_R |\mathbf{i}_R|^2$, and the following expression for the electrical torque:

$$\begin{aligned} \tau_e &= \frac{n_p P_e}{\omega_r} = \frac{3n_p}{2K^2} \frac{R_R}{\omega_2} |\mathbf{i}_R|^2 = \frac{3n_p}{2K^2} \frac{R_R}{\omega_2} \frac{|\mathbf{v}_s|^2}{(\omega_1 L_\sigma)^2 + (R_R/s)^2} \\ &= \frac{3n_p}{2K^2} \frac{s}{\omega_1 R_R} \frac{|\mathbf{v}_s|^2}{(sX_\sigma/R_R)^2 + 1} \end{aligned} \quad (5.69)$$

where $X_\sigma = \omega_1 L_\sigma$.

Maximum Torque

Maximum torque τ_e^{\max} is also called *pull-out torque* (or breakdown torque), as the IM is pulled out of normal operation (and stops) if the load torque exceeds τ_e^{\max} . Equation (5.69) has its maximum for the *pull-out slip* $s = s_p = R_R/X_\sigma$; typical values of s_p are between 10% and 20%. This is much larger than the nominal slip, which is only a couple of percents. We obtain

$$\tau_e^{\max} = \frac{3n_p}{2K^2} \frac{|\mathbf{v}_s|^2}{2\omega_1 X_\sigma}. \quad (5.70)$$

With (5.70), we can also express (5.69) as

$$\tau_e = \frac{s}{s_p} \frac{2\tau_e^{\max}}{(s/s_p)^2 + 1} = \frac{2s_p s}{s^2 + s_p^2} \tau_e^{\max}. \quad (5.71)$$

Low-to-Nominal Torque

At normal operating conditions, i.e., low-to-nominal torque, $s^2 \ll s_p^2$, so (5.69) can be approximated as

$$\tau_e \approx \frac{3n_p}{2K^2} \frac{s}{\omega_1 R_R} |\mathbf{v}_s|^2 = \frac{2s}{s_p} \tau_e^{\max}. \quad (5.72)$$

Thus, there is an approximately linear relationship between slip and torque. For a typical ratio $s/s_p = 1/5$, it is seen that the nominal torque is only 40% of the maximum torque. Thus, the IM has the capability to deliver torque above the nominal. But, since this requires overcurrent, $|\mathbf{i}_s| > I_{\text{base}}$, higher-than-nominal torque can be allowed only during shorter intervals (seconds, up to one minute).

Starting Torque

At starting, $\omega_r = 0$, so $s = (\omega_1 - 0)/\omega_1 = 1$, giving

$$\tau_e^{\text{start}} = \frac{3n_p}{2K^2} \frac{1}{\omega_1 R_R} \frac{|\mathbf{v}_s|^2}{\left(\frac{X_\sigma}{R_R}\right)^2 + 1} = \left\{ \left(\frac{X_\sigma}{R_R} \right)^2 \gg 1 \right\} \approx \frac{3n_p}{2K^2} \frac{R_R}{\omega_1 X_\sigma^2} |\mathbf{v}_s|^2 = 2s_p \tau_e^{\max}. \quad (5.73)$$

We find that the starting torque is typically about 30% of the maximum torque (and lower than the nominal torque). That the starting torque is fairly low is often a problem. It is interesting to note that the starting torque is proportional to the rotor resistance, whereas the nominal torque is inversely proportional to the rotor resistance. One method for increasing the starting torque is therefore to use a rotor with slip rings (i.e., the rotor winding is not short-circuited) connected to a set of external resistances, *de facto* giving a larger R_R . As the motor accelerates, the external resistances are automatically disconnected, and the slip rings are short circuited.

A more elegant solution is to design the rotor slots such that the rotor resistance varies with the speed. The induction of rotor current is due to the relative movement between the stator current vector and the rotor, so the frequency of the actual rotor current (in rotor coordinates) is the slip frequency. At starting, when ω_r is small, the slip frequency is 50 Hz (in Europe). At higher speeds, the slip frequency is normally less than 2 Hz (corresponding to a slip around 4%). If the rotor slots are designed—using the skin effect—so that the resistance at higher frequencies is larger than the dc resistance, the desired high starting and low nominal-speed rotor resistance is obtained. Such a rotor slot design is shown in Figure 5.14. The resulting design is called a double-cage rotor. At higher frequencies, the current penetration is poor; current is conducted only in the outer cage, which has a small cross section and high resistance. At low frequencies, the current penetrates into the inner cage, which has much lower resistance.

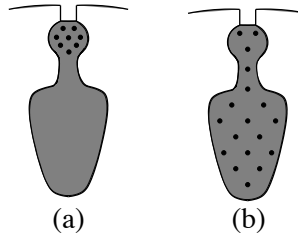


Figure 5.14. Rotor slot design (double-cage rotor) giving (a) concentrated current distribution (high resistance) at higher rotor frequencies, and (b) uniform distribution (low resistance) at low rotor frequencies.

Summary

$$\tau_e \approx \begin{cases} \tau_e^{\max} = \frac{3n_p}{2K^2} \frac{|\mathbf{v}_s|^2}{2\omega_1 X_\sigma} & \text{at pull-out, } s = s_p \\ \frac{2s}{s_p} \tau_e^{\max} & \text{at normal operation} \\ 2s_p \tau_e^{\max} & \text{at starting} \end{cases} \quad (5.74)$$

where $s_p = R_R/X_\sigma$.

Stator Current

From the equivalent circuit, we find the following expression for the stator current, again neglecting the magnetizing current:

$$\mathbf{i}_s = \frac{\mathbf{v}_s}{jX_\sigma + R_R/s} = \frac{s}{X_\sigma} \frac{X_\sigma}{R_R} \frac{\mathbf{v}_s}{jsX_\sigma/R_R + 1} \quad (5.75)$$

giving

$$|\mathbf{i}_s| = \frac{s}{s_p X_\sigma} \frac{|\mathbf{v}_s|}{\sqrt{(s/s_p)^2 + 1}}. \quad (5.76)$$

From this relation we obtain the special cases of low-to-nominal torque [$(s/s_p)^2 \ll 1$], maximum torque ($s = s_p$), and starting [$s = 1$, $(s/s_p)^2 \gg 1$] as

$$|\mathbf{i}_s| = \begin{cases} \frac{s}{s_p} \frac{|\mathbf{v}_s|}{X_\sigma}, & \text{low-to-nominal torque} \\ \frac{1}{\sqrt{2}} \frac{|\mathbf{v}_s|}{X_\sigma}, & \text{maximum torque} \\ \frac{|\mathbf{v}_s|}{X_\sigma}, & \text{starting.} \end{cases} \quad (5.77)$$

With $s/s_p = 1/5$ at nominal torque, and $X_\sigma = 0.2$ pu, we obtain the per-unit values 1, 3.5, and 5 at nominal torque, maximum torque, and starting, respectively. The large starting current is typical for line-connected induction motors (and quite similar to the dc motor case, see Figure 4.12). This may be a problem, because the drive may, as a dc motor, trip due to overcurrent. One method for solving the problem is to start the motor Y-connected (thereby reducing the current by $1/\sqrt{3}$) and switch to a Δ connection at a sufficiently high speed.

Numerically Calculated Relations

Since the above expressions for torque and current were derived using a simplified model with the magnetizing current and stator resistance neglected, they are approximations. In Figure 5.15 we compare the results to those for the full model for the parameters $n_p = 1$, $R_s = 0.04$, $R_R = 0.02$, $L_\sigma = 0.2$, and $L_M = 2$ pu, and with power-invariant vector scaling. Note that the torque is normalized with respect to the nominal torque $\tau_e^N = \kappa = 0.8$ pu given by (5.65). As can be seen, the correspondence is good, except that the simplified model over estimates the maximum torque and that the true model gives a nonzero stator current also at $\omega_r = 1$ pu: the magnetizing current.

We also in Figure 5.15 plot the rotor flux modulus. It is seen that when the torque is nominal, $\tau_e = \tau_e^N$, then $\psi_R = 0.89$ pu, i.e., the nominal value according to (5.64). For small slips ($\omega_r \approx 1$ pu), the flux is still approximately nominal, whereas it is much lower when the slip is large (speed much lower than 1 pu).

PROBLEM 5.4

A fan is driven by an induction motor which is directly connected in a Δ to a 400-V (line-to-line), 50-Hz three-phase voltage. The power drawn by the fan is given by $P_m = k\omega_m^3$, where $k = 0.0024 \text{ kgm}^2$. Suppose that $P_m \approx 1 \text{ kW}$; what is then likely the number of pole pairs of the IM?

5.2.10 Transient Impedance

Let us also briefly analyze the transient behavior of the IM. Suppose that a transient voltage—e.g., a step—is applied at the stator terminals. To calculate the *immediate* transient response of the stator current to the voltage transient, it can safely be assumed that the magnetizing current is constant, as the magnetizing inductance L_M is much larger than the total leakage inductance L_σ .

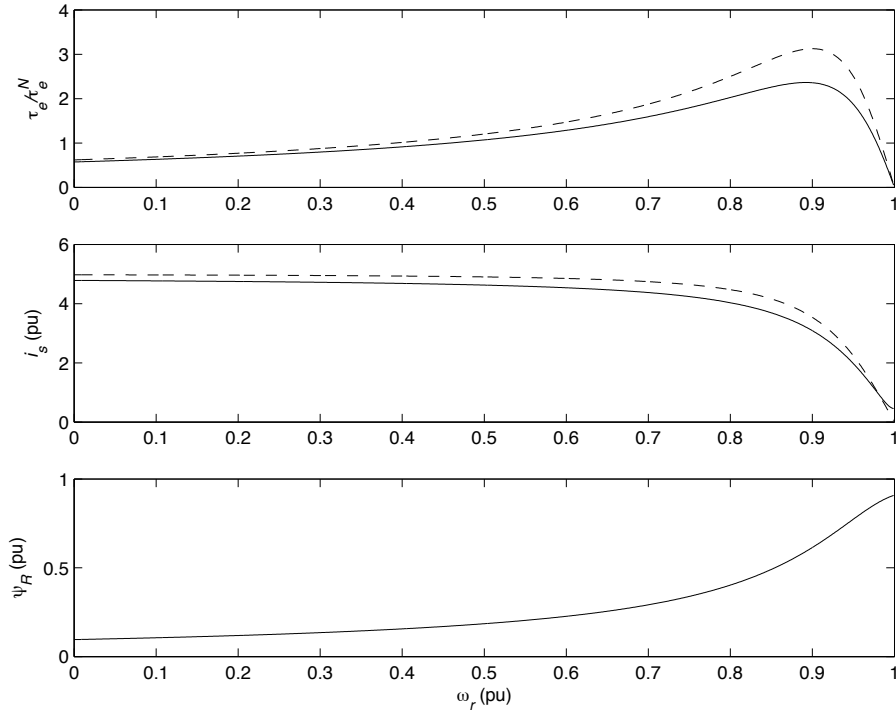


Figure 5.15. Numerically calculated torque, current modulus, and flux modulus as functions of the speed for the full IM model (solid) and the approximate model (dashed).

The entire transient response therefore goes through the rotor circuit. Approximating the rotor emf as constant during the transient, the transient impedance seen from the stator terminals is

$$\mathbf{Z}_\sigma^s(p) = R_\sigma + pL_\sigma \quad (5.78)$$

where $R_\sigma = R_s + R_R$. As the transfer function from voltage to current is the inverse of the impedance, the Laplace transform of the impulse response is

$$\mathbf{Z}_\sigma^s(p)^{-1} = \frac{1}{R_\sigma + pL_\sigma} \quad (5.79)$$

which has a pole at $p = -R_\sigma/L_\sigma$. The impulse response thus converges with the transient time constant

$$T_\sigma = \frac{L_\sigma}{R_\sigma}. \quad (5.80)$$

One should keep in mind, though, that a characterization of the transient response using this type of model holds only for the immediate response. If a voltage step is applied, the magnetizing current will eventually change, resulting in a slow transient response with the rotor time constant $T_r = L_M/R_R$. The rotor time constant is significantly larger than the transient time constant. Let us consider again the per-unit values $R_s = 0.04$, $R_R = 0.02$, $L_\sigma = 0.2$, and $L_M = 2$. Then

$T_\sigma = 3.3$ pu and $T_r = 100$ pu, which for a base frequency of 50 Hz translate to 11 ms and 318 ms, respectively.

Transients are important to consider in variable-speed drives which use closed-loop stator current control. As will be seen in Chapter 6, current control is preferably made in synchronous coordinates, so we should also pay attention to the synchronous-frame transient impedance. Since dq transformation implies replacing p by $p + j\omega_1$, we immediately obtain

$$\mathbf{Z}_\sigma(p) = R_\sigma + (p + j\omega_1)L_\sigma. \quad (5.81)$$

This time, the inverse transient impedance has a single complex pole at $p = -1/T_\sigma - j\omega_1$. Therefore, the immediate transient response will be a damped oscillation of angular frequency ω_1 .

5.2.11 Starting Dynamics of Line-Connected IMs

In both variable-speed and line-connected drives, it is important to study the transient response of the motor. The classical book by Kovács [51] is devoted to the topic of transient analysis of ac motors. Since we already have discussed the steady-state characteristics of line-connected IMs, it is insightful to make a brief discussion also of the dynamics.

Instantaneous Maximum Starting Current

In (5.77) we calculated the starting current using a steady-state motor model. This is not entirely correct; as we shall see below, the stator current is pulsating during the startup. The starting current 5 pu obtained from (5.77) in the example illustrated in Figure 5.15 is the mean value. The instantaneous maximum starting current is even larger. To calculate this, it can again be assumed that the magnetizing current is equal to zero: the immediate stator current response to an application of stator voltage goes through the rotor circuit. The relation between stator voltage and current is then the transient impedance. Let the applied stator voltage vector be

$$\mathbf{v}_s^s = V e^{j(\omega_1 t + \varphi)} \Leftrightarrow \mathbf{v}_s = V e^{j\varphi}, \quad t \geq 0. \quad (5.82)$$

Taking the Laplace transform yields

$$\mathbf{I}_s(p) = \frac{1}{\mathbf{Z}_\sigma(p)} \mathbf{V}_s(p) = \frac{1}{(p + j\omega_1)L_\sigma + R_\sigma} \frac{V e^{j\varphi}}{p} \quad (5.83)$$

giving

$$\mathbf{i}_s = \mathcal{L}^{-1}\{\mathbf{I}_s(p)\} = \frac{V e^{j\varphi}}{j\omega_1 L_\sigma + R_\sigma} \left(1 - e^{-(j\omega_1 + R_\sigma/L_\sigma)t}\right), \quad t \geq 0 \quad (5.84)$$

and (again with $X_\sigma = \omega_1 L_\sigma$)

$$|\mathbf{i}_s|^2 = \frac{V^2}{X_\sigma^2 + R_\sigma^2} \left(1 + e^{-2R_\sigma t/X_\sigma} - 2e^{-R_\sigma t/X_\sigma} \cos \omega_1 t\right), \quad t \geq 0. \quad (5.85)$$

As $R_\sigma/X_\sigma < 1$ ($R_\sigma/X_\sigma \ll 1$ for large motors which have small per-unit resistances), the instantaneous maximum value of (5.85) occurs approximately when $\cos \omega_1 t = -1$, i.e., when $t = \pi/\omega_1$. Substituting this value in (5.85) yields

$$|\mathbf{i}_s|_{\max} \approx \frac{V}{X_\sigma} \left(1 + e^{-\pi R_\sigma/X_\sigma}\right) \quad (5.86)$$

where R_σ^2 has been neglected. With the same parameter values as before, $R_\sigma = 0.04 + 0.02 \text{ pu} = 0.06 \text{ pu}$ and $L_\sigma = 0.2 \text{ pu}$, we have $|\mathbf{i}_s|_{\max} \approx 6.9 \text{ pu}$ for $V = \omega_1 = 1 \text{ pu}$, to be compared to the previously obtained 5 pu.

Starting Transient

From the steady-state theory we know to expect a fairly low starting torque. The torque then increases with the speed, reaches the maximum (pull-out) torque when $s = s_p$, and finally settles to a value proportional to the slip. Let us simulate a two-pole IM using a steady-state electrical model and the following mechanical model (cf. Paragraph 4.2.3), with a load torque proportional to the speed:

$$J \frac{d\omega_r}{dt} = \tau_e - b\omega_r \quad (5.87)$$

where $J = 100 \text{ pu}$. The motor parameters are $R_s = 0.04$, $R_R = 0.02$, $L_\sigma = 0.2$, and $L_M = 2 \text{ pu}$, giving $\kappa = 0.80$, whereas $\omega_{\text{base}} = 314 \text{ rad/s}$. The load torque is nominal ($\tau_e^N = \kappa = 0.8 \text{ pu}$) at base speed, i.e., $b = 0.8 \text{ pu}$.

The simulation depicted in **Figure 5.16** (dashed lines) looks nice enough; it shows precisely what can be expected from the steady-state theory. However, we have not taken into account the electrical dynamics, so the result is incorrect. This can be seen in the stator current: the maximum is somewhat lower than 5 pu—a value also found by the steady-state theory—which is less than the instantaneous maximum of 6.9 pu obtained from (5.86).

A simulation using the true dynamic electrical model of the IM has been overlayed (solid lines) in **Figure 5.16**. Now, the instantaneous maximum stator current of the simulation agrees with the theoretical 6.9 pu. Furthermore, it can be observed that the starting torque is pulsating and that the mean torque over the startup is somewhat lower than the torque of the steady-state simulation. Hence, in reality it takes longer time for the speed to reach the steady-state value of (slightly below) 1 pu than in the incorrect simulation.

The reason for the erroneous result of the simulation using a steady-state electrical model is that flux dynamics are slow—in the same range as the mechanical dynamics—due to a magnetizing inductance which is much larger than the leakage inductance. The electrical dynamics therefore cannot be neglected as seen from the mechanical dynamics. Thus, one should be cautious about drawing too general conclusions from the steady-state electrical model for the induction motor, i.e., the standard equivalent circuit of Figure 5.12.

The starting transient of an induction motor is very dependent on the relation between the inertia J , the load torque, and the damping of the electrical dynamics. Light rotors and mechanical loads—having small J —of course give shorter speed rise time, but also give a system that is not as well damped. It is illustrative to present two additional simulations. In **Figure 5.17**, the inertia has been lowered from 100 to 30 pu, and the load torque is set to zero. As can be seen, the speed rise time is now significantly shorter than previously, whereas the dynamics are obviously much less damped. Note the tendency to oscillations, particularly in the torque, which is not at all captured in the incorrect simulation.

Lowering the inertia further to 10 pu (which is perhaps unreasonably small for a practical IM with base frequency 50 Hz) yields the simulation results depicted in **Figure 5.18**. Now, the rotor speed and the electrical quantities do not settle to constant values, but keep oscillating with constant amplitudes. This is a well-known phenomenon which has been acknowledged ever since the invention of the IM. The phenomenon is known as *hunting*, and is a result of the nonlinear characteristics of the IM dynamics. As mentioned in Paragraph 5.2.2, the electrical dynamics can

often be regarded linear, with some coefficients that vary with ω_r . This simplification is not valid when the mechanical dynamics are fast.

With this we conclude the discussion on the open-loop dynamics of the induction motor, and note that closed-loop control reduces but does not eliminate the risk for oscillations. The flux dynamics of the IM make this motor type more difficult to analyze and control than other motor types.

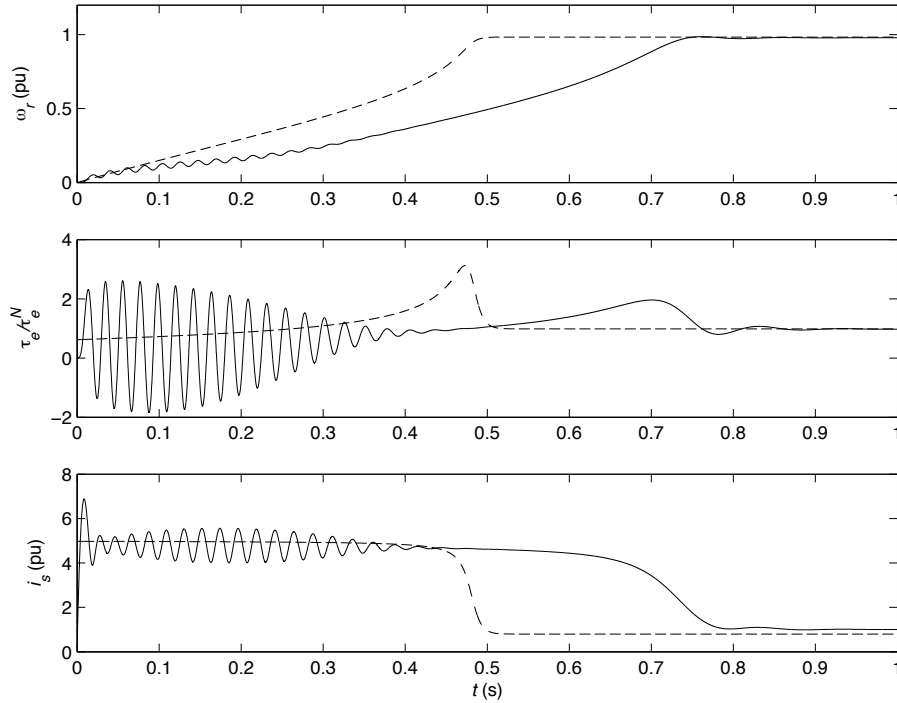


Figure 5.16. Startup simulations of a line-connected IM drive using dynamic (solid) and steady-state (dashed) electrical models, respectively, for $J = 100$ pu.

5.2.12 Volts-per-Hertz Control

The traditional method for controlling converter-fed induction motors is to linearly vary both the stator voltage magnitude and the stator frequency with the speed reference ω_{ref} as follows:

$$\omega_1 = \omega_{\text{ref}} + \hat{\omega}_2 \quad (5.88)$$

$$|\mathbf{v}_s| = \begin{cases} \frac{|\omega_1|}{\omega_{\text{base}}} V_{\text{base}}, & |\omega_1| \leq \omega_{\text{base}} \\ V_{\text{base}}, & |\omega_1| > \omega_{\text{base}} \end{cases} \quad (5.89)$$

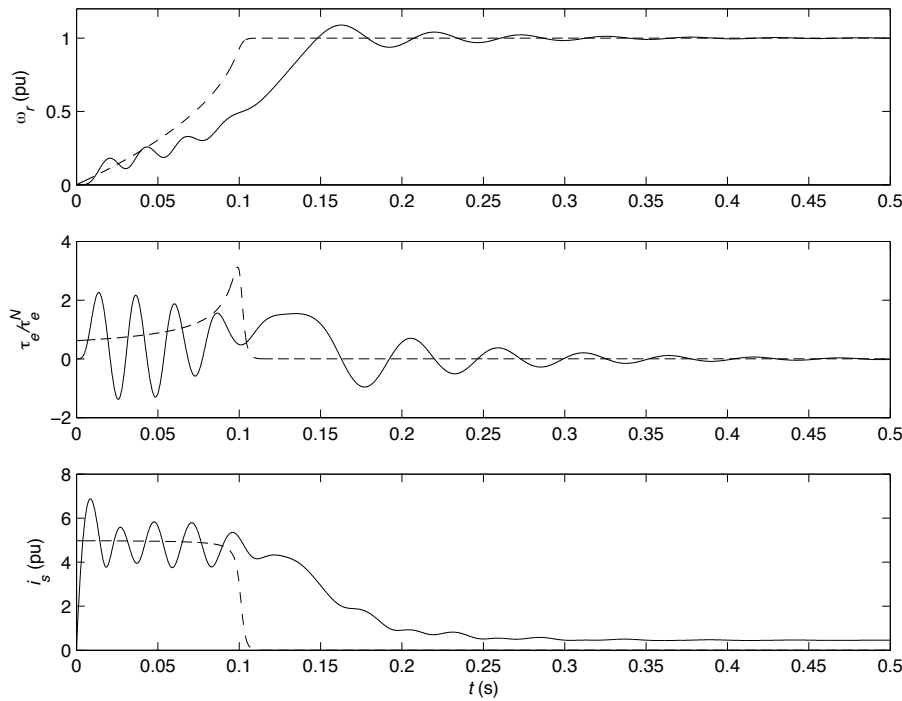


Figure 5.17. Startup simulations of a line-connected IM drive using dynamic (solid) and steady-state (dashed) electrical models, respectively, with lower inertia ($J = 30 \text{ pu}$) and zero load torque.

where $\hat{\omega}_2$ is an estimate of the angular slip frequency. (If precise speed control is not necessary, $\hat{\omega}_2$ can be set to zero.) This is known as volts-per-hertz control, and is an open-loop control scheme; measurement of neither current nor speed is needed. It is also a scalar control scheme, as only the modulus—not the phase—of the stator voltage is controlled using a VSC.

PROBLEM 5.5

How is field weakening obtained in volts-per-hertz control?

Due to its simplicity, volts-per-hertz control is frequently used in practice, but the control scheme is associated with several drawbacks.

- Because the stator current is not controlled in closed loop, there will be transients similar to that when starting a line-connected IM. For steps in the speed reference, there will be transient reductions in the flux and transient overcurrents. These effects can be reduced or eliminated by low-pass filtering the speed reference before it is used in the control algorithm. See Figure 5.19.
- These transients are fairly slow, typically with large oscillations in the torque, as seen in Figure 5.19. Fast and precise torque control is not possible.
- The method cannot be used for synchronous motors, as these require proper vectorial placement of the stator current relative the rotor flux in order to obtain a non-oscillating torque, as will be seen in the next section.

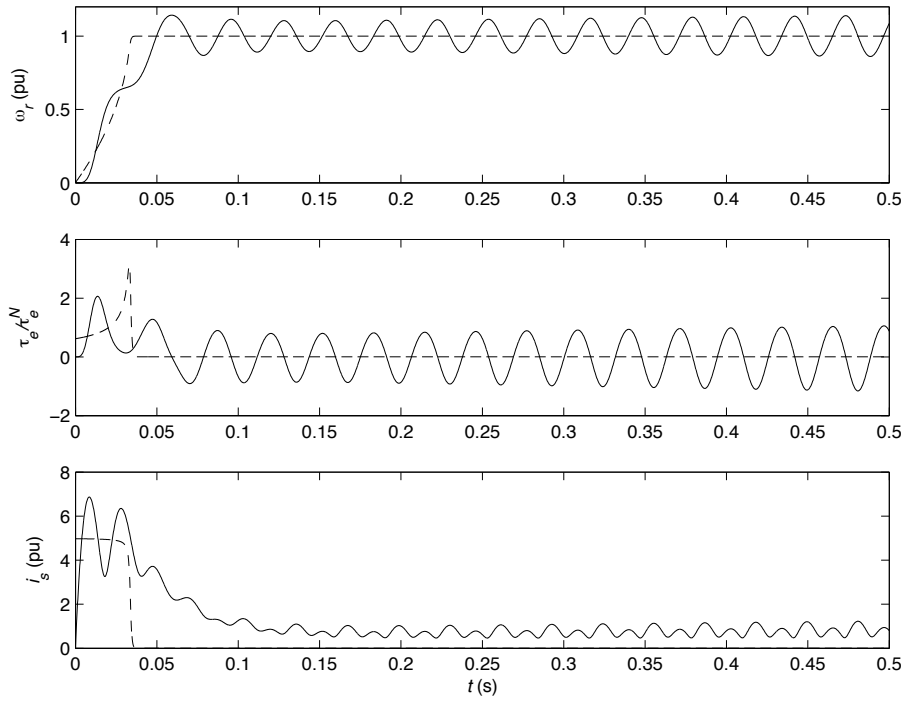


Figure 5.18. Startup simulations of a line-connected IM drive using dynamic (solid) and steady-state (dashed) electrical models, respectively, with even lower inertia ($J = 10 \text{ pu}$) and zero load torque.

PROBLEM 5.6

A two-pole induction motor with the parameters $L_M = 200 \text{ mH}$, $L_\sigma = 20 \text{ mH}$, $R_s \approx 0$, and $R_R = 0.3 \Omega$ is fed from a converter using volts-per-hertz control. Determine the stator voltage and the stator frequency when the mechanical speed is 1800 rpm and the load torque is 100 Nm. Also determine the efficiency of the motor at this operating point.

5.3 Dynamic Model for the Permanent-Magnet Synchronous Motor

We begin by studying the model for round-rotor PMSMs. The (more complicated) model for salient PMSMs then follows in Paragraph 5.3.8. The stator circuit of the PMSM is similar to that of the IM, so the same equation, (5.5), must hold

$$\mathbf{v}_s^s - R_s \mathbf{i}_s^s - \frac{d\psi_s^s}{dt} = 0. \quad (5.90)$$

In this case, the stator flux is given by

$$\psi_s^s = L_s \mathbf{i}_s^s + \psi_R^s \quad (5.91)$$

where L_s is the stator inductance and ψ_R^s is the rotor flux linkage, which is produced by the permanent magnets. The rotor flux defines the d axis of the rotor, which is displaced by the

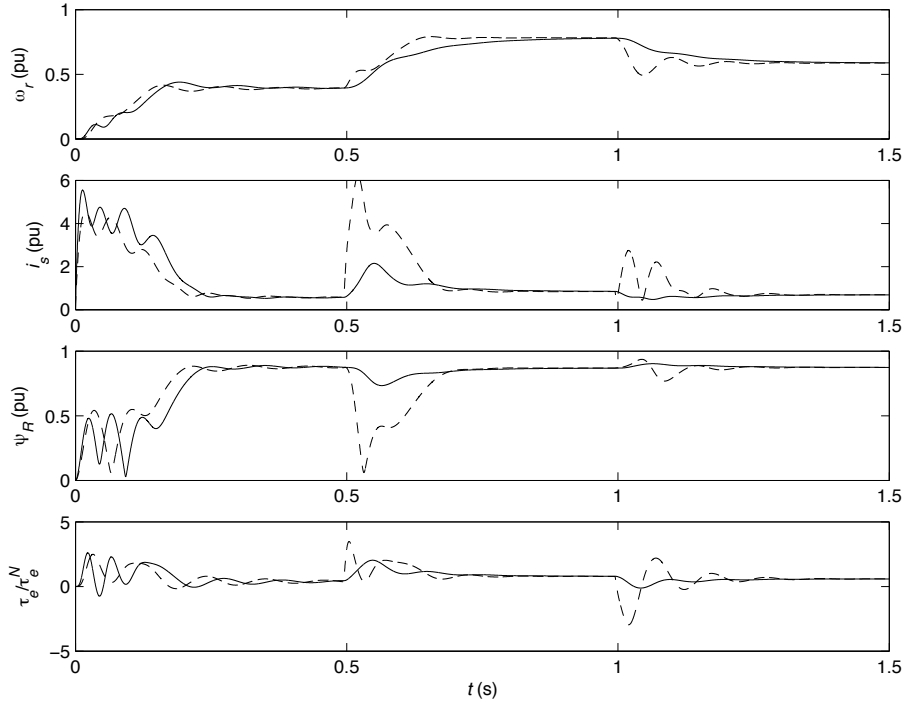


Figure 5.19. Volts-per-hertz control of an IM drive with $J = 100$ pu. Steps in the speed reference are made at $t = 0$, $t = 0.5$ s, and $t = 1$ s. Solid curves show response with low-pass-filtered speed reference, dashed curves without.

flux angle θ relative the α axis, as shown in Figure 5.3. Hence, the rotor flux vector is given by $\psi_R^s = \psi_R e^{j\theta}$. The flux modulus ψ_R can be assumed constant, so for a constant L_s

$$\frac{d\psi_s^s}{dt} = L_s \frac{d\mathbf{i}_s^s}{dt} + j\omega_r \psi_R e^{j\theta} \quad (5.92)$$

where $\omega_r = \dot{\theta}$. Now, (5.90) can be written as

$$L_s \frac{d\mathbf{i}_s^s}{dt} = \mathbf{v}_s^s - R_s \mathbf{i}_s^s - \underbrace{j\omega_r \psi_R e^{j\theta}}_{\mathbf{E}^s} \quad (5.93)$$

where the term $\mathbf{E}^s = j\omega_r \psi_R e^{j\theta}$ is the back emf (unlike the IM, there is no difference between the rotor, flux, and back emfs for the PMSM). This equation can be represented by the dynamic equivalent circuit depicted in Figure 5.20.

5.3.1 Transformation to Synchronous Coordinates

For the PMSM—perhaps even more so than for the IM—it is insightful to transform the equations to synchronous coordinates. Transforming (5.93) with the angle θ_1 we obtain

$$L_s \frac{d(e^{j\theta_1} \mathbf{i}_s)}{dt} = e^{j\theta_1} \mathbf{v}_s - R_s e^{j\theta_1} \mathbf{i}_s - j\omega_r \psi_R e^{j\theta} \quad (5.94)$$

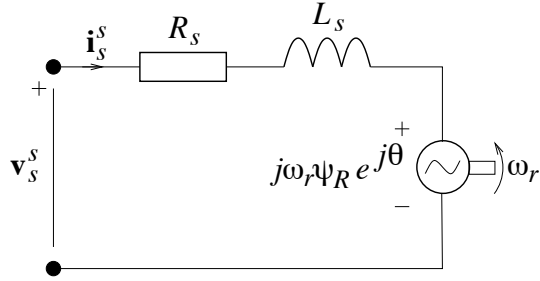


Figure 5.20. Dynamic equivalent circuit for the round-rotor PMSM.

and, again with $\omega_1 = \dot{\theta}_1$,

$$L_s \frac{d\mathbf{i}_s}{dt} = \mathbf{v}_s - (R_s + j\omega_1 L_s) \mathbf{i}_s - j\omega_r \psi_R e^{j(\theta - \theta_1)} \quad (5.95)$$

$$= \mathbf{v}_s - (R_s + j\omega_1 L_s) \mathbf{i}_s - \underbrace{j\omega_r \psi_R e^{j\tilde{\theta}}}_{\mathbf{E}} \quad (5.96)$$

where $\tilde{\theta} = \theta - \theta_1$ is the error angle between the actual flux angle and the synchronous coordinate system used in the dq transformation. In this equation we see that in order for the back-emf term $j\omega_r \psi_R e^{j\tilde{\theta}}$ to be constant, $\tilde{\theta}$ has to be constant. The applied stator voltage must rotate synchronously with the rotor of the PMSM. When $\theta_1 = \theta$, i.e., the field orientation is perfect, then $\omega_1 = \omega_r$ and (5.96) reduces to

$$L_s \frac{d\mathbf{i}_s}{dt} = \mathbf{v}_s - (R_s + j\omega_r L_s) \mathbf{i}_s - j\omega_r \psi_R. \quad (5.97)$$

5.3.2 Motor Parameters

The stator resistance of a PMSM is in the same range as that of an IM, i.e., 0.01 pu to 0.1 pu. On the other hand, the stator inductance is typically much smaller for a PMSM than for an IM: 0.2 pu to 0.4 pu for magnetically round rotors with surface-mounted magnets (see Paragraph 5.3.8 for salient PMSMs). This is in the range of the leakage inductance of the IM. The reason is that the permeability of the magnets is approximately equal to the permeability of the airgap. The magnets thus affect the magnetic flux path in the same way as widening the airgap by the magnet thickness. Also, the airgap of a PMSM is usually made wider than that of an IM of similar rating, as previously mentioned.

5.3.3 Torque Production and Control Principle

The torque equation (5.53) applies also to the PMSM

$$\tau_e = \frac{3n_p}{2K^2} \operatorname{Im}\{\boldsymbol{\psi}_R^* \mathbf{i}_s\} \quad (5.98)$$

and with $\boldsymbol{\psi}_R = \psi_R e^{j\tilde{\theta}}$ we obtain

$$\tau_e = \frac{3n_p}{2K^2} \operatorname{Im}\left\{\left(\psi_R e^{j\tilde{\theta}}\right)^* \mathbf{i}_s\right\} = \frac{3n_p}{2K^2} \psi_R \left(i_q \cos \tilde{\theta} - i_d \sin \tilde{\theta}\right). \quad (5.99)$$

Hence, if $\tilde{\theta}$ is not constant, the torque of the PMSM will pulsate. If a PMSM is line connected, then—unlike an IM—it generally will not start as the torque will be pulsating. We have thus shown that, in order to control a PMSM with high performance, the flux angle θ must be known. As θ is also the physical rotor position, a position sensor—a digital position encoder or a resolver—has to be used, or θ has to be estimated. See Chapter 8.

Perfect Field Orientation

With exact knowledge of the flux angle, $\theta_1 = \theta$, (5.99) reduces to

$$\tau_e = \frac{3n_p}{2K^2} \psi_R i_q. \quad (5.100)$$

This relation is similar to (5.55) for the IM. It is again only the current component i_q that contributes to the torque, so it is apparent that the two motor types can be controlled using similar principles. Since the flux is created from inside the rotor, i_d can be controlled to zero, giving maximum torque for a certain stator current modulus. A PMSM therefore requires a smaller stator current modulus than an IM of similar power rating.

For the PMSM it can be said that the magnetization is “paid once and for all” when the motor is purchased. For the IM, the magnetization has to be supplied from the stator, which is paid for by a larger stator current (which may require a converter of higher current rating), giving increased losses in the stator resistance as well. This may offset the extra investment cost of a PMSM as compared to an IM of similar rating.

5.3.4 Rotor Flux and Base Frequency

For $i_d = 0$ we obtain the following steady-state relations from (5.97):

$$v_d = -\omega_r L_s i_q \quad (5.101)$$

$$v_q = R_s i_q + \omega_r \psi_R. \quad (5.102)$$

When the torque is low, $i_q \approx 0$, we have $|v_s| = |v_q| = |\omega_r| \psi_R$. Hence, at base speed,

$$V_{\text{base}} \approx \omega_{\text{base}} \psi_R \quad (5.103)$$

so it is logical to select the base frequency as

$$\omega_{\text{base}} = \frac{V_{\text{base}}}{\psi_R}. \quad (5.104)$$

Then, $\psi_R = 1$ pu (unlike for the IM, which has $\psi_R < 1$ pu).

5.3.5 Field Weakening

As ψ_R is constant, field weakening requires making i_d negative. In the steady state with a small i_q , $v_d = R_s i_d - \omega_r L_s i_q$ is also small, whereas

$$v_q = \omega_r (L_s i_d + \psi_R) \approx V_{\text{base}}. \quad (5.105)$$

But $|i_d|$ must not be made larger than I_{base} , so

$$\omega_r^{\max} = \frac{V_{\text{base}}}{\psi_R - L_s I_{\text{base}}}. \quad (5.106)$$

For L_s in the interval 0.2 to 0.4 pu we get ω_r^{\max} from 1.3 to 1.7 pu. The field-weakening range for round-rotor PMSMs is thus normally much smaller than for IMs.

5.3.6 Transient Impedance

The impedance of the PMSM, as observed from the stator terminals, is given by

$$\mathbf{Z}_s^s(p) = R_s + pL_s \quad \mathbf{Z}_s(p) = R_s + (p + j\omega_1)L_s. \quad (5.107)$$

Since there is no magnetizing branch in the equivalent circuit of the PMSM, this is also the transient impedance. Comparing to the transient impedance of the IM—(5.78)—we see that the resistive part is roughly half that of the IM ($R = R_s + R_R$). The stator inductance is, as mentioned previously, in the same per-unit range as the leakage inductance of the IM. Thus, the time constant of the PMSM

$$T_s = \frac{L_s}{R_s} \quad (5.108)$$

is in per-unit value typically larger than the transient time constant T_σ the IM.

5.3.7 Power Factor

One benefit of the PMSM as compared to the IM is that it can be operated with unity power factor. In the steady state at higher speeds (when the stator-resistance voltage drop can be neglected), and with perfect field orientation, we have

$$\mathbf{v}_s = j\omega_r(L_s \mathbf{i}_s + \psi_R) \quad (5.109)$$

giving

$$\mathbf{v}_s \mathbf{i}_s^* = \omega_r \psi_R i_q + j\omega_r [\psi_R i_d + L_s(i_d^2 + i_q^2)]. \quad (5.110)$$

The active and reactive powers—cf. (2.132) and (2.133)—are proportional to the real and imaginary parts of (5.110)

$$P \sim \omega_r \psi_R i_q \quad Q \sim \omega_r [\psi_R i_d + L_s(i_d^2 + i_q^2)] \quad (5.111)$$

so by controlling i_d such that $\psi_R i_d + L_s(i_d^2 + i_q^2) = 0$, rather than just letting $i_d = 0$, unity power factor is obtained. However, even when $i_d = 0$ the power factor

$$\cos \varphi = \frac{P}{\sqrt{P^2 + Q^2}} = \frac{1}{\sqrt{1 + \left(\frac{L_s i_q}{\psi_R}\right)^2}} \quad (5.112)$$

is fairly high. At base flux ($\psi_R = 1$ pu) and base current ($i_q = 1$ pu), and with a typical inductance $L_s = 0.5$ pu, a power factor of 0.89 is obtained. Let us compare this to an induction motor. The relation for the IM corresponding to (5.109) is given by

$$\mathbf{v}_s = j\omega_1(L_\sigma \mathbf{i}_s + \Psi_R). \quad (5.113)$$

For perfect field orientation we have

$$\mathbf{v}_s \mathbf{i}_s^* = j\omega_1[L_\sigma(i_d^2 + i_q^2) + \psi_R i_d] + \omega_1 \psi_R i_q \quad (5.114)$$

which yields

$$\cos \varphi = \frac{P}{\sqrt{P^2 + Q^2}} = \frac{1}{\sqrt{1 + \left[\frac{L_\sigma(i_d^2 + i_q^2) + \psi_R i_d}{\psi_R i_q}\right]^2}}. \quad (5.115)$$

PROBLEM 5.7

Suppose that $L_M = 2$ pu and $L_\sigma = 0.2$ pu. What is then the power factor of the IM for **a)** the nominal load and **b)** half the nominal load?

PROBLEM 5.8

Find an expression for how i_d should be selected in order to give unity power factor for the PMSM.

PROBLEM 5.9

A two-pole, Y-connected PMSM with surface-mounted magnets has the nominal phase voltage and speed 230 V and 4000 rpm, respectively. The stator resistance is negligible and the stator inductance is 20 mH.

- a)** What is the modulus of the space vector for the rotor flux linkage assuming rms-value scaling?
- b)** The converter is rated 20 A (phase current). What is the maximum attainable speed in the steady state? **Hint:** Field weakening; assume perfect field orientation.
- c)** The load torque reaches 20 Nm over a short period of time. How should i_q be chosen if the load torque is to be balanced by the electrical torque? Is the converter's current rating exceeded?
- d)** Can unity power factor (seen from the converter, i.e., the stator terminals) be obtained for the operating condition in c)?
- e)** Determine the maximum obtainable steady-state electrical torque for unity power factor.

PROBLEM 5.10

An eight-pole PMSM is fed from a converter. The mechanical speed is 1500 rpm and the load torque is 100 Nm. The stator inductance is 5 mH and the stator resistance can be neglected. By closed-loop control, the stator current is regulated such that it is in phase with the stator voltage, whose rms phase voltage is 100 V.

The current references are changed, such that $i_d = 0$ is obtained. Which rms phase stator voltage is now required in order to maintain the torque and speed?

PROBLEM 5.11

An converter-fed two-pole PMSM operates with the stator frequency 17 Hz, producing a power of 2.0 kW to the mechanical load. The stator current is controlled such that $i_d = 0$, rms-value space-vector scaling is used, the rotor position is measured, and the motor parameters are $R_s = 0.5 \Omega$, $L_s = 6.0$ mH, and $\psi_R = 0.312$ Vs.

- a)** Find an expression for the stator current vector in stationary coordinates.
- b)** The control unit ceases to work, locking all three converter switches in the “1” position. Determine the stator current vector in synchronous coordinates as a function of time after the occurrence of this fault. The rotor speed can be assumed constant.

5.3.8 Salient PMSMs and Reluctance SMs

As the model otherwise would become extremely complicated, the mutual inductance of a salient SM is assumed to vary sinusoidally, cf. (5.2). Yet, complex space vectors cannot be used to model

salient PMSMs. The good thing is that equivalent real space vectors can be introduced instead, keeping essentially the same notation as in complex quantities. Restricting the study to the case of perfect field orientation, replacing complex space vectors by real vectors and replacing j by the matrix \mathbf{J} in (2.114), (5.97) is transformed to

$$\mathbf{L}_s \frac{di_s}{dt} = \mathbf{v}_s - (R_s \mathbf{I} + \mathbf{J}\omega_r L_s)i_s - \mathbf{J}\omega_r \psi_R, \quad \psi_R = \begin{bmatrix} \psi_R \\ 0 \end{bmatrix} \quad (5.116)$$

where \mathbf{I} is here the 2×2 identity matrix. As the stator inductance is not constant around the airgap, but equal to L_d and L_q along the d and q axes, respectively, \mathbf{L}_s is a matrix

$$\mathbf{L}_s = \begin{bmatrix} L_d & 0 \\ 0 & L_q \end{bmatrix}. \quad (5.117)$$

In component form we obtain

$$L_d \frac{di_d}{dt} = v_d - R_s i_d + \omega_r L_q i_q \quad (5.118)$$

$$L_q \frac{di_q}{dt} = v_q - R_s i_q - \omega_r (L_d i_d + \psi_R). \quad (5.119)$$

Also in this case, the equations can be represented as an equivalent circuit. However, due to the saliency, separate circuits are required for the d and q axes; see Figure 5.21. Thus, the dynamics are different in the two directions. Disregarding the cross coupling between the d and q axes, the transient impedances are, respectively, given by

$$Z_d(p) = R_s + pL_d \quad Z_q(p) = R_s + pL_q. \quad (5.120)$$

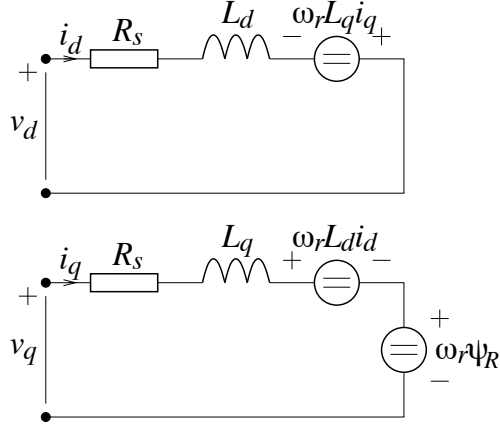


Figure 5.21. Dynamic equivalent circuit for the salient PMSM.

The mechanical power can be found by calculating the total active power developed in the emfs in Figure 5.21. With $E_d = -\omega_r L_q i_q$ and $E_q = \omega_r (L_d i_d + \psi_R)$, we have

$$\frac{3}{2K^2}(E_d i_d + E_q i_q) = \frac{3}{2K^2}\omega_r [\psi_R i_q + (L_d - L_q)i_d i_q]. \quad (5.121)$$

Dividing this expression by $\omega_m = \omega_r/n_p$, a formula for the electrical torque is obtained as

$$\tau_e = \frac{3n_p}{2K^2} [\psi_R i_q + (L_d - L_q) i_d i_q]. \quad (5.122)$$

Compared to (5.100), there is now an additional term: $\frac{3n_p}{2K^2} (L_d - L_q) i_d i_q$, which is due to the saliency of the rotor. This is the *reluctance torque*. When the saliency $L_d - L_q$ is relatively large it may be a good idea to use a nonzero i_d in order to maximize the torque production for a given stator current modulus, by utilizing the reluctance torque. Assuming that $\sqrt{i_d^2 + i_q^2} = I_{\text{base}}$ it can be shown that (5.122) is maximized for

$$\frac{i_d}{i_q} = \underbrace{\frac{(\sqrt{1+8\chi^2}-1)\operatorname{sgn}(\chi)}{\sqrt{2}\sqrt{4\chi^2+\sqrt{1+8\chi^2}-1}}}_{r(\chi)} \approx \chi, \quad \chi = \frac{(L_d - L_q)I_{\text{base}}}{\psi_R} \quad (5.123)$$

where the approximation holds for small χ . This is illustrated in Figure 5.22; notice that the linear approximation holds quite well also for the relatively large saliency $\chi = -0.4$.

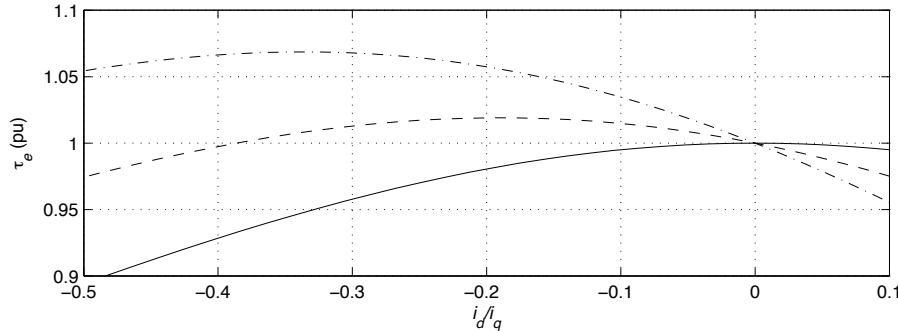


Figure 5.22. Maximum torque of a salient PMSM for (solid) $\chi = 0$, (dashed) $\chi = -0.2$, and (dash-dotted) $\chi = -0.4$.

Inductances and Field Weakening

Mounting the magnets inside the rotor allows the airgap width to be smaller. The d and q direction stator inductances are therefore larger in per-unit value than the stator inductance of a PMSM with surface-mounted magnets. Characteristic per-unit values are $0.4 < L_d < 0.7$ and $0.7 < L_q < 1$. This allows a larger field-weakening range. For salient PMSMs, it is easily seen that L_d replaces L_s in (5.106)

$$\omega_r^{\max} = \frac{V_{\text{base}}}{\psi_R - L_d I_{\text{base}}}. \quad (5.124)$$

Thus, ω_r^{\max} between 1.7 pu and 3.3 pu can be obtained with a salient PMSM.

Reluctance SMs

A motor with $L_d \neq L_q$ produces torque even when there is no magnetization in the rotor: $\psi_R = 0$. This is called a reluctance synchronous motor (RSM) or a synchronous reluctance motor (SynRM). Clearly, to obtain a reluctance torque, neither i_d nor i_q must be zero. It is not difficult to deduce that $|i_d| = |i_q|$ yields maximum torque for a certain current modulus. This can be shown by letting $i_d = \sqrt{2}I \cos \delta$ and $i_q = \sqrt{2}I \sin \delta$. Then

$$i_d i_q = 2I^2 \cos \delta \sin \delta = I^2 \sin 2\delta \quad (5.125)$$

which is maximized for $\delta = 45^\circ$.

The drawback of RSMs as compared to PMSMs is that a large i_d is required. This implies that the power factor will be lower, in the same range as for an IM. This is quite natural, since in both cases magnetization is made from the stator.

5.4 Unified IM/PMSM Model

Having derived dynamic models for the IM and PMSM, it will now be shown that these can be unified as one common model [32], assuming a round-rotor PMSM. One purpose of the unified model is to give better insight in the similarities and differences of sensorless control of IMs and PMSMs, see further Chapters 8 and 9.

Consider the IM model given by (5.35)–(5.36)

$$L_\sigma \frac{d\mathbf{i}_s^s}{dt} = \mathbf{v}_s^s - R_s \mathbf{i}_s^s - \frac{d\psi_R^s}{dt} \quad (5.126)$$

$$\frac{d\psi_R^s}{dt} = R_R \mathbf{i}_s^s - \left(\frac{R_R}{L_M} - j\omega_r \right) \psi_R^s. \quad (5.127)$$

The key to obtaining a unified IM/PMSM model is to express the rotor flux in polar form also for the IM

$$\psi_R^s = \psi_R e^{j\theta}. \quad (5.128)$$

Transforming (5.127) to synchronous coordinates using the transformation angle θ_1 , $\mathbf{i}_s = e^{-j\theta_1} \mathbf{i}_s^s$, results in

$$\frac{d(\psi_R e^{j\theta})}{dt} = R_R e^{j\theta_1} \mathbf{i}_s - \left(\frac{R_R}{L_M} - j\omega_r \right) \psi_R e^{j\theta} \quad (5.129)$$

giving

$$\begin{aligned} (\dot{\psi}_R + j\dot{\theta}\psi_R) e^{j\theta} &= R_R e^{j\theta_1} \mathbf{i}_s - \left(\frac{R_R}{L_M} - j\omega_r \right) \psi_R e^{j\theta} \\ \Rightarrow \dot{\psi}_R + j\dot{\theta}\psi_R &= R_R e^{-j\tilde{\theta}} \mathbf{i}_s - \left(\frac{R_R}{L_M} - j\omega_r \right) \psi_R \end{aligned} \quad (5.130)$$

where, as for the SM, $\tilde{\theta} = \theta - \theta_1$. Equation (5.126) is transformed to synchronous coordinates in a similar way

$$L_\sigma \frac{d\mathbf{i}_s}{dt} = \mathbf{v}_s - (R_s + j\omega_1 L_\sigma) \mathbf{i}_s - (\dot{\psi}_R + j\dot{\theta}\psi_R) e^{j\tilde{\theta}}. \quad (5.131)$$

Now, splitting (5.130) into real and imaginary parts yields

$$\dot{\psi}_R = R_R(i_d \cos \tilde{\theta} + i_q \sin \tilde{\theta}) - \frac{R_R}{L_M} \psi_R \quad (5.132)$$

$$\dot{\theta} = \omega_r + \frac{R_R i_q}{\psi_R} (i_q \cos \tilde{\theta} - i_d \sin \tilde{\theta}). \quad (5.133)$$

Not surprisingly, for perfect field orientation, $\tilde{\theta} = 0$, these two relations simplify to the ideal flux modulus dynamics (5.45) and the slip relation (5.46), respectively

$$\dot{\psi}_R = R_R i_d - \frac{R_R}{L_M} \psi_R \quad (5.134)$$

$$\dot{\theta} = \omega_r + \frac{R_R i_q}{\psi_R} \quad (5.135)$$

giving $\omega_1 = \dot{\theta}_1 = \dot{\theta}$.

We now adapt this model to the round-rotor PMSM. Since this motor has no rotor resistance, it is logical to start by letting $R_R = 0$ in (5.132) and (5.133), yielding

$$\dot{\psi}_R = 0 \quad (\text{the PMSM's flux modulus is constant}) \quad (5.136)$$

$$\dot{\theta} = \omega_r \quad (\text{the PMSM rotates synchronously}). \quad (5.137)$$

Hence, quite interestingly, the flux dynamics (5.132)–(5.133) are valid also for the PMSM, simply by letting $R_R = 0$. Substituting these the relations in (5.131) yields

$$L_\sigma \frac{d\mathbf{i}_s}{dt} = \mathbf{v}_s - (R_s + j\omega_1 L_\sigma) \mathbf{i}_s - j\omega_r \psi_R e^{j\tilde{\theta}}. \quad (5.138)$$

But this relation is identical to the stator current dynamics of the PMSM, (5.96), except that the leakage inductance L_σ should be replaced by the stator inductance L_s .

5.5 Mechanical Dynamics and Speed Control

The mechanical dynamics (4.16) for the dc motor also apply to the IM and the PMSM, assuming perfect field orientation and that the reluctance torque can be neglected for salient SMs. To take the number of pole pairs into account, ω_r should be replaced by the mechanical rotor speed ω_m , however

$$J \frac{d\omega_m}{dt} = \frac{3n_p}{2K^2} \psi_R i_q - \tau_l. \quad (5.139)$$

The load torque τ_l can be modeled as in (4.78) as a viscous part plus a part due to external conditions:

$$\tau_l = b\omega_m + \tau_L. \quad (5.140)$$

Since ω_r is the variable appearing in the electrical dynamics of the IM and the PMSM, it is convenient to express (5.139) in ω_r rather than ω_m :

$$\frac{J}{n_p} \frac{d\omega_r}{dt} = \frac{3n_p}{2K^2} \psi_R i_q - b \frac{\omega_r}{n_p} - \tau_L \quad (5.141)$$

or

$$J' \frac{d\omega_r}{dt} = \frac{3n_p}{2K^2} \psi_R i_q - b' \omega_r - \tau_L \quad (5.142)$$

where $J' = J/n_p$ and $b' = b/n_p$. This mechanical model is formally equal to that for the mechanical dynamics of the dc motor, (4.79). Speed controllers for IM and PMSM drives can therefore be designed as in Section 4.6, simply by making the following substitutions:

$$J \rightarrow \frac{J}{n_p} \quad b \rightarrow \frac{b}{n_p} \quad \psi \rightarrow \frac{3n_p \hat{\psi}_R}{2K^2} \quad i \rightarrow i_q \quad (5.143)$$

where $\hat{\psi}_R$ is an estimate of the rotor flux for IMs (in Chapter 9 it is shown how this can be obtained), whereas it is an estimate of the permanent-magnet flux for PMSMs. This yields the following controller parameter selections:

$$b_a = \frac{2K^2(\alpha_s \hat{J} - \hat{b})}{3n_p^2 \hat{\psi}_R} \quad k_{ps} = \frac{2K^2 \alpha_s \hat{J}}{3n_p^2 \hat{\psi}_R} \quad k_{is} = \frac{2K^2 \alpha_s^2 \hat{J}}{3n_p^2 \hat{\psi}_R}. \quad (5.144)$$

In the speed controller algorithm, it must be taken into account that limitation is necessary such that $i_d^2 + i_q^2 \leq I_{\max}^2$, where I_{\max} is the maximum allowed short-term stator current (which should be reduced to I_{base} after the maximum time that overcurrent is allowed). This yields Algorithm 5.1 and the block diagram shown in Figure 5.23.

Algorithm 5.1

Speed Controller for AC Drives

$$\begin{aligned} e_s &= \omega_{\text{ref}} - \omega_r \\ i_{q,\text{nom}}^{\text{ref}} &= k_{ps} e_s + k_{is} I_s - b_a \omega_r \\ i_q^{\text{ref}} &= \text{sat} \left(i_{q,\text{nom}}^{\text{ref}}, \sqrt{I_{\max}^2 - (i_d^{\text{ref}})^2} \right) \\ I_s &= I_s + T_s \left[e_s + \frac{1}{k_{ps}} (i_q^{\text{ref}} - i_{q,\text{nom}}^{\text{ref}}) \right] \end{aligned}$$

5.5.1 Normalization

Starting with base value for torque given in (5.65)

$$\tau_{\text{base}} = \frac{3n_p}{2K^2} \frac{V_{\text{base}} I_{\text{base}}}{\omega_{\text{base}}} \quad (5.145)$$

it is logical to select the base values for inertia and viscous damping constant as

$$J_{\text{base}} = \frac{n_p \tau_{\text{base}}}{\omega_{\text{base}}^2} \quad b_{\text{base}} = \frac{n_p \tau_{\text{base}}}{\omega_{\text{base}}}. \quad (5.146)$$

(Note that unlike the dc-motor base values in Table 4.2, these base values include the number of pole pairs.) This gives the following normalization of the mechanical dynamics:

$$J_n \frac{d\omega_{rn}}{dt_n} = \psi_{Rn} i_{qn} - b_n \omega_{rn} - \tau_{Ln}. \quad (5.147)$$

This equation is *not* formally equal to (5.142), as the factor $3n_p/2K^2$ has been removed. Exercise caution when using it!

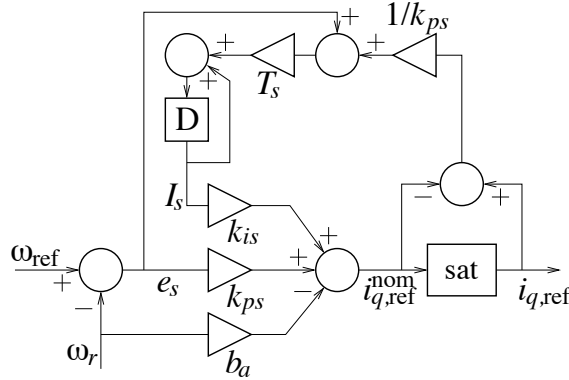


Figure 5.23. Digitally implemented two-degrees-of-freedom speed controller for ac drives.

5.6 Determination of Motor Parameters

As will be shown in the subsequent chapters, control of ac motor drives requires (at least fairly) accurate estimates of the motor parameters. Therefore, we in this section study methods for determining such from provided data and tests. We focus on IMs and round-rotor PMSMs. Throughout the section, rms-value space-vector scaling, $K = 1/\sqrt{2}$, is assumed. This is merely done for convenience, and does not dictate the same choice in the control system designed based on the obtained motor parameters.

5.6.1 Induction Motors

Name-Plate Data

Most induction motors are equipped with a name plate, on which important data are given. The following data for nominal operation are usually provided.

- RMS phase voltage and current for Y connection V_N and I_N .
- Output power P_{out}^N .
- Stator frequency in Hz f_N .
- Mechanical rotor speed in rpm n_N .
- Power factor $\cos \varphi_N$.

From these data, a number of important quantities and relations, which also hold for nominal operation, can be derived:

- Apparent input power: $S_{\text{in}}^N = 3V_N I_N$.
- Input power (active): $P_{\text{in}}^N = S_{\text{in}}^N \cos \varphi_N$.
- Efficiency: $\eta_N = P_{\text{out}}^N / P_{\text{in}}^N$.
- Angular stator frequency: $\omega_N = 2\pi f_N$.

- Mechanical rotor speed in rad/s: $\omega_m^N = 2\pi n_N / 60$.
- Number of pole pairs n_p : If the IM had rotated synchronously, then $n_p = \omega_N / \omega_m^N$. Due to the slip, ω_m^N is lower than the synchronous speed, though, so we get $n_p = \text{int}(\omega_N / \omega_m^N)$ where $\text{int}(\cdot)$ indicates integer part. Example: $\omega_N = 314$ rad/s (50 Hz) and $\omega_m^N = 100$ rad/s $\Rightarrow n_p = \text{int}(3.14) = 3$ (a six-pole motor).
- Electrical rotor speed in rad/s: $\omega_r^N = n_p \omega_m^N$.
- Slip: $s_N = (\omega_N - \omega_r^N) / \omega_N$.
- Torque: $\tau_e^N = P_{\text{out}}^N / \omega_m^N$.

Locked-Rotor and No-Load Tests

From the name-plate data obtained, only one motor parameter can be determined with good accuracy: the rotor resistance. Equation (5.72) gives the following relation:

$$R_R = \frac{3n_p}{2K^2} \frac{s|\mathbf{v}_s|^2}{\omega_1 \tau_e}.$$

With $K = 1/\sqrt{2}$ we get, at nominal operating conditions,

$$\hat{R}_R = \frac{3n_p s_N V_N^2}{\omega_N \tau_e^N}. \quad (5.148)$$

To obtain the remaining parameters, tests must be made. The stator resistance is particularly straightforward to obtain, as it is found simply by ohm measurement across the stator terminals.

In order to determine the inductances, two tests are useful. (Both resistances are also obtained in the process, giving alternative ways of determining them.)

- In the **locked-rotor test**, the rotor is barred from moving (giving $\omega_r = 0 \Leftrightarrow s = 1$). Using the nominal frequency, the stator voltage is then increased to a value V_{lr} (rms phase voltage) when the phase rms current reaches the base value. The (active) input power is then measured (using a watt meter): P_{lr} . Because the total resistance in the rotor circuit is only R_R (as compared to R_R/s normally), the magnetizing branch is for practical purposes short circuited, cf. Figure 5.10. The total impedance is then the transient impedance (5.81)

$$\mathbf{Z}_\sigma(j\omega_N) = R_s + R_R + j\omega_N L_\sigma.$$

Since the rotor is locked, all of the active input power is dissipated in the total resistance $R_s + R_R$

$$P_{lr} = 3(R_s + R_R)|\mathbf{i}_s|^2 = 3(R_s + R_R)I_N^2 \Rightarrow \hat{R}_s + \hat{R}_R = \frac{P_{lr}}{3I_N^2}. \quad (5.149)$$

The power developed in the leakage inductance is, of course, reactive and equal to $Q_{lr} = \sqrt{S_{rl}^2 - P_{rl}^2}$, where the apparent power S_{rl} is given by $S_{rl} = 3V_{lr}I_N$. Hence,

$$\begin{aligned} Q_{lr} &= 3\omega_N L_\sigma |\mathbf{i}_s|^2 = 3\omega_N L_\sigma I_N^2 \\ \Rightarrow \hat{L}_\sigma &= \frac{V_{lr}}{\omega_N I_N} \sqrt{1 - \left(\frac{P_{lr}}{3V_{lr}I_N} \right)^2}. \end{aligned} \quad (5.150)$$

- Remaining to be determined is the magnetizing inductance. In the **no-load test**, base voltage with base frequency is applied, and the motor is allowed to run light (no mechanical load). The slip is then approximately zero, so the rotor circuit is broken up. The IM then draws approximately the nominal magnetizing current as stator current: $|\mathbf{i}_s| = I_{\text{nl}}$ (which is measured), and the following steady-state relation holds:

$$\mathbf{v}_s = [R_s + j\omega_N(L_\sigma + L_M)]\mathbf{i}_s.$$

The voltage drop across the stator resistance is negligible, so

$$V_N = \omega_N(L_\sigma + L_M)I_{\text{nl}} \Rightarrow \hat{L}_M = \frac{V_N}{\omega_N I_{\text{nl}}} - \hat{L}_\sigma. \quad (5.151)$$

If the power P_{nl} is measured using a watt meter, the stator resistance can be obtained as

$$\hat{R}_s = \frac{P_{\text{nl}}}{3I_{\text{nl}}^2}. \quad (5.152)$$

Example 5.1 An IM with the following name-plate data is provided:

$$1.6 \text{ kW} \quad 220 \text{ V}/3.8 \text{ A (Y)} \quad 1430 \text{ rpm} \quad 50 \text{ Hz} \quad \cos \varphi = 0.76$$

and the results of locked-rotor and no-load tests are

$$P_{\text{lr}} = 377 \text{ W} \quad V_{\text{lr}} = 51.5 \text{ V} \quad I_{\text{nl}} = 2.0 \text{ A}.$$

A VSC with the dc-link voltage $V_{dc} = 540 \text{ V}$ is used.

Check whether the converter is correctly selected for this motor, then find the nominal torque, efficiency, and slip, as well as the base values and per-unit motor parameters for rms-value scaling.

Solution. From (3.21) we obtain $V_{\text{base}} = 540/\sqrt{6} = 220 \text{ V}$ for $K = 1/\sqrt{2}$, which shows that the converter is perfectly matched to the motor.

The nominal speed $n_N = 1430$ yields $\omega_m^N = 2\pi \cdot 1430/60 = 150 \text{ rad/s}$. This being a little less than half the nominal angular frequency, 314 rad/s, indicates that this is a four-pole motor ($n_p = 2$). Nominal slip: $s_N = (314 - 2 \cdot 150)/314 = 4.8\%$. With $P_{\text{out}}^N = 1.6 \text{ kW}$ we have $\tau_e^N = 1600/150 = 10.7 \text{ Nm}$. We find that the nominal input power is $P_{\text{in}}^N = 3V_N I_N \cos \varphi_N = 1.9 \text{ kW}$, so $\eta_N = 1.6/1.9 = 84\%$. Using now (5.148)–(5.151), we obtain

$$\hat{R}_R = 4.1 \Omega \quad \hat{R}_s = 4.6 \Omega \quad \hat{L}_\sigma = 33 \text{ mH} \quad \hat{L}_M = 0.32 \text{ H}.$$

For $K = 1/\sqrt{2}$ we get $I_{\text{base}} = 3.8 \text{ A}$. With $\omega_{\text{base}} = 314 \text{ rad/s}$, we find the base values for impedance and inductance:

$$Z_{\text{base}} = 58 \Omega \quad L_{\text{base}} = 0.18 \text{ H}$$

giving in turn the following per-unit parameters:

$$\hat{L}_M = 1.8 \quad \hat{L}_\sigma = 0.18 \quad \hat{R}_s = 0.079 \quad \hat{R}_R = 0.071.$$



PROBLEM 5.12

The following measurements were taken from a Y-connected induction motor for a stator frequency of 50 Hz.

	<i>No-load test</i>	<i>Locked-rotor test</i>
Active power (W)	170	750
Phase voltage (V)	230	70
Phase current (A)	5.0	9.0

- a) Calculate the motor parameters as given by the inverse- Γ model.
- b) What are the base values for voltage, current, and frequency, provided that the tests were conducted as recommended and that rms-value space-vector scaling is used?
- c) Determine the motor parameters in per-unit values.

5.6.2 Permanent-Magnet Synchronous Motors

Some—but not all—PMSMs are equipped with a name plate similar to that of IMs. With V_N , I_N , P_{out}^N , f_N , n_N , and $\cos \varphi_N$ given on the name plate, other quantities can be derived in exactly the same way as for IMs in Paragraph 5.6.1, except that $n_p = \omega_N/\omega_m^N$, since there is no slip.

Unlike the IM, *all* motor parameters can be determined from the name plate, however. Obviously, we have

$$\hat{\psi}_R = \frac{V_N}{\omega_N}. \quad (5.153)$$

Furthermore, by taking (5.96) in the steady state and multiplying by \mathbf{i}_s^* , the input–output complex power balance is obtained as follows:

$$\mathbf{v}_s \mathbf{i}_s^* = (R_s + j\omega_1) |\mathbf{i}_s|^2 + \mathbf{E} \mathbf{i}_s^*$$

so, with $\omega_1 = \omega_r = \omega_N$

$$\begin{aligned} P_{\text{in}}^N &= 3V_N I_N \cos \varphi_N = 3 \operatorname{Re}\{\mathbf{v}_s \mathbf{i}_s^*\} = 3R_s I_N^2 + \underbrace{3 \operatorname{Re}\{\mathbf{E} \mathbf{i}_s^*\}}_{P_{\text{out}}^N} \\ Q_{\text{in}}^N &= 3V_N I_N \sin \varphi_N = 3 \operatorname{Im}\{\mathbf{v}_s \mathbf{i}_s^*\} = 3\omega_N L_s I_N^2 + \underbrace{3 \operatorname{Im}\{\mathbf{E} \mathbf{i}_s^*\}}_{Q_{\text{out}}^N}. \end{aligned}$$

This immediately gives

$$\hat{R}_s = \frac{V_N}{I_N} \cos \varphi_N - \frac{P_{\text{out}}^N}{3I_N^2}. \quad (5.154)$$

To find L_s , we have $\mathbf{E} = j\omega_r \psi_R e^{j\tilde{\theta}} \Rightarrow |\mathbf{E}| = \omega_N \psi_R = V_N$, so

$$(P_{\text{out}}^N)^2 + (Q_{\text{out}}^N)^2 = (3V_N I_N)^2 \Rightarrow Q_{\text{out}}^N = \pm 3V_N I_N \sqrt{1 - \left(\frac{P_{\text{out}}^N}{3V_N I_N}\right)^2}$$

where only the minus sign is relevant, since reactive power must be produced in the back emf in order to get the desired high power factor. Hence, we obtain $\text{Im}\{\mathbf{Ei}_s^*\} \leq 0$, and

$$\hat{L}_s = \frac{V_N}{\omega_N I_N} \left(\sin \varphi_N + \sqrt{1 - \left(\frac{P_{\text{out}}^N}{3V_N I_N} \right)^2} \right). \quad (5.155)$$

If full name-plate data are not provided, there should at least be motor data available that specify nominal stator voltage and current, V_N and I_N . These given, the motor parameters can be determined from the following tests.

- **Rotation test.** Connect mechanically the PMSM to a suitable motor, and rotate the shaft with a constant speed ω_m . Leave the stator terminals open and measure the resulting stator voltage and frequency, V_s (rms value) and ω_s . This yields $\hat{\psi}_R = V_s/\omega_s$ and $n_p = \omega_s/\omega_m$. The nominal stator frequency is then obtained as $\omega_N = V_N/\hat{\psi}_R$.
- **Locked-rotor test.** Bar the rotor from moving and excite the motor with a variable stator voltage of angular frequency ω_N . Increase the voltage to the value V_{lr} , at which nominal stator current is obtained. Measure the input power P_{lr} . With $R_R = 0$ and L_s replacing L_σ , (5.149) and (5.150) can then be used to determine R_s and L_s as

$$P_{\text{lr}} = 3R_s|\mathbf{i}_s|^2 = 3R_s I_N^2 \Rightarrow \hat{R}_s = \frac{P_{\text{lr}}}{3I_N^2} \quad (5.156)$$

$$Q_{\text{lr}} = 3\omega_N L_s |\mathbf{i}_s|^2 = 3\omega_N L_s I_N^2 \\ \Rightarrow \hat{L}_s = \frac{V_{\text{lr}}}{\omega_N I_N} \sqrt{1 - \left(\frac{P_{\text{lr}}}{3V_{\text{lr}} I_N} \right)^2}. \quad (5.157)$$

5.6.3 Parameter Variations

The motor parameters obtained from name-plate data and/or the tests described above are subject to variation. Parameter variations must be taken into account in the design of the control system; details are given in Chapters 8 and 9. The motor parameters for IMs and PMSMs vary as follows.

L_M : The inductance obtained in the no-load test or from name-plate data is that for the nominal flux. As illustrated in Figure 4.8(b) for the field-winding inductance of the dc motor, this is a slightly saturated inductance. In the field-weakening range when the flux is reduced, L_M may increase up to 20% from the nominal value.

L_σ : Also for this parameter, a slightly saturated value is obtained in the locked-rotor test or from name-plate data. The effect of saturation tends not to be as significant as for the magnetizing inductance, though this is very dependent on the rotor slot design. Generally speaking, a fairly constant L_σ can be assumed, however.

R_s and R_R : The resistances are often measured with the motor at room temperature. It is said that the “cold values” of the resistances are obtained. During operation, the temperature increases, often to above 100°C, see [68]. The stator and rotor resistances then generally increase: between 50% and 100% above the “cold values.” The increase of the stator resistance is particularly troublesome for low-speed operation; see Chapters 8 and 9.

L_s : The situation is similar to that of L_σ for an IM, i.e., only small variations.

PROBLEM 5.13 _____

On the name plate of a PMSM, the following data are provided: 230 V, 25 A, 16.5 kW, 50 Hz, 1000 rpm. That is, the nominal power factor is missing. After operating the motor under nominal conditions for about an hour, it is stopped and the resistance across the stator terminals is measured, giving 0.3Ω .

- a) Why was the motor operated under nominal conditions before the measurement was made?
- b) Find the stator inductance and the nominal power factor from the provided data.

CHAPTER 6

Vector Control Fundamentals

Vector control implies that a three-phase VSC is controlled using space vectors. The concept was invented in the late 1960s by a research group in Braunschweig, Germany, led by Prof. Werner Leonhard. The development was spurred by the desire to begin applying the emerging technology of converter-fed induction motor drives to applications where thus far dc motor drives had been used. Methods traditionally used for induction motor control (see Paragraph 5.2.12) had been found inadequate; the fast dynamic response of a controlled dc motor drive was not achieved.

In vector control, which is also known as *field-oriented control* or simply *field orientation*, a *dq* frame that rotates synchronously with the flux of the motor is constructed, and current control is often performed in this frame. This allows ac motors to be controlled using similar algorithms as for dc motors—see Section 4.4—enabling fast dynamic response. Two variants of the concept were proposed in the theses of Blaschke and Hasse [6, 36].

Whereas vector control initially was developed for induction motor drives, the control concept was subsequently applied also to synchronous motor drives, and to VSCs connected to the grid. These three applications are considered in the reverse order, in Chapters 9, 8, and 7, respectively. In this chapter we discuss the general principles of vector control before going into details. We also extend the methods for current control of the dc motor—using single-phase VSCs or buck converters—of Section 4.4 to three-phase VSCs. As much as possible, the theory from Section 4.4 is relied upon and extended. Also included is an introduction to synchronization control using a phase-locked loop (PLL).

6.1 Principle of Vector Control

Vector control is often introduced as applied to induction motors. This application is technically the most challenging one and also the one most difficult to grasp. Therefore, we postpone the details of vector control of induction motors until Chapter 9, and start by applying the concept to converters connected to a general load or source, which may be either an ac motor or a three-phase grid. In the latter case there is a simplification to be obtained: the grid frequency is near constant, whereas the stator frequency of an ac motor drive varies with the speed.

The general load or source is modeled as a series connection of a resistance, an inductance, and a voltage source, as shown in Figure 6.1. This is a model for a

- **permanent-magnet synchronous motor**, see Figure 5.20, with

$$\mathbf{v}^s = \mathbf{v}_s^s \quad \mathbf{i}^s = \mathbf{i}_s^s \quad R = R_s \quad L = L_s \quad (6.1)$$

and back emf

$$\mathbf{E}^s = \frac{d\psi_R^s}{dt} = j\omega_r \psi_R e^{j\theta} \quad (6.2)$$

an

- **induction motor**, see Figure 5.11, with

$$\mathbf{v}^s = \mathbf{v}_s^s \quad \mathbf{i}^s = \mathbf{i}_s^s \quad R = R_s \quad L = L_\sigma \quad (6.3)$$

and flux emf

$$\mathbf{E}^s = \frac{d\psi_R^s}{dt} \quad (6.4)$$

and a

- **grid-connected converter**, where R and L respectively are resistance and inductance of the converter's input filter, whereas \mathbf{E}^s is the voltage at the point of common coupling (PCC). As mentioned, unlike the back emf for a PMSM or the flux emf for an IM, the PCC voltage can be assumed to have a near-constant frequency. On the other hand, the PCC voltage is not necessarily constant to its amplitude and phase; particularly during grid fault situations, large transients—often including significant negative-sequence voltages—may occur.

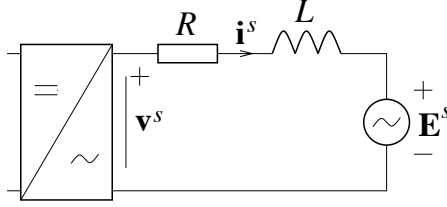


Figure 6.1. Converter connected to a circuit consisting of a resistive–inductive impedance and a voltage source.

In the stationary reference frame, the dynamic model for the system in Figure 6.1 is given by

$$L \frac{di^s}{dt} = \mathbf{v}^s - R\mathbf{i}^s - \mathbf{E}^s. \quad (6.5)$$

In Chapter 5 we introduced the concept of field orientation for ac motors, which implies orienting a rotating dq reference frame along the rotor-flux vector. The rotor flux serves as phase reference for the dq frame. Because \mathbf{E}^s is the derivative of the rotor flux according to (6.2) and (6.4), it is natural for the general case (i.e., including grid-connected converters) to let the dq frame be perpendicular to \mathbf{E}^s , as this results in rotor-flux orientation for ac drives. This is accomplished by considering \mathbf{E}^s in polar form as

$$\mathbf{E}^s = jEe^{j\theta}. \quad (6.6)$$

6.1.1 Transformation to Synchronous Coordinates

Let us transform (6.5) to a synchronously rotating reference frame, using the dq transformation

$$\mathbf{v} = e^{-j\theta_1} \mathbf{v}^s \quad \mathbf{i} = e^{-j\theta_1} \mathbf{i}^s. \quad (6.7)$$

With $\omega_1 = \dot{\theta}_1$ we obtain

$$L \frac{d\mathbf{i}}{dt} = \mathbf{v} - (R + j\omega_1 L)\mathbf{i} - \underbrace{jEe^{j\tilde{\theta}}}_{\mathbf{E}} \quad (6.8)$$

where $\tilde{\theta} = \theta - \theta_1$. Suppose now that θ is measurable, so that $\theta_1 = \theta$ can be selected. As noted in Section 5.2, this is known as perfect field orientation. In the steady state, (6.8) then reduces to

$$\mathbf{v} = (R + j\omega_1 L)\mathbf{i} + jE. \quad (6.9)$$

The complex output power at voltage \mathbf{E} is

$$\begin{aligned} \mathbf{S} &= \frac{3}{2K^2} \mathbf{E}\mathbf{i}^* = \{\mathbf{E} = jE, \mathbf{i} = i_d + ji_q\} = \frac{3}{2K^2} E(i_q + ji_d) \Rightarrow \\ P &= \frac{3}{2K^2} Ei_q \quad Q = \frac{3}{2K^2} Ei_d. \end{aligned} \quad (6.10)$$

Thus, the active and reactive powers P and Q can be controlled simply by controlling appropriately the current components i_q and i_d . Unity power factor is obtained by letting $i_d = 0$. For a grid-connected converter, i_q and i_d thus are the active- and reactive-power-producing current components, respectively, whereas for an ac motor drive (cf. Chapter 5) they are referred to as the torque- and flux-producing current components, respectively.

6.2 Introduction to Vector Current Control

The load or source model in Figure 6.1, applied for the definition of vector control, is directly applicable also for current control. That is, the controlled process is the series admittance with resistance R and inductance L . For a grid-connected converter, R and L are respectively the converter input filter's resistance and inductance, as discussed previously. For a round-rotor PMSM drive, the correspondences (6.1) are valid also for vector control control. For an IM drive there is a difference from (6.3), though. For current control, the electrical dynamics are determined by the IMs transient impedance $\mathbf{Z}_\sigma^s(p) = R_\sigma + pL_\sigma$ [cf. (5.78)], so the parameter correspondences are in this case

$$R = R_\sigma = R_s + R_R \quad L = L_\sigma. \quad (6.11)$$

That said, owing to the usage of an “active resistance” (see further below), the controller design is fairly insensitive to R , so letting $R = R_s$ by mistake makes little practical difference.

The differential equation for the system depicted in Figure 6.1 is in the synchronous reference frame given by (6.8). This complex dynamic model is of order one. Splitting the real and imaginary parts, we obtain the following second-order model:

$$L \frac{di_d}{dt} = v_d - Ri_d + \omega_1 Li_q - E_d \quad (6.12)$$

$$L \frac{di_q}{dt} = v_q - Ri_q - \omega_1 Li_d - E_q. \quad (6.13)$$

These are two cross-coupled first-order subsystems. The cross-coupling is initiated by the terms $\omega_1 Li_q$ and $\omega_1 Li_d$.

As an alternative to the circuit model in Figure 6.1 a block diagram can also be used, see Figure 6.2. Here, the complex transfer function $\mathbf{G}(s)$ is obtained by applying the Laplace transform to (6.8)

$$\mathbf{G}(s) = \frac{1}{(s + j\omega_1)L + R}. \quad (6.14)$$

This corresponds to the dc motor transfer function (4.37). The new twist is the term $j\omega_1 L$, which is caused by the transformation to synchronous coordinates: $s \rightarrow s + j\omega_1$. This is the reason for the cross-coupling between (6.12) and (6.13). As before, \mathbf{E} is modeled as a load disturbance that subtracts from the input signal \mathbf{v} , i.e., the voltage impressed by the converter. The output signal is, of course, the current vector.

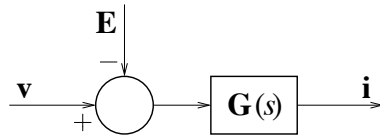


Figure 6.2. Block diagram for the three-phase load.

Due to the relative simplicity of the dynamic model, it is not very difficult to design a well-performing current controller. After briefly reviewing some strategies that have been proposed for the purpose, we shall study synchronous-frame current controllers in some detail. This is mainly an extension of the theory developed in Section 4.4.

6.3 Review of Methods for Three-Phase Current Control

Several different methods for current control of VSCs—particularly as applied to variable-speed ac motor drives—have been suggested. In the years around 1985, many good papers on the topic appeared, adding new and important results. Some of these papers, as well as more recent ones, are referenced below. A good source for more information is the book by Bose [10, Chapters 4, 5].

6.3.1 Hysteresis Control

This scheme is illustrated in Figure 6.3. It is a direct extension of the hysteresis control scheme for buck converters described in Section 3.2. Each phase current is measured, fed back, and subtracted from its reference (a sinusoid). The error signal is then fed to a hysteresis comparator, the output of which forms the switching signal to the respective converter leg. As in the single-phase case, one advantage of this control method is that it is simple to implement (at least in analog electronics), since control and PWM are merged. By decreasing the tolerance band, the switching frequency is increased. Another benefit is the quick response to a reference change.

There are also some drawbacks associated with the method, however.

- The switching frequency is not constant. The variations are opposite to those desired for good control; the highest switching frequency is associated with low fundamental frequencies. This can be mitigated by varying the tolerance band.

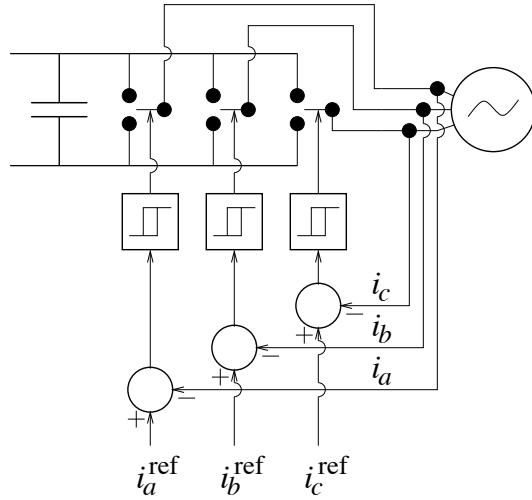


Figure 6.3. Three-phase hysteresis current control.

- The actual band to which the current is confined is, somewhat surprisingly, *twice* the dead-band. The phenomenon occurs because the phase currents interact in the load. (The problem can be circumvented by using more elaborate hysteresis schemes.)
- The PWM may enter a state of very fast switchings at low fundamental frequencies, or even chaotic behavior [63]. This is highly undesirable.
- The method is simple to implement in analog electronics but more difficult in digital electronics. If the hysteresis comparator is implemented on a DSP (or in hardware, e.g., an in FPGA), a very high sampling rate must be used in order to prevent timing errors.

Since ease of implementation (in analog electronics) no longer is an objective—owing to powerful DSPs—the method is not as attractive as it once was.

6.3.2 Stationary-Frame PI Control

In this scheme, i_α and i_β are controlled directly in the stationary reference frame. One coordinate transformation is still needed for synchronization, namely, from the synchronous-frame reference vector $\mathbf{i}_{\text{ref}} = i_d^{\text{ref}} + j i_q^{\text{ref}}$ to the stationary-frame equivalent $\mathbf{i}_{\text{ref}}^s$. This is required because i_d^{ref} and i_q^{ref} still must be the inputs to the current controller, as they are set proportionally to the desired reactive and active powers or flux and torque, respectively, see (6.10). Most commonly, two standard PI controllers (one each for the α and β axes) are used. The controller output vector forms command signals to the PWM algorithm. See Figure 6.4.

Unlike hysteresis control, this scheme uses two stages: control and modulation. The drawback of this control scheme is that *the actual current will not track the reference in the steady state*, which was pointed out in [71]. Somewhat surprisingly, the origin of this phenomenon was debated for several years. The explanation was given in [67]. To quote [67, p. 679].

“The fact that this error exists in a current regulated R – L load suggests that the error observed in ac drives at higher frequencies previously attributed to so-called back EMF

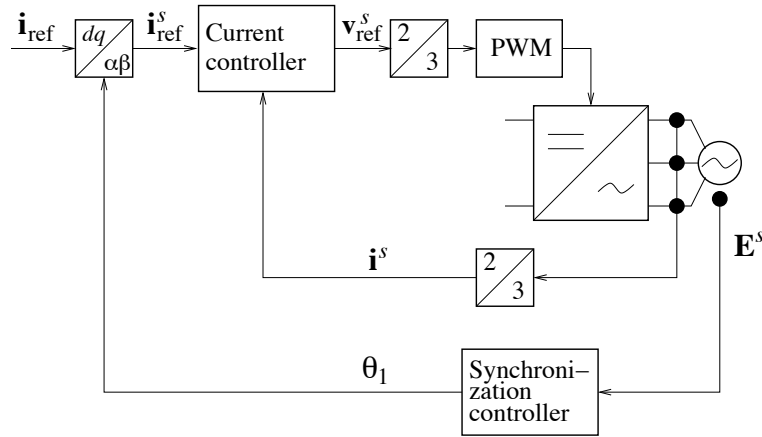


Figure 6.4. Stationary-frame PI control.

or ‘running up against the bus’ is neither, but rather a consequence of the stationary regulator itself. Therefore, whether the load is static or dynamic is immaterial from the standpoint of phase shift and magnitude error present in the steady state currents.”

PI controllers are inherently incapable of giving zero steady-state control error for a sinusoidal reference. The integral action removes the error only in case the reference is *constant* in the steady state. In fact, there is little reason to use integral action at all if a sinusoid is to be tracked! The pole at the origin of the PI controller should be removed and replaced by a pole pair at $\pm j\omega_1$, i.e., the controller *de facto* becomes a resonator.

6.3.3 Synchronous-Frame PI Control

The disadvantage of stationary-frame PI control can easily be remedied. Using a DSP, the $\alpha\beta$ sinusoidal signals can be *dq* transformed to the synchronously rotating reference frame—i.e., to dc signals in the steady state—where standard PI control works properly. This is illustrated in Figure 6.5, where a PLL is used for synchronization, see Section 6.5. Only one additional coordinate transformation is required as compared to stationary-frame current control. Synchronous-frame PI (or PI-type) controllers are therefore often the most attractive choice for current control, due to their simplicity and ability to provide good performance. Therefore, the rest of the chapter will focus on this control scheme.

If coordinate transformations yet are undesirable, the control algorithm can be transformed to and implemented in stationary coordinates, as shown in [67]. This in effect moves the integrator *dq*-frame pole at $s = 0$ to an $\alpha\beta$ -frame pole at $s = -j\omega_1$. It should be stressed that if one desires to implement stationary-frame current control, this scheme should be used rather than standard PI control.

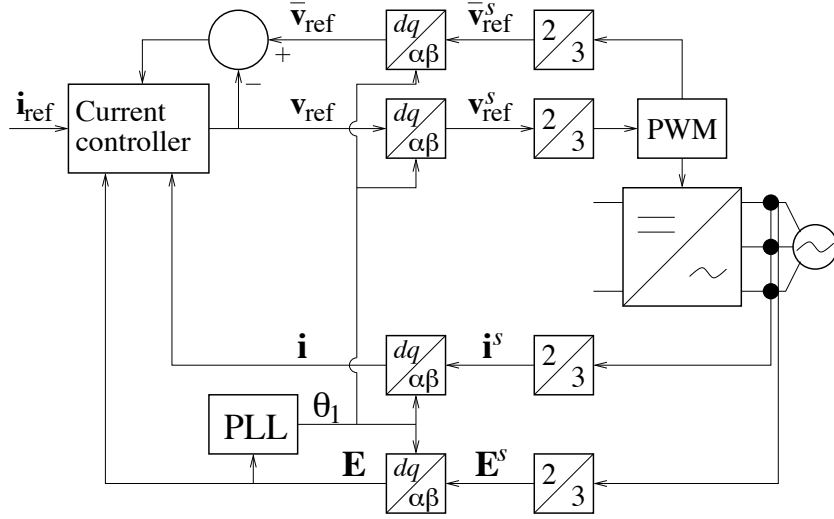


Figure 6.5. Vector control system with synchronous-frame current control using measurement of \mathbf{E}^s for synchronization.

6.4 Design of Synchronous-Frame Current Controllers

Having motivated in the previous section why current control preferably should be made in synchronous coordinates, it will now be seen how such controllers can be designed. We here follow, but also add to, the method presented in [27].

Consider (6.8) and the real equivalents, (6.12)–(6.13). The latter two equations represent two cross-coupled first-order subsystems. The cross coupling is initiated by the term $j\omega_1 L \mathbf{i}$ in (6.8), since multiplication by j maps the d axis on the q axis and vice versa

$$\mathbf{i}' = j\mathbf{i} \Rightarrow i'_d + ji'_q = j(i_d + ji_q) = -i_q + ji_d. \quad (6.15)$$

The first step in the controller design is to cancel this cross coupling. This is easily done—provided that the inductance L is known with fairly good accuracy—by adding a decoupler $j\omega_1 \hat{L} \mathbf{i}$ to the inner “active resistance” feedback loop (which was introduced in Section 4.4 in order to improve the disturbance rejection capability). We get

$$\mathbf{v} = \mathbf{v}' + (j\omega_1 \hat{L} - R_a) \mathbf{i} + \hat{\mathbf{E}} \quad (6.16)$$

where R_a is the “active resistance.” Term $\hat{\mathbf{E}}$ is an optional feedforward of the PCC voltage and the back emf, respectively for grid-connected VSCs and ac drives. See Figure 6.6.

The optional feedforward term is selected differently depending on the application.

- For grid-connected VSCs, the feedforward term can be set as a first-order low-pass filtering of the measured \mathbf{E}

$$\hat{\mathbf{E}} = \frac{\alpha_f}{p + \alpha_f} \mathbf{E} \quad (6.17)$$

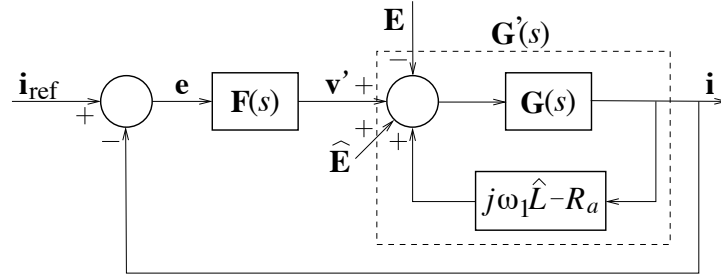


Figure 6.6. Current control with an inner decoupling and “active damping” loop. $\mathbf{F}(s)$ and $\mathbf{G}(s)$ are the complex-valued transfer functions of the PI controller and the load, respectively.

where typically $\alpha_f < \alpha_c$. This result in

$$\tilde{\mathbf{E}} = \mathbf{E} - \hat{\mathbf{E}} = \left(1 - \frac{\alpha_f}{p + \alpha_f}\right) \mathbf{E} = \frac{p}{p + \alpha_f} \mathbf{E}. \quad (6.18)$$

So, in the steady state (i.e., $p = 0$), $\tilde{\mathbf{E}} = 0$, i.e., the influence of the PCC voltage is mitigated.

- For ac drives, the feedforward term can be set as an estimate of the back emf for a PMSM and the flux emf for an IM

$$\hat{\mathbf{E}} = j\omega_1 \hat{\Psi}_R. \quad (6.19)$$

In both cases, though, only a partial cancellation is obtained, so an “active resistance” is often useful to improve the rejection of variations in \mathbf{E} . We obtain (ideally, if $\hat{L} = L$) from (6.8)

$$L \frac{di}{dt} = \mathbf{v}' - (R + R_a)\mathbf{i} - \tilde{\mathbf{E}}. \quad (6.20)$$

This equation has no complex coefficients, so the cross coupling has been removed. Also, the dynamics have been speeded up from R/L to $(R + R_a)/L$. A current controller having \mathbf{v}' as output is then used in an outer loop, see Figure 6.6. The decoupled system from \mathbf{v}' to \mathbf{i} has the transfer function

$$\mathbf{G}'(s) = \frac{1}{sL + R + R_a}. \quad (6.21)$$

As this is a first-order complex system (representing two noninteracting first-order systems in the d and q paths, respectively), PI control is appropriate

$$\mathbf{F}(s) = k_p + \frac{k_i}{s}. \quad (6.22)$$

Following Section 4.4, we select

$$k_p = \alpha_c \hat{L} \quad k_i = \alpha_c (\hat{R} + R_a) \quad (6.23)$$

where α_c is the closed-loop-system bandwidth. If the inner feedback loop is made as fast as the closed-loop system, i.e.,

$$\frac{R + R_a}{L} = \alpha_c \Rightarrow R_a = \alpha_c \hat{L} - \hat{R} \quad (6.24)$$

then the selection for the integral gain simplifies to $k_i = \alpha_c^2 \hat{L}$. On the other hand, if one-degree-of-freedom PI control is used by letting $\hat{R} = 0$, then $k_i = \alpha_c \hat{R}$. The controller is described by

$$\mathbf{e} = \mathbf{i}_{\text{ref}} - \mathbf{i} \quad (6.25)$$

$$\frac{d\mathbf{I}}{dt} = \mathbf{e} \quad (6.26)$$

$$\mathbf{v}_{\text{ref}} = k_p \mathbf{e} + k_i \mathbf{I} + (j\omega_1 \hat{L} - R_a) \mathbf{i} + \hat{\mathbf{E}} \quad (6.27)$$

where $\mathbf{I} = I_d + jI_q$ is the complex integrator state variable.

6.4.1 Bandwidth Selection

Selection of the closed-loop-system bandwidth can be made based on the desired closed-loop-system rise time t_{rc} , as $\alpha_c = \ln 9/t_{rc}$; typical rise times for state-of-the-art VSCs are in the millisecond range or below, giving α_c in the range of thousands of radians per second. Yet, to gain stability robustness—see Section 4.4 for details—the bandwidth should not exceed 10% and 4% of the angular sampling frequency, respectively for one-degree-of-freedom and two-degrees-of-freedom control, cf. (4.73) and (4.75). That is,

$$\alpha_c \leq \begin{cases} 0.1\omega_s, & \text{if } R_a = 0 \\ 0.04\omega_s, & \text{if } R_a = \alpha_c \hat{L} - \hat{R}. \end{cases} \quad (6.28)$$

Example 6.1 Design a current controller for an induction motor having the following data:

Base voltage: 230 V

Base current: 10 A

Base frequency: 50 Hz

Total leakage inductance: $L = L_\sigma = 20 \text{ mH}$

Total resistance: $R = R_s + R_R = 3 \Omega$

Desired stator current rise time: 1 ms.

The inner feedback (“active resistance”) loop should be as fast as the closed-loop system.

Solution. The impedance base value is $230/10 = 23 \Omega$, so in per-unit values the total leakage inductance is $314 \cdot 10 \cdot 10^{-3}/23 = 0.28$ and the total resistance $3/23 = 0.13$. For a current rise time of 1 ms, a closed-loop bandwidth of $2.2/10^{-3} = 2200 \text{ rad/s}$ is needed, i.e., $\alpha_c = 7.0 \text{ pu}$. This yields the following controller parameters in per-unit values:

$$R_a = \alpha_c L - R = 1.8 \quad k_p = \alpha_c L = 2.0 \quad k_i = \alpha_c^2 L = 13.7.$$



6.4.2 PWM, Time-Delay Compensation, and Antiwindup

The current controller’s output signal \mathbf{v}_{ref} transformed to stationary coordinates, $\mathbf{v}_{\text{ref}}^s = e^{j\theta_1} \mathbf{v}_{\text{ref}}$, forms the command voltage vector to the PWM algorithm. Algorithm 3.1 is used to generate the appropriate reference signals from $\mathbf{v}_{\text{ref}}^s$. From Paragraph 3.12 we know that PWM using synchronous sampling gives a time delay $T_d = 1.5T_s$. In addition, we know from Paragraph 2.7.3

that the dq transformation of a time delay gives an undesired rotation of the dq frame by the angle $-\omega_1 T_d$. This angle can be compensated for in the $\alpha\beta$ transformation by adding $\omega_1 T_d$ to the transformation angle θ_1 as

$$\mathbf{v}_{\text{ref}}^s = e^{j(\theta_1 + \omega_1 T_d)} \mathbf{v}_{\text{ref}}, \quad T_d = 1.5 T_s. \quad (6.29)$$

Using $\mathbf{v}_{\text{ref}}^s$, the PWM algorithm computes the PWM phase-reference and also the realizable vector $\bar{\mathbf{v}}_{\text{ref}}$ (which differs from $\mathbf{v}_{\text{ref}}^s$ in the saturation region). As for dc-drive current control, the ideal control algorithm (6.25)–(6.27) has to be modified using “back calculation” in order to avoid integrator windup in the saturation region. This implies adding a term to (6.26) [cf. (4.68)–(4.70)] as follows:

$$\mathbf{e} = \mathbf{i}_{\text{ref}} - \mathbf{i} \quad (6.30)$$

$$\frac{d\mathbf{I}}{dt} = \mathbf{e} + \frac{1}{k_p} (\bar{\mathbf{v}}_{\text{ref}} - \mathbf{v}_{\text{ref}}) \quad (6.31)$$

$$\mathbf{v}_{\text{ref}} = k_p \mathbf{e} + k_i \mathbf{I} + (j\omega_1 \hat{L} - R_a) \mathbf{i} + \hat{\mathbf{E}} \quad (6.32)$$

$$\bar{\mathbf{v}}_{\text{ref}} = \text{PWM}(\mathbf{v}_{\text{ref}}, \theta_1 + \omega_1 T_d). \quad (6.33)$$

“PWM” here indicates the PWM algorithm including coordinate transformations. Euler discretization of the integrator results in Algorithm 6.1, which is expressed in real vector form. The corresponding vector block diagram is depicted in Figure 6.7.

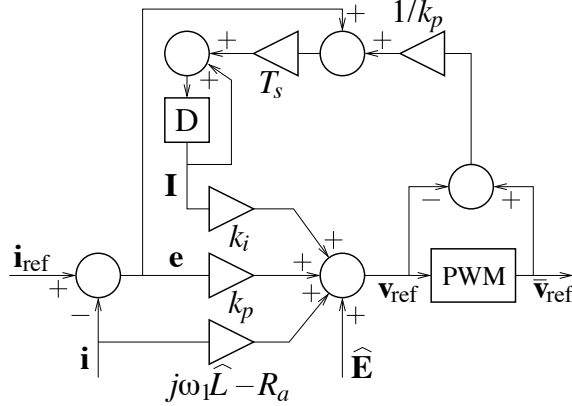


Figure 6.7. Digitally implemented current controller in complex space-vector form.

Example 6.2 In this example, we simulate current control of a PMSM with the parameter values $L = 0.5$ pu and $R = 0.05$ pu. In the current controller design procedure, slightly inaccurate parameter values are available: $\hat{L} = 0.6$ pu and $\hat{R} = 0.08$ pu. The controller is designed for a current rise time of 1 ms for a 50-Hz base frequency, which yields $\alpha_c = 7$ pu. Back-emf feedforward is not used.

Step responses of the stator current are depicted in Figure 6.8. At $\omega_r = 0.5$ pu, i_q^{ref} is first stepped up from 0 to 0.6 pu at $t = 0$, and down to 0.1 pu at $t = 5$ ms. At the first step, maximum available converter voltage is reached. Therefore, the rise time is longer than the desired 1 ms. At the second step, the maximum voltage is only touched, so the rise time (or, in this case more

appropriately, fall time) equals the ideal 1 ms. The controller is robust to the slightly inaccurate parameter values used. Note particularly that i_d hardly deviates at all from its reference $i_d^{\text{ref}} = 0$.

Figure 6.9 shows the difference in performance when no “back calculation” is used. Now, the overshoot for the first step response is significant.



Algorithm 6.1

Vector Current Controller

$$\begin{aligned} \begin{bmatrix} i_d \\ i_q \end{bmatrix} &= \begin{bmatrix} \cos(\theta_1) & \sin(\theta_1) \\ -\sin(\theta_1) & \cos(\theta_1) \end{bmatrix} \begin{bmatrix} i_\alpha \\ i_\beta \end{bmatrix} \\ \begin{bmatrix} e_d \\ e_q \end{bmatrix} &= \begin{bmatrix} i_d^{\text{ref}} \\ i_q^{\text{ref}} \end{bmatrix} - \begin{bmatrix} i_d \\ i_q \end{bmatrix} \\ \begin{bmatrix} v_d^{\text{ref}} \\ v_q^{\text{ref}} \end{bmatrix} &= k_p \begin{bmatrix} e_d \\ e_q \end{bmatrix} + k_i \begin{bmatrix} I_d \\ I_q \end{bmatrix} - \begin{bmatrix} R_a & \omega_1 \hat{L} \\ -\omega_1 \hat{L} & R_a \end{bmatrix} \begin{bmatrix} i_d \\ i_q \end{bmatrix} + \begin{bmatrix} \hat{E}_d \\ \hat{E}_q \end{bmatrix} \\ \theta'_1 &= \theta_1 + \omega_1 T_d \\ \begin{bmatrix} v_\alpha^{\text{ref}} \\ v_\beta^{\text{ref}} \end{bmatrix} &= \begin{bmatrix} \cos(\theta'_1) & -\sin(\theta'_1) \\ \sin(\theta'_1) & \cos(\theta'_1) \end{bmatrix} \begin{bmatrix} v_d^{\text{ref}} \\ v_q^{\text{ref}} \end{bmatrix} \\ [\bar{v}_\alpha, \bar{v}_\beta] &= \text{PWM}([v_\alpha, v_\beta]) \\ \begin{bmatrix} \bar{v}_d^{\text{ref}} \\ \bar{v}_q^{\text{ref}} \end{bmatrix} &= \begin{bmatrix} \cos(\theta'_1) & \sin(\theta'_1) \\ -\sin(\theta'_1) & \cos(\theta'_1) \end{bmatrix} \begin{bmatrix} \bar{v}_\alpha^{\text{ref}} \\ \bar{v}_\beta^{\text{ref}} \end{bmatrix} \\ \begin{bmatrix} I_d \\ I_q \end{bmatrix} &= \begin{bmatrix} I_d \\ I_q \end{bmatrix} + T_s \begin{bmatrix} e_d + \frac{1}{k_p} (\bar{v}_d^{\text{ref}} - v_d^{\text{ref}}) \\ e_q + \frac{1}{k_p} (\bar{v}_q^{\text{ref}} - v_q^{\text{ref}}) \end{bmatrix} \end{aligned}$$

6.5 Synchronization Control Using a Phase-Locked Loop

Since vector control relies on aligning a rotating dq reference frame perpendicularly to the space vector \mathbf{E}^s , one crucial component in any vector control system is a controller that performs synchronization with the rotation of \mathbf{E}^s . How the synchronization problem is solved differs greatly from one application to another, as we shall see in Chapters 7, 8, and 9. In some applications, the phase angle θ is directly available for measurement. Usually, though, it is available only indirectly from certain measurable signals, often the components of $\mathbf{E}^s = jEe^{j\theta} = E_\alpha + jE_\beta$

$$E_\alpha = -E \sin \theta \quad E_\beta = E \cos \theta. \quad (6.34)$$

The synchronization controller shall be designed so that θ_1 tracks θ , given the information available—i.e., characteristically (6.34)—with sufficient accuracy and speed. In addition, various disturbances that are always present in the signals—but not explicitly shown in (6.34)—should be suppressed. At a glance, this task may seem simple. From (6.34), just compute $-E_\alpha/E_\beta = \tan \theta$ and then apply the inverse tangent function. This method is impractical, however, since $E_\beta = E \cos \theta = 0$ two times per each fundamental period, leading to division by zero, or by a small number at the

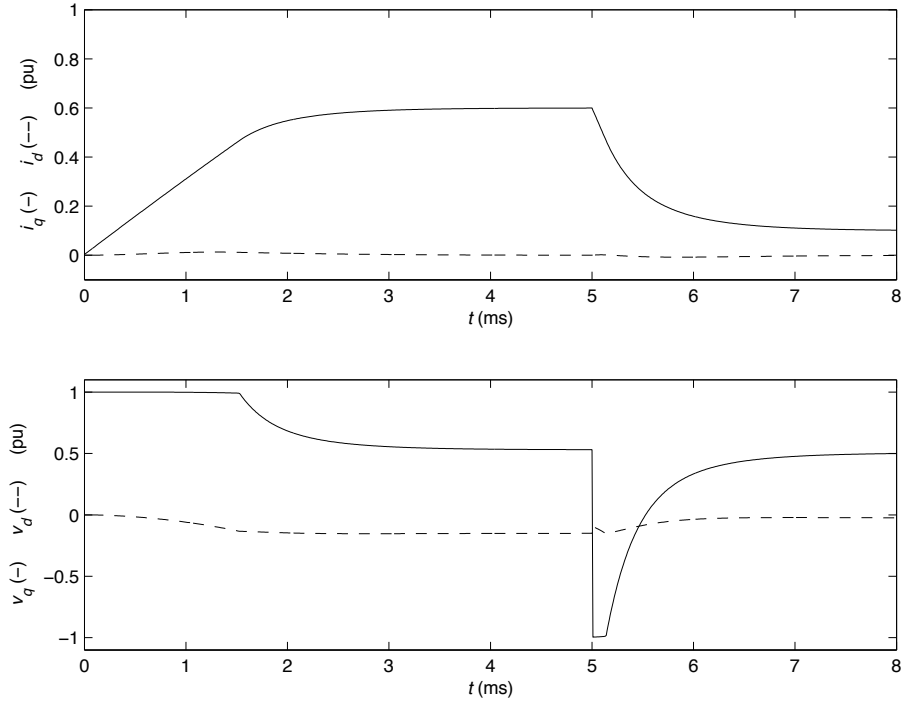


Figure 6.8. Current control with “back calculation” of a PMSM.

very least. The obtained estimate θ_1 would very likely be quite distorted by noise. An improvement can be obtained by applying the two-argument inverse tangent function as

$$\theta_1 = \text{atan}2(-E_\alpha, E_\beta)$$

but yet a noisy estimate is likely to be obtained. In addition, to obtain ω_1 , differentiation of θ_1 is required, resulting in further noise amplification. To avoid these problems, most synchronization controllers use some variant of a phase-locked loop, the fundamentals of which we now shall present.

Transforming \mathbf{E}^s to synchronous coordinates using the angle θ_1 yields, as shown in (6.8)

$$\mathbf{E} = e^{-j\theta_1} \mathbf{E}^s = jE e^{j\tilde{\theta}} \quad (6.35)$$

whose components are

$$E_d = -E \sin \tilde{\theta} \quad E_q = E \cos \tilde{\theta}. \quad (6.36)$$

Synchronism implies that $\tilde{\theta} = 0 \Rightarrow E_d = 0$. Consequently, θ_1 can in principle be obtained by integrating E_d . Provided that stability is obtained, adjustment of θ_1 will then continue through the integration until $\sin \tilde{\theta} = 0$, which in PLL terminology is known as phase lock. Let us construct a general PLL algorithm by starting with an estimate $\hat{\omega}_g$ of $\omega_g = \theta$. For a grid-connected VSC this is simply the nominal angular grid frequency, e.g., $\hat{\omega}_g = 2\pi \cdot 50$ rad/s or $\hat{\omega}_g = 2\pi \cdot 60$ rad/s.

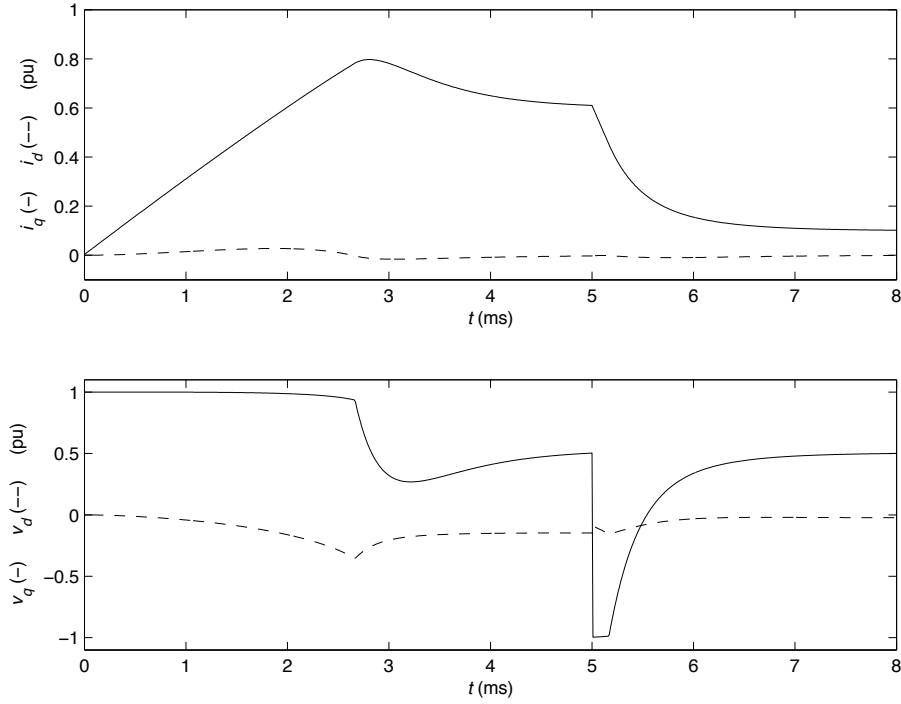


Figure 6.9. Current control without “back calculation” of a PMSM.

To $\hat{\omega}_g$, corrective terms proportional to $-E_d$ and the integral thereof are added

$$\hat{\omega}_g - k_{pp}E_d - \underbrace{k_{ip} \int E_d dt}_{\omega_i}. \quad (6.37)$$

This signal is then filtered through a low-pass filter in order to suppress noise. The filter output is the instantaneous fundamental angular frequency ω_1 . Often, a first-order filter is sufficient

$$\omega_1 = \frac{\alpha_l}{p + \alpha_l} (\hat{\omega}_g - k_{pp}E_d + \omega_i). \quad (6.38)$$

Finally, the aforementioned integration is applied, i.e., ω_1 is integrated into the transformation angle θ_1 as

$$\theta_1 = \int \omega_1 dt. \quad (6.39)$$

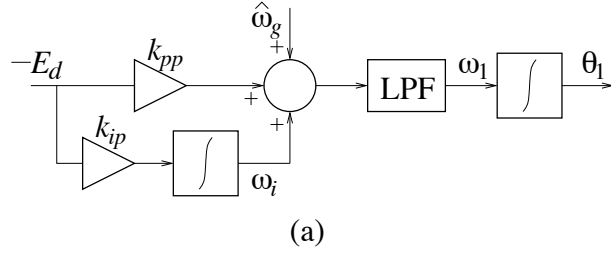
A block diagram showing this PLL is depicted in Figure 6.10(a). As the dq and $\alpha\beta$ transformations require taking cosine and sine of θ_1 for calculating the transformation factors $e^{\pm j\theta_1} = \cos \theta_1 \pm j \sin \theta_1$, such computations have to be added, but are not shown in the figure. Because the transformation factors are obtained indirectly via integration of the fundamental angular frequency followed by trigonometric operations, this type of synchronization method is called *indirect field*

orientation (IFO). Algorithm 6.2 illustrates a software implementation of the PLL using Euler discretization of the integrators and the low-pass filter. In the integrator whose output is θ_1 the output is computed modulo 2π , as illustrated Figure 6.10(b), to avoid endless ramping of θ_1 , which eventually might lead to numerical overflow.

Algorithm 6.2

Phase-Locked Loop

$$\begin{aligned}\omega_i &= \omega_i - T_s k_{ip} E_d \\ \omega_1 &= \omega_1 + T_s \alpha_l (\hat{\omega}_g - k_{pp} E_d + \omega_i - \omega_1) \\ \theta_1 &= \text{mod}(\theta_1 + T_s \omega_1, 2\pi)\end{aligned}$$



(a)

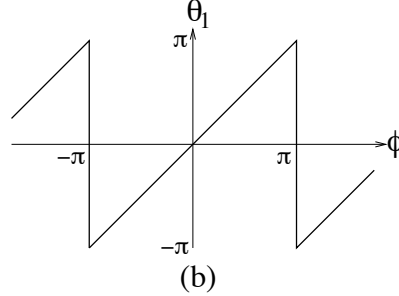


Figure 6.10. (a) PLL block diagram. (b) Computation modulo 2π : $\theta_1 = \text{mod}(\phi, 2\pi)$.

6.5.1 Analysis

Suppose that the low-pass-filter bandwidth α_l is high enough, so that impact of the low-pass filter can be neglected. From (6.37)–(6.39) we then obtain

$$\dot{\omega}_i = -k_{ip} E_d \quad (6.40)$$

$$\dot{\theta}_1 = \omega_1 = \hat{\omega}_g + \omega_i - k_{pp} E_d. \quad (6.41)$$

This system can be analyzed by introducing $\tilde{\omega}_g = \omega_g - \hat{\omega}_g$, where $\dot{\omega}_g \approx 0$ is assumed, and $\tilde{\theta} = \theta - \theta_1$. Since $E_d = -E \sin \tilde{\theta}$, we obtain the following nonlinear dynamic system:

$$\dot{\omega}_i = k_{ip}E \sin \tilde{\theta} \quad (6.42)$$

$$\dot{\tilde{\theta}} = \tilde{\omega}_g - \omega_i - k_{pp}E \sin \tilde{\theta}. \quad (6.43)$$

A number of observations can be made from inspecting (6.42)–(6.43).

Local Stability and Pole Placement

The local stability can be investigated by assuming a small $\tilde{\theta}$, such that $\sin \tilde{\theta} \approx \tilde{\theta}$. This allows (6.42)–(6.43) to be linearized as

$$\dot{\omega}_i = k_{ip}E\tilde{\theta} \quad (6.44)$$

$$\dot{\tilde{\theta}} = \tilde{\omega}_g - \omega_i - k_{pp}E\tilde{\theta} \quad (6.45)$$

which can be expressed as the state-space model $\dot{\mathbf{x}} = \mathbf{A}\mathbf{x} + \mathbf{B}\tilde{\omega}_g$, where $\mathbf{x} = [\omega_i, \tilde{\theta}]^T$ and

$$\mathbf{A} = \begin{bmatrix} 0 & k_{ip}E \\ -1 & -k_{pp}E \end{bmatrix} \quad \mathbf{B} = \begin{bmatrix} 0 \\ 1 \end{bmatrix}. \quad (6.46)$$

The characteristic polynomial of \mathbf{A} is given by

$$\det(s\mathbf{I} - \mathbf{A}) = s^2 + k_{pp}Es + k_{ip}E. \quad (6.47)$$

The system is locally asymptotically stable for $k_{pp} > 0$, $k_{ip} > 0$, and $E > 0$. Its poles (i.e., the eigenvalues of \mathbf{A}) can be placed arbitrarily by properly selecting k_{pp} and k_{ip} . For example, the selection

$$k_{pp} = \frac{2\alpha_p}{\hat{E}} \quad k_{ip} = \frac{\alpha_p^2}{\hat{E}} \quad (6.48)$$

where α_p is the synchronization-loop bandwidth and \hat{E} is an estimate of E , yields a double pole at $s = -\alpha_p$ if $\hat{E} = E$. This selection gives a relatively high integral gain k_{ip} , which is useful for variable-speed drives when the synchronous frequency may vary significantly and relatively quickly. On the other hand, for grid-connected VSCs the synchronous frequency only varies slightly about its nominal value and on a slower time scale. Then, weaker integral action is sufficient, which is obtained by selecting

$$k_{pp} = \frac{\alpha_p}{\hat{E}} \quad k_{ip} = \frac{\alpha_p\alpha_{ip}}{\hat{E}} \quad (6.49)$$

where $\alpha_{ip} \ll \alpha_p$. In this case, for $\hat{E} = E$ the characteristic polynomial is $s^2 + \alpha_ps + \alpha_p\alpha_{ip} \approx (s + \alpha_p)(s + \alpha_{ip})$. Regardless whether (6.48) or (6.49) is used, it is normally appropriate to make the synchronization loop at least one decade slower than the current control loop, i.e.,

$$\alpha_p \ll \alpha_c. \quad (6.50)$$

A separation of two decades or more is not uncommon, though; whereas α_c typically is in the range of thousands of radians per second, α_p is typically in the range of tens to hundreds of radians per second. In order not to slow down the PLL dynamics, the low-pass-filter bandwidth should be selected as

$$\alpha_l \gg \alpha_p. \quad (6.51)$$

PROBLEM 6.1

Select k_{pp} and k_{ip} such that the poles instead are placed at $s = (-1 \pm j)\alpha_p/\sqrt{2}$ (a conjugated pole pair placed with a 45° angle relative the imaginary axis and the distance α_p from the origin).

Steady-State Performance

The steady-state properties of (6.42)–(6.43) can be investigated by setting $\dot{\omega}_i = \dot{\theta} = 0$. From (6.42) we then get $\sin \tilde{\theta} = 0$. Substituting this in (6.43) yields $\omega_i = \tilde{\omega}_g$. This shows that a deviation $\tilde{\omega}_g$ of the estimated $\tilde{\omega}_g$ from the actual ω_g does not result in a static angular error, owing to the integrator (with output ω_i). However, if $k_{ip} = 0$ and $\omega_i = 0$, then from (6.43) we get the static angular error

$$\tilde{\theta} = \arcsin\left(\frac{\tilde{\omega}_g}{k_{pp}E}\right). \quad (6.52)$$

Global Stability

The nonlinear dynamics (6.42)–(6.43) have an infinite number of equilibrium points: $\tilde{\omega}_g^* = 0$ and $\tilde{\theta}^* = 2n\pi$, n integer. As shown in Appendix A, the PLL is globally stable; that is, regardless of the starting point $[\tilde{\omega}_g(0), \tilde{\theta}(0)]^T$, ω_i converges to $\tilde{\omega}_g$ and $\tilde{\theta}$ converges to $2n\pi$. Unfortunately, even if $\tilde{\theta}(0) \approx 0$, there is no guarantee that $n = 0$ if $\tilde{\omega}_g(0)$ is large; the estimator may fall several revolutions, n , behind the motor. This is known as *cycle slips* in PLL terminology and *pole slipping* in synchronous machine terminology. In some cases, slipping can be prevented by modifying the PLL [86].

CHAPTER 7

Vector Control of Grid-Connected VSCs

CHAPTER 8

Vector Control of PMSM Drives

If a position sensor—e.g., a digital position encoder—is mounted at the shaft of a PMSM, then the flux angle θ becomes readily measurable. This allows setting the dq -frame angle θ_1 equal to the measured θ in the PMSM vector control system, which effectively reduces to just the current controller. Vector control of a position-sensored PMSM drive is thus relatively straightforward.

Somewhat more care is needed when a resolver is used as position sensor. A resolver is a position sensor that allows measurement of cosine and sine of the rotor position. A variant of the PLL presented in Section 6.5 can be applied for extracting θ_1 from the resolver signals, as shown in Section 8.1.

Position sensors are expensive, delicate, prone to failure, often difficult to mount, and require extra cabling. Therefore it is desirable to avoid them, relying instead on position estimation. This is called *sensorless control*, or, to be more precise, *position-sensorless control*.

In Section 8.2, sensorless PMSM drives with a (magnetically) round rotor are considered, i.e., PMSMs with magnets mounted on the surface of the rotor. In this case, estimation of the rotor position is made using a variant of the PLL presented in Section 8.2.1 from information available in the back emf. It is very difficult to gain good performance at low speeds, so particular focus is on solving this problem.

In Section 8.3 we consider sensorless drives with PMSMs that have rotors with buried or inset magnets, giving a salient rotor. This allows position estimation using injection of a high-frequency signal, providing good performance at all speeds.

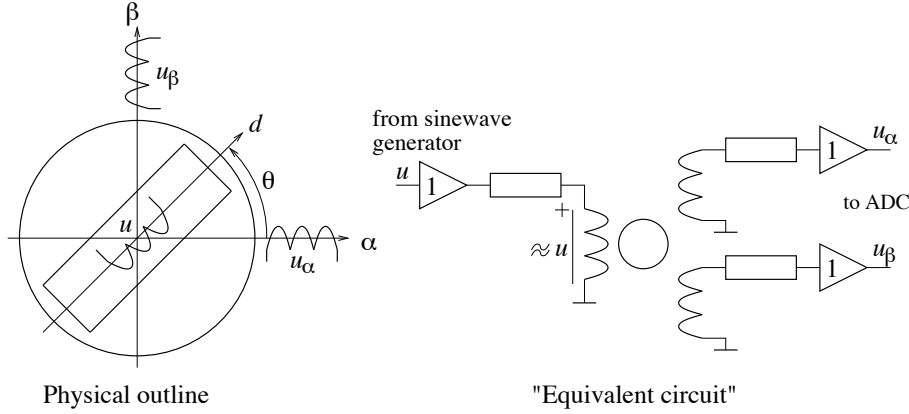
The chapter is finished by discussions of vector current control for salient PMSMs and field-weakening control, in Sections 8.4 and 8.5, respectively.

8.1 Position-Sensored Control Using Resolvers

A resolver is a miniature ac machine. Its rotor winding is supplied by a low-voltage signal (typically with a peak value of 5 V) at, usually, 5 kHz. The stator is wound with two perpendicular coils, in which voltages are induced. The amplitudes of the induced voltages are functions of the rotor position. See Figure 8.1. (An alternative is the “variable-reluctance” resolver which does not have a rotor winding [25].) If a resolver is mounted on the same shaft as a PMSM, then the resolver’s rotor position will coincide with the PMSM’s rotor position, provided that they have the same number of pole pairs and that they are correctly aligned.

8.1.1 Excitation

Let the resolver excitation signal be $u = U \cos \omega_e t$. As the voltage drop across the rotor resistance can be neglected, u is approximately the voltage across the rotor winding. The voltage components

**Figure 8.1.** Principle of a resolver.

induced in the stator winding are then, ideally,

$$u_\alpha = U \cos \theta \cos \omega_e t \quad u_\beta = U \sin \theta \cos \omega_e t. \quad (8.1)$$

That is, cosine and sine, respectively, of the rotor position modulated with the carrier frequency ω_e . The algorithm or circuit that performs this extraction is known as a resolver-to-digital converter.

It is desirable that the excitation signal u should be as ideal a sinusoidal voltage as possible. Demodulation of (8.1) can be performed by multiplying both u_α and u_β by the excitation signal, followed by low-pass filtering [88]. As an alternative, we here present a very simple resolver excitation and tracking scheme which is proposed in [26]. The idea is based on utilizing synchronous sampling; samples of u_α and u_β are taken once each period of the excitation signal. The resolver algorithm should thus use the same sampling frequency as the excitation frequency, i.e., 5 kHz, normally. Via a one-bit D/A converter, the algorithm generates a squarewave signal of angular frequency ω_e . This signal is filtered through an analog (active) low-pass filter, such that the fundamental frequency component at ω_e is phase shifted -90° , whereas harmonics at $3\omega_e$, $5\omega_e$, etc. are attenuated. Sampling is then made ideally at (in practice near) the peak values of u_α and u_β . The principle is illustrated in Figure 8.2. Thus, no signal demodulation is needed, which reduces the complexity of the system.

Filter Design

To achieve a phase shift of -90° , at least a second-order filter is required. At this low filter order, the difference in stopband attenuation between various filter types is not tremendous, so let us pick a Butterworth filter [74] for simplicity. With the Laplace variable s normalized with the angular cutoff frequency, the second-order Butterworth filter has the following transfer function:

$$H_{BW}(s) = \frac{1}{s^2 + \sqrt{2}s + 1} \quad (8.2)$$

giving the phase function

$$\arg H_{BW}(j\omega) = -\arctan \frac{\omega\sqrt{2}}{1 - \omega^2}. \quad (8.3)$$

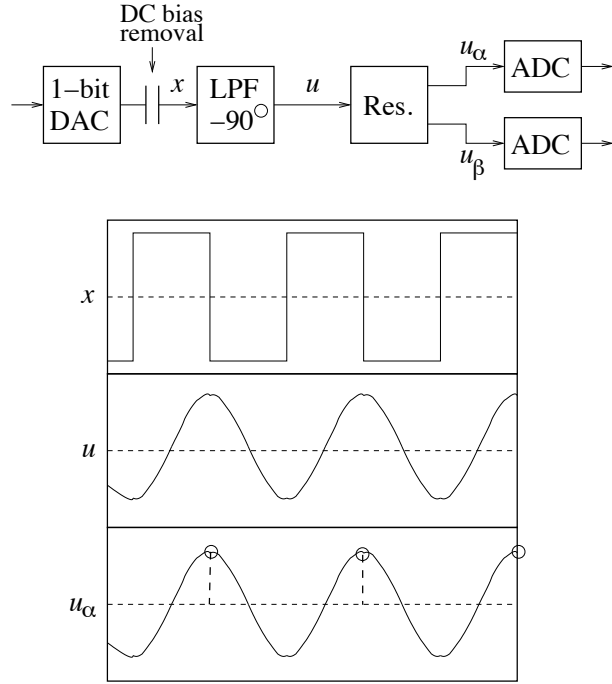


Figure 8.2. Principle of proposed resolver excitation and sampling.

So, the cutoff frequency of the filter should be set to the resolver excitation frequency (5 kHz normally) to obtain a phase shift of -90° . An active RC realization is shown in Figure 8.3. Figure 8.4 shows two periods of the input and output signals. Note that sampling is not made exactly at the peaks. This is due to a small harmonic distortion; the output signal is not a pure sinusoid.

8.1.2 Tracking

The synchronously sampled resolver output signals are ideally

$$u_\alpha = U \cos \theta \quad u_\beta = U \sin \theta. \quad (8.4)$$

With θ_1 as the position estimate, the following error signal to be used as PLL input can be obtained:

$$E_d = u_\alpha \sin \theta_1 - u_\beta \cos \theta_1 = -U \sin(\theta - \theta_1) = -U \sin \tilde{\theta} \quad (8.5)$$

allowing (6.40)–(6.41) to be applied to extract θ_1 . Equation (6.48) with $\hat{E} \rightarrow \hat{U}$, where \hat{U} is an estimate of U (i.e., 5 V, normally) is useful for selection of the PLL gains. Algorithm 8.1 shows an implementation of the proposed tracking scheme. The sampling period T_s is the inverse of the resolver excitation frequency. Parameters k_{pp} and k_{ip} can be chosen according to (6.48).

Algorithm 8.1

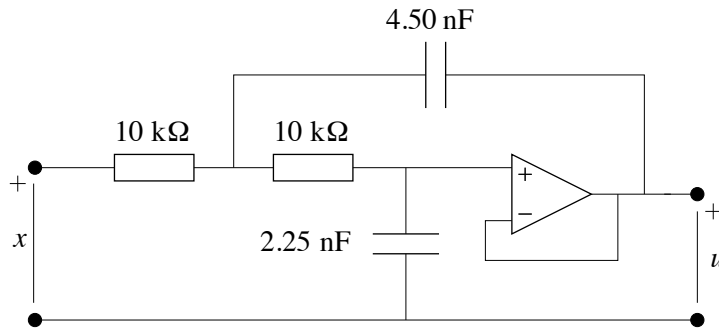


Figure 8.3. Second-order Butterworth low-pass filter with cutoff frequency 5 kHz.

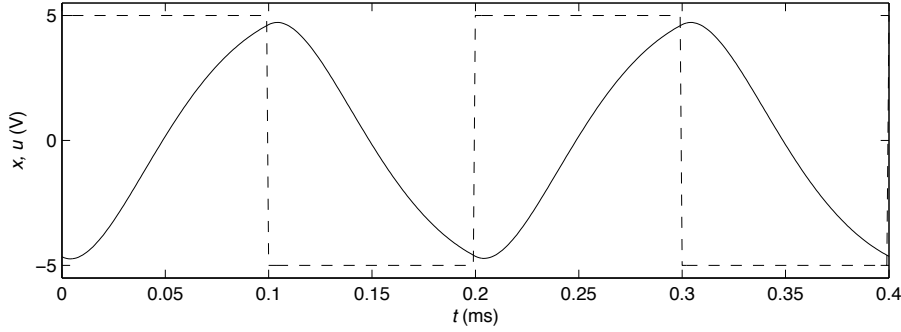


Figure 8.4. Squarewave input signal x (dashed) and resolver excitation signal u (solid).

PLL for Resolver Tracking

$$\begin{aligned} E_d &= u_\alpha \sin \theta_1 - u_\beta \cos \theta_1 \\ \omega_i &= \omega_i - T_s k_{ip} E_d \\ \omega_1 &= \omega_1 + T_s \alpha_l (-k_{pp} E_d + \omega_i - \omega_1) \\ \theta_1 &= \text{mod}(\theta_1 + T_s \omega_1, 2\pi) \end{aligned}$$

8.2 Position-Sensorless Control Using Back-EMF Information

When a position sensor is not used, the rotor position must be estimated from other sources of information. PMSMs with salient rotors allow the injection of a high-frequency test signal, as will be shown in Section 8.3. This option is not available for round-rotor PMSMs (with surface-mounted magnets), or is at least difficult to use. Position estimation must then rely on an estimate of the back emf obtained using the stator voltage and current as

$$\hat{\mathbf{E}} = \mathbf{v}_s - (\hat{R}_s + j\omega_1 \hat{L}_s) \mathbf{i}_s. \quad (8.6)$$

The back-emf estimate can be expressed in the actual back emf and the parameter errors $\tilde{R}_s = R_s - \hat{R}_s$ and $\tilde{L}_s = L_s - \hat{L}_s$. Solving for \mathbf{v}_s in (5.96) and substituting this in (8.6), the following relation is obtained:

$$\hat{\mathbf{E}} = (\tilde{R}_s + j\omega_1 \tilde{L}_s) \mathbf{i}_s + \underbrace{j\omega_r \psi_R e^{j\tilde{\theta}}}_{\mathbf{E}} \quad (8.7)$$

where $d\mathbf{i}_s/dt$ has been neglected, since, as discussed in Chapter 6, the current control loop is assumed to have a much higher bandwidth than the synchronization loop. For the somewhat optimistic assumption that $\tilde{R}_s = \tilde{L}_s = 0$, we get $\hat{\mathbf{E}} = \mathbf{E}$, and in component form

$$\hat{E}_d = -\omega_r \psi_R \sin \tilde{\theta} \quad \hat{E}_q = \omega_r \psi_R \cos \tilde{\theta}. \quad (8.8)$$

Inspecting these components, the following conclusions can be drawn.

- When ω_r is sufficiently large (and its sign is known), a position estimate θ_1 can be obtained using a PLL, since a deviation from $\tilde{\theta} = 0$ immediately will be reflected in \hat{E}_d . Sensorless control of round-rotor PMSMs is not difficult at higher speeds.
- On the other hand, when ω_r is small \hat{E}_d is no longer a reliable indicator, because \hat{E}_d will be small even when $\tilde{\theta}$ is large. The estimator becomes susceptible to measurement noise and erroneous model parameters, which are not taken into account in (8.8). Sensorless control at low speeds is therefore difficult.
- Startup is particularly troublesome. Since $\mathbf{E} = 0$ for $\omega_r = 0$, the estimator is then “blind.” The rotor position is not revealed until the motor starts to rotate; the initial error angle $\tilde{\theta}(0)$ may attain any value between 0 and 2π . If $\tilde{\theta}(0)$ happens to be small [$\theta_1(0)$ happens by luck to be close to $\theta(0)$], then the PMSM will start rotating in the desired direction. However, when $\tilde{\theta}(0)$ is large (approximately $90^\circ < \tilde{\theta}(0) < 270^\circ$), the PMSM will commence to rotate in the wrong direction, which is highly undesirable. This cannot be prevented, but it is important that the system yet synchronizes and the rotation reverses quickly. The estimator must be carefully designed in order to obtain this property.
- As the back emf vanishes at low speeds, not only startup but also rotation reversal is difficult. Instead of reversal, lockup at a low speed may occur.

It is by no means easy to design an estimator that gives good performance at low speeds. The situation is compounded by the fact that in practice, the parameter errors \tilde{R}_s and \tilde{L}_s are generally not negligible. Particularly, the stator resistance varies with the temperature of the motor, as we know from Paragraph 5.6.3.

8.2.1 PLL for Sensorless PMSM Drives

The PLL of Section 6.5 can easily be adapted for the case of sensorless control of the PMSM using back-emf information, i.e., (8.8). The first modification is to replace the constant estimate $\hat{\omega}_g$ in (6.38) (see also Figure 6.10) by a varying estimate, since the speed of the motor is variable. Assuming that $\tilde{\theta}$ is small, such that $\cos \tilde{\theta} \approx 1$, and that the flux-modulus estimate is accurate, $\hat{\psi}_R \approx \psi_R$, then from (8.8) it follows that $\hat{E}_q/\hat{\psi}_R \approx \omega_r$. Thus, we select

$$\hat{\omega}_g = \frac{\hat{E}_q}{\hat{\psi}_R}. \quad (8.9)$$

Without integral action in the PLL (which is not needed, because of the varying $\hat{\omega}_g$), i.e., $k_{ip} = \omega_i = 0$, and with $k_{pp} = \lambda_s/\hat{\psi}_R$ introduced to allow a dimensionless gain λ_s , then (6.38) can be expressed as

$$\dot{\theta}_1 = \omega_1 = \frac{\alpha_l}{p + \alpha_l} \frac{\hat{E}_q - \lambda_s \hat{E}_d}{\hat{\psi}_R} \quad (8.10)$$

where

$$\lambda_s = \lambda \operatorname{sgn} \omega_1, \quad \lambda > 0. \quad (8.11)$$

The low-pass-filter bandwidth should preferably be selected significantly larger than the speed-control-loop bandwidth, i.e.,

$$\alpha_l \gg \alpha_s. \quad (8.12)$$

If there is no speed controller, then the recommendation $\alpha_l \ll b/J$ ensures that the low-pass filter has much higher bandwidth than the open-loop mechanical dynamics.

Gain selection (8.11) ensures convergence of θ_1 . For accurate model parameters, i.e., $\hat{R}_s = R_s$, $\hat{L}_s = L_s$, and $\hat{\psi}_R = \psi_R$, then, with impact of the low-pass filter neglected, (8.10) can be expressed as

$$\dot{\theta}_1 = \omega_r \cos \tilde{\theta} - \lambda_s \omega_r \sin \tilde{\theta}. \quad (8.13)$$

For a small $\tilde{\theta}$, such that $\sin \tilde{\theta} \approx \tilde{\theta}$ and $\cos \tilde{\theta} \approx 1$, (8.13) can be combined with $\dot{\theta} = \omega_r$ as

$$\dot{\tilde{\theta}} = -\lambda_s \omega_1 \tilde{\theta}. \quad (8.14)$$

Thus, as long as $\omega_r \neq 0$ and ω_1 and ω_r have equal signs, then $\tilde{\theta}$ converges asymptotically to zero.

In practice, to reduce noise and eliminate the need for measuring the converter output voltage, references are preferably used instead of measured quantities in (8.6)

$$\hat{\mathbf{E}} = \bar{\mathbf{v}}_s^{\text{ref}} - (\hat{R}_s + j\omega_1 \hat{L}_s) \mathbf{i}_s^{\text{ref}} \quad (8.15)$$

where $\bar{\mathbf{v}}_s^{\text{ref}}$ is the limited (to the PWM hexagon) reference vector. A block diagram of the sensorless vector control system is depicted in Figure 8.5.

8.2.2 Analysis and Parameter Selection

We shall first select gain parameter λ . A proposal for elimination of the estimator's sensitivity to the stator resistance is then presented, which significantly improves the capability of the sensorless drive of reversing rotation under load.

Selection of λ for Quick Synchronization at Startup

It is relatively easy to show that, when ω_1 and ω_r have equal signs, the estimator synchronizes for any initial error angle $\tilde{\theta}(0)$ [46]. However, when the motor starts rotating in the wrong direction, the signs of ω_r and ω_1 are different. It is important that the properties of the estimator are such

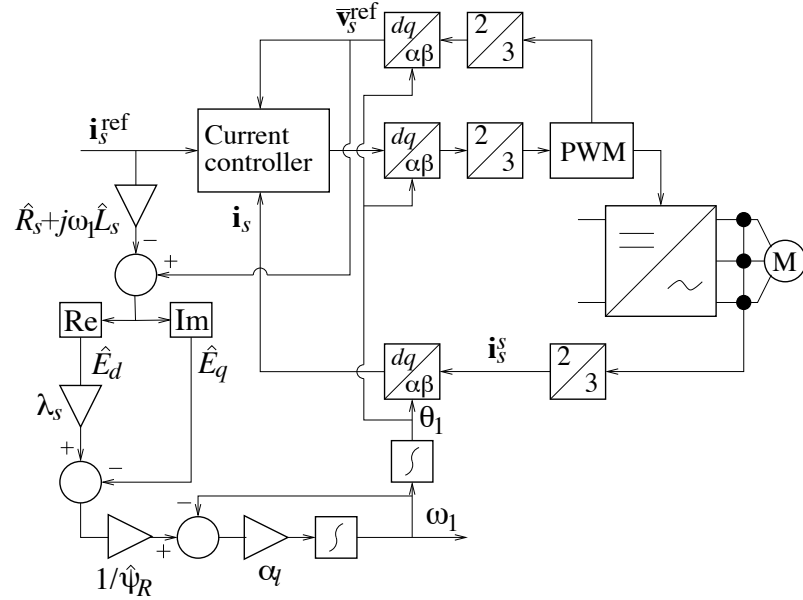


Figure 8.5. Vector control system for sensorless round-roto PMSM drives using a PLL variant.

that ω_1 then changes sign fairly quickly. The discontinuous nonlinearity $\text{sgn } \omega_1$ in (8.11) makes an analytic proof difficult (or even impossible). Therefore, we resort to simulating the system. By making repeated simulations for various initial values: $\tilde{\theta}(0) = n\Delta\theta$, $n = 1, 2, \dots, 360^\circ/\Delta\theta$, for a small $\Delta\theta$, the convergence properties can be investigated for a certain value of λ .

Figure 8.6 shows simulations for $\omega_r > 0$, three different gain parameter values: $\lambda = \{1, 2, 5\}$, and $\Delta\theta = 10^\circ$. The simulations are made in a normalized time scale $\tau = \omega_r t$, where a constant ω_r for simplicity is assumed. The following conclusions can be drawn.

- Synchronization is guaranteed; $\tilde{\theta}$ converges regardless of the initial error angle, for all three choices of λ .
- Making $\lambda < 2$ slows down the convergence noticeably, as seen by comparing the plots for $\lambda = 1$ and $\lambda = 2$.
- Selecting $\lambda > 2$ has only marginal impact, as seen by comparing the plots for $\lambda = 2$ and $\lambda = 5$.

Selecting $\lambda = 2$ (or slightly larger) is therefore a good recommendation.

Selection of i_d for Stable Rotation Reversal

So far, the parameter errors in (8.7) have not been taken into account. We shall now consider the static impacts of \tilde{R}_s and \tilde{L}_s . If the real and imaginary parts of the right-hand side of (8.7) are substituted for \hat{E}_d and \hat{E}_q in (8.10), by setting $\dot{\omega}_1 = 0$ and solving for ω_1 (observing that ω_1

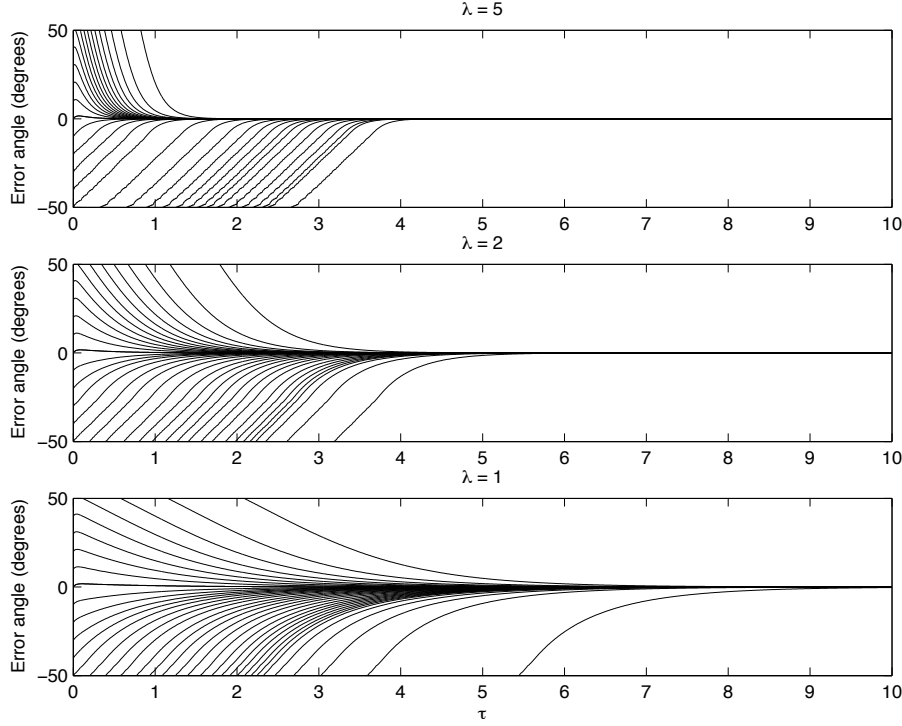


Figure 8.6. Simulations for $\omega_r > 0$ and three different choices of λ .

appears in the expressions for \hat{E}_d and \hat{E}_q), the following relation is found:

$$\omega_1 = \frac{\tilde{R}_s(i_q - \lambda_s i_d) + \omega_r \psi_R (\cos \tilde{\theta} + \lambda_s \sin \tilde{\theta})}{\tilde{\psi}_R - \tilde{L}_s(i_d + \lambda_s i_q)}. \quad (8.16)$$

From this relation, the steady-state position error can be found by setting $\omega_1 = \omega_r$, i.e., assuming synchronous rotation in the steady state. Under the simplifying assumption that the position error is small, such that $\cos \tilde{\theta} \approx 1$, we obtain by solving for $\sin \tilde{\theta}$

$$\sin \tilde{\theta} = \frac{\tilde{R}_s(\lambda_s i_d - i_q)}{\lambda_s \omega_r \psi_R} - \frac{\tilde{\psi}_R}{\lambda_s \psi_R} - \frac{\tilde{L}_s(i_d + \lambda_s i_q)}{\lambda_s \psi_R} \quad (8.17)$$

where $\tilde{\psi}_R = \psi_R - \hat{\psi}_R$. Conclusions can be drawn as follows.

- At low speeds, the first term on the right-hand side of (8.17) dominates, due to its inverse proportionality to ω_r . Nonsalient PMSMs are normally operated with $i_d = 0$, giving $\sin \tilde{\theta} \approx -\tilde{R}_s i_q / (\lambda_s \omega_r \psi_R)$ for small ω_r . A large stator resistance error \tilde{R}_s and/or a large current i_q (i.e., high torque) dictates that a certain lowest operating speed must be observed in order to keep the position error sufficiently small. Clearly, rotation reversal under load for $i_d = 0$ is difficult, unless the stator resistance is known with very good accuracy.

- If the stator current is controlled such that $i_d = i_q/\lambda_s$ (instead of the usual $i_d = 0$), the sensitivity to \tilde{R}_s vanishes. Using a nonzero i_d to some extent reduces the current available for torque production, since $i_d^2 + i_q^2 \leq I_{\max}^2$, where I_{\max} is the maximum permissible current modulus. We get

$$|i_q| \leq \frac{I_{\max}}{\sqrt{1 + 1/\lambda^2}}. \quad (8.18)$$

For a fairly large λ , the reduction in $|i_q|$ is not significant. For example, $\lambda = 2$ yields $|i_q| \leq 0.89I_{\max}$, whereas $\lambda = 3$ yields $|i_q| \leq 0.95I_{\max}$. Controlling the stator current such that $i_d = i_q/\lambda_s$ is therefore a feasible strategy.

- The parameter error $\tilde{\psi}_R$ is normally small, due to a fairly constant magnet flux.
- For fairly large λ , the position error due to the term $\tilde{L}_s i_d / (\lambda_s \psi_R) = \{i_d = i_q/\lambda_s\} = \tilde{L}_s i_q / (\lambda^2 \psi_R)$ will be small.
- Hence, the unavoidable position error, for $i_d = i_q/\lambda_s$ with λ reasonably large ($\lambda \geq 2$), is given by

$$\sin \tilde{\theta} \approx -\frac{\tilde{L}_s i_q}{\psi_R}. \quad (8.19)$$

It should be noted that, for a load torque which is constant or has constant sign, i_d will change sign at the moment of rotation reversal. Due to the well-known fact that i_d does not produce torque in a nonsalient PMSM at accurate field orientation conditions, using a nonzero i_d will not affect the operation of the motor in other ways than reducing the maximum $|i_q|$ according to (8.18). Making $i_d = i_q/\lambda_s$ is, however, required only at low speeds, since the stator resistance is not sensitive at high. Once out of the low-speed region, typically around $\omega_\Delta = 0.1\omega_{\text{base}}$, it is safe to let $i_d^{\text{ref}} = 0$.

Remark 8.1 Eliminating the sensitivity to the stator resistance is equivalent to using the instantaneous reactive power $v_d i_q - v_q i_d$ for estimation purposes [31, 65]. From (8.10) we have, with $\lambda_s = i_q/i_d$,

$$\frac{\hat{E}_q - \lambda_s \hat{E}_d}{\hat{\psi}_R} = \frac{\hat{E}_q - i_q \hat{E}_d / i_d}{\hat{\psi}_R} = \frac{\hat{E}_q i_d - \hat{E}_d i_q}{\hat{\psi}_R i_d}$$

in the steady state, where now $v_d i_q - v_q i_d$ implicitly appears as a term in the numerator.

Speed Control

Closed-loop speed control of a sensorless drive is not different from a sensored drive. Speed controllers are designed in identical ways in both cases, except that in the sensorless case the estimated speed $\hat{\omega}_r$ is fed back rather than the measured speed. Since an SM rotates synchronously, $\hat{\omega}_r = \omega_1$.

Even if α_l and λ are chosen following the previously given recommendations, the synchronization loop may affect the speed control loop. In [46] it is shown that if the stator inductance is overestimated, giving $\tilde{L}_s < 0$, then the speed control loop may turn unstable at higher speeds, especially if the bandwidth α_s is high. In order to guarantee stability, one should make sure that

$$\hat{L}_s < L_s. \quad (8.20)$$

Algorithm and Evaluation

Algorithm 8.2 illustrates the proposed PLL variant. For $|\omega_1| < \omega_\Delta$, $i_d^{\text{ref}} = i_q^{\text{ref}}/\lambda_s$ to eliminate sensitivity to the stator resistance, whereas for $|\omega_1| > \omega_\Delta$, $i_d^{\text{ref}} = 0$.

Algorithm 8.2

PLL for Sensorless PMSM Control Using Back-EMF Information

```

 $\lambda_s = \lambda \operatorname{sgn}(\omega_1)$ 
if  $|\omega_1| < \omega_\Delta$ 
     $i_d^{\text{ref}} = i_q^{\text{ref}}/\lambda_s$ 
else
     $i_d^{\text{ref}} = 0$ 
endif
 $\hat{E}_d = \bar{v}_d^{\text{ref}} - \hat{R}_s i_d^{\text{ref}} + \omega_1 \hat{L}_s i_q^{\text{ref}}$ 
 $\hat{E}_q = \bar{v}_q^{\text{ref}} - \hat{R}_s i_q^{\text{ref}} - \omega_1 \hat{L}_s i_d^{\text{ref}}$ 
 $\omega_1 = \omega_1 + T_s \alpha_l \left( \frac{\hat{E}_q - \lambda_s \hat{E}_d}{\hat{\psi}_R} - \omega_1 \right)$ 
 $\theta_1 = \operatorname{mod}(\theta_1 + T_s \omega_1, 2\pi)$ 

```

Example 8.1 Figures 8.7 and 8.8 show experimental results for a 4.2-kW, six-pole PMSM with the per-unit parameters $R_s = 0.03$, $L_s = 0.27$, $\psi_R = 1.0$, and $J = 3500$, while in the estimator, $\lambda = 2$ is used. In Figure 8.7 it can be observed that, even though the initial error angle is large, once operation commences at $t = 1$ s, $\tilde{\theta}$ converges to a small value in less than half a second. The rotation reversals are made with hardly any transient error angle. In Figure 8.8 it can be noticed that slow ramp-wise rotation reversals under load also can be accomplished successfully. In this case, a fairly large transient error angle results around $\omega_1 = 0$, but synchronism is kept and the rotation reversals are completed successfully.



8.3 Position-Sensorless Control Using Saliency and Signal Injection

For salient PMSMs, very accurate position estimation also at low speeds can be obtained using methods based on signal injection. In the following, we review the method proposed by Corley and Lorenz [15]. Since the injection of an extra signal will lead to at least some additional losses and torque ripple, a smooth transition to back-emf-based estimation should be made as the speed increases. We in this section show how a PLL can be adapted for usage also with the signal-injection method.

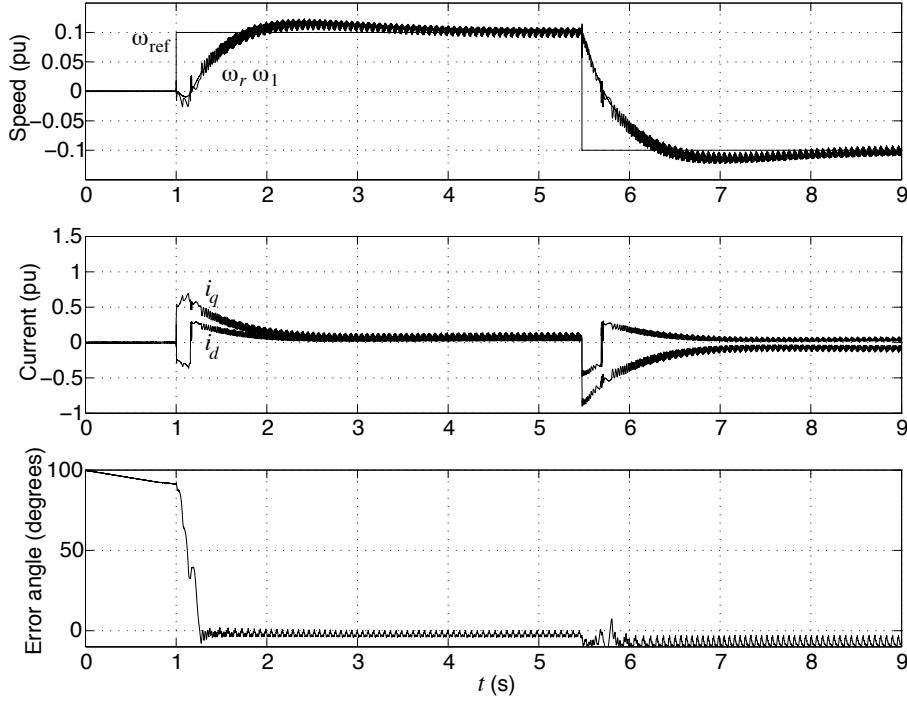


Figure 8.7. Startup and rotation reversals under no-load conditions of a nonsalient sensorless PMSM drive.

8.3.1 Signal Injection and Position Extraction

The idea is to inject a high-frequency voltage in what is *assumed* to be the d direction. This is made by adding a component to the d -direction voltage reference as

$$v_d^{\text{ref}'} = V \cos \omega_e t + v_d^{\text{ref}}. \quad (8.21)$$

Typically, the frequency of the added component is selected around 500 Hz, i.e., $\omega_e = 2\pi \cdot 500$ rad/s. From the current in the assumed q direction, rotor position information can be extracted, provided that the rotor is salient and the direction of the saliency (i.e., the sign of $L_q - L_d$) is known. Figure 8.9 illustrates the method.

At standstill, (5.116) is reduced to

$$i_s = \underbrace{e^{j\tilde{\theta}}(pL + R)^{-1}e^{-j\tilde{\theta}}}_{G(p, \tilde{\theta})} v_s. \quad (8.22)$$

With the stationary sinusoidal excitation (8.21), we need to consider $p = j\omega_e$ only:

$$G(j\omega_e, \tilde{\theta}) = e^{j\tilde{\theta}}(j\omega_e L + R)^{-1}e^{-j\tilde{\theta}} \approx e^{j\tilde{\theta}}(j\omega_e L)^{-1}e^{-j\tilde{\theta}} = \frac{1}{j\omega_e} e^{j\tilde{\theta}} L^{-1} e^{-j\tilde{\theta}} \quad (8.23)$$

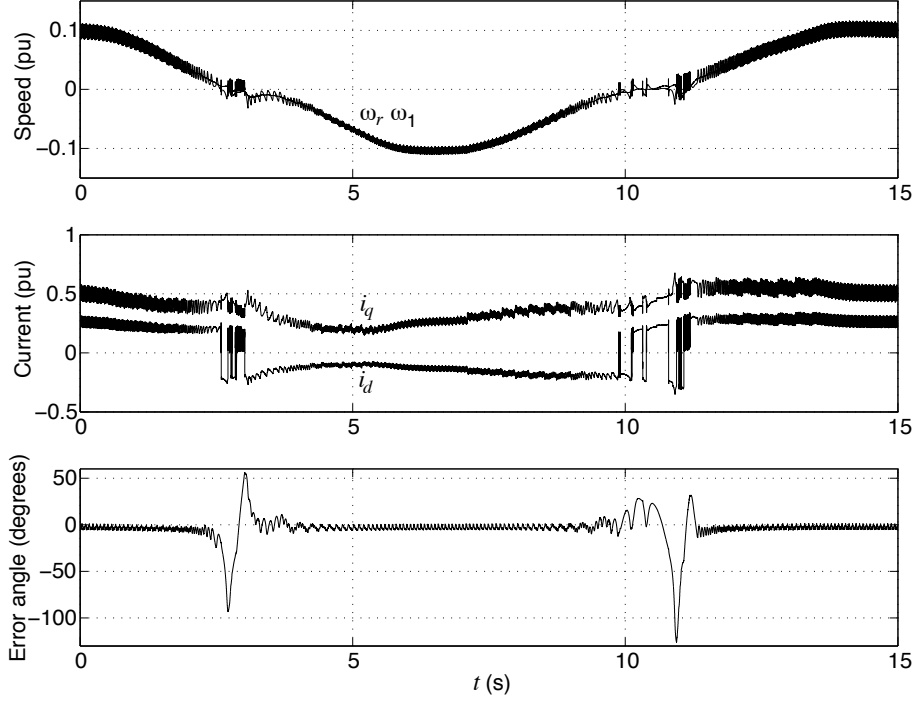


Figure 8.8. Ramp-wise rotation reversals under load of a nonsalient sensorless PMSM drive.

the approximation since $\{\omega_e L_d, \omega_e L_q\} \gg R_s$. We have

$$L^{-1} = \begin{bmatrix} \frac{1}{L_d} & 0 \\ 0 & \frac{1}{L_q} \end{bmatrix} = \frac{L_q + L_d}{2L_q L_d} \begin{bmatrix} 1 & 0 \\ 0 & 1 \end{bmatrix} + \frac{L_q - L_d}{2L_q L_d} \begin{bmatrix} 1 & 0 \\ 0 & -1 \end{bmatrix} \quad (8.24)$$

which yields

$$\begin{aligned} e^{J\tilde{\theta}} L^{-1} e^{-J\tilde{\theta}} &= \frac{L_q + L_d}{2L_q L_d} I + \frac{L_q - L_d}{2L_q L_d} e^{J\tilde{\theta}} \begin{bmatrix} 1 & 0 \\ 0 & -1 \end{bmatrix} e^{-J\tilde{\theta}} \\ &= \frac{L_q + L_d}{2L_q L_d} I + \frac{L_q - L_d}{2L_q L_d} \begin{bmatrix} \cos 2\tilde{\theta} & \sin 2\tilde{\theta} \\ \sin 2\tilde{\theta} & -\cos 2\tilde{\theta} \end{bmatrix}. \end{aligned} \quad (8.25)$$

Thus, from d voltage to q current we have the frequency function

$$G_{dq}(j\omega_e, \tilde{\theta}) = [0 \ 1] G(j\omega_e, \tilde{\theta}) \begin{bmatrix} 1 \\ 0 \end{bmatrix} = \frac{1}{j\omega_e} \frac{L_q - L_d}{2L_q L_d} \sin 2\tilde{\theta} \quad (8.26)$$

yielding the measured current

$$i_q = V \operatorname{Re}\{G_{dq}(j\omega_e, \tilde{\theta})e^{j\omega_e t}\} + i_{q0} = \frac{V}{\omega_e} \frac{L_q - L_d}{2L_q L_d} \sin 2\tilde{\theta} \sin \omega_e t + i_{q0}. \quad (8.27)$$

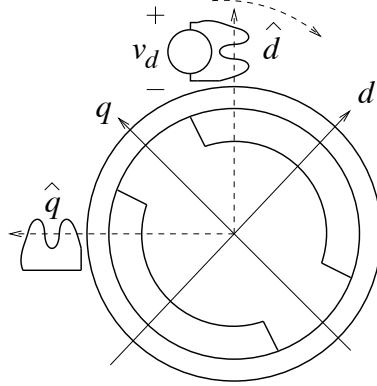


Figure 8.9. Estimation of the position using saliency and signal injection.

This signal is an amplitude modulation of the carrier $\sin \omega_e t$ by the envelope $\sin 2\tilde{\theta}$, to which the dc component i_{q0} is added, which acts as a bias to the modulated signal. To remove this bias, the measured current is first fed through a high-pass filter (HPF). A simple first-order filter is perfectly adequate

$$H_{\text{HP}}(s) = \frac{s}{s + \alpha_h} \Rightarrow i_q^f = H_{\text{HP}}(p)i_q. \quad (8.28)$$

The cut-off frequency α_h of this filter should be selected low, typically in the range of $\alpha_h/2\pi = 1$ Hz $\Leftrightarrow \alpha_h \approx 6$ rad/s. To appreciate this, note that i_{q0} is only dc in the steady state; due to closed-loop current control it follows its reference i_q^{ref} , which varies with the dynamics of the speed control loop (closed-loop speed control assumed). Hence, the cut-off frequency of the high-pass filter should preferably be selected no lower than the speed-control-loop bandwidth α_s , so that the dynamics of i_{q0} fall within the stopband of the high-pass filter. With the mentioned $\alpha_h = 6$ rad/s, a speed rise time of $2.2/\alpha_s = 2.2/\alpha_h \approx 0.4$ s is allowed for, showing that the cut-off frequency has to be selected higher than 1 Hz only for very fast servo drives.

To demodulate, the filtered signal is multiplied by $\sin \omega_e t$, giving

$$\begin{aligned} \varepsilon &= i_q^f \sin \omega_e t = \frac{V}{\omega_e} \frac{L_q - L_d}{2L_q L_d} \sin 2\tilde{\theta} \sin^2 \omega_e t \\ &= \underbrace{\frac{V}{\omega_e} \frac{L_q - L_d}{4L_q L_d} \sin 2\tilde{\theta}}_{(*)} - \underbrace{\frac{V}{\omega_e} \frac{L_q - L_d}{4L_q L_d} \sin 2\tilde{\theta} \cos 2\omega_e t}_{(**)}. \end{aligned} \quad (8.29)$$

In this function the term (*) carries the vital position error information. The other term, (**), acts as high-frequency disturbance. This disturbance is not significant, however, as it disappears as $\tilde{\theta}$ becomes small. The PLL can be used for speed and position estimation, using $E_d \rightarrow= -\varepsilon$.

8.4 Vector Current Control of Salient PMSMs

In Chapter 6, synchronous-frame current controller design based on complex space vectors is considered. For this reason, the obtained controller is not immediately applicable to salient PMSMs.

Extending the theory to such motors is straightforward, however. The dynamic model for the salient PMSM, (5.118)–(5.119), can be expressed in real vector form as

$$\begin{bmatrix} L_d \frac{di_d}{dt} \\ L_q \frac{di_q}{dt} \end{bmatrix} = \begin{bmatrix} v_d \\ v_q \end{bmatrix} - \begin{bmatrix} R_s & -\omega_r L_q \\ \omega_r L_d & R_s \end{bmatrix} \begin{bmatrix} i_d \\ i_q \end{bmatrix} - \begin{bmatrix} E_d^b \\ E_q^b \end{bmatrix}. \quad (8.30)$$

Decoupling and an “active resistance” are introduced by letting

$$\begin{bmatrix} v_d \\ v_q \end{bmatrix} = \begin{bmatrix} v'_d \\ v'_q \end{bmatrix} - \begin{bmatrix} R_{ad} & -\omega_1 \hat{L}_q \\ \omega_1 \hat{L}_d & R_{aq} \end{bmatrix} \begin{bmatrix} i_d \\ i_q \end{bmatrix} \quad (8.31)$$

ideally giving

$$\begin{bmatrix} L_d \frac{di_d}{dt} \\ L_q \frac{di_q}{dt} \end{bmatrix} = \begin{bmatrix} v'_d \\ v'_q \end{bmatrix} - \begin{bmatrix} R_s + R_{ad} & 0 \\ 0 & R_s + R_{aq} \end{bmatrix} \begin{bmatrix} i_d \\ i_q \end{bmatrix} - \begin{bmatrix} E_d^b \\ E_q^b \end{bmatrix}. \quad (8.32)$$

The two inner feedback loops are now decoupled. By selecting

$$R_{ad} = \alpha_c \hat{L}_d - \hat{R}_s \quad R_{aq} = \alpha_c \hat{L}_q - \hat{R}_s \quad (8.33)$$

both loops get bandwidth α_c , ideally. In operator notation

$$i_d = \frac{1}{(p + \alpha_c)L_d} v'_d \quad i_q = \frac{1}{(p + \alpha_c)L_q} v'_q. \quad (8.34)$$

The outer loops are then closed with two PI controllers. Applying direct synthesis yields

$$v'_d = \frac{\alpha_c \hat{L}_d (p + \alpha_c)}{p} (i_d^{\text{ref}} - i_d) \quad v'_q = \frac{\alpha_c \hat{L}_q (p + \alpha_c)}{p} (i_q^{\text{ref}} - i_q). \quad (8.35)$$

That is,

$$k_{pd} = \alpha_c \hat{L}_d \quad k_{id} = \alpha_c^2 \hat{L}_d \quad (8.36)$$

$$k_{pq} = \alpha_c \hat{L}_q \quad k_{iq} = \alpha_c^2 \hat{L}_q. \quad (8.37)$$

Incorporating “back calculation” yields Algorithm 8.3.

Algorithm 8.3

Vector Current Control of Salient PMSMs

$$\begin{aligned}
\begin{bmatrix} i_d \\ i_q \end{bmatrix} &= \begin{bmatrix} \cos(\theta_1) & \sin(\theta_1) \\ -\sin(\theta_1) & \cos(\theta_1) \end{bmatrix} \begin{bmatrix} i_\alpha \\ i_\beta \end{bmatrix} \\
\begin{bmatrix} e_d \\ e_q \end{bmatrix} &= \begin{bmatrix} i_d^{\text{ref}} \\ i_q^{\text{ref}} \end{bmatrix} - \begin{bmatrix} i_d \\ i_q \end{bmatrix} \\
\begin{bmatrix} v_d^{\text{ref}} \\ v_q^{\text{ref}} \end{bmatrix} &= \begin{bmatrix} k_{pd}e_d \\ k_{pq}e_q \end{bmatrix} + \begin{bmatrix} k_{id}I_d \\ k_{iq}I_q \end{bmatrix} - \begin{bmatrix} R_{ad} & \omega_1 \hat{L}_q \\ -\omega_1 \hat{L}_d & R_{aq} \end{bmatrix} \begin{bmatrix} i_d \\ i_q \end{bmatrix} + \begin{bmatrix} 0 \\ \hat{E}_q \end{bmatrix} \\
\theta'_1 &= \theta_1 + \omega_1 T_d \\
\begin{bmatrix} v_\alpha^{\text{ref}} \\ v_\beta^{\text{ref}} \end{bmatrix} &= \begin{bmatrix} \cos(\theta'_1) & -\sin(\theta'_1) \\ \sin(\theta'_1) & \cos(\theta'_1) \end{bmatrix} \begin{bmatrix} v_d^{\text{ref}} \\ v_q^{\text{ref}} \end{bmatrix} \\
[\bar{v}_\alpha, \bar{v}_\beta] &= \text{PWM}(v_\alpha, v_\beta) \\
\begin{bmatrix} \bar{v}_d^{\text{ref}} \\ \bar{v}_q^{\text{ref}} \end{bmatrix} &= \begin{bmatrix} \cos(\theta'_1) & \sin(\theta'_1) \\ -\sin(\theta'_1) & \cos(\theta'_1) \end{bmatrix} \begin{bmatrix} \bar{v}_\alpha^{\text{ref}} \\ \bar{v}_\beta^{\text{ref}} \end{bmatrix} \\
\begin{bmatrix} I_d \\ I_q \end{bmatrix} &= \begin{bmatrix} I_d \\ I_q \end{bmatrix} + T_s \begin{bmatrix} e_d + \frac{1}{k_{pd}} (\bar{v}_d^{\text{ref}} - v_d^{\text{ref}}) \\ e_q + \frac{1}{k_{pq}} (\bar{v}_q^{\text{ref}} - v_q^{\text{ref}}) \end{bmatrix}
\end{aligned}$$

8.5 Field-Weakening Control

For operation above base speed the flux must be reduced, since the stator voltage then has reached its maximum. This is made by manipulating the reference i_d^{ref} for the flux-producing current component. One convenient strategy for this manipulation is to introduce an integrating field-weakening controller

$$i_d^{\text{ref}} = k_{\text{fw}} \int [V_{\text{base}}^2 - (v_d^{\text{ref}})^2 - (v_q^{\text{ref}})^2] dt \Big|_{I_{\min}}^{I_{\text{nom}}} \quad (8.38)$$

where v_d^{ref} and v_q^{ref} are the ideal voltage references from the current controller (vector $\mathbf{v}_s^{\text{ref}} = v_d^{\text{ref}} + jv_q^{\text{ref}}$, see Algorithm 6.1), before the PWM algorithm is applied (giving $\bar{\mathbf{v}}_s^{\text{ref}} = \bar{v}_d^{\text{ref}} + j\bar{v}_q^{\text{ref}}$). The algorithm described by (8.38) works as follows. When $|\mathbf{v}_s^{\text{ref}}| > V_{\text{base}}$, i.e., the current controller wants to put out a voltage that exceeds the base voltage, i_d^{ref} is decreased from its nominal value I_{nom} , but not below the minimum value I_{\min} . When $|\mathbf{v}_s^{\text{ref}}| < V_{\text{base}}$, i_d^{ref} is increased, but not above the nominal value. This way, the flux is reduced precisely as much as required to achieve $|\mathbf{v}_s| = V_{\text{base}}$ in the field-weakening region. Saturation is avoided in the steady state, cf. Figure 3.15. For round-rotor PMSMs $I_{\text{nom}} = 0$, normally (giving $i_d = 0$ below base speed), whereas for salient PMSMs (5.123) can be applied to obtain maximum torque by letting

$$I_{\text{nom}} = r(\chi) i_q^{\text{ref}} \approx \frac{(L_d - L_q) I_{\text{base}}}{\hat{\psi}_R} i_q^{\text{ref}}. \quad (8.39)$$

The minimum shall be selected as

$$-I_{\text{base}} < I_{\min} < 0 \quad (8.40)$$

because if $I_{\min} = -I_{\text{base}}$, then $i_d = I_{\min}$ implies that $i_q = 0$ to prevent overcurrent, meaning that zero torque is produced. A block diagram of the suggested controller is depicted in Figure 8.10. Notice that the nominal $i_{q,\text{nom}}^{\text{ref}}$ must be saturated as follows to avoid overcurrent in the field-weakening range

$$i_q^{\text{ref}} = \text{sat} \left(i_{q,\text{nom}}^{\text{ref}}, \sqrt{I_{\max}^2 - (i_d^{\text{ref}})^2} \right) \quad (8.41)$$

where I_{\max} shall be reduced to I_{base} after the maximum time that overcurrent is allowed.

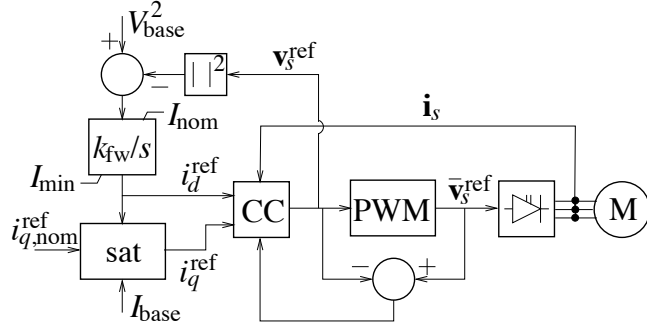


Figure 8.10. Field-weakening controller for PMSM drives, where “sat” is implemented according to (8.41). “CC” is the current controller with “back calculation.” (To avoid clutter, stationary/synchronous coordinate transformations are not shown.)

8.5.1 Gain Selection

Selecting the gain k_{fw} in (8.38) requires analysis of the dynamics of i_d given by (8.38). These are nonlinear, because of the quadratic terms in the input signal to the integrator, i.e., the integrand in (8.38). Let us denote the integrand as

$$f(i_d) = V_{\text{base}}^2 - (v_d^{\text{ref}})^2 - (v_q^{\text{ref}})^2. \quad (8.42)$$

In the steady state, with perfect field orientation, we have [cf. (5.58)]

$$v_d = -\omega_1 L_q i_q \quad v_q = \omega_1 (L_d i_d + \psi_R) \quad (8.43)$$

with the voltage drop across the stator resistance neglected. Substitution in (8.42) yields

$$f(i_d) = V_{\text{base}}^2 - (\omega_1 L_q i_q)^2 - [\omega_1 (L_d i_d + \psi_R)]^2 \quad (8.44)$$

which can be linearized around an operating point i_d^* as

$$f(i_d) \approx \underbrace{f(i_d^*)}_{0} + \frac{df(i_d)}{di_d}(i_d - i_d^*) = -2\omega_1 L_d \underbrace{(L_d i_d^* + \psi_R)}_{v_q^*} (i_d - i_d^*) \quad (8.45)$$

As i_d is made negative during field-weakening operation, $|i_q|$ must be reduced to prevent overcurrent. Consequently, it is not unreasonable to approximate $V_{\text{base}}^2 = v_d^2 + v_q^2 \approx v_q^2$, which in turn

yields $v_q^* \approx V_{\text{base}} \operatorname{sgn} \omega_1$ and

$$\frac{df(i_d)}{di_d} \approx -2|\omega_1|L_d V_{\text{base}}. \quad (8.46)$$

This allows (8.38) to be linearized as

$$\frac{di_d^{\text{ref}}}{dt} = -\underbrace{2k_{\text{fw}}|\omega_1|L_d V_{\text{base}}}_{\alpha_{\text{fw}}}(i_d - i_d^*). \quad (8.47)$$

Assuming that the field-weakening control is made significantly slower than the current control, then $i_d = i_d^{\text{ref}}$ can be assumed in (8.45), which shows that the closed-loop dynamics of the field-weakening control has bandwidth α_{fw} . Obviously, α_{fw} should be chosen much lower than the current-control-loop bandwidth for the assumption of time-scale separation with the current control loop to hold, but it should preferably be chosen larger than the speed-control-loop bandwidth, i.e.,

$$\alpha_s < \alpha_{\text{fw}} \ll \alpha_c. \quad (8.48)$$

This results in the following recommendation for gain selection:

$$k_{\text{fw}} = \frac{\alpha_{\text{fw}}}{2\hat{L}_d V_{\text{base}} \max(|\omega_1|, \omega_{\text{base}})}. \quad (8.49)$$

A constant gain is used below base speed, whereas k_{fw} is decreased as $1/|\omega_1|$ above base speed to maintain the closed-loop bandwidth α_{fw} . Algorithm 8.4 is obtained.

Algorithm 8.4

Field-Weakening Controller for PMSM Drives

$$\begin{aligned} i_d^{\text{ref}} &= i_d^{\text{ref}} + \frac{T_s \alpha_{\text{fw}}}{2\hat{L}_d V_{\text{base}} \max(|\omega_1|, \omega_{\text{base}})} [V_{\text{base}}^2 - (v_d^{\text{ref}})^2 - (v_q^{\text{ref}})^2] \\ i_d^{\text{ref}} &= \min[\max(i_d^{\text{ref}}, I_{\min}), I_{\text{nom}}] \\ i_q^{\text{ref}} &= \text{sat} \left(i_{q,\text{nom}}^{\text{ref}}, \sqrt{I_{\max}^2 - (i_d^{\text{ref}})^2} \right) \end{aligned}$$

CHAPTER 9

Vector Control of IM Drives

It is well known that the flux of an IM cannot readily be measured. Consequently, a flux estimator of some kind is fundamental to any IM vector control system. There are two archetypical flux estimators: the current model, which is based on the rotor circuit of the IM, and the voltage model, which is based on the stator circuit. Both estimator types can be implemented either in the $\alpha\beta$ frame or in the dq frame. The resulting vector control systems types are known as direct field orientation (DFO) and indirect field orientation (IFO), respectively. We shall in this chapter consider both the mentioned flux estimators, as well as variants of them. We shall also consider both DFO and IFO, though our preference is IFO. The reason for this preference is the same as the preference for current control in the dq frame rather than the $\alpha\beta$ frame: the quantities are constant rather than constantly oscillating in the steady state.

Vector control of IM drives is both similar to and different from vector control of PMSM drives. The main difference is as follows.

Due to the asynchronous rotation of the IM, measurement of the rotor position—unlike for the PMSM—does not reveal the rotor flux angle.

This complicates the flux estimator, but yet, if the rotor speed—or just the rotor speed—is measured it is a great help, because it makes estimating the flux angle accurately a lot easier, particularly at low speeds. This will be shown in Section 9.1. Speed-sensored control of IM drives is more complicated than position-sensored control of PMSM drives, but not tremendously so.

For cost and reliability reasons, speed sensors for IMs should preferably be avoided. The flux angle then has to be estimated without the help of speed measurement. In the low-speed range this greatly reduces the stability robustness of the drive, as we shall find in Section 9.2. Concerning sensorless control there are two significant differences between the PMSM and the IM.

- Unlike the PMSM, the initial rotor flux angle $\tilde{\theta}(0)$ of the IM is *known when the drive is started*. This is because the rotor flux is created from the stator by controlling the d -direction current component to a constant value before a torque-producing (q -direction) current component is applied. For this reason, synchronization at startup is not a problem, even without a speed sensor.
- On the other hand, also because the rotor flux is created from the stator, the flux is dynamic. Loss of accuracy in the field orientation may result in undesired demagnetization and loss of torque. For this reason, stable rotation reversals under load are quite difficult to accomplish with sensorless IM drives.

A discussion of field-weakening control is made in Section 9.3. The chapter is finished by a presentation of the well-known scheme direct torque control (DTC), which can be found in Section 9.4. This is a control method that effectively merges field orientation, current control, and PWM.

9.1 Speed-Sensored Control

9.1.1 Direct Field Orientation Using the Current Model

By simulating the rotor circuit of the IM, given by (5.36), the following flux estimator is obtained:

$$\frac{d\hat{\Psi}_R^s}{dt} = \hat{R}_R \mathbf{i}_s^s - \left(\frac{\hat{R}_R}{\hat{L}_M} - j\omega_r \right) \hat{\Psi}_R^s. \quad (9.1)$$

This estimator is called the current model. An implementation of the current model as it stands, i.e., in the $\alpha\beta$ frame, yields a DFO vector control system. Even though a flux estimate in Cartesian $\alpha\beta$ coordinates is obtained, it is instructive to express it in polar form as $\hat{\Psi}_R^s = \hat{\psi}_R e^{j\theta_1}$. This reveals that the $\alpha\beta$ and dq transformation factors $e^{\pm j\theta_1}$ can be obtained by normalizing the flux estimate as

$$\frac{\hat{\Psi}_R^s}{|\hat{\Psi}_R^s|} = \frac{\hat{\psi}_\alpha + j\hat{\psi}_\beta}{\sqrt{\hat{\psi}_\alpha^2 + \hat{\psi}_\beta^2}} = e^{j\theta_1} \quad \frac{(\hat{\Psi}_R^s)^*}{|\hat{\Psi}_R^s|} = \frac{\hat{\psi}_\alpha - j\hat{\psi}_\beta}{\sqrt{\hat{\psi}_\alpha^2 + \hat{\psi}_\beta^2}} = e^{-j\theta_1}. \quad (9.2)$$

That is, cosine and sine of the transformation angle are calculated implicitly as

$$\cos \theta_1 = \frac{\hat{\psi}_\alpha}{\sqrt{\hat{\psi}_\alpha^2 + \hat{\psi}_\beta^2}} \quad \sin \theta_1 = \frac{\hat{\psi}_\beta}{\sqrt{\hat{\psi}_\alpha^2 + \hat{\psi}_\beta^2}}. \quad (9.3)$$

Avoiding trigonometric operations was imperative before powerful microprocessors became available, which allowed digital implementation of control algorithms. For implementation in analog electronics, DFO thus was preferable, even though the square-root and division operations in (9.3) yet posed difficulties that had to be circumvented. DFO tended to be more popular than IFO well into the age of digital implementation, perhaps for pure historical reasons.

9.1.2 Properties of the Current Model

By inspecting (9.1), the following drawbacks of the current model are revealed.

- The current model is a speed-*sensored* flux estimator, because ω_r is used in the estimator equations.
- The current model is sensitive to \hat{R}_R and \hat{L}_M . Detuned (erroneous) model parameters affect the estimated flux angle, giving imperfect field orientation. (This effect will be quantified in the analysis made in the following.) The magnetizing inductance and (particularly) the rotor resistance both change during operation, as discussed in Paragraph 5.6.3.

Outweighing these drawbacks is one strong benefit: the current model is guaranteed always to give robustly stable operation in the low-speed region. See further Paragraph 9.1.4.

9.1.3 Indirect Field Orientation Using the Current Model

By assuming Ψ_R real—i.e., perfect field orientation—the flux equation (5.40) reduces to a simpler form, that can be rearranged as the ideal flux-modulus dynamics (5.45) and the slip relation

(5.46). The current model can be transformed in an identical manner. First, let us transform (9.1) to synchronous coordinates

$$\frac{d\hat{\Psi}_R}{dt} = \hat{R}_R \mathbf{i}_s - \left(\frac{\hat{R}_R}{\hat{L}_M} + j\omega_2 \right) \hat{\Psi}_R \quad (9.4)$$

and let the flux estimate be real: $\hat{\Psi}_R = \hat{\psi}_R$ (as the field orientation of the flux estimator itself is always perfect). By separating the real and imaginary parts, we obtain

$$\frac{d\hat{\psi}_R}{dt} = \hat{R}_R i_d - \frac{\hat{R}_R}{\hat{L}_M} \hat{\psi}_R \quad (9.5)$$

$$\omega_2 = \omega_1 - \omega_r = \frac{\hat{R}_R i_q}{\hat{\psi}_R}. \quad (9.6)$$

Equation (9.6) is usually referred to simply as the slip relation, but later we shall generalize it and therefore it will be named as the *standard slip relation*. The angular stator frequency is computed using (9.6) and is then integrated into the transformation angle

$$\omega_1 = \omega_r + \frac{\hat{R}_R i_q^{\text{ref}}}{\hat{\psi}_R}, \quad \dot{\theta}_1 = \omega_1 \quad (9.7)$$

where reference i_q^{ref} is used rather than the measured component in order to reduce noise. Similarly, i_d^{ref} should be used in (9.5), giving

$$\frac{d\hat{\psi}_R}{dt} = \hat{R}_R i_d^{\text{ref}} - \frac{\hat{R}_R}{\hat{L}_M} \hat{\psi}_R. \quad (9.8)$$

This scheme is a direct IFO correspondence to the DFO variant of the current model (9.1). IFO is generally preferable to DFO, since all quantities (except θ_1) are constant in the steady state and ω_1 is an explicit variable in the control algorithm. Figure 9.1 shows a block diagram of an IFO vector control system. The flux estimator, whose output is ω_1 , may be implemented using the equations for the current model—see Algorithm 9.1—or a variant thereof. If (9.7)–(9.8) are employed, then the signal path for $\bar{\mathbf{v}}_{\text{ref}}$ into the flux-estimator block is unused.

Algorithm 9.1

Current Model

$$\begin{aligned} \omega_1 &= \omega_r + \frac{\hat{R}_R i_q^{\text{ref}}}{\hat{\psi}_R} \\ \theta_1 &= \text{mod}(\theta_1 + T_s \omega_1, 2\pi) \\ \hat{\psi}_R &= \hat{\psi}_R + T_s \hat{R}_R \left(i_d^{\text{ref}} - \frac{\hat{\psi}_R}{\hat{L}_M} \right) \end{aligned}$$

Remark 9.1 If ψ_{ref} is constant and, from (5.48), $i_d^{\text{ref}} = \psi_{\text{ref}}/\hat{L}_M$, then it is seen in (9.5) that $\hat{\psi}_R$ converges to ψ_{ref} . Hence, for a constant ψ_{ref} , i.e., if field weakening is not used, (9.5) need not be implemented; $\hat{\psi}_R$ in (9.7) can be replaced by ψ_{ref} .

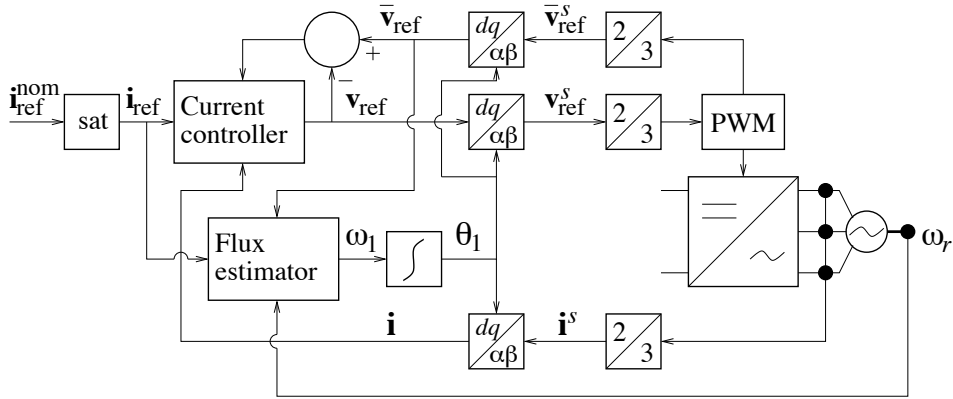


Figure 9.1. IFO vector control system for IM drives.

9.1.4 Analysis of the Current Model

It is straightforward to show that the current model (9.5)–(9.6) with $i_d = \psi_{ref}/\hat{L}_M$ gives perfect field orientation, assuming accurate model parameters. With $\hat{L}_M = L_M$ and $\hat{R}_R = R_R$, (9.5) is subtracted from (5.40) and $\tilde{\psi}_R = \psi_R - \hat{\psi}_R$ is introduced, giving

$$\dot{\tilde{\psi}}_R = R_R i_q - \frac{R_R}{L_M} \tilde{\psi}_R - j\omega_2 (\tilde{\psi}_R - \hat{\psi}_R). \quad (9.9)$$

Substituting (9.6) in (9.9) yields the following simplification of (9.9):

$$\dot{\tilde{\psi}}_R = - \left(\frac{R_R}{L_M} + j \frac{R_R i_q}{\psi_{ref}} \right) \tilde{\psi}_R \quad (9.10)$$

which has the solution

$$\tilde{\psi}_R(t) = \tilde{\psi}_R(0) \exp \left(- \frac{R_R}{L_M} t + j R_R \int_0^t \frac{i_q}{\psi_{ref}} d\tau \right). \quad (9.11)$$

Hence, $|\tilde{\psi}_R| = |\tilde{\psi}_R(0)| e^{-R_R t / L_M}$, i.e., ψ_R converges exponentially to $\hat{\psi}_R$ with the rotor time constant L_M/R_R . In turn, $\hat{\psi}_R$ converges to ψ_{ref} because of the open-loop simulation (9.5). So, convergence of ψ_R to the desired ψ_{ref} is guaranteed for all operating conditions, including varying i_q and ψ_{ref} . This is a unique and very strong stability property of the current model.

Note, however, the assumption of correct model parameters. Although it has been shown that the current model is quite tolerant to erroneous model parameters with regard to stability [16], detuning of the model parameters \hat{R}_R and \hat{L}_M will lead to erroneous field orientation, giving degraded performance. The steady-state rotor flux resulting from detuned model parameters is

easy to calculate from (5.40)

$$\begin{aligned}\Psi_R &= \frac{R_R \mathbf{i}_s}{R_R/L_M + j\omega_2} = \{(9.6), i_d = \psi_{\text{ref}}/\hat{L}_M\} = \frac{R_R(\psi_{\text{ref}}/\hat{L}_M + ji_q)}{R_R/L_M + j\hat{R}_R i_q/\psi_{\text{ref}}} \\ &= \underbrace{\frac{L_M \psi_{\text{ref}}}{\hat{L}_M} \frac{1 + \frac{R_R \hat{L}_M}{\hat{R}_R L_M} \left(\frac{\hat{R}_R L_M i_q}{R_R \psi_{\text{ref}}} \right)^2}{1 + \left(\frac{\hat{R}_R L_M i_q}{R_R \psi_{\text{ref}}} \right)^2}}_{\psi_d} + j L_M i_q \underbrace{\frac{1 - \frac{\hat{R}_R L_M}{R_R \hat{L}_M}}{1 + \left(\frac{\hat{R}_R L_M i_q}{R_R \psi_{\text{ref}}} \right)^2}}_{\psi_q}. \quad (9.12)\end{aligned}$$

Perfect field orientation, $\psi_q = 0$, is thus obtained when

$$\frac{\hat{L}_M}{\hat{R}_R} = \frac{L_M}{R_R}. \quad (9.13)$$

Otherwise, the field orientation will be inaccurate, and the inaccuracy increases with i_q , i.e., with the torque. From Paragraph 5.6.3 it is known that the rotor resistance tends to vary more than the magnetizing inductance, so \hat{R}_R is the primary critical parameter. Let us also calculate the steady-state electrical torque. Using (9.12) we get

$$\tau_e = \frac{3n_p}{2K^2} \text{Im}\{\Psi_R^* \mathbf{i}_s\} = \frac{3n_p}{2K^2} \frac{\hat{R}_R L_M^2 \psi_{\text{ref}} i_q}{R_R \hat{L}_M^2} \frac{1 + \left(\frac{\hat{L}_M i_q}{\psi_{\text{ref}}} \right)^2}{1 + \left(\frac{\hat{R}_R L_M i_q}{R_R \psi_{\text{ref}}} \right)^2}. \quad (9.14)$$

The ideal linear relation between τ_e and i_q is obtained only when (9.13) holds. Figure 9.2 illustrates (9.14) for $\psi_{\text{ref}} = 0.9$ pu, $L_M = \hat{L}_M = 2$ pu, $R_R = 0.05$ pu, and three values of \hat{R}_R . If the resistance parameter values are obtained from “cold” measurements, then \hat{R}_R is normally an underestimate of R_R , which reduces the torque for higher $|i_q|$. Slower speed response than for perfect field orientation can be expected for larger speed-reference steps, when maximum current is applied.

PROBLEM 9.1

Why is a larger-than-nominal electrical torque obtained for $i_q = 1$ pu?

Example 9.1 Equation (9.14) suggests that \hat{R}_R should be obtained for a “hot” motor, giving an overestimated \hat{R}_R for many operating conditions, and consequently higher torque, according to Figure 9.2. Let us investigate by simulation whether overestimating rather than underestimating the rotor resistance gives better performance.

A two-pole IM drive which uses the current model for flux estimation, $\omega_{\text{base}} = 100\pi$ rad/s, and the per-unit parameters $\psi_{\text{ref}} = 0.9$, $L_M = 2$, $\hat{L}_M = 1.8$, $L_\sigma = 0.2$, $R_s = R_R = 0.05$, $J = 1000$, and $b = 0.1$ is considered. The speed control loop is tuned for a rise time of 0.35 s and the load torque is approximately 50% of the nominal. In Figure 9.3, the reference speed is first changed rampwise around $\omega_r = 0$; it is thereafter at $t = 4$ s changed in a step to 1.5 pu in order to investigate the

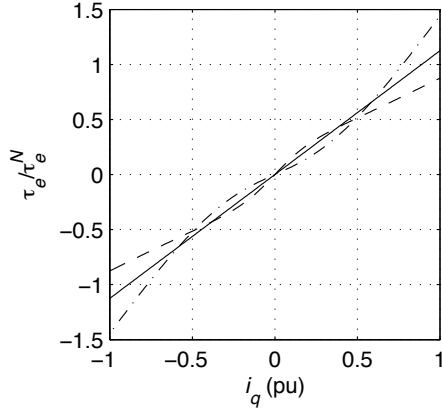


Figure 9.2. Normalized electrical torque as function of i_q when the current model is used for flux estimation and (solid) $\hat{R}_R = 0.05$ pu—correct value, (dashed) $\hat{R}_R = 0.03$ pu—underestimated, and (dash-dotted) $\hat{R}_R = 0.07$ pu—overestimated.

performance in the field-weakening region (during which the controller to be designed in Section 9.3 has already been incorporated), and is at $t = 6$ s decreased to 0.5 pu. It can be observed that the performance is good, even when \hat{R}_R is detuned, except for the large reference step at $t = 4$ s when maximum current is used. As underestimating \hat{R}_R gives lower torque, the dashed speed curve shows a slower response. The response is also slower when \hat{R}_R is overestimated, however, because there is a transient reduction in ψ_d which was not predicted by the steady-state theory. Note further that the slightly detuned \hat{L}_M hardly affects the field orientation at all: $\psi_q \approx 0$ as long as $\hat{R}_R = R_R$. Clearly, good performance requires that \hat{R}_R is reasonably accurate, not only that it is overestimated.



9.1.5 Improved Flux Estimation

The current model dates back to the pioneering days of vector control of the late 1960s and early 1970s. Its sensitivity to the rotor resistance was found at an early stage, but it took ten more years until an effective solution to the problem was presented. In 1980, Garcés proposed on-line adaptation of the model rotor resistance, using an error function based on the instantaneous reactive power [23]. Analog implementation was suggested, because the microprocessors available at that time were not fast enough to allow digital implementation. During the following two decades, a plethora of more or less similar adaptation schemes surfaced.

A few years after the proposal for rotor-resistance estimation, i.e., in the mid-1980s, alternatives to the current model began to appear in publications. All these alternatives involve the stator equation (5.35) [in addition the rotor equation (5.36), which forms the basis for the current model]. The stator equation can be rearranged as

$$\mathbf{v}_s^s = R_s \mathbf{i}_s^s + L_\sigma \frac{d\mathbf{i}_s^s}{dt} + \mathbf{E}^s, \quad \mathbf{E}^s = \frac{d\psi_R^s}{dt}. \quad (9.15)$$

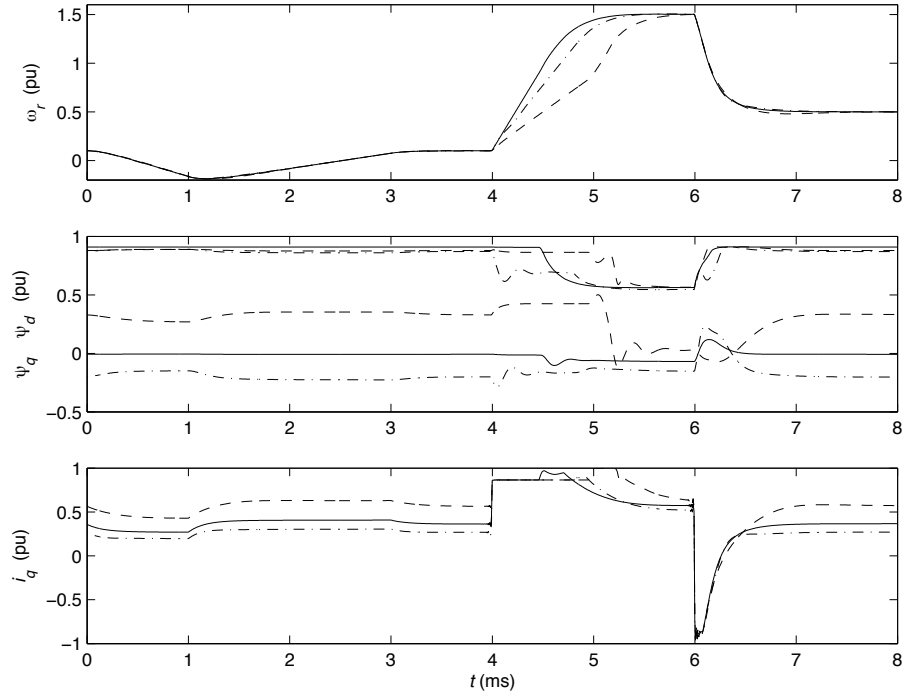


Figure 9.3. Simulation of an IM drive using the current model for flux estimation and (solid) $\hat{R}_R = 0.05$ pu—correct value, (dashed) $\hat{R}_R = 0.03$ pu—underestimated, and (dash-dotted) $\hat{R}_R = 0.07$ pu—overestimated.

A flux-emf estimate can be obtained by subtracting from the stator voltage estimates of the voltage drops across the stator resistance and leakage inductance

$$\hat{\mathbf{E}}^s = \mathbf{v}_s^s - \hat{R}_s \dot{\mathbf{i}}_s^s - \hat{L}_\sigma \frac{d\mathbf{i}_s^s}{dt}. \quad (9.16)$$

This estimate can be used in various ways to improve the flux-estimation accuracy. Direct integration of $\hat{\mathbf{E}}^s$ is one straightforward option, which yields the so-called voltage model, see further Section 9.2. Many of the proposed alternative flux-estimation methods—including those analyzed in the pioneering work by Verghese and Sanders [84]—incorporate (9.15) in an *observer*. This is a simulation of a state-space system—in our case the IM electrical dynamics—augmented with feedback of the error between the actual output and that of the model. The error is scaled with the observer gain. This has the effect of driving unmeasurable state variables (in this case, the flux components) as close as possible to their correct values. By appropriate selection of the observer gain, an estimator that is less sensitive to the rotor resistance than the current model can be designed. This is conceptually more straightforward than on-line adaptation of the model rotor resistance, because the idea is simply to use a better estimator rather than manipulating the parameters of the current model. Several observer designs boil down to a flux estimator that makes a seamless transition from the current model to the voltage model (or a variant of thereof) as the speed rises, e.g., [44]. Most proposed observers are DFO flux estimation schemes.

To obtain an improved IFO flux estimator, (9.16) is transformed to synchronous coordinates

$$\hat{\mathbf{E}} = \mathbf{v}_s - (\hat{R}_s + j\omega_1 \hat{L}_\sigma) \mathbf{i}_s - \hat{L}_\sigma \frac{d\mathbf{i}_s}{dt}. \quad (9.17)$$

If the model parameters were accurate, i.e., $\hat{R}_s = R_s$ and $\hat{L}_\sigma = L_\sigma$, then $\hat{\mathbf{E}} = \mathbf{E}$, where

$$\mathbf{E} = j\omega_1 \boldsymbol{\psi}_R + \frac{d\boldsymbol{\psi}_R}{dt} \quad (9.18)$$

which can be expressed in component form as

$$E_d = \dot{\psi}_d - \omega_1 \psi_q \quad (9.19)$$

$$E_q = \dot{\psi}_q + \omega_1 \psi_d. \quad (9.20)$$

Alternatively, the rotor flux can be expressed in polar form as $\boldsymbol{\psi}_R^s = \psi_R e^{j\theta}$, giving

$$\mathbf{E} = e^{-j\theta_1} \mathbf{E}^s = e^{-j\theta_1} \frac{d\boldsymbol{\psi}_R^s}{dt} = (\dot{\psi}_R + j\dot{\theta}\psi_R) e^{j\tilde{\theta}}, \quad \tilde{\theta} = \theta - \theta_1 \quad (9.21)$$

and the following expressions for the components:

$$E_d = \dot{\psi}_R \cos \tilde{\theta} - \dot{\theta}\psi_R \sin \tilde{\theta} \quad (9.22)$$

$$E_q = \dot{\psi}_R \sin \tilde{\theta} + \dot{\theta}\psi_R \cos \tilde{\theta}. \quad (9.23)$$

At higher speeds, $|\dot{\psi}_R| \ll |\dot{\theta}\psi_R|$ can be assumed (because the flux modulus varies with the rotor time constant, i.e., relatively slowly), which allows the approximations

$$E_d \approx -\dot{\theta}\psi_R \sin \tilde{\theta} \quad (9.24)$$

$$E_q \approx \dot{\theta}\psi_R \cos \tilde{\theta}. \quad (9.25)$$

Particularly it can be noted that perfect field orientation yields $E_d \approx 0$. This property is fundamental for the design of an improved IFO flux estimator.

9.1.6 Modified Current Model

In Section 6.5, theory for synchronization control using a PLL was presented. The PLL input signal that drives the dq -frame angle θ_1 to its correct value is $-E_d$, see Figure 6.10. A comparison shows that (9.24)–(9.25) are identical to (6.36) with $E = \dot{\theta}\psi_R$. This indicates that a PLL can be used to enhance the accuracy of the flux estimate in the vector control system for an IM drive. Let us revisit (6.38), which determines how ω_1 is calculated by the PLL. The equation is repeated here for clarity, with $\omega_i = 0$, i.e., without integral action in the PLL

$$\omega_1 = \frac{\alpha_l}{p + \alpha_l} (\hat{\omega}_g - k_{pp} E_d). \quad (9.26)$$

In an IM drive, neither the flux, nor the flux emf, can be measured, but we can use the estimated flux-emf component \hat{E}_d obtained by taking the real part of (9.17) in lieu of E_d . In addition, $\hat{\omega}_g$ has to be replaced by an estimate of the angular flux frequency, and such we have: it is readily given by the standard slip relation as $\hat{\omega}_g = \omega_r + \hat{R}_R i_q / \hat{\psi}_R$. This results in a modified current model (MCM)

$$\omega_1 = \frac{\alpha_l}{p + \alpha_l} \left(\omega_r + \frac{\hat{R}_R i_q}{\hat{\psi}_R} - k_{pp} \hat{E}_d \right). \quad (9.27)$$

which, in effect, is the current model embedded in a PLL. It is convenient to further modify (9.27) by introducing $k_{pp} = \lambda_s/\hat{\psi}_R$, which allows a dimensionless gain λ_s . We also use the reference i_q^{ref} instead of the measured current component

$$\omega_1 = \frac{\alpha_l}{p + \alpha_l} \left(\omega_r + \frac{\hat{R}_R i_q^{\text{ref}} - \lambda_s \hat{E}_d}{\hat{\psi}_R} \right). \quad (9.28)$$

For $\lambda_s = 0$, (9.28) reverts to the standard slip relation (9.7), albeit with a low-pass filter added. Equation (9.28) may therefore be called a *generalized slip relation*.

Often, because the current control loop is much faster than the flux dynamics, $\hat{L}_\sigma d\mathbf{i}_s/dt$ can be neglected in (9.17). In addition, reference voltage and current components should be used rather than the corresponding measured components (cf. Figure 9.1), giving

$$\hat{E}_d = \bar{v}_d^{\text{ref}} - \hat{R}_s i_d^{\text{ref}} + \omega_1 \hat{L}_\sigma i_q^{\text{ref}}. \quad (9.29)$$

These modifications reduce the noise level of \hat{E}_d . The low-pass filter in (9.28) gives further noise reduction. Selecting the filter bandwidth α_l may require some trial-and-error work to obtain an adequate compromise between good noise reduction and small enough lag. Suitable selections are within the range

$$\frac{R_R}{L_M} \ll \alpha_l < \alpha_c \quad (9.30)$$

i.e., much higher than the inverse rotor time constant, but lower than the current-control-loop bandwidth.

9.1.7 Analysis and Parameter Selection of the Modified Current Model

Remaining to do is to select gain λ_s and to evaluate the performance of the modified current model. If the modification is successful, then a lower parameter sensitivity than for the standard current model should result. Finding an adequate gain selection requires some analysis. To this end, let us express the flux dynamics (5.40) in component form

$$\dot{\psi}_d = R_R i_d - \frac{R_R}{L_M} \psi_d + (\omega_1 - \omega_r) \psi_q \quad (9.31)$$

$$\dot{\psi}_q = R_R i_q - \frac{R_R}{L_M} \psi_q - (\omega_1 - \omega_r) \psi_d. \quad (9.32)$$

Accurate model parameters are assumed, as otherwise the analysis would get far too complicated. Under this assumption we have $\hat{E}_d = E_d$, which is given by (9.19) as $E_d = -\omega_1 \psi_q + \dot{\psi}_d$. Using (9.31) and $i_d = \psi_{\text{ref}}/L_M$, (9.19) can equivalently be expressed as

$$E_d = \frac{R_R}{L_M} (\psi_{\text{ref}} - \psi_d) - \omega_r \psi_q. \quad (9.33)$$

Equation (9.33) is then substituted in (9.28). Owing to the bandwidth selection (9.30), the low-pass filter in (9.28) can be considered in the steady state as observed from the flux dynamics, giving

$$\omega_1 = \omega_r + \frac{R_R i_q}{\psi_{\text{ref}}} - \frac{\lambda_s}{\psi_{\text{ref}}} \left[\frac{R_R}{L_M} (\psi_{\text{ref}} - \psi_d) - \omega_r \psi_q \right] \quad (9.34)$$

where we also have substituted $\hat{\psi}_R \rightarrow \psi_{\text{ref}}$. This substitution is adequate for analysis purposes, since $\hat{\psi}_R$ is given by the open-loop simulation (9.5) and thus always converges to ψ_{ref} . In (9.34) it can be observed that, unlike the standard current model, ω_1 is now not only a function of ω_r and i_q , but also of the actual flux components. A nonlinear feedback of the flux is created via the integration ω_1 into θ_1 and the usage of the latter in the coordinate transformations. This alters the flux dynamics from those obtained when the standard current model is used, i.e., (9.10). Substituting (9.34) in (9.31)–(9.32), it is found that this nonlinear feedback creates a nonlinear system in the state variables ψ_d and ψ_q

$$\dot{\psi}_d = \frac{R_R}{L_M}(\psi_{\text{ref}} - \psi_d) + \left[\frac{R_R i_q}{\psi_{\text{ref}}} - \frac{\lambda_s}{\psi_{\text{ref}}} \left(\frac{R_R}{L_M}(\psi_{\text{ref}} - \psi_d) - \omega_r \psi_q \right) \right] \psi_q \quad (9.35)$$

$$\dot{\psi}_q = R_R i_q - \frac{R_R}{L_M} \psi_q - \left[\frac{R_R i_q}{\psi_{\text{ref}}} - \frac{\lambda_s}{\psi_{\text{ref}}} \left(\frac{R_R}{L_M}(\psi_{\text{ref}} - \psi_d) - \omega_r \psi_q \right) \right] \psi_d. \quad (9.36)$$

This system has an equilibrium point at $[\psi_d = \psi_{\text{ref}}, \psi_q = 0]$, around which the system is now linearized. Introducing the error variable $\tilde{\psi}_d = \psi_d - \psi_{\text{ref}}$, the linearized state-space system becomes

$$\begin{bmatrix} \dot{\tilde{\psi}}_d \\ \dot{\psi}_q \end{bmatrix} = \underbrace{\begin{bmatrix} -\frac{R_R}{L_M} & \frac{R_R i_q}{\psi_{\text{ref}}} \\ -\frac{\lambda_s R_R}{L_M} - \frac{R_R i_q}{\psi_{\text{ref}}} & -\frac{R_R}{L_M} - \lambda_s \omega_r \end{bmatrix}}_{\mathbf{A}} \begin{bmatrix} \tilde{\psi}_d \\ \psi_q \end{bmatrix}. \quad (9.37)$$

The characteristic polynomial is given by

$$\det(s\mathbf{I} - \mathbf{A}) = s^2 + \left(\lambda_s \omega_r + \frac{2R_R}{L_M} \right) s + \lambda_s \omega_1 \frac{R_R}{L_M} + \left(\frac{R_R}{L_M} \right)^2 + \left(\frac{R_R i_q}{\psi_{\text{ref}}} \right)^2. \quad (9.38)$$

where $\omega_1 = \omega_r + R_R i_q / \psi_{\text{ref}}$. At higher speeds, ω_1 and ω_r have equal signs. If λ_s is given the same sign as ω_r , then all coefficients are positive and the system is asymptotically stable. Care must be taken to ensure that the coefficients are positive also at low speeds, though, when the signs of ω_1 and ω_r may differ. For this reason, it is recommended that λ_s should be ramped up with the speed as (see Figure 9.4)

$$\lambda_s = \text{sat}(\lambda \omega_r / \omega_\Delta, \lambda) = \begin{cases} \frac{\lambda \omega_r}{\omega_\Delta}, & |\omega_r| \leq \omega_\Delta \\ \lambda \text{sgn} \omega_r, & |\omega_r| > \omega_\Delta \end{cases} \quad (9.39)$$

where reasonable parameter values are

$$1 \leq \lambda \leq 2 \quad 0.05 \omega_{\text{base}} \leq \omega_\Delta \leq 0.2 \omega_{\text{base}}. \quad (9.40)$$

In the low-speed range the properties of the standard current model thus are preserved—including its robust stability, but also its high rotor-resistance sensitivity. In the higher-speed range, $|\omega_r| > \omega_\Delta$, (9.38) can be approximated by considering R_R and ω_2 small, giving

$$\det(s\mathbf{I} - \mathbf{A}) \approx s^2 + \lambda |\omega_r| s + \lambda |\omega_r| \frac{R_R}{L_M} \approx (s + \lambda |\omega_r|) \left(s + \frac{R_R}{L_M} \right). \quad (9.41)$$

There are two poles widely separated on the negative real axis. The “slow” pole at $s = -R_R/L_M$ corresponds mainly to the dynamics of ψ_d (and are equal to the open-loop flux dynamic obtained using the standard current model), whereas the “fast” pole at $s = -\lambda|\omega_r|$ corresponds mainly to the dynamics of ψ_q . Gain λ_s has the effect of “speeding up” ψ_q , but not ψ_d . This can be regarded as a speedup of the field orientation, i.e., the adjustment of θ_1 , whereas the flux-modulus dynamics by the physical characteristics of the IM remain trapped at the rotor time constant. This is a expected result, since the incorporation of the current model in a PLL logically should enhance the synchronization properties. Algorithm 9.2 illustrates an implementation of the modified current model with the proposed selection of λ_s .

Algorithm 9.2

Modified Current Model

$$\begin{aligned}\hat{E}_d &= \bar{v}_d^{\text{ref}} - \hat{R}_s i_d^{\text{ref}} + \omega_1 \hat{L}_\sigma i_q^{\text{ref}} \\ \lambda_s &= \text{sat}(\lambda\omega_r/\omega_\Delta, \lambda) \\ \omega_1 &= \omega_1 + T_s \alpha_l \left(\omega_r + \frac{\hat{R}_R i_q^{\text{ref}} - \lambda_s \hat{E}_d}{\hat{\psi}_R} - \omega_1 \right) \\ \theta_1 &= \text{mod}(\theta_1 + T_s \omega_1, 2\pi) \\ \hat{\psi}_R &= \hat{\psi}_R + T_s \hat{R}_R \left(i_d^{\text{ref}} - \frac{\hat{\psi}_R}{\hat{L}_M} \right)\end{aligned}$$

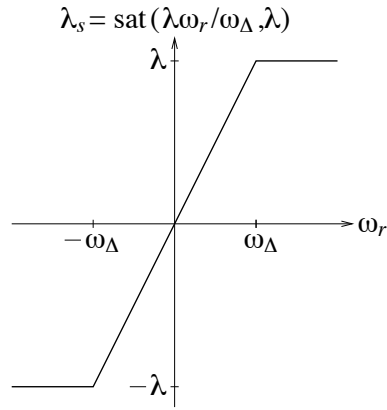


Figure 9.4. Selection of gain λ_s .

9.1.8 Parameter Sensitivity of the Modified Current Model

In the low-speed region the modified current model has properties that are similar to those of the standard current model, due to gain selection (9.39). The sensitive parameters are thus \hat{R}_R and \hat{L}_M . When analyzing the impact of erroneous model parameters at higher speeds, i.e., $|\omega_r| \geq \omega_\Delta$,

the voltage drop across the stator resistance can be neglected. With $\dot{\psi}_d$ neglected in (9.19), this yields $\hat{E}_d \approx -\omega_1(\tilde{L}_\sigma i_q + \psi_q)$, where $\tilde{L}_\sigma = L_\sigma - \hat{L}_\sigma$, and

$$\omega_1 = \omega_r + \frac{\hat{R}_R i_q}{\psi_{\text{ref}}} + \frac{\lambda|\omega_1|}{\psi_{\text{ref}}}(\tilde{L}_\sigma i_q + \psi_q). \quad (9.42)$$

Substitution of (9.42) in (9.32) yields

$$\dot{\psi}_q = R_R i_q - \frac{R_R}{L_M} \psi_q - \left[\frac{\hat{R}_R i_q}{\psi_{\text{ref}}} + \frac{\lambda|\omega_1|}{\psi_{\text{ref}}}(\tilde{L}_\sigma i_q + \psi_q) \right] \psi_d \quad (9.43)$$

whose steady-state properties are considered, i.e., $\dot{\psi}_q = 0$. Assuming that $\psi_d = \psi_{\text{ref}}$ and $R_R/L_M \ll \lambda|\omega_1|$, solving for ψ_q in (9.43) yields

$$\psi_q \approx - \left(\tilde{L}_\sigma + \frac{\hat{R}_R}{\lambda|\omega_1|} \right) i_q. \quad (9.44)$$

If λ is sufficiently large, the error due to \hat{R}_R can be neglected. Thus, we find that the leakage inductance is the only sensitive parameter of the modified current model at higher speeds, given that gain λ_s is properly selected. Since the leakage inductance tends to vary much less than the rotor resistance, it can be concluded that the objective for the modification of the current model has been fulfilled.

Example 9.2 Let us see whether improved performance as compared to Example 9.1 (Figure 9.3) is obtained by the modified current model. We again simulate a two-pole IM with the per-unit parameters $J = 1000$, $b = 0.1$, $L_M = 2$, $L_\sigma = 0.2$, and $R_s = R_R = 0.05$. The speed control loop is tuned for a rise time of 0.35 s and the load torque is approximately 50% of the nominal. The per-unit model parameters are $\hat{L}_M = 1.8$, $\hat{L}_\sigma = 0.22$, $\hat{R}_s = 0.03$, and $\hat{R}_R = 0.025$. In the gain selection, $\omega_\Delta = 0.2$ pu and $\lambda = 1$.

As in Example 9.1, the speed reference is first changed rampwise, giving slow positive-to-negative and negative-to-positive rotation reversals. At $t = 4$ s, the speed reference is changed to 1.5 pu, and is finally at $t = 6$ set to 0.5 pu. Figure 9.5 shows the results. Whereas at low speeds the field orientation suffers due to the detuning of the model rotor resistance, once the speed increases accurate field orientation is obtained. This allows faster speed response for the step to 1.5 pu than the standard current model for an erroneous \hat{R}_R , cf. Figure 9.3.



9.2 Speed-Sensorless Control

The difficulty of controlling an IM drive increases tremendously if the rotor speed cannot be measured, i.e., the drive is speed sensorless. The challenge of speed-sensorless control of an IM drive lies not in estimation of the rotor speed *per se*, but rather in accurately estimating the rotor flux without knowledge of the speed. Neither the standard current model nor the modified current model can be employed without modification, as they use ω_r in their equations.

One such modification is to use a speed estimate $\hat{\omega}_r$ in place of ω_r in the (generalized) slip relation. This speed estimate can be obtained in at least three different ways.

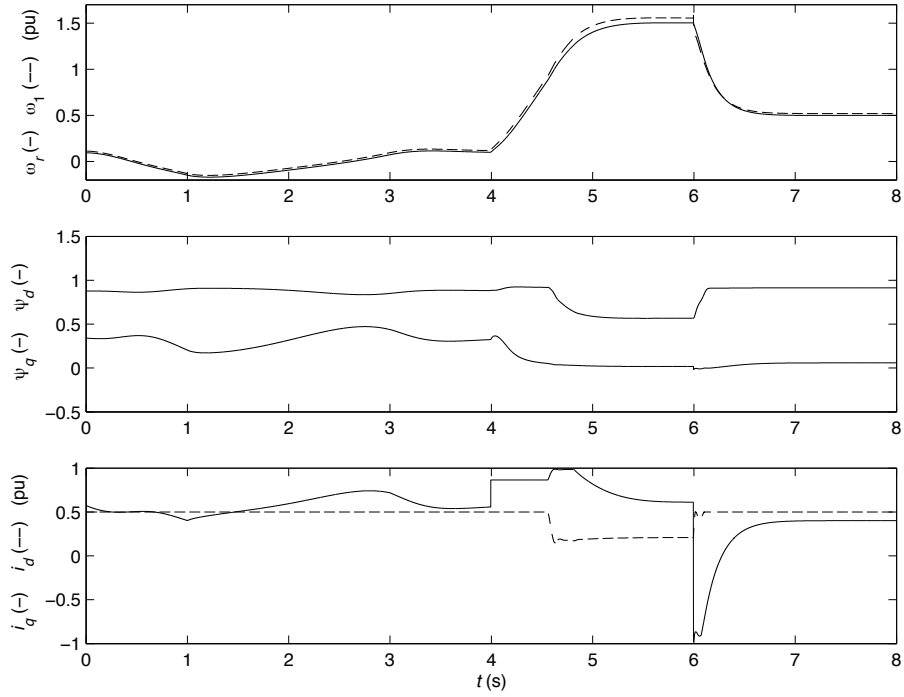


Figure 9.5. Simulations of an IM drive using the modified current model.

- 1) Extraction of rotor-slot harmonics from the stator current [43].
- 2) Extraction of information obtained from naturally occurring or artificially created rotor saliences [45].
- 3) Extraction of information available in the fundamental-wave excitation.

The first two methods are very reliable, provided that they can be used. But rotor-slot harmonics tend to vanish for IMs that have skewed rotors [21] and to create saliences artificially is generally not feasible. The effect of naturally occurring saliences is often very small. Therefore, it is often necessary to rely on the third option, but when doing so, the properties of, e.g., the standard or modified current model become drastically altered [35]. Particularly, the excellent low-speed stability robustness is lost. A better approach is therefore to completely replace the current model as flux estimator in a sensorless IM drive. Preferable to use is a flux estimator that does not use the rotor speed in its equations at all. This is called an *inherently sensorless* flux estimator [31].

9.2.1 Direct Field Orientation Using the Voltage Model With Modifications

The first inherently sensorless flux estimator proposed is the voltage model, which is obtained as follows. Whereas the current model is a simulation of the rotor circuit of the IM, the voltage model is a simulation of the stator circuit as given by (9.16). A flux estimate can be obtained by

integrating (9.16), giving

$$\hat{\Psi}_R^s = \int (\mathbf{v}_s^s - \hat{R}_s \mathbf{i}_s^s) dt - \hat{L}_\sigma \mathbf{i}_s^s \quad (9.45)$$

or, in operator form with the flux-emf estimate $\hat{\mathbf{E}}^s$ introduced

$$\hat{\Psi}_R^s = \frac{1}{p} \hat{\mathbf{E}}^s, \quad \hat{\mathbf{E}}^s = \mathbf{v}_s^s - (\hat{R}_s + p \hat{L}_\sigma) \mathbf{i}_s^s. \quad (9.46)$$

Notice that ω_r does not appear on the right-hand side of (9.45); the voltage model is indeed inherently sensorless. However, neither does $\hat{\Psi}_R^s$; the flux estimate is obtained by open-loop integration, which indicates that the resulting flux dynamics will be marginally stable. Analysis confirms this conjecture. The voltage model therefore cannot be used as it stands, but needs modification to give an asymptotically stable system. We shall, in two steps, modify the voltage model such that stability is gained, while accuracy is not sacrificed.

Modification I: Low-Pass Filter (Approximate Integrator)

The standard modification is to replace the open-loop integration in (9.45) by a low-pass filter, which can also be regarded as adding a “leakage term” to the integral on right-hand side of (9.45)

$$\hat{\Psi}_R^s = \int (\mathbf{v}_s^s - \hat{R}_s \mathbf{i}_s^s - \alpha_v \hat{\Psi}_R^s) dt - \hat{L}_\sigma \mathbf{i}_s^s \quad (9.47)$$

or, in operator form

$$\hat{\Psi}_R^s = \frac{1}{p + \alpha_v} \hat{\mathbf{E}}^s. \quad (9.48)$$

Obviously, this introduces an error to the flux estimate, which can be quantified by combining (9.48) with (9.46)

$$\hat{\Psi}_R^s = \frac{p}{p + \alpha_v} \Psi_R^s. \quad (9.49)$$

In the steady state, with $p = j\omega_1$, we have

$$\hat{\Psi}_R^s = \frac{j\omega_1}{j\omega_1 + \alpha_v} \Psi_R^s. \quad (9.50)$$

For a small ω_1 and a constant filter bandwidth α_v , such that $|\omega_1| < \alpha_v$, the resulting error would be significant. To rectify this, it is useful to select α_v proportional to the angular stator frequency

$$\alpha_v = \lambda |\omega_1|. \quad (9.51)$$

This was proposed in [11, 76]; there called a “programmable low-pass filter.” An error which is constant for all stator frequencies (sign changes excluded) is obtained

$$\begin{aligned} \hat{\Psi}_R^s &= \frac{j\omega_1}{j\omega_1 + \lambda |\omega_1|} \Psi_R^s = \frac{1}{1 - j\lambda_s} \Psi_R^s \\ \Rightarrow \frac{\hat{\Psi}_R^s}{\Psi_R^s} &= \frac{\hat{\psi}_R}{\psi_R} e^{-j\tilde{\theta}} = \frac{1}{1 - j\lambda_s} = \frac{1}{\sqrt{1 + \lambda^2}} e^{j \arctan \lambda_s} \end{aligned} \quad (9.52)$$

where $\lambda_s = \lambda \operatorname{sgn} \omega_1$. Now, if λ is fairly small, so is the error angle: $\lambda = 0.1 \Rightarrow \tilde{\theta} = \pm 5.7^\circ$ and $\lambda = 0.2 \Rightarrow \tilde{\theta} = \pm 11.3^\circ$, whereas in both cases $\hat{\psi}_R$ is practically equal to ψ_R .

Modification II: Compensation Gain

The small value of λ required to avoid large error angles unfortunately does not give sufficient damping. Although the system is asymptotically stable (i.e., the poles are located in the LHP, not on the imaginary axis), analysis shows that the poles are still located close to the imaginary axis, at

$$p \approx -\frac{\lambda|\omega_1|}{2} \pm j\omega_1 \quad (9.53)$$

for smaller λ . A poorly damped system with oscillatory response results. From Paragraph 2.2.8, we know that pole placement with an angle relative the imaginary axis of at least 45° can be recommended, in order to obtain a well-damped system. This obviously requires a fairly large gain λ . Steps must then be taken to compensate for the resulting error angle, which otherwise would become unacceptably large.

Consider (9.52). The error due to the low-pass filter can be perfectly compensated in the steady state by scaling $\hat{\Psi}_R^s$ with the complex gain $1 - j\lambda_s$, as

$$\hat{\Psi}_R^{s'} = \int (\mathbf{v}_s^s - \hat{R}_s \mathbf{i}_s^s - \lambda_s \omega_1 \hat{\Psi}_R^s) dt - \hat{L}_\sigma \mathbf{i}_s^s \quad (9.54)$$

$$\hat{\Psi}_R^s = (1 - j\lambda_s) \hat{\Psi}_R^{s'} \quad (9.55)$$

or, in operator form

$$\hat{\Psi}_R^s = \frac{1 - j\lambda_s}{p + \lambda_s \omega_1} \hat{\mathbf{E}}^s. \quad (9.56)$$

The result is known as the statically compensated voltage model (SCVM), whose block diagram is shown in Figure 9.6.

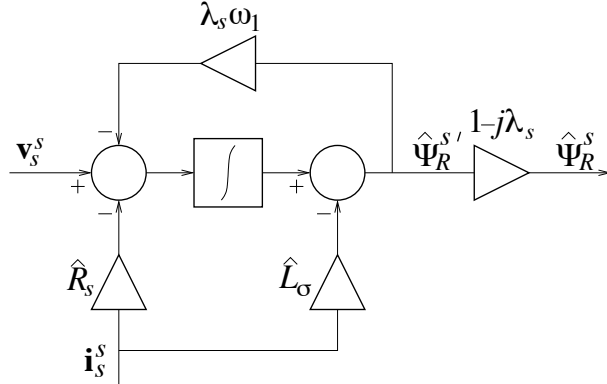


Figure 9.6. Block diagram for the SCVM.

9.2.2 Indirect Field Orientation Using the Statically Compensated Voltage Model

For the current model we concluded that IFO is often preferable to DFO. This holds for the SCVM as well. An IFO implementation of the SCVM is readily obtained by expressing the flux estimate

in polar coordinates, as $\hat{\psi}_R^s = \hat{\psi}_R e^{j\theta_1}$, in (9.56). We obtain

$$(p + \lambda_s \omega_1)(\hat{\psi}_R e^{j\theta_1}) = (1 - j\lambda_s) \hat{\mathbf{E}}^s \Rightarrow \\ \dot{\hat{\psi}}_R + (j\omega_1 + \lambda_s \omega_1) \hat{\psi}_R = e^{-j\theta_1} (1 - j\lambda_s) \hat{\mathbf{E}}^s = (1 - j\lambda_s) \hat{\mathbf{E}} \quad (9.57)$$

where [cf. (9.17)]

$$\hat{\mathbf{E}} = \hat{E}_d + j\hat{E}_q = \mathbf{v}_s - [\hat{R}_s + (p + j\omega_1 \hat{L}_\sigma)] \mathbf{i}_s. \quad (9.58)$$

Equation (9.57) can now be split into its real and imaginary parts, from which $\dot{\hat{\psi}}_R$ and ω_1 can be solved as

$$\dot{\hat{\psi}}_R = -\lambda_s \omega_1 \hat{\psi}_R + \hat{E}_d + \lambda_s \hat{E}_q \quad (9.59)$$

$$\omega_1 = \frac{\hat{E}_q - \lambda_s \hat{E}_d}{\hat{\psi}_R}. \quad (9.60)$$

Equation (9.59) can be simplified by substituting (9.60) in (9.59), whose right-hand side simplifies to

$$-\lambda_s \frac{\hat{E}_q - \lambda_s \hat{E}_d}{\hat{\psi}_R} \hat{\psi}_R + \hat{E}_d + \lambda_s \hat{E}_q = (1 + \lambda_s^2) \hat{E}_d. \quad (9.61)$$

Since \hat{E}_d and \hat{E}_q are functions of ω_1 [cf. (9.58)], (9.60) should include a low-pass filter to avoid an algebraic loop between the left- and right-hand sides. We thus get

$$\dot{\hat{\psi}}_R = \gamma \hat{E}_d \quad (9.62)$$

$$\omega_1 = \frac{\alpha_l}{p + \alpha_l} \frac{\hat{E}_q - \lambda_s \hat{E}_d}{\hat{\psi}_R}, \quad \dot{\theta}_1 = \omega_1 \quad (9.63)$$

where

$$\lambda_s = \lambda \operatorname{sgn} \omega_1 \quad \gamma = 1 + \lambda_s^2. \quad (9.64)$$

It is interesting to note that (9.63) is identical to the PLL for PMSM drives, (8.10), even though the SCVM was derived in a completely different way than the PLL. One addition has been made, namely, that the SCVM the flux-modulus estimate $\hat{\psi}_R$ is dynamic according to the update law (9.62). In (9.58), references should be used rather than measured variables. In addition, since the flux dynamics are much slower than the current dynamics, the derivative term $p \hat{L}_\sigma \mathbf{i}_s$ can generally be neglected (as was made for the modified current model). In component form we thus get

$$\hat{E}_d = \bar{v}_d^{\text{ref}} - \hat{R}_s i_d^{\text{ref}} + \omega_1 \hat{L}_\sigma i_q^{\text{ref}} \quad (9.65)$$

$$\hat{E}_q = \bar{v}_q^{\text{ref}} - \hat{R}_s i_q^{\text{ref}} - \omega_1 \hat{L}_\sigma i_d^{\text{ref}}. \quad (9.66)$$

Remaining is to obtain an estimate of the rotor speed. This is straightforward; the standard slip relation (9.6) is simply used “backwards.” With ω_1 obtained from (9.63), an estimate of the angular slip frequency is subtracted

$$\hat{\omega}_r = \omega_1 - \frac{\hat{R}_R i_q^{\text{ref}}}{\psi_{\text{ref}}}. \quad (9.67)$$

If $\hat{\omega}_r$ is used in a speed controller whose output is i_q^{ref} , then a low-pass filter has to be added to avoid an algebraic loop between (9.67) and the speed controller

$$\hat{\omega}_r = \frac{\alpha_l}{p + \alpha_l} \left(\omega_1 - \frac{\hat{R}_R i_q^{\text{ref}}}{\psi_{\text{ref}}} \right). \quad (9.68)$$

Parameters α_l and λ of the SCVM are similar to those of the modified current model, and similar selection recommendations apply

$$\frac{R_R}{L_M} \ll \alpha_l < \alpha_c \quad 1 \leq \lambda \leq 2. \quad (9.69)$$

Algorithm 9.3 illustrates an IFO implementation of the SCVM, whereas Figure 9.7 shows the block diagram of an IM vector control system utilizing the SCVM, excluding the estimator (9.67) for $\hat{\omega}_r$ to avoid clutter. Notice that the only difference as compared to the PMSM vector control system using a PLL variant, shown in Figure 8.5, is the added estimator for $\hat{\psi}_R$.

Algorithm 9.3

Statically Compensated Voltage Model

$$\begin{aligned} \hat{E}_d &= \bar{v}_d^{\text{ref}} - \hat{R}_s i_d^{\text{ref}} + \omega_1 \hat{L}_\sigma i_q^{\text{ref}} \\ \hat{E}_q &= \bar{v}_q^{\text{ref}} - \hat{R}_s i_q^{\text{ref}} - \omega_1 \hat{L}_\sigma i_d^{\text{ref}} \\ \lambda_s &= \lambda \operatorname{sgn}(\omega_1) \\ \gamma &= 1 + \lambda_s^2 \\ \omega_1 &= \omega_1 + T_s \alpha_l \left(\frac{\hat{E}_q - \lambda_s \hat{E}_d}{\hat{\psi}_R} - \omega_1 \right) \\ \theta_1 &= \operatorname{mod}(\theta_1 + T_s \omega_1, 2\pi) \\ \hat{\psi}_R &= \hat{\psi}_R + T_s \gamma \hat{E}_d \\ \hat{\omega}_r &= \hat{\omega}_r + T_s \alpha_l \left(\omega_1 - \frac{\hat{R}_R i_q^{\text{ref}}}{\hat{\psi}_R} - \hat{\omega}_r \right) \end{aligned}$$

9.2.3 Properties of the Statically Compensated Voltage Model

The SCVM does not use \hat{R}_R in any of its equations for determination of ω_1 . From this fact it can be concluded that the SCVM is completely *insensitive to the rotor resistance at all speeds*. This is a universal property for all sensorless IM control systems [35]. On the other hand, an erroneous \hat{R}_R affects the accuracy of the speed estimate, as can be deduced from (9.67).

Let us compare the generalized slip relations that result from the modified current model, (9.28), and the SCVM, (9.63). Both are repeated here, somewhat differently expressed

$$\omega_1 = \frac{\alpha_l}{p + \alpha_l} \left(\omega_r + \frac{\hat{R}_R i_q^{\text{ref}}}{\hat{\psi}_R} - \frac{\lambda_s \hat{E}_d}{\hat{\psi}_R} \right) \quad (\text{MCM}) \quad (9.70)$$

$$\omega_1 = \frac{\alpha_l}{p + \alpha_l} \left(\frac{\hat{E}_q}{\hat{\psi}_R} - \frac{\lambda_s \hat{E}_d}{\hat{\psi}_R} \right). \quad (\text{SCVM}) \quad (9.71)$$

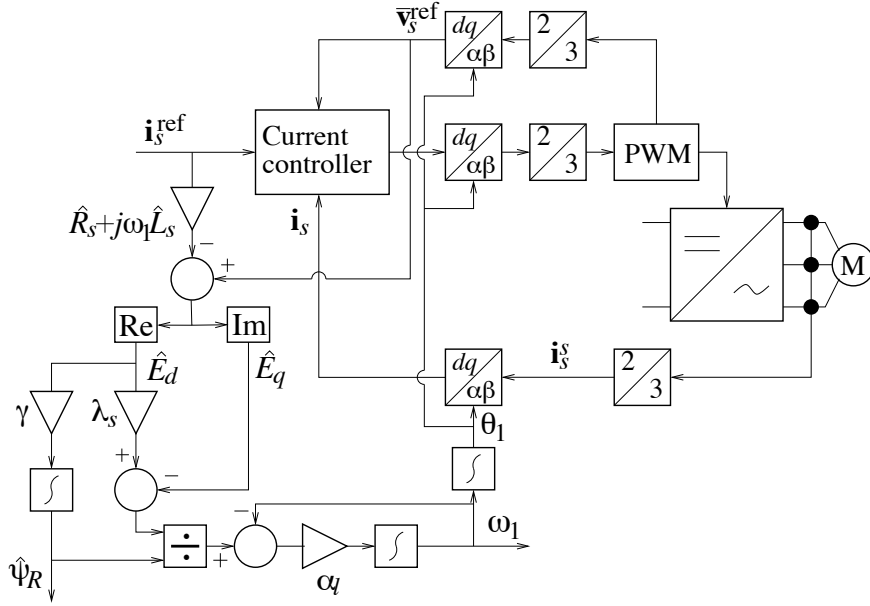


Figure 9.7. IFO vector control system using the SCVM for speed-sensorless IM drives.

We find that both generalized slip relations have the same structure. Equation (9.71) is effectively obtained by substituting

$$\omega_r + \frac{\hat{R}_R i_q^{\text{ref}}}{\hat{\psi}_R} \rightarrow \frac{\hat{E}_q}{\hat{\psi}_R} \quad (9.72)$$

in (9.70). Here, $\omega_r + \hat{R}_R i_q^{\text{ref}}/\hat{\psi}_R$ is the angular-flux-frequency estimate obtained from the standard slip relation. Since ω_r is not available in a speed-sensorless drive, the substitution shown in (9.72)—or something similar—has to be made. The effect of this substitution can be understood from (9.25): $E_q \approx \dot{\theta}\psi_R \cos \tilde{\theta}$. For accurate model parameters, $\hat{E}_q = E_q$. If, in addition, we assume that $\hat{\psi}_R \approx \psi_R$ and $\tilde{\theta} \approx 0$, then

$$\frac{\hat{E}_q}{\hat{\psi}_R} \approx \dot{\theta} \quad (9.73)$$

i.e., the desired estimate of the angular flux frequency. Since $\hat{E}_q/\hat{\psi}_R$ gives a good estimate of $\dot{\theta}$ only if certain assumptions hold, it can intuitively be understood that the stability properties of the SCVM are radically different from those of the MCM at low speeds. Instability phenomena may appear, whose elimination require a slight redesign of the SCVM, see Paragraphs 9.2.4 and 9.2.5.

On the other hand, because $E_d \approx -\dot{\theta}\psi_R \sin \tilde{\theta}$ [cf. (9.24)], the common term $-\hat{E}_d/\hat{\psi}_R$ in the generalized slip relations of the MCM and the SCVM has the effect of increasing the convergence rate of ψ_q , as was found in Paragraph 9.1.7, forcing θ_1 to converge to a value close to θ faster. Consequently, the SCVM has properties similar to the MCM in the higher-speed range. That is, the only sensitive parameter is the leakage inductance, which impacts the field-orientation accuracy according to (9.44).

9.2.4 Instability Phenomena for Regeneration-Mode Operation

In a sensorless IM drive, difficulties arise at low frequencies, where most schemes—including the SCVM—suffer from a number of instability phenomena. Typically, instabilities tend to develop in the regeneration mode, when speed and torque have different signs. There are two particularly detrimental instability phenomena.

- **Flux collapse** [29, 70, 72]. The field orientation deteriorates in a way so that the IM is unintentionally demagnetized, which is illustrated in Figure 9.8(a). The magnetizing current component i_d in the dq frame used by the control system (i.e., that of the estimated flux) is positive. When the error angle $\tilde{\theta}$ is positive and large, while $i_q < 0$, the *actual* flux-producing current component i_d^R —which is the stator current vector projected on the rotor flux vector—becomes negative, demagnetizing the motor. (This may also occur when $\tilde{\theta} < 0$ and $i_q > 0$.) Electrical torque is lost, and uncontrolled rotation in the direction of the load torque results.
- **Frequency lockup** [64] (or speed estimation failure [18]). The field orientation deteriorates, such that the electrical torque reduces to a point where it equals the load torque, causing lockup close to zero stator frequency. The flux emf—being proportional to the stator frequency, see (9.24)–(9.25)—then vanishes, leaving the flux estimator—whose inputs are \hat{E}_d and \hat{E}_q , see (9.62)–(9.63)—“blind.” Instead of the flux collapsing, the actual flux-producing current component i_d^R will be larger than i_d , resulting in over-fluxed operation and a saturating magnetizing inductance; see Figure 9.8(b).

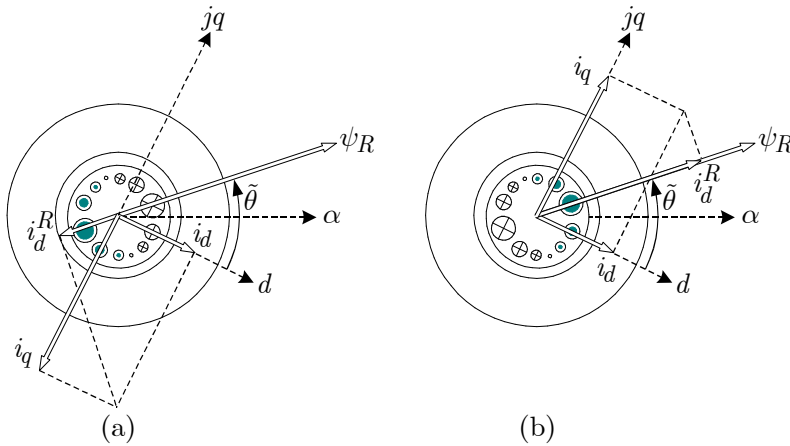


Figure 9.8. Vector diagrams illustrating (a) flux collapse and (b) frequency lockup.

For some flux estimators the unstable region is wide (in the worst case, all negative speeds for positive load torques, and vice versa), whereas a well-designed estimator has only a narrow unstable region, close to zero stator frequency, or—in the ideal case—no unstable region at all. A sensorless IM control system that is devoid of an unstable region may be called *completely stable*. In [34], general theory for complete stabilization of some different flux estimator types is presented.

It is very difficult to guarantee complete stability, particularly with model parameter inaccuracies taken into account. Yet, if the drive does not dwell in the low-speed region, so that the

unstable region is passed through quickly, then there is not enough time for an instability to develop fully. (Still, instability tendencies may be noticed in the form of large flux transients.) Slow rotation reversals under constant load should therefore be avoided, if possible, for a sensorless IM drive.

9.2.5 Complete Stabilization of the Statically Compensated Voltage Model

In [33], a redesign of the SCVM is proposed, with the aim of obtaining complete stability. The redesign is simple; it merely involves a gain selection that is slightly different from (9.64)

$$\lambda_s = \text{sat}(\lambda\hat{\omega}_r/\omega_\Delta, \lambda) \quad \gamma = 1 - \frac{\lambda\hat{R}_R}{\omega_\Delta\hat{L}_M}. \quad (9.74)$$

Notice that the modified selection of λ_s is identical to that of modified voltage model, (9.39), but with $\hat{\omega}_r$ replacing ω_r . By this redesign, the regeneration mode remains stable, but only if \hat{R}_s is a very accurate estimate of the true stator resistance. [\hat{R}_R and \hat{L}_M in (9.74) are not critical [35].] Yet better performance can be obtained if the sensitivity to \hat{R}_s can be reduced. Methods for achieving this—including on-line adaptation—are discussed in [35] and papers cited therein. Algorithm 9.4 shows the redesigned SCVM.

Algorithm 9.4

Statically Compensated Voltage Model Redesigned for Complete Stability

$$\begin{aligned}\hat{E}_d &= \bar{v}_d^{\text{ref}} - \hat{R}_s i_d^{\text{ref}} + \omega_1 \hat{L}_\sigma i_q^{\text{ref}} \\ \hat{E}_q &= \bar{v}_q^{\text{ref}} - \hat{R}_s i_q^{\text{ref}} - \omega_1 \hat{L}_\sigma i_d^{\text{ref}} \\ \lambda_s &= \text{sat}(\lambda\hat{\omega}_r/\omega_\Delta, \lambda) \\ \gamma &= 1 - \frac{\lambda\hat{R}_R}{\omega_\Delta\hat{L}_M} \\ \omega_1 &= \omega_1 + T_s \alpha_l \left(\frac{\hat{E}_q - \lambda_s \hat{E}_d}{\hat{\psi}_R} - \omega_1 \right) \\ \theta_1 &= \text{mod}(\theta_1 + T_s \omega_1, 2\pi) \\ \hat{\psi}_R &= \hat{\psi}_R + T_s \gamma \hat{E}_d \\ \hat{\omega}_r &= \hat{\omega}_r + T_s \alpha_l \left(\omega_1 - \frac{\hat{R}_R i_q^{\text{ref}}}{\hat{\psi}_R} - \hat{\omega}_r \right)\end{aligned}$$

Remark 9.2 Algorithm 9.3 is an IFO equivalent to the DFO variant of the SCVM shown in Figure 9.6. Algorithm 9.4, on the other hand, has no DFO equivalent for complex space vectors.

Example 9.3 Experimental results for the redesigned SCVM with a four-pole, 22-kW, 50-Hz IM drive will now be presented. The motor parameters are $L_M = 2.8$ pu, $L_\sigma = 0.21$ pu, $R_s = 0.023$ pu, and $R_R = 0.034$ pu. The following inaccurate (in order to evaluate the robustness to parameter errors) model parameters are selected: $\hat{L}_M = 0.9L_M$, $\hat{L}_\sigma = 1.1L_\sigma$, and $\hat{R}_R = 0.9R_R$. The critical model parameter \hat{R}_s is explicitly stated for each experiment. In the SCVM, $\omega_\Delta = 0.05$ pu and $\lambda = \sqrt{2}$. Two experiments are made, where in both experiments the speed reference ω_{ref} is stepped

through the sequence 0.2 pu, 0, -0.2 pu, and is then slowly ramped up at $t = 8$ s, starting from $\omega_{\text{ref}} = -0.2$ pu. A constant load torque that requires $i_q = 0.6$ pu to balance is applied.

Figure 9.9 shows results of the first experiment, with $\hat{R}_s = R_s$. The performance is good, but some ‘‘bumps’’ can be seen in $\hat{\psi}_R$ and i_q for zero-speed operation and zero-frequency crossing. Since it is unlikely that the stator resistance is perfectly modeled, a narrow unstable region is likely present, but passage through it is made sufficiently fast to prevent instabilities from developing.

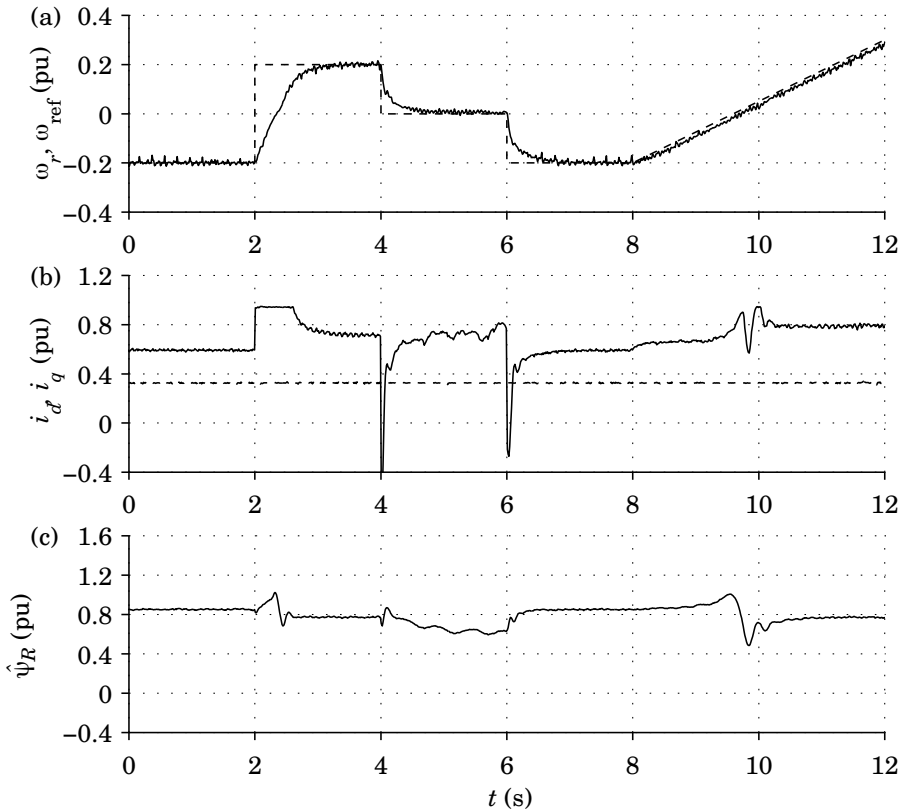


Figure 9.9. Successful operation for the ideal case $\hat{R}_s = R_s$.

The second experiment uses an underestimated model stator resistance $\hat{R}_s = 0.7R_s$, see Figure 9.10. The speed step from -0.2 pu to 0.2 pu at $t = 2$ s is barely completed, which indicates stability problems. At $t = 9.5$ s, a flux collapse occurs for the slow speed ramping against the load torque. The experiment is interrupted at $t = 10.5$ s.



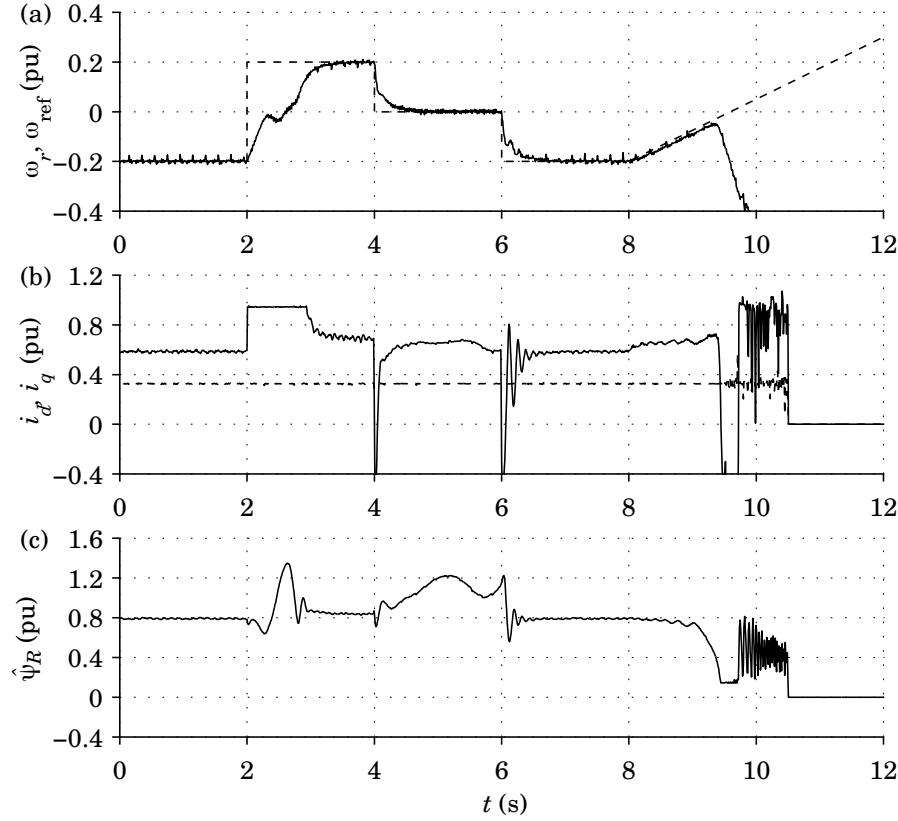


Figure 9.10. Operation giving a flux collapse with $\hat{R}_s = 0.7R_s$.

9.3 Field-Weakening Control

Field-weakening control of the IM can use a similar control method as for the PMSM, see (8.38) and Figure 9.11. The algorithm for modifying the d -direction current reference is given by

$$i_d^{\text{ref}} = k_{\text{fw}} \int [V_{\text{base}}^2 - (v_d^{\text{ref}})^2 - (v_q^{\text{ref}})^2] dt \Big|_{I_{\min}}^{I_{\text{nom}}} \quad (9.75)$$

In this case, though, the nominal value should be selected as

$$I_{\text{nom}} = \frac{\psi_{\text{ref}}}{\hat{L}_M} \quad (9.76)$$

whereas the minimum value should be selected large enough to prevent complete demagnetization, e.g.,

$$I_{\min} = 0.1I_{\text{nom}}. \quad (9.77)$$

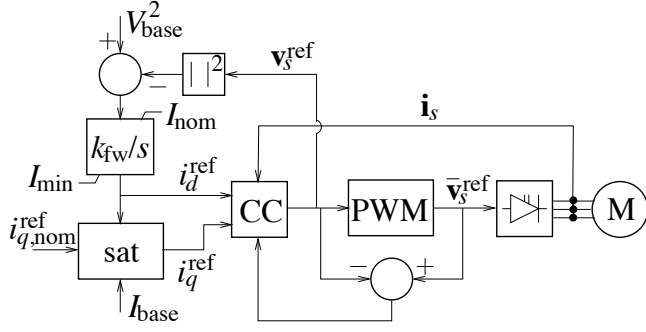


Figure 9.11. Field-weakening controller for IM drives, where “sat” is implemented according to (9.94). “CC” is the current controller with “back calculation.” (To avoid clutter, the dq and $\alpha\beta$ coordinate transformations are not shown.)

9.3.1 Gain Selection

To find a selection recommendation for k_{fw} , the IM correspondence to (8.42) for the PMSM is considered. The voltage components are obtained by substituting $L_d \rightarrow L_\sigma$ and $L_q \rightarrow L_\sigma$ in (8.43)

$$v_d = -\omega_1 L_\sigma i_q \quad v_q = \omega_1 (L_\sigma i_d + \psi_R) \quad (9.78)$$

yielding the following correspondence to (8.44):

$$f(i_d, \psi_R) = V_{base}^2 - (\omega_1 L_\sigma i_q)^2 - [\omega_1 (L_\sigma i_d + \psi_R)]^2. \quad (9.79)$$

In this case, though, the flux modulus is not constant; the dynamics (??) must be taken into account. Hence, f is a function of two variables. Linearization and making approximations similar to those made in the analysis of field-weakening control in the PMSM case yield

$$\begin{aligned} f(i_d, \psi_R) &\approx \frac{\partial f(i_d, \psi_R)}{\partial i_d} (i_d - i_d^*) + \frac{\partial f(i_d, \psi_R)}{\partial \psi_R} (\psi_R - \psi_R^*) \\ &\approx -2|\omega_1| [L_\sigma (i_d - i_d^*) + \psi_R - \psi_R^*] V_{base} \end{aligned} \quad (9.80)$$

giving the second-order system

$$\frac{di_d}{dt} = -2k_{fw}|\omega_1|V_{base}L_\sigma \left(i_d - i_d^* + \frac{\psi_R - \psi_R^*}{L_\sigma} \right) \quad (9.81)$$

$$\frac{d\psi_R}{dt} = R_R i_d - \frac{R_R}{L_M} \psi_R. \quad (9.82)$$

We introduce $\alpha_{fw} = 2k_{fw}|\omega_1|V_{base}L_\sigma$ as the bandwidth of (9.81). System (9.81)–(9.82) can be expressed in state-space form with the matrix $\mathbf{A} = \begin{bmatrix} -\alpha_{fw} & -\alpha_{fw}/L_\sigma \\ R_R & -R_R/L_M \end{bmatrix}$, giving the characteristic polynomial

$$\det(s\mathbf{I} - \mathbf{A}) = s^2 + \left(\alpha_{fw} + \frac{R_R}{L_M} \right) s + \alpha_{fw} R_R \left(\frac{1}{L_\sigma} + \frac{1}{L_M} \right). \quad (9.83)$$

Assuming that $\alpha_{fw} \gg R_R/L_M$ and approximating $1/L_\sigma + 1/L_M \approx 1/L_\sigma$ (since $L_M \gg L_\sigma$), we get

$$\det(s\mathbf{I} - \mathbf{A}) \approx s^2 + \alpha_{fw}s + \frac{\alpha_{fw}R_R}{L_\sigma} \quad (9.84)$$

whose roots (i.e., the poles of the system) are

$$s = -\frac{\alpha_{\text{fw}}}{2} \pm \sqrt{\frac{\alpha_{\text{fw}}^2}{4} - \frac{\alpha_{\text{fw}} R_R}{L_\sigma}}. \quad (9.85)$$

This shows that a reasonable bandwidth selection is

$$\alpha_{\text{fw}} = \frac{2\hat{R}_R}{\hat{L}_\sigma} \quad (9.86)$$

since poles at $s = (-1 \pm j)R_R/L_\sigma$ then ideally (for accurate model parameters) are obtained, i.e., with the desired minimum angle of 45° relative the imaginary axis. The resulting dynamics are fast; the response time L_σ/R_R is roughly twice the transient time constant given in (5.80), and in the range of 1/10 of the rotor time constant L_M/R_R . The dynamic properties for smaller speed changes in the field-weakening region are thus normally excellent. The corresponding gain selection is

$$k_{\text{fw}} = \frac{\hat{R}_R}{\hat{L}_\sigma^2 V_{\text{base}} \max(|\omega_1|, \omega_{\text{base}})} \quad (9.87)$$

which yields a constant gain below base speed (where field-weakening control is not used).

9.3.2 Maximum Torque

In the field-weakening range, maximum torque is mostly obtained by applying the nominal current, i.e., $\sqrt{i_d^2 + i_q^2} = I_{\text{base}}$. This is called field-weakening region I. Interestingly, though, above a certain stator frequency, maximum torque is obtained for a current lower than the nominal. This is called field-weakening region II. The torque-maximizing component i_q to be applied there can be found as follows.

The electrical torque is proportional to $\psi_R i_q$ and, hence, to $i_d i_q$ in the steady state, since $\psi_R = L_M i_d$ in the steady state under perfect field orientation. Equation (9.78) then can be expressed as

$$v_d = -\omega_1 L_\sigma i_q \quad v_q = \omega_1 (L_\sigma + L_M) i_d \quad (9.88)$$

which shows that the electrical torque is proportional to

$$i_d i_q = -\frac{v_d v_q}{\omega_1^2 (L_\sigma + L_M) L_\sigma} \quad (9.89)$$

in the steady state. If the nominal voltage is applied, i.e., $\sqrt{v_d^2 + v_q^2} = V_{\text{base}}$, then maximum electrical torque is obtained when¹

$$|v_d| = |v_q| = \frac{V_{\text{base}}}{\sqrt{2}}. \quad (9.90)$$

From (9.88) it is found that this corresponds to the following relation for the current components:

$$|i_q| = \xi i_d, \quad \xi = \frac{L_\sigma + L_M}{L_\sigma}. \quad (9.91)$$

¹This can be shown in a similar fashion as (5.125).

So, provided that the model parameters are accurate, maximum torque can be obtained by selecting the q -component reference as

$$|i_q^{\text{ref}}| = \hat{\xi} i_d^{\text{ref}}, \quad \hat{\xi} = \frac{\hat{L}_\sigma + \hat{L}_M}{\hat{L}_\sigma}. \quad (9.92)$$

This selection would result in overcurrent in field-weakening region I. Calculation of the break point where (9.91) yields nominal current gives the angular stator frequency at which field-weakening region II begins. We get

$$\begin{aligned} i_d^2 + i_q^2 &= \left(\frac{1}{\xi^2} + 1 \right) i_q^2 = \frac{1 + \xi^2}{\xi^2} \left(\frac{v_q}{\omega_1 L_\sigma} \right)^2 = \frac{1 + \xi^2}{\xi^2} \left(\frac{V_{\text{base}}}{\sqrt{2} \omega_1 L_\sigma} \right)^2 = I_{\text{base}}^2 \\ \Rightarrow |\omega_1| &= \sqrt{\frac{1 + \xi^2}{2\xi^2}} \frac{V_{\text{base}}}{L_\sigma I_{\text{base}}}. \end{aligned} \quad (9.93)$$

For example, for $L_M = 2$ pu and $L_\sigma = 0.2$ pu, (9.93) yields $|\omega_1| \geq 3.55$ pu for $V_{\text{base}} = I_{\text{base}} = 1$ pu. This is quite high an angular stator frequency, which shows that field-weakening region II is used only in applications that require operation deep into the field-weakening range. Figure 9.12 shows typical steady-state characteristics for operation into the field-weakening range, again for $L_M = 2$ pu and $L_\sigma = 0.2$ pu. Notice the sharp drop-off in the electrical torque that results if $|i_q|$ is not reduced according to (9.92) in field-weakening region II. The algorithm for selection of the torque-maximizing reference can be written as

$$i_q^{\text{ref}} = \text{sat} \left[i_{q,\text{nom}}^{\text{ref}}, \min \left(\sqrt{I_{\text{max}}^2 - (i_d^{\text{ref}})^2}, \hat{\xi} i_d^{\text{ref}} \right) \right] \quad (9.94)$$

where I_{max} shall be reduced to I_{base} after the maximum time that overcurrent is allowed.

The resulting field-weakening controller is identical to that for PMSM drives, see Figure 8.10, except that I_{nom} , I_{min} , and the saturation scheme for i_q^{ref} are chosen differently. See also Algorithm 9.5.

Algorithm 9.5

Field-Weakening Controller for IM Drives

$$\begin{aligned} i_d^{\text{ref}} &= i_d^{\text{ref}} + \frac{T_s \hat{R}_R}{\hat{L}_\sigma^2 V_{\text{base}} \max(|\omega_1|, \omega_{\text{base}})} [V_{\text{base}}^2 - (v_d^{\text{ref}})^2 - (v_q^{\text{ref}})^2] \\ i_d^{\text{ref}} &= \min[\max(i_d^{\text{ref}}, I_{\text{min}}), I_{\text{nom}}] \\ \hat{\xi} &= \frac{\hat{L}_\sigma + \hat{L}_M}{\hat{L}_\sigma} \\ i_q^{\text{ref}} &= \text{sat} \left[i_{q,\text{nom}}^{\text{ref}}, \min \left(\sqrt{I_{\text{max}}^2 - (i_d^{\text{ref}})^2}, \hat{\xi} i_d^{\text{ref}} \right) \right] \end{aligned}$$

Remark 9.3 During field-weakening operation L_M is usually somewhat larger than during normal operation, because it is no longer saturated. A saturation model or an on-line adaptation scheme for \hat{L}_M can be used to improve performance.

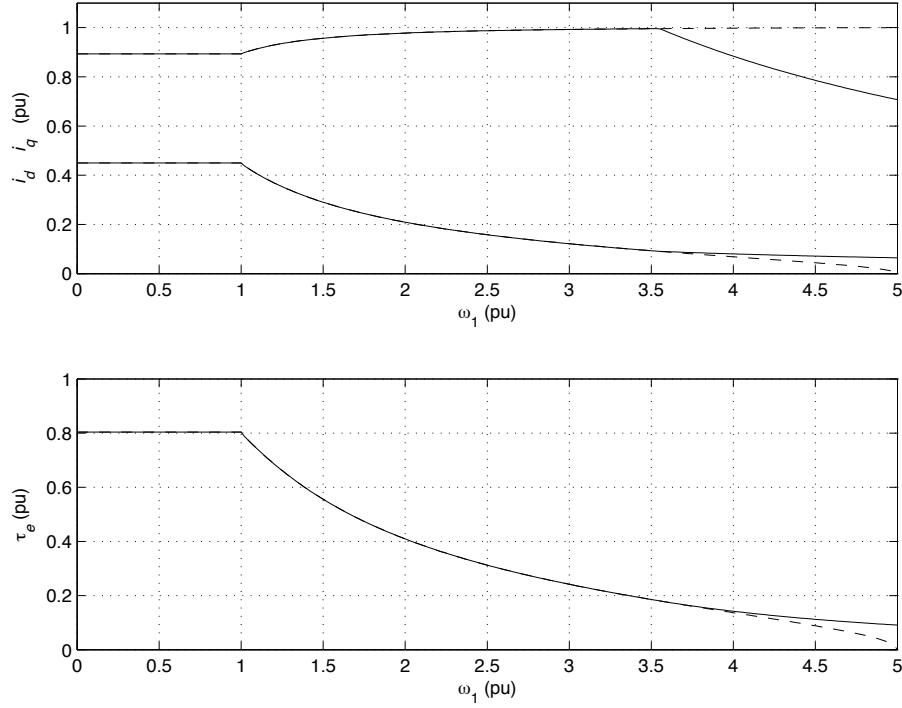


Figure 9.12. Current components and maximum obtainable electrical torque from zero stator frequency up into field-weakening region II. The dashed curves show results obtained when $|i_q|$ is not appropriately reduced in field-weakening region II.

Remark 9.4 Perfect field orientation is assumed in the above analysis. In [30] it is shown that leakage inductance should be overestimated for good performance during operation in field-weakening region II

$$\hat{L}_\sigma \geq L_\sigma. \quad (9.95)$$

Example 9.4 We again consider a two-pole IM, with similar electrical parameters to that in Example 9.1, i.e., $\omega_{\text{base}} = 100\pi$ rad/s and the per-unit parameters $\psi_{\text{ref}} = 0.9$, $L_M = 2$, $L_\sigma = 0.2$, and $R_s = R_R = 0.05$. The speed control loop is tuned for a rise time of 0.35 s, but light mechanical dynamics with the per-unit parameters $J = 100$ and $b = 0.02$ together with zero external load torque are this time considered. The current model with accurate model motor parameters is used for field orientation. Algorithm 5.1 (speed controller), Algorithm 9.1 (current model), and Algorithm 9.5 (field-weakening controller) are combined as shown in Algorithm 9.6.

Algorithm 9.6

Current Model With Speed and Field-Weakening Controllers

$$\begin{aligned}
i_d^{\text{ref}} &= i_d^{\text{ref}} + \frac{T_s \hat{R}_R}{\hat{L}_\sigma^2 V_{\text{base}} \max(|\omega_1|, \omega_{\text{base}})} [V_{\text{base}}^2 - (v_d^{\text{ref}})^2 - (v_q^{\text{ref}})^2] \\
i_d^{\text{ref}} &= \min[\max(i_d^{\text{ref}}, I_{\min}), I_{\text{nom}}] \\
\hat{\psi}_R &= \hat{\psi}_R + T_s \hat{R}_R \left(i_d^{\text{ref}} - \frac{\hat{\psi}_R}{\hat{L}_M} \right) \\
b_a &= \frac{2K^2(\alpha_s \hat{J} - \hat{b})}{3n_p^2 \hat{\psi}_R} \\
k_{ps} &= \frac{2K^2 \alpha_s \hat{J}}{3n_p^2 \hat{\psi}_R} \\
k_{is} &= \frac{2K^2 \alpha_s^2 \hat{J}}{3n_p^2 \hat{\psi}_R} \\
e_s &= \omega_{\text{ref}} - \omega_r \\
i_{q,\text{nom}}^{\text{ref}} &= k_{ps} e_s + k_{is} I_s - b_a \omega_r \\
\hat{\xi} &= \frac{\hat{L}_\sigma + \hat{L}_M}{\hat{L}_\sigma} \\
i_q^{\text{ref}} &= \text{sat} \left[i_{q,\text{nom}}^{\text{ref}}, \min \left(\sqrt{I_{\max}^2 - (i_d^{\text{ref}})^2}, \hat{\xi} i_d^{\text{ref}} \right) \right] \\
I_s &= I_s + T_s \left[e_s + \frac{1}{k_{ps}} (i_q^{\text{ref}} - i_{q,\text{nom}}^{\text{ref}}) \right] \\
\omega_1 &= \omega_r + \frac{\hat{R}_R i_q^{\text{ref}}}{\hat{\psi}_R} \\
\theta_1 &= \text{mod}(\theta_1 + T_s \omega_1, 2\pi)
\end{aligned}$$

Three slightly different variants are tested.

- **Variant 1.** Algorithm 9.6 is used as it stands.
- **Variant 2.** The saturation scheme for i_q^{ref} of Algorithm 5.1

$$i_q^{\text{ref}} = \text{sat} \left(i_{q,\text{nom}}^{\text{ref}}, \sqrt{I_{\max}^2 - (i_d^{\text{ref}})^2} \right)$$

is used by mistake. Thus, no reduction of $|i_q|$ is made in field-weakening region II.

- **Variant 3.** Gain scheduling of the speed-controller parameters with the varying flux estimate is not made. Instead, the nominal flux is used in the gain selections as

$$b_a = \frac{2K^2(\alpha_s \hat{J} - \hat{b})}{3n_p^2 \psi_{\text{ref}}} \quad k_{ps} = \frac{2K^2 \alpha_s \hat{J}}{3n_p^2 \psi_{\text{ref}}} \quad k_{is} = \frac{2K^2 \alpha_s^2 \hat{J}}{3n_p^2 \psi_{\text{ref}}}.$$

Performance is evaluated by stepping the speed reference from 0 to 4 pu. The results for the three variants are shown in Figure 9.13. Two observations can be made.

- For Variant 2, the speed setpoint is not attained, because not enough torque is produced in field-weakening region II.
- For Variant 3, ω_r makes a slight overshoot and i_q makes an undershoot after the speed reference is reached.

It can be concluded that torque maximization according to (9.94) and gain scheduling of the speed controller parameters with the estimated flux modulus both improve performance.

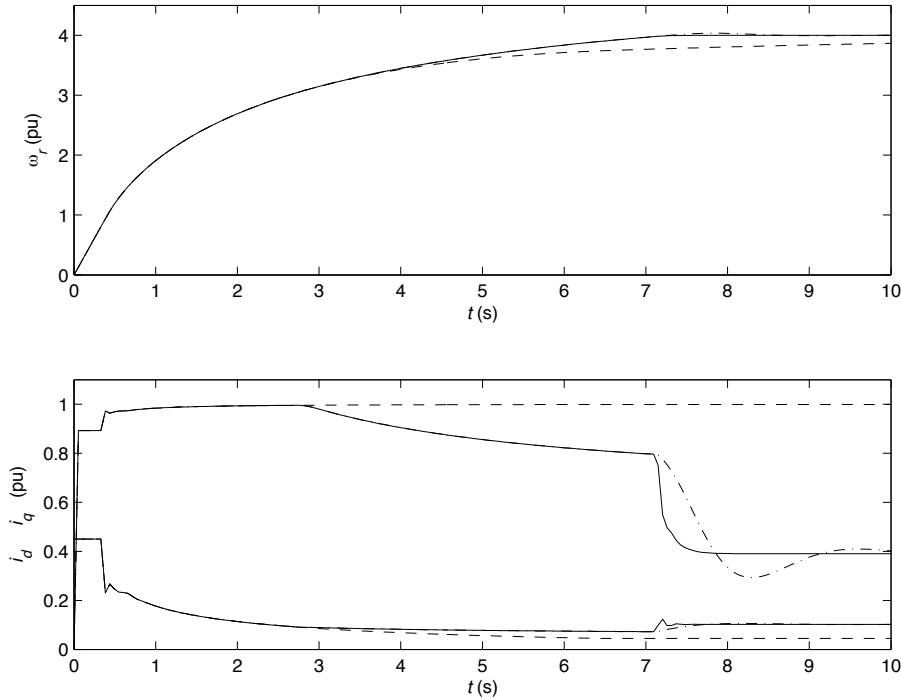


Figure 9.13. Simulation of an IM drive for a speed-reference step to 4 pu. The solid, dashed, and dash-dotted curves respectively show results for Variants 1, 2, and 3 of Algorithm 9.6.



9.4 Direct Torque Control

In vector control, motor control and converter control can usually be considered as separate functions: the converter control creates the PWM pattern based on the voltage reference generated by the motor control. When a hysteresis control scheme is used for current control, see Paragraphs 3.1.3 and 6.3.1, current control and PWM are merged, since the current control forms the switching

signal to the respective inverter leg. Direct torque control (DTC) is a step further in this direction. The DTC scheme was independently invented by Takahashi and Noguchi [80] and Depenbrock [17] in the mid-1980s. Later, the DTC principle was successfully applied to commercial IM drives by ABB [82].

9.4.1 Control Principle

The main idea of DTC, as originally suggested by Takahashi and Noguchi in [80], is to keep the stator flux and the electrical torque within specified tolerance bands by always choosing the voltage vector that is most suitable for the situation. The method departs from the idea of coordinate transformation and the analogy with dc motor control. It also departs from the principle of rotor-flux orientation, using instead stator-flux orientation (SFO), but without the explicit usage of a stator-flux-oriented dq frame. The hysteresis control principle allows the torque to be controlled at the fastest possible rate of change. In addition, there is no overshoot in the torque response.

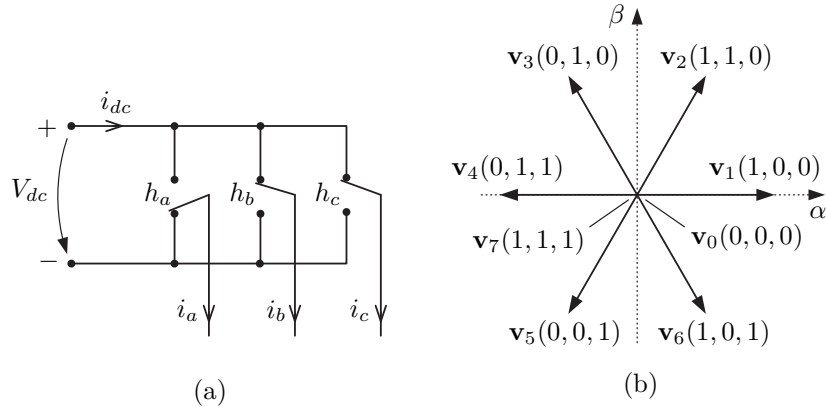


Figure 9.14. (a) Change-over switch model of a three-phase VSC. (b) Space vectors produced (in stator coordinates).

In the three-phase VSC model shown in Figure 9.14(a), the change-over switches are coupled either to the negative potential (down) or the positive potential (up). The dc-link voltage is denoted by V_{dc} , and the switching functions h_a , h_b , and h_c of each phase equal either 0 or 1, corresponding to the switch positions down and up, respectively. All switch positions can be defined by the combination (h_a, h_b, h_c) of the switching functions. For example, the switch positions in Figure 9.14(a) are defined by the combination $(0, 1, 1)$ of the switching functions. The possible voltage vectors of the converter output (and the corresponding switching functions) are shown in Figure 9.14(b) in stator coordinates. The magnitude of the nonzero vectors v_1, \dots, v_6 is $2KV_{dc}/3$, and the angle between adjacent voltage vectors is 60° . Two zero vectors are available: v_0 and v_7 .

In the DTC algorithm, the most suitable voltage vector is chosen based on the stator equation in stator coordinates (5.29), rewritten here as

$$\mathbf{v}_s^s = R_s \mathbf{i}_s^s + \frac{d\psi_s^s}{dt}. \quad (9.96)$$

During one switching combination, the stator voltage vector \mathbf{v}_n , $n = \{0, \dots, 7\}$ is constant over

the time span Δt . The resulting change of the stator flux is

$$\Delta\psi_s^s = \psi_s^s - \psi_{s,0}^s = \int_0^{\Delta t} (\mathbf{v}_s^s - R_s \mathbf{i}_s^s) dt \approx \mathbf{v}_n \Delta t. \quad (9.97)$$

The stator-flux vector thus changes in the direction of the applied voltage vector, and the rate of change is proportional to the dc-link voltage when the effect of the stator resistance is small. Consequently, the flux can be changed in six directions. When a zero vector is used, the flux vector practically stops moving. When controlling the stator flux vector, the complex plane is subdivided into six sectors as shown in Figure 9.15. The borders of the sectors are in the middle of the angles between adjacent voltage vectors.

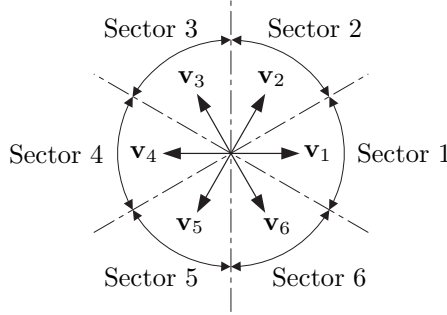


Figure 9.15. Definition of the six sectors.

The stator flux vector is controlled to follow the flux-reference circle within a hysteresis band, as depicted in Figure 9.16. The voltage vectors (and the time periods in which they are used) are chosen in such a way that, in addition to the flux, the torque remains within a certain tolerance band. From (5.25)–(5.26) we find that the stator- and rotor-flux vectors are related as

$$\psi_s^s = \psi_R^s + L_\sigma \mathbf{i}_s^s. \quad (9.98)$$

This relation allows, by substituting $\mathbf{i}_s^s = (\psi_s^s - \psi_R^s)/L_\sigma$ in (5.54), the torque expression to be expressed as

$$\tau_e = \frac{3n_p}{2K^2 L_\sigma} \operatorname{Im} \{(\psi_R^s)^* \psi_s^s\}. \quad (9.99)$$

The stator flux in effect takes the place of the stator current. Quick torque changes are thus obtained by holding the rotor flux constant and changing the stator flux. [Owing to the leakage flux contribution $L_\sigma \mathbf{i}_s^s$ in (9.98), the stator flux reacts quicker to changes in the stator voltage than the rotor flux.] Expressing the flux vectors in polar form allows (9.99) to be expressed as

$$\tau_e = \frac{3n_p}{2K^2 L_\sigma} \psi_R \psi_s \sin(\theta_{\psi s} - \theta_{\psi R}) \quad (9.100)$$

where $\theta_{\psi s}$ and $\theta_{\psi R}$ respectively are the stator- and rotor-flux angles, as shown in Figure 9.17(a). According to (9.100), the torque is proportional to sine of the angle $\theta_{\psi s} - \theta_{\psi R}$ between the flux vectors as well as to their magnitudes. A fast change of the torque can be achieved by accelerating

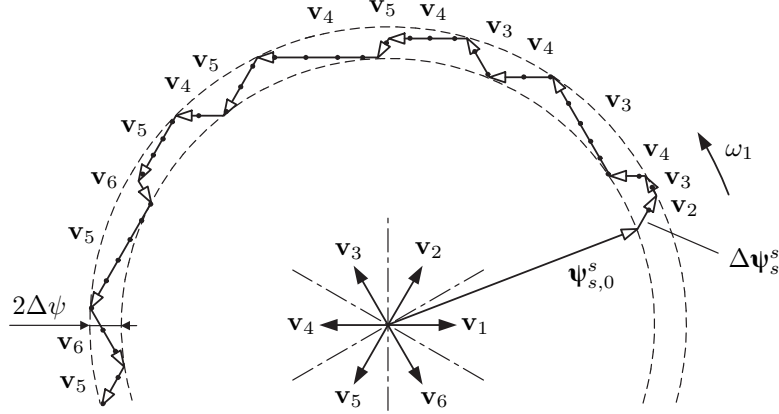


Figure 9.16. Path of stator flux vector showing the voltage vectors used in DTC. Zero voltage vectors are illustrated by dots.

or decelerating the stator-flux vector, which can be accomplished by proper selection of the stator voltage vectors, i.e., by selection of consecutive switching states. The stator-current vector is not directly controlled, and it can be considered as a secondary quantity in the DTC. It is to be noted that (9.100) is not used for control purposes; it is shown here only for describing the behavior of the motor.

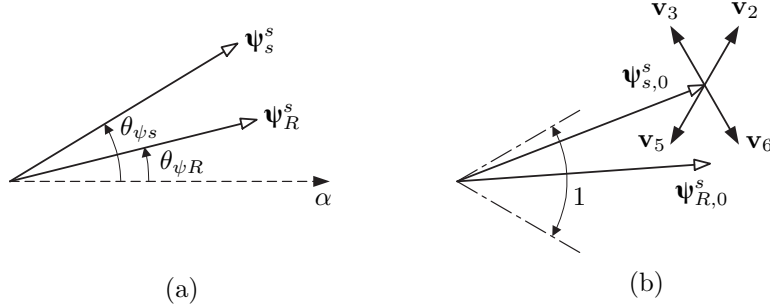


Figure 9.17. Illustrations of DTC principle. (a) Stator-flux and rotor-flux angles. (b) Voltage vectors that can be chosen in Sector 1.

In Figure 9.17(b), the rotational direction and the torque of the motor are assumed to be positive (counterclockwise) and the stator-flux vector is in Sector 1. For increasing the stator flux, either voltage vector \mathbf{v}_2 or \mathbf{v}_6 is to be chosen. The stator flux can be decreased by choosing voltage vector \mathbf{v}_3 or \mathbf{v}_5 . The torque can be increased by advancing the stator-flux vector, i.e., by increasing the angle between the two flux vectors. Voltage vectors \mathbf{v}_2 or \mathbf{v}_3 can be used for this purpose. The torque can be decreased by using voltage vectors \mathbf{v}_5 or \mathbf{v}_6 , but zero vectors \mathbf{v}_0 and \mathbf{v}_7 also decrease the torque; the stator-flux vector is then stopped and the rotor-flux vector continues to rotate when the rotor is rotating. Normally, zero vectors are used for decreasing the torque, except at low speeds.

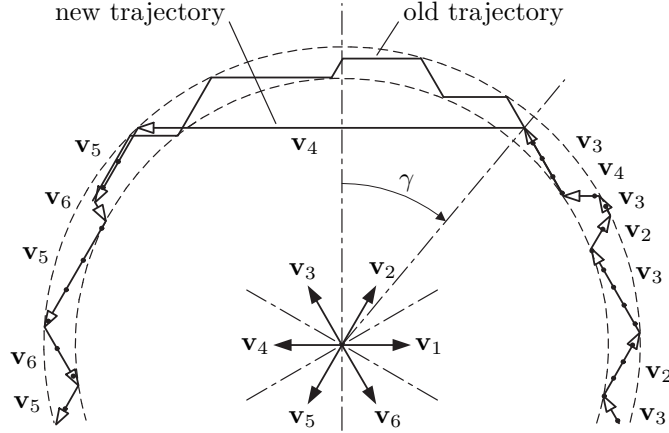


Figure 9.18. Path of stator flux vector when the border between Sectors 2 and 3 is shifted for obtaining a rapid torque change.

As illustrated in Figure 9.16, a voltage vector is used in one sector to increase the stator flux, and the same voltage vector is used in the next sector to decrease the stator flux. The trajectory of the stator flux vector forms a piecewise linear approximation of a circle. Figure 9.18 shows a situation in which, following a rapid change in the torque reference, the border separating Sectors 2 and 3 is shifted backwards by the angle γ . Now, the converter chooses between voltage vectors \mathbf{v}_4 and \mathbf{v}_5 instead of \mathbf{v}_3 and \mathbf{v}_4 , respectively. It is to be noted that the linear speed of the stator-flux vector along its trajectory is constant and is proportional to the dc-link voltage. Therefore, the flux vector arrives to a new location in a shorter time than if it had traveled along the regular trajectory. A rapid increase of the torque is achieved by this acceleration of the stator-flux vector, because that vector quickly moves away from the rotor-flux vector. It is to be noted that this simple method, based on shifting the border between two adjacent sectors, is only an illustrative example. In practice, more elaborate methods are used for choosing the voltage vectors when rapid changes in the torque are requested.

Depenbrock's DSC scheme differs from the described principle in the sense that the prescribed flux path is a hexagon rather than a circle. All but six switchings per period of the fundamental excitation are used to reduce the torque ripple. This scheme therefore generates quite low torque ripple. Notably, low-order torque harmonics are small or absent [2], which is important when the switching frequency is low, as mechanical resonances otherwise may be excited. The difference between the two schemes is illustrated in Figure 9.19.

9.4.2 Control System

A control system based on the DTC method is depicted in Figure 9.20. The stator flux can be estimated by a variant of the voltage model, e.g., the SCVM, obtained simply by omitting all terms proportional to \hat{L}_σ from the equations.

The only motor parameter needed for the flux estimation is the stator resistance estimate \hat{R}_s . The torque estimate is calculated in stator coordinates by means of the torque expression

$$\hat{\tau}_e = \frac{3n_p}{2K^2} \operatorname{Im} \{(\boldsymbol{\psi}_s^s)^* \mathbf{i}_s^s\}. \quad (9.101)$$

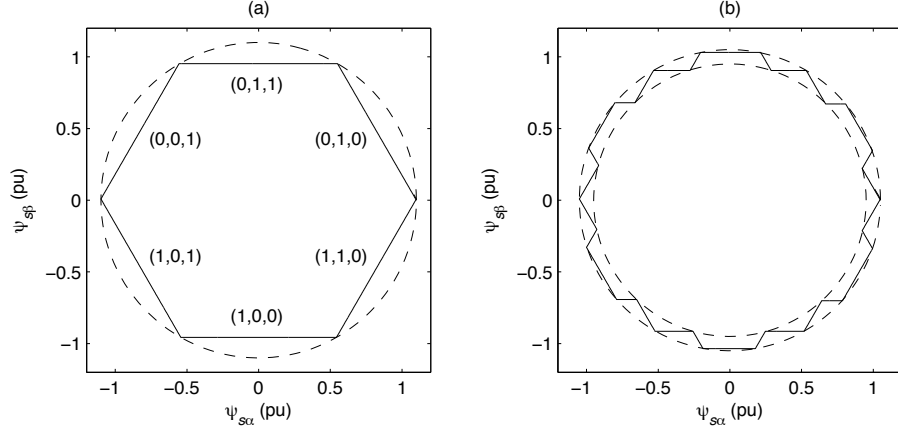


Figure 9.19. Flux paths. (a) DSC (Depenbrock): hexagonal. (b) DTC (Takahashi–Noguchi): ideally circular. (Note that, unlike the rotor flux, the nominal modulus of the stator flux is 1 pu.)

The difference between the flux-modulus reference ψ_s^{ref} and the estimated stator-flux modulus $\hat{\psi}_s$ is fed to the hysteresis controller for the flux, whose output signal is d_ψ . Similarly, the difference between the torque reference τ_{ref} and the torque estimate $\hat{\tau}_e$ is fed to the hysteresis controller for the torque, whose output signal is d_τ . The flux controller is usually a two-level comparator, whereas the torque controller is a three-level comparator (taking the direction of rotation into account). The output signals d_ψ and d_τ of the hysteresis controllers give information about the direction in which the flux should be changed: d_ψ about the flux magnitude and d_τ about the flux angle. Based on this information and the angle estimate $\hat{\theta}_{\psi s}$ of the flux (giving the sector of the flux), the switching logic chooses the actual voltage vector to be used.

The principle of the switching logic can be explained as follows. The tolerance band of the hysteresis controller for the stator flux linkage is denoted as $2\Delta\psi$. The output of the flux controller is changed to

$$\begin{aligned} d_\psi &= 1 && \text{if } \hat{\psi}_s < \psi_s^{\text{ref}} - \Delta\psi, \\ d_\psi &= -1 && \text{if } \hat{\psi}_s > \psi_s^{\text{ref}} + \Delta\psi. \end{aligned}$$

The tolerance band of the hysteresis controller for the torque is denoted by $2\Delta\tau$. The output of this controller also depends on the direction of rotation. When the flux is rotated in the positive direction, the output of the torque controller is changed to

$$\begin{aligned} d_\tau &= 1 && \text{if } \hat{\tau}_e < \tau_{\text{ref}} - \Delta\tau, \\ d_\tau &= 0 && \text{if } \hat{\tau}_e > \tau_{\text{ref}} + \Delta\tau. \end{aligned}$$

When the flux is rotated in the negative direction, the output of the torque controller is changed to

$$\begin{aligned} d_\tau &= 0 && \text{if } \hat{\tau}_e < \tau_{\text{ref}} - \Delta\tau, \\ d_\tau &= -1 && \text{if } \hat{\tau}_e > \tau_{\text{ref}} + \Delta\tau. \end{aligned}$$

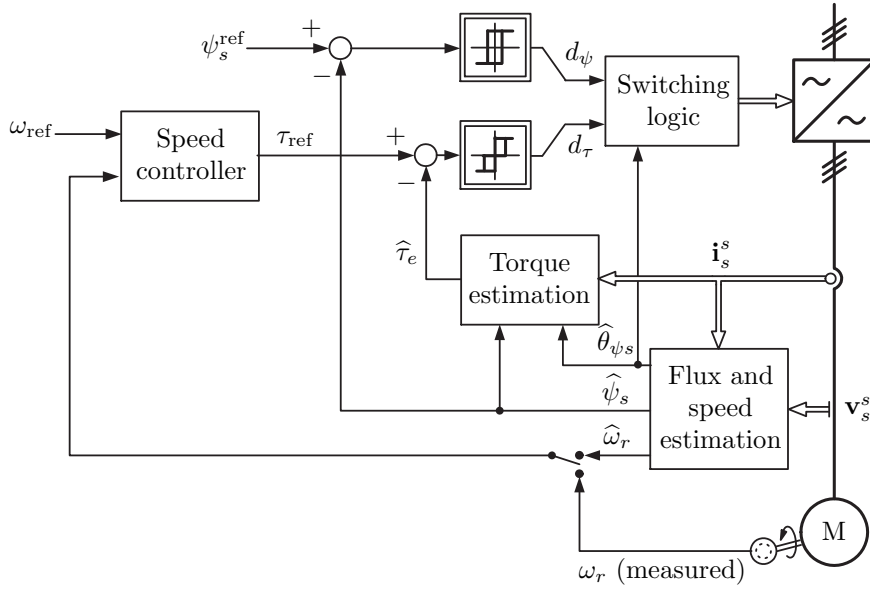


Figure 9.20. DTC system.

Table 9.1. Voltage vectors to be selected by the switching logic. Zero voltage vectors (denoted by “0”) are realized by means of \mathbf{v}_0 or \mathbf{v}_7 , depending on the previous voltage vector.

d_τ	d_ψ	Sector 1	Sector 2	Sector 3	Sector 4	Sector 5	Sector 6
1	1	\mathbf{v}_2	\mathbf{v}_3	\mathbf{v}_4	\mathbf{v}_5	\mathbf{v}_6	\mathbf{v}_1
1	-1	\mathbf{v}_3	\mathbf{v}_4	\mathbf{v}_5	\mathbf{v}_6	\mathbf{v}_1	\mathbf{v}_2
0	1	0	0	0	0	0	0
0	-1	0	0	0	0	0	0
-1	1	\mathbf{v}_6	\mathbf{v}_1	\mathbf{v}_2	\mathbf{v}_3	\mathbf{v}_4	\mathbf{v}_5
-1	-1	\mathbf{v}_5	\mathbf{v}_6	\mathbf{v}_1	\mathbf{v}_2	\mathbf{v}_3	\mathbf{v}_4

The voltage vectors chosen by the switching logic are presented in Table 9.1 for all sectors. Zero voltage vectors are denoted by “0” in the table; the actual choice between the zero vectors \mathbf{v}_0 and \mathbf{v}_7 should minimize the number of switchings.

Let us consider positive direction of rotation. The torque is increased when $d_\tau = 1$. In this case, the switching logic chooses a voltage vector that rotates the stator-flux vector forward. Therefore,

- in the motoring mode, the stator flux vector rotates further away from the rotor flux vector and the torque increases, whereas
- in the regenerating mode (when the stator flux lags the rotor flux), the stator flux vector gets closer to the rotor flux vector and the torque becomes less negative.

The torque is decreased when $d_\tau = 0$. In this case, the switching logic chooses a zero voltage vector that practically stops the stator flux, and the rotor flux continues to rotate. Therefore,

- in the motoring mode, the rotor-flux vector gets closer to the stator-flux vector, and the torque and the shaft power decrease, and

- in the generating mode, the rotor-flux vector rotates further away from the stator-flux vector, and the torque becomes more negative.

When the direction of rotation is negative, the torque is changed more negative when $d_\tau = -1$, and more positive when $d_\tau = 0$. In addition to the hysteresis control of the torque, the magnitude of the stator flux is increased when $d_\psi = 1$, and it is decreased when $d_\psi = -1$. When $d_\tau = 0$, a zero vector is chosen regardless of the flux control.

9.4.3 Discussion

The hysteresis control requires a high sampling frequency and computing speed of the control system in order to detect when the flux or the torque gets outside the hysteresis band. Typically, the estimates of the flux linkage and torque are calculated at a sampling frequency of 40 kHz or higher (corresponding to sampling intervals of 25 μ s or less).

The hysteresis control is characterized by a somewhat chaotic behavior. The switching frequency of the inverter varies depending on the operating point and motor parameters. In addition, the switchings are not exactly repeated during subsequent rotations of the stator flux vector. Therefore, there is a continuous variation in the number and length of voltage pulses fed to the motor. In some cases, a slow subharmonic voltage fluctuation can occur, specially when the stator frequency is low. Subharmonic components can also be seen in the torque, which can cause problems in the form of mechanical vibrations. In order to avoid these problems, the tolerance bands of the hysteresis controllers must be varied so that the switching frequency is high at all stator frequencies. On the other hand, the switching losses in the semiconductor components set an upper limit to the switching frequency.

In the literature, various suggestions have been presented for modifying the DTC method. A simple example is to replace the hysteresis controllers with linear controllers in the flux and torque control loops for obtaining a stator voltage reference, and to use a PWM scheme for the realization of the voltage reference instead of the switching logic. In this way, various problems of the DTC method can be solved, but its ability to a fast torque response is lost. A survey of DTC-based methods can be found in [13].

9.4.4 Stator-Flux Orientation

Unlike all other vector control schemes discussed in this chapter, DTC uses stator-flux orientation (SFO) instead of rotor-flux orientation (RFO). Is SFO an alternative to RFO also in standard vector control, employing an inner synchronous-frame current control loop and an outer flux estimator and synchronization loop? Let us analyze SFO in such a system.

From (5.9) we know that the stator voltage, stator current, and stator flux are related as

$$\frac{d\psi_s^s}{dt} = \mathbf{v}_s^s - R_s \mathbf{i}_s^s. \quad (9.102)$$

Thus, the voltage model for stator-flux estimation simplifies to

$$\frac{d\hat{\psi}_s^s}{dt} = \mathbf{v}_s^s - \hat{R}_s \mathbf{i}_s^s \quad (9.103)$$

(i.e., the voltage drop across the leakage inductance vanishes, as compared to the corresponding relation for the rotor flux). In, e.g., IFO implementation of the SCVM, the flux-emf components

are computed as

$$\hat{E}_d = v_d^{\text{ref}} - \hat{R}_s i_d^{\text{ref}} \quad \hat{E}_q = v_q^{\text{ref}} - \hat{R}_s i_q^{\text{ref}}. \quad (9.104)$$

The problem of an algebraic loop forming because ω_1 is computed from \hat{E}_d and \hat{E}_q , but is also used to compute these components, disappears. Moreover, the estimator's sensitivity to \hat{L}_σ vanishes, leaving the stator resistance as the only sensitive parameter.

Let us now consider the rotor circuit in the IM's dynamic equivalent circuit. Substituting $\psi_R = \psi_s - L_\sigma \mathbf{i}_s$ in (5.40), we obtain

$$\begin{aligned} \frac{d\psi_s}{dt} - L_\sigma \frac{d\mathbf{i}_s}{dt} &= R_R \mathbf{i}_s - \left(\frac{R_R}{L_M} + j\omega_2 \right) (\psi_s - L_\sigma \mathbf{i}_s) \\ \Rightarrow \frac{d\psi_s}{dt} &= L_\sigma \frac{d\mathbf{i}_s}{dt} + \left[\left(1 + \frac{L_\sigma}{L_M} \right) R_R + j\omega_2 L_\sigma \right] \mathbf{i}_s - \left(\frac{R_R}{L_M} + j\omega_2 \right) \psi_s. \end{aligned} \quad (9.105)$$

Neglecting $d\mathbf{i}_s/dt$ as seen from the slower flux dynamics, and assuming perfect field orientation, i.e., taking the stator flux real, we obtain by splitting the real and imaginary parts

$$\frac{d\psi_s}{dt} = \left(1 + \frac{L_\sigma}{L_M} \right) R_R i_d - \omega_2 L_\sigma i_q - \frac{R_R}{L_M} \psi_s \quad (9.106)$$

$$0 = \left(1 + \frac{L_\sigma}{L_M} \right) R_R i_q + \omega_2 L_\sigma i_d - \omega_2 \psi_s. \quad (9.107)$$

In (9.106) it is seen that the flux modulus is determined not only by i_d , but also (to a lesser degree) by i_q . Whereas a constant i_d is used in RFO (except in the field-weakening region), in SFO i_d must be modified with the torque (i.e., with i_q and ω_2) in order to keep the stator-flux modulus constant. For this purpose, an outer flux control loop—with fairly low bandwidth—can be used. Following the theory for the SCVM, the flux modulus can be estimated as follows:

$$\frac{d\hat{\psi}_s}{dt} = \gamma \hat{E}_d. \quad (9.108)$$

The error $\psi_s^{\text{ref}} - \hat{\psi}_s$ is then fed to an integrator, whose output is i_d^{ref} . A variant of the current model can be obtained. The slip relation in SFO is found from (9.107)

$$\omega_1 = \omega_r + \frac{\left(1 + \frac{\hat{L}_\sigma}{\hat{L}_M} \right) \hat{R}_R i_q}{\hat{\psi}_s - \hat{L}_\sigma i_d}, \quad \dot{\theta}_1 = \omega_1 \quad (9.109)$$

which is more complicated than that in RFO.

To summarize and add some results not explicitly derived, SFO has been found to have the following properties as compared to RFO.

- **Inherently sensorless flux estimator (SCVM):** Simpler; the low-pass filter used for avoiding an algebraic loop can be removed.
- **Accuracy of flux estimation and field orientation:** Better; \hat{R}_s is the only critical parameter.
- **Flux control:** More complicated; i_d must be varied, even below base speed.

- **Sensored control using the current model:** More complicated slip relation.
- **Speed estimation in sensorless control:** More complicated. Here, the slip relation (9.109) can be used “backwards” [cf. (9.67)].
- **Low-speed stability properties for sensorless control:** Similar. Analysis shows that the problems regarding flux collapse and frequency lockup remain.
- **Field weakening:** Slightly simpler. The standard method of reducing the stator flux as $1/|\omega_1|$ in the field-weakening region has been shown to give close to maximum torque [87] (which is not true for the rotor flux [49]).
- **Current control:** Slightly simpler. It can be shown that the cross-coupling term $j\omega_1 L_\sigma \mathbf{i}_s$ in RFO is in SFO replaced by $j\omega_2 L_\sigma \mathbf{i}_s$. This term is small enough to be neglected, so decoupling is not necessary for good performance.

Clearly, there are both pros and cons of SFO as compared to RFO; the choice of method appears often to be made based on personal preferences of each researcher, design engineer, or engineering team. We in this book prefer RFO because it is more general, being applicable to IMs, PMSMs, and in effect also grid-connected inverters, with a minimum of modifications necessary.

APPENDIX A

Lyapunov Stability Theory

Linearization, as described in Section 2.3, may establish *local* stability about an equilibrium point. If possible, it is desirable to show that a nonlinear system is *globally* stable. That is, regardless of the starting point $x(0)$, it can be guaranteed than x converges asymptotically to the equilibrium point, which we here for simplicity take as the origin. This can be accomplished by means of Lyapunov's second (or direct) method. A Lyapunov function is a function with the following properties:

1. $V(x) > 0, x \neq 0; V(0) = 0.$
2. $\dot{V}(x) = \frac{dV(x)}{dx} \dot{x} = \frac{dV(x)}{dx} f(x) \leq 0.$

If, in addition, the function is unbounded, i.e., $V(\infty) = \infty$, it is said to be a *global* Lyapunov function. If $\dot{V}(x) < 0, x \neq 0$, it is said to be a *strict* Lyapunov function.

A Lyapunov function can be considered as the energy stored in the system. Naturally, the energy has to be positive—hence, the first property—and if energy is always dissipated—i.e., $\dot{V}(x) \leq 0$ —it appears logical that the system is stable. We formulate this as the following theorem, the proof of which can be found e.g., in [48].

Theorem A.1 Suppose that there exists a Lyapunov function $V(x)$ for the system

$$\dot{x} = f(x).$$

Then the equilibrium point $x^* = 0$ is **stable**. Furthermore, it is **globally stable** if $V(x)$ is a global Lyapunov function, and **asymptotically stable** if $V(x)$ is a strict Lyapunov function.

If a strict Lyapunov function is not global, there may be several equilibrium points to which x may converge. (Such a case will soon be encountered.) The good thing is that x cannot go into a limit cycle or diverge.

Lyapunov theory provides an extremely powerful tool for stability analysis of nonlinear systems. The problem is that finding a Lyapunov function is not always trivial. In many cases, the energy stored in the system can be used as a Lyapunov function, though.

Example A.1 Circuit with nonlinear resistor. Consider the *RLC* circuit in Figure A.1. The resistor is a nonlinear one with the characteristic that the voltage–current relationship is given by

$$v_R = ki_R^3.$$

The circuit is therefore nonlinear. However, since the power developed in the resistor, $v_R i_R = ki_R^4$, is non-negative, energy is always dissipated in the circuit, so it should be stable. To prove this, we let the energy stored in the reactive components be a Lyapunov function candidate:

$$V(x) = \frac{1}{2}L_1 x_1^2 + \frac{1}{2}C_2 x_2^2 + \frac{1}{2}L_3 x_3^2.$$

This is a global function, since $V(\infty) = \infty$ regardless of which one of the variables x_1 , x_2 , or x_3 that is made infinitely large. Applying Ohm's and Kirchhoff's laws yields the following equations:

$$\dot{x}_1 = -\frac{k}{L_1}x_1^3 - \frac{1}{L_1}x_2 \quad (\text{A.1})$$

$$\dot{x}_2 = \frac{1}{C_2}(x_1 - x_3) \quad (\text{A.2})$$

$$\dot{x}_3 = \frac{1}{L_3}x_2. \quad (\text{A.3})$$

Differentiating the Lyapunov function candidate then yields

$$\begin{aligned} \dot{V}(x) &= L_1x_1\dot{x}_1 + C_2x_2\dot{x}_2 + L_3x_3\dot{x}_3 \\ &= L_1x_1\left(-\frac{k}{L_1}x_1^3 - \frac{1}{L_1}x_2\right) + C_2x_2\frac{1}{C_2}(x_1 - x_3) + L_3x_3\frac{1}{L_3}x_2 \\ &= -kx_1^4 \leq 0. \end{aligned}$$

Quite naturally, the time derivative of the stored energy is the power dissipated in the nonlinear resistor. The energy is thus a Lyapunov function and the circuit is, indeed, stable.

Is the circuit asymptotically stable? Since \dot{V} is not a function of x_2 and x_3 , V is not a strict Lyapunov function. It is only guaranteed that x_1 converge to 0. Once $x_1 = 0$, then $\dot{V} = 0$, i.e.,

$$V(x)|_{x_1=0} = \frac{1}{2}C_2x_2^2 + \frac{1}{2}L_3x_3^2 = \text{constant}. \quad (\text{A.4})$$

Hence, although x_2 and x_3 cannot diverge, it cannot immediately be guaranteed that x_2 and x_3 will not enter a limit cycle once x_1 has converged. The system is asymptotically stable, however. This can be deduced by the following reasoning.

1. $\dot{V} < 0$ as long as $x_1 \neq 0$; thus, x_1 converges asymptotically to 0. Clearly, when $x_1 \equiv 0$, then $\dot{x}_1 \equiv 0$.
2. But $x_1 \equiv \dot{x}_1 \equiv 0$ requires—see (A.1)—that $x_2 \equiv 0$. Thus, $\dot{x}_2 \equiv 0$.
3. From (A.2) it follows that when $\dot{x}_2 \equiv 0$ and $x_1 \equiv 0$, then $x_3 \equiv 0$.

Thus, we have shown that the equilibrium point $x_1^* = x_2^* = x_3^* = 0$ is globally asymptotically stable. This method for checking asymptotic stability is known as LaSalle's invariance principle [48].

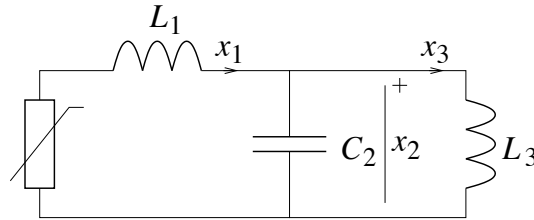


Figure A.1. RLC circuit with nonlinear resistor.

♣

Example A.2 Standard slip relation derived using Lyapunov theory. In some cases, Lyapunov theory is useful for finding a nonlinear control law. A Lyapunov function candidate V is selected. A control law which assures that $\dot{V} \leq 0$ is then derived. Consider the differential equations for the rotor flux of the induction motor in synchronous coordinates

$$\begin{aligned}\dot{\psi}_d &= R_R i_d - \frac{R_R}{L_M} \psi_d + \omega_2 \psi_q \\ \dot{\psi}_q &= R_R i_q - \frac{R_R}{L_M} \psi_q - \omega_2 \psi_d.\end{aligned}$$

We want ψ_d to converge to ψ_{ref} and ψ_q to 0. Let us assume that the motor parameters are known and $i_d = \psi_{\text{ref}}/L_M$, where ψ_{ref} is constant. Introducing $\tilde{\psi}_d = \psi_d - \psi_{\text{ref}}$ yields

$$\begin{aligned}\dot{\tilde{\psi}}_d &= -\frac{R_R}{L_M} \tilde{\psi}_d + \omega_2 \psi_q \\ \dot{\psi}_q &= R_R i_q - \frac{R_R}{L_M} \psi_q - \omega_2 (\tilde{\psi}_d + \psi_{\text{ref}}).\end{aligned}$$

Now, let us take

$$V = \frac{1}{2}(\tilde{\psi}_d^2 + \psi_q^2) \quad (\text{A.5})$$

as a Lyapunov function candidate. This yields

$$\dot{V} = \tilde{\psi}_d \dot{\tilde{\psi}}_d + \psi_q \dot{\psi}_q = -\frac{R_R}{L_M} (\tilde{\psi}_d^2 + \psi_q^2) + (R_R i_q - \omega_2 \psi_{\text{ref}}) \psi_q.$$

Thus, it is not guaranteed that $\dot{V} \leq 0$, so V is not automatically a Lyapunov function. But since ω_2 is an input signal available for manipulation (via $\omega_1 = \omega_r + \omega_2$, if ω_r is measured), we can choose

$$\omega_2 = \frac{R_R i_q}{\psi_{\text{ref}}} \quad (\text{A.6})$$

in order to cancel the last two terms, and obtain

$$\dot{V} = -\frac{R_R}{L_M} (\tilde{\psi}_d^2 + \psi_q^2) \leq 0.$$

The resulting system is globally asymptotically stable. This example has shown that the standard slip relation (A.6) can be derived as a step in making V a Lyapunov function.

♣

Example A.3 Global stability of the PLL, which was claimed in Section 6.5.1, will now be proven. Let us consider (6.42)–(6.43) with $\tilde{\omega}_i = \tilde{\omega}_s - \omega_i$:

$$\begin{aligned}\dot{\tilde{\omega}}_i &= -k_{ip} E \sin \tilde{\theta} \\ \dot{\tilde{\theta}} &= \tilde{\omega}_i - k_{pp} E \sin \tilde{\theta}\end{aligned}$$

and take

$$V(\tilde{\omega}_i, \tilde{\theta}) = \frac{1}{2}\tilde{\omega}_i^2 + k(1 - \cos \tilde{\theta})$$

as Lyapunov function candidate, where k is a positive constant to be selected. Clearly, $V(0, 2n\pi) = 0$ (n integer) and $V > 0$ otherwise. Differentiating yields

$$\begin{aligned}\dot{V} &= \tilde{\omega}_i \dot{\tilde{\omega}}_i + k \sin \tilde{\theta} \dot{\tilde{\theta}} = -k_{ip}E\tilde{\omega}_i \sin \tilde{\theta} + k \sin \tilde{\theta}(\tilde{\omega}_i - k_{pp}E \sin \tilde{\theta}) \\ &= -kk_{pp}E \sin^2 \tilde{\theta} + (k - k_{ip}E)\tilde{\omega}_i \sin \tilde{\theta} = \{k = k_{ip}E\} \\ &= -k_{ip}k_{pp}E^2 \sin^2 \tilde{\theta} \leq 0.\end{aligned}$$

This shows that the PLL is stable, but what about global and asymptotic stability? Because there is an infinite number of equilibrium points: $[\tilde{\omega}_i, \tilde{\theta}] = [0, 2n\pi]$, the system is not globally stable in a strict sense. However, if all equilibrium points are considered equal—which is logical, as they differ only by one revolution (2π) along the $\tilde{\theta}$ axis—the system can be considered globally stable. There is no guarantee for convergence to the *closest* equilibrium point, however, which causes the mentioned slipping phenomenon.



APPENDIX B

CORDIC Algorithm

In most vector control systems, at least two coordinate transformations have to be performed: transformation of the measured stator current vector from stator to synchronous coordinates and of the converter voltage command vector from synchronous to stationary coordinates. These coordinate transformations can all be expressed as

$$\underbrace{\begin{bmatrix} x' \\ y' \end{bmatrix}}_{\mathbf{v}'} = \underbrace{\begin{bmatrix} \cos \theta & -\sin \theta \\ \sin \theta & \cos \theta \end{bmatrix}}_{e^{J\theta}} \underbrace{\begin{bmatrix} x \\ y \end{bmatrix}}_{\mathbf{v}} \quad (\text{B.1})$$

which is an $\alpha\beta$ transformation. The dq transformation is obtained by substituting $\theta \Rightarrow -\theta$. While coordinate transformations were difficult to handle when implemented in analog electronics, they present little difficulties if implemented digitally. The tool which allows coordinate transformations (or, perhaps more accurate, coordinate rotations) to be performed with ease is known as the coordinate rotation digital computer (CORDIC) algorithm; invented by Volder in the 1950s [85]. The algorithm has since been used in almost all scientific calculators to calculate cosine and sine, since this is merely a special case of (B.1) with $x = 1, y = 0$, yielding

$$\begin{bmatrix} x' \\ y' \end{bmatrix} = \begin{bmatrix} \cos \theta \\ \sin \theta \end{bmatrix}. \quad (\text{B.2})$$

Let us derive the CORDIC algorithm and see how it can be used to implement the $\alpha\beta$ transformation.

It is obvious that the coordinate transformation (B.1) can be broken down into a series of N coordinate rotations:

$$v' = e^{J\theta} v = e^{J\alpha_0} e^{J\alpha_1} \cdots e^{J\alpha_{N-1}} v \quad (\text{B.3})$$

if $\alpha_0 + \alpha_1 + \cdots + \alpha_{N-1} = \theta$. This can also be expressed as the iteration

$$v_{n+1} = e^{J\alpha_n} v_n, \quad n = 0, 1, \dots, N-1, \quad v_0 = v \quad (\text{B.4})$$

and $v' = v_N$. Equation (B.4) can be expressed as

$$\begin{aligned} \begin{bmatrix} x_{n+1} \\ y_{n+1} \end{bmatrix} &= \begin{bmatrix} x_n \cos \alpha_n - y_n \sin \alpha_n \\ x_n \sin \alpha_n + y_n \cos \alpha_n \end{bmatrix} \\ &= \cos \alpha_n \begin{bmatrix} x_n - y_n \tan \alpha_n \\ y_n + x_n \tan \alpha_n \end{bmatrix}, \quad n = 0, 1, \dots, N-1. \end{aligned} \quad (\text{B.5})$$

The key to obtaining a simple algorithm is to select the angles α_n such that

$$\tan \alpha_n = \begin{cases} 2^{-n}, & \alpha_n > 0 \\ -2^{-n}, & \alpha_n < 0. \end{cases} \quad (\text{B.6})$$

This allows transformation angles in the range $-99.9^\circ < \theta < 99.9^\circ$, since

$$\arctan(1) + \arctan\left(\frac{1}{2}\right) + \arctan\left(\frac{1}{4}\right) + \dots = 99.883^\circ. \quad (\text{B.7})$$

Then the multiplication by $\tan \alpha_n$ can be implemented merely as n binary right shifts, so the algorithm now reads

$$\begin{bmatrix} x_{n+1} \\ y_{n+1} \end{bmatrix} = k_n \begin{bmatrix} x_n - \operatorname{sgn}(\alpha_n) y_n 2^{-n} \\ y_n + \operatorname{sgn}(\alpha_n) x_n 2^{-n} \end{bmatrix}, \quad n = 0, 1, \dots, N-1. \quad (\text{B.8})$$

where $k_n = \cos(\arctan 2^{-n})$. The sign of α_n is determined as follows. Suppose that a coordinate rotation of $\theta = 60^\circ$ is desired. For $n = 0$, the angle is advanced by $\arctan 1 = 45^\circ$, and for $n = 1$ by $\arctan 1/2 = 26.6^\circ$. This yields a sum of 71.6° , so for $n = 2$, the angle has to be negative: $\alpha_2 = -\arctan 1/4 = -14.0^\circ$. The total angle after these three iterations is 57.6° (we are rapidly converging to the correct angle!), so for $n = 3$, a positive angle is required. These steps can be expressed as follows, using an error angle θ_n (which converges to zero):

$$\theta_0 = \theta \quad \theta_{n+1} = \theta_n - \alpha_n \quad \operatorname{sgn}(\alpha_{n+1}) = \operatorname{sgn}(\theta_{n+1}). \quad (\text{B.9})$$

The only multiplication in the algorithm is that by k_n . However, this multiplication need not be made at each step; it can be implemented as a scaling by the constant

$$K_N = \prod_{n=0}^{N-1} \cos(\arctan 2^{-n}) \quad (\text{B.10})$$

made when initializing the algorithm, i.e.,

$$\begin{bmatrix} x_0 \\ y_0 \end{bmatrix} = K_N \begin{bmatrix} x \\ y \end{bmatrix}$$

$$\begin{bmatrix} x_{n+1} \\ y_{n+1} \end{bmatrix} = \begin{bmatrix} x_n - \operatorname{sgn}(\alpha_n) y_n 2^{-n} \\ y_n + \operatorname{sgn}(\alpha_n) x_n 2^{-n} \end{bmatrix}, \quad n = 0, 1, \dots, N-1. \quad (\text{B.11})$$

K_N is known as the aggregate constant and it converges to $0.6073\dots$ as $N \rightarrow \infty$. (The convergence is fast; the first four decimal positions remain unchanged for $N > 7$.)

The scaling by K_N is thus the only multiplication needed when implementing the CORDIC algorithm. (If only cosine and sine are to be computed, no multiplications at all are needed, since then $x = 1$, $y = 0$.) To keep track of the angle increments α_n , a look-up table for the function $\arctan 2^{-n}$ is needed. This table only requires N positions, however. The number of iterations N does not have to be particularly large in order to obtain a good resolution. Eight iterations yields $\cos 2^{-8} = 0.22^\circ$ and ten iterations $\cos 2^{-10} = 0.056^\circ$. Clearly, N need not be selected larger than the number of bits used in the A/D and D/A conversions of the stator current and voltage signals, as this already puts a limit on the resolution.

We are now ready to present the complete CORDIC algorithm.

Algorithm B.1

CORDIC Algorithm

```

$$\begin{bmatrix} x \\ y \end{bmatrix} = K_N \begin{bmatrix} x \\ y \end{bmatrix}$$

for  $n = 0$  to  $N - 1$ 

$$\alpha = \operatorname{sgn}(\theta) \arctan(2^{-n})$$


$$\begin{bmatrix} x \\ y \end{bmatrix} = \begin{bmatrix} x \\ y \end{bmatrix} + \operatorname{sgn}(\theta) \begin{bmatrix} -y \\ x \end{bmatrix} 2^{-n}$$


$$\theta = \theta - \alpha$$

end
return  $[x, y]$ 
```

Bibliography

- [1] M. Alaküla, "On the control of saturated synchronous machines," *Ph.D. Dissertation*, Lund Institute of Technology, Sweden, May 1993.
- [2] E. Ch. Andresen and A. Haun, "Influence of the pulselwidth modulation control method on the performance of frequency inverter induction motor drives," *Eur. Trans. Electr. Power*, Vol. 3, No. 2, Mar./Apr. 1993, pp. 151–161.
- [3] G. J. Armstrong and D. J. Atkinson, "A comparison of model reference adaptive system and extended Kalman filter estimators for sensorless vector drives," *Proc. Eur. Conf. Power Electron. Appl.*, Trondheim, Norway, Vol. 1, Sept. 1997, pp. 424–429.
- [4] K. J. Åström and B. Wittenmark, *Computer-Controlled Systems: Theory and Design*, 2nd Ed., Prentice Hall, Englewood Cliffs, NJ, 1990.
- [5] K. J. Åström and B. Wittenmark, *Adaptive Control*, 2nd Ed., Addison-Wesley, Reading, MA, 1995.
- [6] F. Blaschke, "The principle of field orientation as applied to the new TRANSVECTOR closed-loop control system for rotating-field machines," *Siemens Review*, No. 2, 1972, pp. 217–223.
- [7] R. Blasco-Giménez, G. M. Asher, M. Sumner, and K. J. Bradley, "Dynamic performance limitations for MRAS based sensorless induction motor drives. Part 1: Stability and analysis for the closed loop drive," *IEE Proc.-Electr. Power Appl.*, Vol. 143, No. 2, Mar. 1996, pp. 113–122
- [8] R. Blasco-Giménez, G. M. Asher, M. Sumner, and K. J. Bradley, "Dynamic performance limitations for MRAS based sensorless induction motor drives. Part 2: Online parameter tuning and dynamic performance studies," *IEE Proc.-Electr. Power Appl.*, Vol. 143, No. 2, Mar. 1996, pp. 123–134
- [9] M. H. J. Bollen, *Understanding Power Quality Problems: Voltage Sags and Interruptions*, IEEE Press, 2000.
- [10] B. K. Bose (Ed.), *Power Electronics and Variable Frequency Drives*, IEEE Press, Piscataway, NJ, 1996.
- [11] B. K. Bose and N. R. Patel, "A programmable cascaded low-pass filter-based flux synthesis for a stator flux-oriented vector-controlled induction motor drive," *IEEE Trans. Ind. Electron.*, *IEEE Trans. Ind. Electron.*, Vol. 44, No. 2, Feb. 1997, pp. 140–143.
- [12] F. Briz, M. W. Degner, and R. D. Lorenz, "Dynamic analysis of current regulators for ac motors using complex vectors," *IEEE Trans. Ind. Appl.*, Vol. 35, No. 2, Nov./Dec. 1999, pp. 1424–1432.

- [13] G. S. Buja and M. P. Kazmierkowski, ‘‘Direct torque control of PWM inverter-fed ac motors—A survey,’’ *IEEE Trans. Ind. Electron.*, Vol. 51, No. 2, Aug. 2004, pp. 744–757.
- [14] J.-W. Choi and S.-K. Sul, ‘‘New control concept—minimum time current control in the three-phase PWM converter,’’ *IEEE Trans. Power Electron.*, Vol. 12, No. 2, Jan. 1997, pp. 124–131.
- [15] M. J. Corley and R. D. Lorenz, ‘‘Rotor position and velocity estimation for a permanent magnet synchronous machine at standstill and high speeds,’’ *IEEE Trans. Ind. Appl.*, Vol. 34, No. 2, July–Aug. 1998, pp. 784–789.
- [16] P. A. S. De Wit, R. Ortega, and I. Mareels, ‘‘Indirect field-oriented control of induction motors is robustly globally stable,’’ *Automatica*, Vol. 32, No. 2, 1996, pp. 1393–1402.
- [17] M. Depenbrock, ‘‘Direct self-control (DSC) of inverter-fed induction machine,’’ *IEEE Trans. Power Electron.*, Vol. 3, No. 2, Oct. 1988, pp. 420–429.
- [18] M. Depenbrock, F. Hoffman, and S. Koch, ‘‘Speed sensorless high performance control for traction drives,’’ in *Proc. Eur. Conf. on Power Electron. and Applicat.*, Trondheim, Norway, Sept. 1997, pp. 418–423.
- [19] M. Depenbrock, C. Foerth, and S. Koch, ‘‘Speed sensorless control of induction motors at very low stator frequencies,’’ in *Proc. Eur. Conf. on Power Electron. and Applicat.*, Geneva, Switzerland, Sept. 1999, CD-ROM.
- [20] W. C. Duesterhoeft, M. W. Schulz, and E. Clarke, ‘‘Determination of instantaneous currents and voltages by means of alpha, beta, and zero components,’’ *Trans. Amer. Inst. Electr. Eng.*, vol. 70, no. 2, July 1951, pp. 1248–1255.
- [21] A. Ferrah, K. J. Bradley, P. J. Hogben-Laing, M. S. Woolfson, G. M. Asher, M. Sumner, J. Cilia, and J. Shuli, ‘‘A speed identifier for induction motor drives using real-time adaptive digital filtering,’’ *IEEE Trans. Ind. Appl.*, Vol. 34, No. 2, Jan./Feb. 1998, pp. 156–162.
- [22] B. Gallwitz, F. Hillenbrand, and C. Landgraf, ‘‘A proposal for avoiding the direct measurement of speed and angular position of the synchronous machine,’’ *Proc. IFAC Control in Power Electron. and Electrical Drives*, Lausanne, Switzerland, 1983, pp. 63–68.
- [23] L. J. Garcés, ‘‘Parameter adaptation for the speed-controlled static ac drive with a squirrel-cage induction motor,’’ *IEEE Trans. Ind. Appl.*, Vol. 16, No. 2, Mar./Apr. 1980, pp. 173–178.
- [24] S. H. Hahn, *Hilbert Transforms in Signal Processing*, Artech House, 1996.
- [25] D. C. Hanselman, ‘‘Resolver signal requirements for high accuracy resolver-to-digital conversion,’’ *IEEE Trans. Ind. Electron.*, Vol. 37, No. 2, Dec. 1990, pp. 556–561.
- [26] L. Harnefors, ‘‘On analysis, control and estimation of variable-speed drives,’’ *Ph.D. Dissertation*, Electrical Machines and Drives, Dept. of Electric Power Eng., Royal Institute of Technol., Stockholm, Sweden, 1997.
- [27] L. Harnefors and H.-P. Nee, ‘‘Model-based current control of ac machines using the internal model control method,’’ *IEEE Trans. Ind. Appl.*, Vol. 34, No. 2, Jan./Feb. 1998, pp. 133–141.
- [28] L. Harnefors and H.-P. Nee, ‘‘A general algorithm for speed and position estimation of ac motors,’’ *IEEE Trans. Ind. Electron.*, Vol. 47, No. 2, Feb. 2000, pp. 77–83.

- [29] L. Harnefors, "Instability phenomena and remedies in sensorless indirect field oriented control," *IEEE Trans. Power Electron.*, Vol. 15, No. 2, July 2000, pp. 733–743.
- [30] L. Harnefors, K. Pietiläinen, and L. Gertmar, "Torque-maximizing field-weakening control: design, analysis, and parameter selection," *IEEE Trans. Ind. Electron.*, Vol. 48, No. 2, Feb. 2001, pp. 161–168.
- [31] L. Harnefors, "Design and analysis of general rotor-flux-oriented vector control systems," *IEEE Trans. Ind. Electron.*, Vol. 48, No. 2, Apr. 2001, pp. 383–390.
- [32] L. Harnefors, M. Jansson, R. Ottersten, and K. Pietiläinen, "Unified sensorless vector control of synchronous and induction motors," *IEEE Trans. Ind. Electron.*, Vol. 50, No. 2, Feb. 2003, pp. 153–160.
- [33] L. Harnefors and R. Ottersten, "Regeneration-mode stabilization of the 'statically compensated voltage model,'" *IEEE Trans. Ind. Electron.*, Vol. 54, No. 2, Apr. 2007, pp. 818–824.
- [34] L. Harnefors and M. Hinkkanen, "Complete stability of reduced-order and full-order observers for sensorless IM drives," *IEEE Trans. Ind. Electron.*, Vol. 55, No. 2, Mar. 2008, pp. 1319–1329.
- [35] L. Harnefors and M. Hinkkanen, "Stabilization of sensorless inductor motor drives—A survey," *IEEE J. Emerg. Select. Topics Power Electron.*, Vol. 2, No. 2, Jun. 2014, pp. 132–142.
- [36] K. Hasse, "Zur Dynamik drehzahlgeregelter Antriebe mit Stromrichter gespeisten Asynchron-Kurzschluss laufermaschinen," *Ph.D. Dissertation* (in German), Technische Hochschule Darmstadt, Darmstadt, Germany, 1969.
- [37] A. M. Hava, S.-K. Sul, R. J. Kerkman, and T. A. Lipo, "Dynamic overmodulation characteristics of triangle intersection PWM methods," *IEEE Trans. Ind. Appl.*, Vol. 35, No. 2, July/Aug. 1999, pp. 896–907.
- [38] R. C. Hilborn, *Chaos and Nonlinear Dynamics: An Introduction for Scientists and Engineers*. London, U.K.: Oxford Univ. Press, 1994.
- [39] M. Hinkkanen, "Analysis and design of full-order flux observers for sensorless induction motors," *IEEE Trans. Ind. Electron.*, Vol. 51, No. 2, Oct. 2004, pp. 1033–1040.
- [40] M. Hinkkanen and J. Luomi, "Stabilization of regenerating-mode operation in sensorless induction motor drives by full-order flux observer design," *IEEE Trans. Ind. Electron.*, Vol. 51, No. 2, Dec. 2004, pp. 1318–1328.
- [41] J. Holtz, "Sensorless control of induction motor drives," *Proc. IEEE*, vol. 90, no. 8, pp. 1359–1394, Aug. 2002.
- [42] G.-C. Hsieh and J. C. Hung, "Phase-locked loop techniques—a survey," *Invited Paper, IEEE Trans. Ind. Electron.*, Vol. 43, No. 6, pp. 609–615, Dec. 1996.
- [43] K. D. Hurst and T. G. Habetler, "Sensorless speed measurement using current harmonics spectral estimation in induction machine drives," *IEEE Trans. Power Electron.*, Vol. 11, No. 2, Jan. 1996, pp. 66–73.

- [44] P. L. Jansen and R. D. Lorenz, "A physically insightful approach to the design and accuracy assessment of flux observers for field oriented induction machine drives," *IEEE Trans. Ind. Appl.*, Vol. 30, No. 2, Jan./Feb. 1994, pp. 101–110.
- [45] P. L. Jansen and R. D. Lorenz, "Transducerless position and velocity estimation in induction and salient ac machines," *IEEE Trans. Ind. Appl.*, Vol. 31, No. 2, pp. 240–247, Mar./Apr. 1995.
- [46] M. Jansson, L. Harnefors, O. Wallmark, and M. Leksell, "Synchronization at startup and stable rotation reversal of nonsalient PMSM drives," accepted to *IEEE Trans. Ind. Electron.*
- [47] M. K. Kazimierczuk and D. Czarkowski, *Resonant Power Converters*. Wiley, 1995.
- [48] H. K. Khalil, *Nonlinear Systems*, Macmillan Publishing, New York, 1992.
- [49] S.-H. Kim and S.-K. Sul, "Maximum torque control of an induction machine in the field weakening region," *IEEE Trans. Ind. Appl.*, Vol. 31, No. 2, July/Aug. 1995, pp. 787–794.
- [50] S.-H. Kim and S.-K. Sul, "Voltage control strategy for maximum torque operation of an induction machine in the field weakening region," *IEEE Trans. Ind. Electron.*, Vol. 44, No. 2, Aug. 1997, pp. 512–518.
- [51] K. P. Kovács, *Transient Phenomena in Electrical Machines*, Elsevier, Amsterdam, 1984.
- [52] H. Kubota, K. Matsuse, and Y. Hori, "Behavior of sensorless induction motor drives in regeneration mode," in *Proc. Power Conversion Conf.*, vol. 2, pp. 549–552, Nagaoka, Japan, 1997.
- [53] H. Kubota, I. Sato, Y. Tamura, K. Matsuse, H. Ohta, and Y. Hori, "Regeneration-mode low-speed operation of sensorless induction motor drive with adaptive observer," *IEEE Trans. Ind. Applicat.*, vol. 38, no. 4, pp. 1081–1086, July/Aug. 2002.
- [54] H. Kubota and Y. Tamura, "Stator resistance estimation for sensorless induction motor drives under regenerating condition," in *Proc. IEEE IECON'02*, vol. 1, pp. 426–430, Nov. 2002.
- [55] J.-W. Lee, "An intelligent current controller using delay time compensation for PWM converter", in *Proc. Eur. Conf. on Power Electron. and Applicat.*, Trondheim, Norway, pp. 342–347, Sept. 1997.
- [56] W. Leonhard, *Control of Electrical Drives*, 2nd Ed., Springer-Verlag, Berlin, 1996.
- [57] T. Matsumoto, L. Chua, and M. Komuro, "The double scroll," *IEEE Trans. Circuits Syst.*, Vol. 32, No. 2, Aug. 1985, pp. 797–818.
- [58] P. Mattavelli and F. P. Marafao, "Repetitive-based control for selective harmonic compensation in active power filters," *IEEE Trans. Ind. Electron.*, Vol. 51, No. 2, Oct. 2004, pp. 1018–1024.
- [59] R. H. Middleton and G. C. Goodwin, *Digital Control and Estimation: A Unified Approach*, Prentice Hall, Englewood Cliffs, NJ, 1990.
- [60] T. J. E. Miller, *Switched Reluctance Motors and Their Control*, Clarendon Press, Oxford, 1993.

- [61] N. Mohan, T. M. Undeland, and W. P. Robbins, *Power Electronics: Converters, Applications and Design*, 3rd Ed. Wiley, 2003.
- [62] M. Morari and E. Zafriou, *Robust Process Control*, Prentice Hall, Englewood Cliffs, NJ, 1989.
- [63] I. Nagy, "Chaotic processes in PWM using tolerance band control for voltage source inverters," *Proc. Fifth IEE Int. Conf. Power Electron. Variab. Speed Drives*, London, UK, Oct. 1994, pp. 66–71.
- [64] R. Ottersten, "On control of back-to-back converters and sensorless induction machines drives," *Ph.D. Dissertation*, Department of Electric Power Eng., Chalmers Univ. of Technol., 2003.
- [65] F.-Z. Peng and T. Fukao, "Robust speed identification for speed-sensorless vector control of induction motors," *IEEE Trans. Ind. Appl.*, Vol. 30, No. 2, Sept./Oct. 1994, pp. Sept./Oct. 1994.
- [66] K. Pietiläinen, L. Harnefors, A. Petersson, and H.-P. Nee, "DC-link stabilization and voltage sag ride-through of inverter drives," accepted to *IEEE Trans. Ind. Electron.*
- [67] T. M. Rowan and R. J. Kerkman, "A new synchronous current regulator and an analysis of current-regulated PWM inverters," *IEEE Trans. Ind. Appl.*, Vol. 22, No. 2, July/Aug. 1986, pp. 678–690.
- [68] C. Sadarangani, *Electrical Machines – Design and Analysis of Induction and Permanent Magnet Motors*, Electr. Machines and Power Electron., Dept. of Electr. Power Eng., Royal Inst. of Technol., 2000.
- [69] M. Saitou, M. Matsui, and N. Shimizu, "A control strategy of single-phase active filter using a novel d-q transformation," in *Conf. Rec. IEEE Ind. Applicat. Soc. Annu. Meeting*, Vol. 2, Oct. 2003, pp. 1222–1227.
- [70] S. Sangwongvanich, "Speed-sensorless vector torque control of induction motors—Stability analysis and realization," in *Proc. IPEC*, Yokohama, Japan, 2001, pp. 310–315.
- [71] C. D. Schauder and R. Caddy, "Current control of voltage-source inverters for fast four-quadrant drive performance," *IEEE Trans. Ind. Appl.*, Vol. 18, No. 2, 1982, pp. 163–171.
- [72] C. Schauder, "Adaptive speed identification for vector control of induction motors without rotational transducers," *IEEE Trans. Ind. Appl.*, Vol. 28, No. 2, Sept./Oct. 1992, pp. 1054–1061.
- [73] D. Seborg, T. Edgar, and D. Mellichamp, *Process Dynamics and Control*, Wiley, 1989.
- [74] A. S. Sedra and P. O. Brackett, *Filter Theory and Design: Active and Passive*, Pitman Publishing Ltd, 1978.
- [75] W. Shepherd and L. Zhang, *Power Converter Circuits*. Marcel Dekker, 2004.
- [76] M.-H. Shin, D.-S. Hyun, S.-B. Cho, and S.-Y. Choe, "An improved stator flux estimation for speed sensorless stator flux orientation control of induction motors," *IEEE Trans. Power Electron.*, Vol. 15, No. 2, Mar. 2000, pp. 312–318.

- [77] S. Skogestad and I. Postlethwaite, *Multivariable Feedback Control*, John Wiley & Sons, Chichester, England, 1996.
- [78] K. Stockman, F. D'huister, and R. Belmans, "Torque capability of a field oriented induction motor drive under voltage sag conditions," in *Proc. 10th Eur. Conf. on Power Electron. and Applicat.*, Toulouse, France, 2003, CD-ROM.
- [79] T. Svensson, "On modulation and control of electronic power convertors," *Ph.D. Dissertation*, Chalmers Univ. of Technol., Gothenburg, Sweden, 1988.
- [80] I. Takahashi and T. Noguchi, "A new quick-response and high-efficiency control strategy of an induction motor," *IEEE Trans. Ind. Appl.*, Vol. 22, No. 2, Sept./Oct. 1986, pp. 820–827.
- [81] R. Teodorescu, F. Blaabjerg, M. Liserre, and P. C. Loh, "Proportional-resonant controllers and filters for grid-connected voltage-source converters," *IEE Proc.-Electr. Power Appl.*, Vol. 153, No. 5, Sep. 2006, pp. 750–762
- [82] P. Tiitinen, P. Pohjalainen, and J. Lalu, "The next generation motor control method: Direct Torque Control (DTC)," *EPE Journal*, Vol. 5, No. 1, Mar. 1995, pp. 14–18.
- [83] E. Twining and D. G. Holmes, "Grid current regulation of a three-phase voltage source inverter with an LCL input filter," *IEEE Trans. Power Electron.*, Vol. 18, No. 2, May 2003, pp. 888–895.
- [84] G. C. Verghese and S. R. Sanders, "Observers for flux estimation in induction machines," *IEEE Trans. Ind. Electron.*, Vol. 35, No. 2, Feb. 1988, pp. 85–94.
- [85] J. E. Volder, "The CORDIC trigonometric computing technique," *IRE Trans. Electron. Comput.*, Vol. 8, No. 3, pp. 330–334, 1959.
- [86] O. Wallmark, L. Harnefors, and O. Carlson, "An improved speed and position estimator for salient permanent-magnet synchronous motors," *IEEE Trans. Ind. Electron.*, Vol. 52, No. 2, Feb. 2005, pp. 255–262.
- [87] X. Xu, R. de Doncker, and D. W. Novotny, "Stator flux orientation control of induction machines in the field weakening region," in *Conf. Rec. IEEE Ind. Applicat. Soc. Annu. Meeting*, Vol. 1, Oct. 1988, pp. 437–443.
- [88] C.-H. Yim, I.-J. Ha, and M.-S. Ko, "A resolver-to-digital conversion method for fast tracking," *IEEE Trans. Ind. Electron.*, Vol. 39, No. 2, Oct. 1992, pp. 369–378.

